Cardiff University

Doctoral Thesis

Resonant Tunnelling in GaAs/AlGaAs Triple Barrier Heterostructures

---

Author:
Craig Allford

Supervisor:
Dr. P.D. Buckle

A thesis submitted in fulfilment of the requirements
for the degree of Doctor of Philosophy

in the

Condensed Matter and Photonics Group
Cardiff School of Physics and Astronomy

19th May 2016

Declaration of Authorship

I, Craig Allford, declare that this thesis titled, 'Resonant Tunnelling in GaAs/AlGaAs Triple Barrier Heterostructures' and the work presented in it are my own. I confirm that:

- This work has not been submitted in substance for any other degree or award at this or any other university or place of learning, nor is being submitted concurrently in candidature for any degree or other award.

  Signed:

  Date:

- This thesis is being submitted in partial fulfilment of the requirements for the degree of Doctor of Philosophy(PhD).

  Signed:

  Date:

- This thesis is the result of my own independent work/investigation, except where otherwise stated. Other sources are acknowledged by explicit references. The views expressed are my own.

  Signed:

  Date:

- I hereby give consent for my thesis, if accepted, to be available for photocopying and for inter-library loan, and for the title and summary to be made available to outside organisations.

  Signed:

  Date:

“The task is...not so much to see what no one has yet seen; but to think what nobody has yet thought, about that which everybody sees.”

- Erwin Schrödinger

CARDIFF UNIVERSITY

Abstract

Quantum Materials and Devices
Cardiff School of Physics and Astronomy

Doctor of Philosophy

Resonant Tunnelling in GaAs/AlGaAs Triple Barrier Heterostructures

by Craig ALLFORD

This thesis describes experimental and theoretical research into triple barrier resonant tunnelling structures which are attractive as potential high frequency oscillators in the terahertz frequency range. A lack of practical and coherent radiation emitters in this frequency range has resulted in it being named the "terahertz gap". However resonant tunnelling structures are seen as potential sources for practical solid state emitters which operate in this frequency range at room temperature.

A series of symmetric and asymmetric GaAs/$\text{Al}_{0.33}\text{Ga}_{0.67}\text{As}$ triple barrier resonant tunnelling structures have been studied at low temperatures to investigate the tunnelling electrical behaviour and origin of the current resonances observed in the current-voltage characteristics of these structures. The effect of charge accumulation in the emitter quantum well has been investigated, and has been found to significantly alter the behaviour of the electrical characteristics of the structures. These investigations have provided a thorough understanding of the behaviour of these structures and has allowed for optimisation of the triple barrier design with a view to being utilised as a high frequency emitter.

The current-voltage characteristics have also been studied as a function of temperature and a novel temperature dependent resonant tunnelling mechanism has been observed. The magnitude of the observed current resonance, which is associated with the energetic alignment to the $n = 1$ quasi-bound subband states increases with increasing sample temperature which is rare behaviour in systems dominated by quantum mechanics.

Finally, the maximum oscillation frequency and output power of these resonant tunnelling structures has been calculated and an optimised triple barrier structure in which charge accumulation in the emitter quantum well does not occur has been designed. Simulated current-voltage characteristics for this design shows it improves the maximum oscillation frequency and maximum output power reported in current state of the art double barrier resonant oscillator structures.

Acknowledgements

I would particularly like to gratefully acknowledge the unwavering support, invaluable guidance and continuous encouragement I have received throughout this process from my primary supervisor, *Dr. Phil Buckle.* I would also like to thank my secondary supervisor, *Dr. Dan Read*, for the enthusiasm and support he has shown over the past three and half years.

I would like to acknowledge *Prof. Mohamed Missous* from the School of Electrical and Electronic Engineering at The University of Manchester who grew the samples studied in this thesis and also to thank former undergraduate project students *Rebecca O'Donnell* and *Robert Legg* for their contributions to this work.

Of course this thesis would not have been completed without the help and support of numerous friends and colleagues at the School of Physics & Astronomy, Cardiff University. I would like to thank all of the technical and administrative support staff who have assisted me throughout my PhD, and I would also like to thanks the academic, postdoctoral and postgraduate community for the social interactions which have made my postgraduate studies a very enjoyable time.

I would like to thank *Kane Esien*, *Simon Olivari* and *Dr. Rob Thomas* for the many memorable and often hysterical random held conversations whilst sharing an office and I would also like to particular acknowledge *Dr. Rob Thomas* for his insight and advice given during our technical discussions.

I must of course also acknowledge my colleagues in the Condensed Matter and Photonics, Quantum Materials & Devices groups with special thanks to *Dr. David Hayes* for insightful discussions and assistance in understanding some of the principles of resonant tunnelling diodes and *George Smith* for the vast quantities of tea he has made during the writing of this thesis.

It is without question that my journey to this point would not have been possible without the unmeasurable love and support given to me by my family and friends. I would like to say an enormous thank you to my mother, *Jill*, father, *Philip*, and sister, *Louise*, for all the support they have given me. I would also like to recognise the support my partner's mother, *Fiona*, has given me during my studies, and to thank my four-legged friends *Hurley Dogg* and *Thor* for their unconditional love and attention also.

This acknowledgement section would not be complete without a mention of that very special person, my partner, *Laura.* You have supported me and brought joy into my life since the first day we met, I can not thank you enough for what you have given me so far, and I am looking forward to our future together.

Finally I would like to acknowledge the Engineering and Physical Research Council (EPSRC) for the studentship which has funded my studies and this work.

Contents

Abstract **i**

Acknowledgements **iii**

Contents **iv**

List of Figures **ix**

List of Tables **xxv**

Abbreviations **xxix**

1 Introduction **1**
- 1.1 Motivation 1
- 1.2 Historical Perspective 2
- 1.3 Recent Developments 4
- 1.4 Outline of Thesis 4
- 1.5 Contributions to the Field 6
- 1.6 List of Publications 7
- 1.7 Conference Presentations 7

2 GaAs and Semiconductor Heterostructures **15**
- 2.1 Basic Properties of GaAs 16
  - 2.1.1 Crystal Structure 16
  - 2.1.2 Electron Behaviour in GaAs 18
  - 2.1.3 Bandstructure of GaAs 20
- 2.2 Semiconductor Heterostructure Engineering 22
  - 2.2.1 Semiconductor Alloying 22
  - 2.2.2 Heterojunctions and Heterostructures 26
    - 2.2.2.1 Heterojunctions 26
    - 2.2.2.2 Heterostructures 27
  - 2.2.3 Quantum Wells 29

2.2.3.1 The Finite Quantum Well 29
2.2.4 Density of States in Three and Two Dimensions 32
2.2.4.1 Three Dimensions 32
2.2.4.2 Two Dimensions 33

3 Practical Realisation of Heterostructure Devices and Experimental Details 37
3.1 Practical Realisation of Heterostructure Devices 37
3.1.1 Molecular Beam Epitaxy (MBE) 37
3.1.2 GaAs/AlGaAs Wafer Design 39
3.1.3 Device Fabrication 41
3.1.3.1 Photolithography 41
3.1.3.2 Chemical Etching 43
3.1.3.3 Ohmic Contact Processing 44
3.1.4 Device Packaging and Design Evolution 45
3.2 Experimental Details 48
3.2.1 Variable Temperature Measurement System 48
3.2.2 Current-Voltage (I(V)) Measurement Set Up 49

4 Tunnelling in Triple Barrier Resonant Tunnelling Structures 53
4.1 Quantum Mechanical Tunnelling 53
4.2 Tunnelling in Multi-Barrier Heterostructures 55
4.3 Resonant Tunnelling 57
4.3.1 Double Barrier Resonant Tunnelling Structures 57
4.3.2 Triple Barrier Resonant Tunnelling Structures 59
4.3.3 Three Dimensional to Two Dimensional Tunnelling 62
4.3.4 The Effects of Series Resistance 64
4.4 The Symmetric Triple Barrier Resonant Tunnelling Structure 66
4.4.1 Positive Bias Characteristic 66
4.4.2 Negative Bias Characteristic 76
4.5 Asymmetric Triple Barrier Resonant Tunnelling Structures 78
4.5.1 Reducing the Collector Quantum Well Width 78
4.6 Perimeter vs Area Analysis 85
4.7 Device Self Heating and Charge Accumulation 98
4.8 Summary 100

5 Thermally Activated Resonant Tunnelling in Triple Barrier Structures 105
5.1 Thermally Activated Resonant Tunnelling
- Symmetric Structure 106
5.2 Thermally Activated Resonant Tunnelling
- Asymmetric Quantum Well Structures 111
5.2.1 Resonant Current Temperature Dependence 114
5.2.2 Critical Alignment Activation Energy 118
5.3 Summary 121

6 Triple Barrier Heterostructures for Terahertz Emitters 125
6.1 Requirements for Terahertz Emission 126

6.2 GaAs/$Al_{0.33}Ga_{0.67}As$ Triple Barrier Resonant Tunnelling Heterostructure Emitters . . . 127
6.2.1 Negative Differential Conductance . . . 128
6.2.2 Output Power . . . 130
6.2.3 Oscillation Frequency and Frequency Dependent Output Power . . 132
6.2.4 GaAs/$Al_{0.33}Ga_{0.67}As$ Triple Barrier Heterostructure Summary . . 140
6.3 Optimisation of Triple Barrier Heterostructures for High Power THz Emitters 141
6.3.1 An Optimised AlAs/$In_{0.90}Ga_{0.10}As$ Triple Barrier Resonant Tunnelling Structure . . . 142
6.3.2 A Strain Compensated Triple Barrier Resonant Tunnelling Structure to Minimise Emitter Quantum Well Charge Accumulation . . 151
6.4 Summary . . . 159

7 Conclusion and Future Investigation **165**
7.1 Conclusions . . . 166
7.2 Future Investigations . . . 169

A Schrödinger-Poisson Modelling **173**
A.1 Computational Methods . . . 173
A.1.1 Finite Difference Method . . . 174
A.1.2 Variable Effective-Mass Shooting Equation . . . 174
A.2 Boundary Conditions and Practical Implementation . . . 175
A.3 Poisson's Equation for Electrostatics . . . 178
A.4 The Self-Consistent Schrödinger-Poisson Model . . . 179

B The WinGreen Simulation Package **183**

C Photoluminescence Excitation Measurements (PLE) **189**

List of Figures

2.1 (a) The face centred cubic (fcc) Bravais lattice. Atoms are located at each of the eight verticies, with additional atoms located at each of the six faces of cube. (b) Zincblende structure of GaAs which shows two interpenetrating fcc sublattices of Ga (red spheres) and As (blue spheres). Covalent bonding between the four nearest neighbour atoms in a tetrahedral structure are shown (blue-red gradient lines). 16

2.2 (a) The Wigner-Seitz unit cell of a body centred cubic lattice (bcc), the bcc is the reciprocal lattice of the face centred cubic (fcc) direct lattice, and as such the Wigner-Seitz unit cell defines the first Brillouin zone of a fcc structure. (b) The first Brillouin zone of a face centred cubic direct lattice shown with a number of high-symmetry points. 17

2.3 A one dimensional periodic potential associated with a chain of idential equally spaces ions. The ion cores are seperated by a distance, a. 18

2.4 (a) The band structure for a monatomic lattice in a weak periodic potential with a perodicity, a (blue dots). The red line shows the E vs k relationship for a free electron. (b) The band structure for a periodic array of atoms, known as the "periodic zone scheme". (c) The band structure in the first Brillouin zone only, the "reduced zone scheme". 19

2.5 (a) Band structure for GaAs calculated by Chelikowsy and Cohen in 1976. A direct bandgap of 1.51 eV is calculated at the zone centre, Γ ($k = 0$), the region indicated by the blue box. (b) Schematic of the region around the band gap at the Γ point (indicated by the blue box). The conduction band (solid red line), light hole (purple dashed line), heavy hole (purple dashed-dotted line) and split off (dotted blue line) valence bands are shown. E_g is the fundamental bandgap, where Δ is the split off energy. 21

2.6 (a) The calculated energy difference between the top of the valence band and bottom of the Γ, X and L valley minima at 0K (solid black line) and 300K (dashed blue line) for $\mathrm{Al}_x\mathrm{Ga}_{(1-x)}\mathrm{As}$ with increasing alloy fraction. A cross over occurs where the smallest energy difference (band gap) switches from the Γ-valley to the X-valley minima. (b) The band gap for $\mathrm{Al}_x\mathrm{Ga}_{(1-x)}\mathrm{As}$ as a function of alloy fraction at 0K (solid black line) and 300K (dashed blue line). 23

2.7 The bandgap energy, E_g (eV) versus lattice constant, a_0, (Å) for several III-V compound semiconductors and their alloys at 300K. The alloy transitions between binary compounds are indicated by solid lines, representing a direct bandgap, and dashed lines, representing an indirect bandgap. . . . 25

2.8 The three types of heterojunctions, type I or straddling gap, type II or staggered gap and type III the broken gap, formed at the interface of two dissimilar materials. 26

2.9 Two different forms of heterostructures created by two type I heterojunctions. (a) The inclusion of a wider bandgap material ($\mathrm{Al}_x\mathrm{Ga}_{(1-x)}\mathrm{As}$) between two layers of narrower band gap material produces a potential barrier in the conduction and valence band edges. (b) Engineering a layer of narrower bandgap material (GaAs) between two layers of wider bandgap material ($\mathrm{Al}_x\mathrm{Ga}_{(1-x)}\mathrm{As}$) results in the formation of a potential well. . . . 28

2.10 A schematic of a triple barrier, double quantum well heterostructure created by alternating layers of GaAs and $Al_xGa_{(1-x)}As$ in the growth direction z. . . . 28

2.11 Schematics of a qunatum well of width d and barrier height V_0. (a) The particle wavefunctions for the $n = 1$ and $n = 2$ confined states are shown in blue. (b) The particle probability density for the $n = 1$ and $n = 2$ confined states are shown in red. . . . 30

2.12 Spheres in k-space of radius $\boldsymbol{k}$ and $\boldsymbol{k} + \mathrm{d}\boldsymbol{k}$. The volume of a shell of thickness $\mathrm{d}\boldsymbol{k}$ is given by subtracting the volume of one sphere from the other. . . . 32

2.13 The calculated density of states (DoS) for: (a) Bulk GaAs, using equation (2.36) (b) A GaAs quantum well of well width 350nm using equation (2.39). For a two-dimensional system the lowest available energy state is no longer at zero, but has been shifted to a higher energy due to the quantum confinement. The spacing in energy of the allowed quantum levels is proportional to $\mathrm{E}^{\frac{1}{2}}$ and hence the 2D DoS fits within the 3D Dos. In the limit where the spacing between the energy levels in a 2D system tends to zero, the 3D DoS and 2D DoS are equivilent. . . . 34

3.1 A simple schematic showing the main components under ultra-high vacuum required for molecular beam epitaxy growth. Several effusion cells of different elements are located such that an evaporated beam of molecules is targeted at a crystalline substrate on a heating block, with mechanical shutters controling which elements are incident on the substrate. . . . 38

3.2 A schematic of the triple barrier resonant tunnelling layer structure, which consists of n-type doped contact layers, undoped spacers layers of GaAs and an active region of three $\mathrm{Al}_{0.33}\mathrm{Ga}_{0.67}\mathrm{As}$ barrier layers, alternating with two GaAs quantum well layers. . . . 39

3.3 A calculated energy band diagram using the model described in appendix B, for a triple barrier resonant tunnelling structure described in section 3.1.2. The valence band edge, E_{VB} and conduction band edge, E_{CB} are shown, along with the calculated Fermi level, E_F, which lays within the conduction band. . . . 40

3.4 Schematics of the main processing steps in the fabrication of triple barrier resonant tunnelling structure devices. (a) Application of S1813 photoresist to the semiconductor substrate. (b) Exposure of the photoresist using ultraviolet radiation and a glass mask patterned with opaque metal. (c) The resultant resist profile after development of exposed resist to be used as an etch mask. (d) The mesa profiles once chemical etching of the substrate has taken place and resist etch maks removed. (e) Application of two layers of resis in a bi-layer process, SF6 and S1813. (f) The resultant resist profile after exposure of the resist to UV radiation and development, an undercut feature can be seen in the SF6 layer. (g) Thermal evaporation from a gold source where a film of metal is deopsited onto the substrate and resist surfaces. (h) The remaining gold contants and mesa profile after removal of the unwanted resist and metal. 42

3.5 An optical image of a typical 20-way ceramic package used for sample mounting. The diced up sample chip is mounted into the package recess using low temperature GE varnish. Electrical bonds are made between the contacts on the semiconductor substrate and the individual pin contacts on the package via a gold wire using a wedge bonding technique. 45

3.6 An optical microscope image of a V1.0 triple barrier resonant tunnelling structure chip. Bond wires can be seen making contacting the gold top of various size mesa structures and the gold bottom contact. The large distance between the device mesas and bottom contact introduces a large series resistance in the measurement circuit and is problematic for resonant tunnelling structure measurements. 46

3.7 An optical microscope image of a V2.0 triple barrier resonant tunnelling structure chip. Bond wires can be seen making contacting the gold top of various size mesa structures and the gold bottom contacts, which are now much closer ($\approx$ 50-500μm) to the devices. This resulted in a reduction of the series resistance introduced into the measurement circuit. 46

3.8 An optical microscope image of the V3.0 design contact mask. The bottom contact surrounds the top contact and is placed such that it will be in very close proximity to the mesa side wall. 47

3.9 A scanning electron microscope image of a 60 μm x 60 μm mesa V3.0 device. The top contact on the top of the mesa and bottom contact, surrounding the mesa can clearly be seen, with the distance between the bottom contact and the mesa sidewall being approximately 5 μm. 47

3.10 A simplified schematic of the main components in a pulse tube cryostat. A helium compressor generates an oscillating pressure, which in turn generates an oscillating gas flow. The expansion of helium gas in the pulse tubes reduces the temperature of the first and second stages. The pulse tubes and temperature stages are held in vacuum and thermally shielded to minimise any heat conduction between outside of the cryostat and the low temperature stages. 48

3.11 A schematic showing the circuit for the current-votlage measurements discussed in chapters 4 and 5. The measurement hardware and four-wire technique used down the device under test (DUT) are explained in the main body text. 50

4.1 A schematic showing a single potential barrier, of height V_0. The wavefunction of a state with less energy than V_0 propagates from the left-hand side of the barrier (region I) and penetrates into the clasically forbidden barrier, region II. The wavefunction decays exponentially in the barrier region, but does not decay totally to zero, it then continues to propagate on the right-hand side of the barrier (region III) with a smaller amplitude than region I. 54

4.2 (a) The calculated transmission probability $T(E)$ as a function of energy for the single potential barrier shown in figure 4.2(b), the method for calculation is based on that described in [3]. (b) A single potential barrier of energy 0.3eV and width 8nm. The effective masses used in the calculation of figure 4.2(a) for the barrier and outer regions are $0.09439m_e$ and $0.067m_e$ respectively, where m_e is the electron rest mass. 54

4.3 (a) The calculated transmission probability $T(E)$, for the double potential barrier single quantum well heterostructure shown in figure 4.3(b) (solid blue line) and the single potential barrier (dotted red line) from figure 4.2. Clear resonant peaks in the tunnelling probability can be seen at energies equal to those of the confined states shown in figure 4.3(b). (b) The potential profile and associated confined state wavefunction (solid blue line) and probability density (dotted red line) for a double barrier single quantum well heterostructure with well width 67Å and barrier widths 8nm. In this structure $n = 1$ and $n = 2$ quantum well states are formed, with the wavefunction only calculated for the barrier and quantum well regions. 56

4.4 (a) The calculated transmission probability $T(E)$, for the triple potential barrier double quantum well heterostructure shown in figure 4.4(b). Four resonant peaks in the tunnelling probability can be seen at energies equal to those of the four confined states shown in figure 4.4(b). A close up of the region indicated by the dashed box shows that although very close together, there are two distinct peaks for the $n = 1$ level. (b) The potential profile and associated confined state wavefunction (solid blue line) and probability density (dotted red line) for a triple barrier double quantum well heterostructure with well widths 67Å and barrier widths 8nm. In this structure two $n = 1$ and two $n = 2$ sub-band quantum well states are formed, with the wavefunction only calculated for the barrier and quantum well regions. 57

4.5 A simulated current density vs voltage plot for a double barrier resonant tunnelling structure showing a resonant current peak followed by a region of negative differential resistance. The labels a,b,c and d refer to figures 4.6(a) to 4.6(d) respectively which show the conduction band potential profile, local density of states (LDOS) and tunnelling probability (T(E)) at each point. 58

4.6 The simulated (details of which can be found in appendix B) conduction band potential profile, local density of states (LDOS) and tunnelling probability for a double barrier resonant tunnelling structure for applied voltages of: (a) 2 mV, (b) 58 mV, (c) 114 mV and (d) 180 mV. 58

4.7 (a) The calculated tunnelling probability, T(E), for a triple barrier resonant tunnelling structure under zero bias, as seen in figure 4.8(a). Two resonant peaks for each quantum well subband can be seen, with the tunnelling probability at the resonant peaks being unity. A magnified look at the $n = 1$ subband resonant peaks is shown inset. (b) The calculated tunnelling probability, T(E), for the structure seen in figure 4.8(b) which has an applied voltage of 50 mV. A dramatic decrease in the tunnelling probability for the $n = 1$ subband resonances can be seen, caused by the energetic misalignment of the subband states. A decrease is also seen in the tunnelling probability for the $n = 2$ subband states, however this is smaller as these states are still partially energetically aligned. 60

4.8 The simulated (details of which can be found in appendix B) conduction band potential profile and local density of states for a triple barrier resonant tunnelling structure for applied voltages of: (a) 0 mV, (b) 50 mV. The tunnelling probability for (a) and (b) are shown in figures 4.7(a) and 4.7(b). 61

4.9 The potential profile and associated probability density (red line) for a triple barrier double quantum well heterostructure with a voltage of 50 mV applied in a linear potential drop model. In this structure two $n = 1$ and two $n = 2$ sub-band quantum well states are formed, however, due to the applied voltage the $n = 1$ states are highly localised to a specific quantum well, which results in a decrease in the tunnelling probability for these energies (as can be seen in figure 4.7(b)). The $n = 2$ states also become more localised to a specific quantum well, however the effect is not as strong. The wavefunctions in this simulation are only calculated for the barrier and quantum well regions. 61

4.10 The electron distribution in the conduction band of a degenerately doped three dimensional semiconductor region, such as the emitter in a resonant tunnelling structure. The distributions are shown for low temperatures of 3K (solid blue), 24K (dotted green) and 45K (dashed red) and it can be seen the maximum carrier density is seen well above the conduction band edge (0.0 eV). 62

4.11 (a) The distribution of occupied states for three dimensions in reciprocal space, this solid sphere at 0K is known as the Fermi sphere. (b) A two dimensional system, confined in the k_z direction. For this state the allowable wavevectors are given by an infinite sheet in the k_x and k_y directions, with thickness Δk_z. 63

4.12 The intersection of a three dimensional and two dimensional (confined in the k_z direction) allowable wavevectors in reciprocal space, for: (a) A small energy (or wavevector, k_z) below the surface of the Fermi sphere. (b) At the equator (in k_z of the Fermi sphere), i.e. the conduction band edge. The wavevectors which fulfil the conservation of momentum and energy requirements for 3D to 2D tunnelling are shown by the formation of a disc of thickness Δk_z where the Fermi sphere and infite sheet overlap (shaded in red). 63

4.13 A simulated current density vs voltage plot for a double barrier resonant tunnelling structure as previously shown in figure 4.5, the blue diamonds indicate the ideal characteristic with no simulated series resistance. A series resistance of 1.5x10^{-6} Ωcm^2 (equivalent to $\approx 42\,\text{m}\Omega$ for a $60\,\mu$m $\times$ $60\,\mu$m diode) has been simulated and added to the ideal I(V) characteristic and is indicated by the plot of red circles and black crosses. The black crosses indicate the data points which could possibly be "lost" by a conventional I(V) measurement circuit. 64

4.14 Simulated current density vs voltage plot for a double barrier resonant tunnelling structure with a simulated series resistance. A bistable region forms due to the introduction of a series resistance, which can lead to a hysteresis in the forward and backwards measured directions. The forward measured direction plot is shown by the black crosses, where the DUT remains in the high current stable state in the bistable region where as the red circles show the backwards measurement direction where the DUT remains in the low current state. 65

4.15 (a) The positive bias, forward and backward direction, Current Density vs Voltage characteristic for a 60 μm x 60 μm nominally symmetric TBRTS. Three main features of interest are visible, with each indicated by a red ellipse and labelled F1, F2 and F3 respectively. (b) An enlarged plot of the feature, F1 from figure 4.15(a). Each of the features, F1, F2 and F3 show a region of negative differential resistance which is characteristic of the resonant tunnelling process. 66

4.16 A schematic of the conduction band edge potential profile for a simple linear voltage drop model, with a voltage of V_s applied. The energy of the first and second QW confined states, $\text{E}_{\text{W}1}$ and $\text{E}_{\text{W}2}$ are assumed to be shifted in energy by the same amount as a point in the middle of their respective QW. Only the length of the undoped spacers and the active region of the device, L_T are considered, whilst the distance to the centre of the first and second QWs are $\text{L}_{\text{W}1}$ and $\text{L}_{\text{W}2}$ respectively. 67

4.17 The calculated conduction band potential profile (black line) and electron probability density (red lines) output from a self-consistent Schrödinger-Poisson model for the nominally symmetric TBRTS. Due to a slight asymmetry in the widths of the first (W1) and second (W2) quantum wells, the electron probability densities are more localised to a specific QW. The states more localised to W1 are known as $\text{E}_{1_{\text{W}1}}$ and $\text{E}_{2_{\text{W}1}}$, where similarly for W2 the $n = 1$ and $n = 2$ states are $\text{E}_{1_{\text{W}2}}$ and $\text{E}_{2_{\text{W}2}}$. 68

4.18 The low voltage ($<$ 200 mV) current-density vs voltage (blue lines) for the nominally symmetric triple barrier resonant tunnelling structure with the current scaled by ×1 and ×20. The red dashed lines indicate the predicted voltages at which the resonances associated with the alignment of the $n = 1$ subband states and the conduction band edge should occur. There is excellent agreement between the theoretical and experimental results. . 69

4.19 The I(V) characteristic (blue solid line) for the nominally symmetric TBRTS centred on the feature F2. Two typical current resonances are overlayed (red diamonds) to illustrate the possibility of that the feature is a construct of two separate resonances, spaced closely in voltage, with the smaller, lower voltage resonance attributed to the energetic alignment of $E_{1_{W1}}$ and E_{CB}, and the second larger resonance attributed to the alignment of a two-dimensional state in the triangular potential of the emitter region, $E_{M_{2D}}$. 70

4.20 (a) The experimental (blue line) and simulated (red triangles) forward bias characteristic for the nominally symmetric TBRTS. (b) The low voltage region of the forward bias experimental (blue) and simulated (red) characteristic for the nominally symmetric structure. There is good agreement between the experimental and simulated voltages at which the resonant peaks occur for features F1 and F3. 70

4.21 (a) The calculated conduction band potential profile (blue solid line) and net charge distribution (red dotted line) for the nominally symmetric structure with 0.125V applied. A positive net charge (which represents an excess of electrons) can be seen in the first quantum well which is circled and labelled point A. (b) The calculated conduction band potential profiles with 0.25V applied for the case with (solid blue line) and without (dashed blue line) charge accumulation. In the situation where charge accumulates in the first quantum well the conduction band edge is held high and results in a pinning of the first QW confined state, $E_{1_{W1}}$ in energeteic alignment with the emitter electron distribution. Where the accumlation of charge in the first quantum well is forbidden $E_{1_{W1}}$ drops below the conduction band edge and so the resonant tunnelling current diminishes. The net charge destribution (red dotted line) for the case with charge accumulation is also shown. 71

4.22 The calculated tunnelling probability for the nominally symmetric TBRTS with 0.15V applied for the situations where charge is allowed (solid black line) and forbidden (dash-dotted black line) to accumulate in the first quantum well are shown. The peaks in the tunnelling probability associated with the $E_{1_{W1}}$ and $E_{1_{W2}}$ confined states are at a higher energy when charge is allowed to accumulate, than when charge accumulation is forbidden. The energy of the conduction band edge, E_{CB} (dashed blue) and Fermi level, E_F (dotted red) are also shown. 72

4.23 The calculated tunneling probability against applied voltage for the nominally symmetric TBRTS at the Fermi level, E_F (red solid line) and conduction band, E_{CB} (blue solid line) for (a) the case where charge is allowed to accumulate in the first quantum and (b) where charge is forbidden to accumulate in the first quantum well. 73

4.24 The experimental forward bias characteristic at x1 (solid blue) and x5 (dotted blue) scales. The simulated characteristic for the nominally symmetric structure is also shown (red triangles) from which it is clear to see another current density resonance feature, F4. This feature is associated with the energetic alignment of the $E_{2_{W2}}$ localised state with the emitter electron distribution. 74

4.25 The experimental current density vs voltage characteristic for the nominally symmetric TBRTS. An estimate of the widths in voltage of the resonances associated with the $E_{1_{W2}}$ and $E_{1_{W1}}$ confined states from simulated results (figures 4.23(a) and 4.23(b) are shown for: (a) The case where charge accumulation in the first quantum well is allowed, V_{1C} and V_{2C}; (b) The case where charge accumulation in the first quantum well is forbidden, V_{1NC} and V_{2NC}. 75

4.26 The calculated conduction band potential (solid blue line) and local density of states (LDOS) for the nominally symmetric TBRTS with 170 mV external voltage applied. Charge accumulation in the first quantum well is forbidden in this case, where a 2D state forms in the triangular well region of the emitter (circled). 75

4.27 (a) The full experimental current-voltage (I(V) characteristic in the forward and reverse bias directions for the nominally symmetric TBRTS at 3K in which it can be seen that there are striking similarities between the forward and reverse bias directions. (b) The forward (solid blue) and reverse (dashed red) I(V) characteristics overlain on the same axis for the nominally symmetric TBRTS at 3K. The small unintentional asymmetry in the two quantum wells and intended asymmetry due to the inclusion of a δ-doped layer in the structure results in the difference between the two characteristics. 77

4.28 The predicted voltages at which the current resonances will occur for the $n = 1$ localised confined states in the forward bias, $E_{1_{W1}}$ (solid circle) and $E_{1_{W2}}$ (solid square), and reverse bias, $-E_{1_{W2}}$ (open square) and $-E_{1_{W1}}$ (open circle) directions. With the increase in quantum well asymmetry it can be seen that in the forward bias direction resonances converge, whilst the reverse bias direction resonances diverge. 79

4.29 The raw current-voltage (I(V)) characteristics for the series of VMBE samples with increasing quantum well asymmetry at 3K. The characteristics for each different structure are offset by 50 mA for clarity and are given in increasing asymmetry order (most symmetric at the bottom, most asymmetric at the top). The forward bias simple model predicted current resonance voltages for the $E_{1_{W1}}$ (blue solid circle) and $E_{1_{W2}}$ (red solid square) are also shown. A very large single resonance is seen in the most asymmetric structure which is attributed to the coincidental energetic alignment of the quantum well confined states with each other and conduction band edge. 80

4.30 The series-resistance adjusted current-voltage (I(V)) characteristics at 3K, an effective resistance of 0.8 Ω has been removed for all characteristics except VMBE 760 (third from bottom) which has had 3.5 Ω removed. Each characteristic is offset by 50 mA from the previous for clarity (for VMBE 787 there is a 100 mA offset) with the most symmetric at the bottom and most asymmetric at the top. The forward bias simple model predicted current resonance voltages for the $E_{1_{W1}}$ (blue solid circle) and $E_{1_{W2}}$ (red solid square) are given and lines to guide the eye to the evolution of the features F1/F2-1, F2-2 and F3 are also shown. 83

4.31 (a) The series resistance adjusted I(V) characteristic for the most asymmetric structure, VMBE 787. The peak (blue) and valley (red) currents of the large single resonance are circled, with the peak-to-valley current ratio of this resonance calculated to be ≈ 6. (b) The calculated peak-to-valley current ratio for the features F1/F2-1, F2-2 and F3 which have discernible NDR regions against quantum well asymmetry. 84
4.32 The measured current-voltage characteristics of five different devices varying in mesa side wall length for (a) the nominally symmetric structure and (b) the most asymmetric structure. A general trend of increasing current magnitude with increasing mesa size is observed. 85
4.33 The low voltage measured current-voltage characteristics of five different devices varying in mesa side wall length for (a) the nominally symmetric structure and (b) the most asymmetric structure. In both samples the low voltage region current does not follow this general trend with the magnitude of the current appearing to be random with device size. 86
4.34 The current values at 50 mV for devices with varying size mesa sizes. (a) The 50 mV current values against the measured device mesa perimeter for the nominally symmetric (red squares) and most asymmetric (blue circles) triple barrier resonant tunnelling structures. There is no clear correlation between the measured current and either calculated perimeter or calculated mesa area. 87
4.35 The parallel conduction adjusted I(V) characteristics of TBRTS devices with varying mesa size for (a) the nominally symmetric structure and (b) the most asymmetric structure. 88
4.36 The measured I(V) characteristics for (a) the nominally symmetric TBRTS and (b) the most asymmetric TBRTS after adjustment to the voltage to take into account the change of the device resistance relative to the constant series resistance. 89
4.37 The valley current at 420 mV for VMBE 755 (red squares) and 520 mV for VMBE 787 (blue circles) plotted against (a) calculated mesa perimeter and (b)calculated mesa area. Second order polynomial fits are made to each data to explore the linearity of each. 90
4.38 The peak current at 340 mV for VMBE 755 (red squares) and 180 mV for VMBE 787 (blue circles) plotted against (a) calculated mesa perimeter and (b) calculated mesa area. Second order polynomial fits are made to each data set and show that the current scales more linearly with perimeter than area, which is an unexpected result. 90
4.39 The peak (green diamonds) and valley (magenta triangles) currents against (a) mesa perimeter and (b) mesa area for the feature F3 in the nominally symmetric triple barrier resonant tunnelling structure I(V) characteristic and (c) mesa perimeter and (d) mesa area for the large single resonance feature in the most asymmetric structure VMBE 787. 91
4.40 The calculated peak-to-valley current ratio for the extracted peak and valley currents for the features VMBE 755 F3 (blue circles) and VMBE 787 F1/F2-1 (red squares) against (a) mesa perimeter and (b) mesa area. Second order polynomial fits to the data are also shown. 93

4.41 (a) The one dimensional current density-voltage characteristic for the nominally symmetric TBRTS after adjustment for the apparent change in series resistance with mesa size. (b) The one dimensional current density-voltage characteristic for the nominally symmetric TBRTS after adjustment for the apparent change in series resistance with mesa size. . . 94

4.42 (a) The one dimensional current density-voltage characteristic for the most asymmetric TBRTS after adjustment for the apparent change in series resistance with mesa size. (b) The one dimensional current density-voltage characteristic for the most asymmetric TBRTS after adjustment for the apparent change in series resistance with mesa size. 94

4.43 An illustration of a TBRTS device under a positive bias V. The current flows from the top contact through the TBRTS active layers, which has a resistance R_{TBRTS} to the bottom contact which is 5 μm from the bottom of the mesa edge. The resistance associated with the GaAs layers (all layers excluding the TBRTS active layers) is given by R_S, which varies and is dependent on the path taken by the current (i.e. the long path, the higher resistance) 95

4.44 The simulated current distribution in arbitrary units for TBRTS devices which are off resonance (a) 159 x 159 μm (c) 59 x 59 μm (e) 5 x 5 μm. The simulated current distribution for on resonance TBRTS are also shown for (b) 159 x 159 μm (d) 59 x 59 μm (f) 5 x 5 μm devices. 96

4.45 The peak areal current density against mesa area for VMBE 787, the most asymmetric structure. With decreasing mesa area the maximum current density increases due to the current path distribution becoming more uniform over the full mesa area as explained by the model in figures 4.43 and 4.44. 97

4.46 The continuous wave (CW) (solid black) and pulsed voltage (dotted red) I(V) characteristics at 3K for (a) the nominally symmetric TBRTS and (b) the most asymmetric TBRTS. The calculated difference between the puled voltage and CW current for each structure is also shown (solid green), focusing on regions of the I(V) characteristic where the device is in a stable (non NDR) state. 99

5.1 The positive bias, forward and backward direction, current-voltage characteristic for a 60 μm x 60 μm nominally symmetric TBRTS at various temperatures (only every 50K shown for clarity). A resonant feature which is not visible at low temperatures, F0, emerges as the sample temperature is increased. (b) An enlarged plot of the emerging resonant feature which exhibits a region of negative differential resistance which is still discernible at 293K. 106

5.2 (a) A schematic of the conduction band potential profile for a totally symmetric TBRTS under zero bias. The electron probability density is also shown (red) and is equally distributed between each of the quantum wells (W1 and W2) and extends across the entire structure, resulting in a high tunnelling probability for charge carriers at these energies. (b) A schematic of the conduction band potential profile for a totally symmetric TBRTS with voltage applied across the device. The electron probability distribution is now localised to a specific quantum well, which dramatically decreases the tunnelling probability of charge carriers at each of the specific quantum well state energies. 107

5.3 (a) The 3D emitter carrier density distribution at various temperatures from 3K (blue) where there is a sharp, well defined distribution to 293K (red) where the carriers are now distributed over many different energies. (b) The conduction band potential profile for a totally symmetric triple barrier resonant tunnelling structure, the electron probability distribution (shown in red) is equally distributed between the emitter and collector quantum wells. 108

5.4 The positive and negative bias, forward and backward direction, I(V) characteristic for a 60 μm x 60 μm nominally symmetric TBRTS at various temperatures (only every 50K shown for clarity). A resonant feature which is not visible at low temperatures, F0 (or -F0 in the negative bias direction), emerges as the sample temperature is increased. (b) An enlarged plot of the emerging resonant feature which exhibits a region of negative differential resistance which is still discernible at 293K. 109

5.5 The extracted peak (red squares) and valley (green triangles) currents from the series resistance adjusted I(V) characteristic for the nominally symmetric TBRTS at various temperatures. The calculated peak-to-valley current ratio (PVCR) is also shown (solid blue crosses). 110

5.6 (a) A schematic of the conduction band potential profile for a asymmetric TBRTS under zero bias. The electron probability density is also shown (red) and is localised to a specific quantum well (W1 or W2) (b) A schematic of the conduction band potential profile for an asymmetric TBRTS with voltage applied across the device which is sufficient to energetically align the quantum well confined states and form an $n = 1$ subband. The electron probability distribution extends across the entire structure resulting in a high transmission probability for charge carriers energetically aligned to this subband. 111

5.7 The positive bias, forward and backwards direction I(V) characteristics at various temperatures for the series of asymmetric TBRTS: (a) VMBE 757, (b) VMBE 760, (c) VMBE 761, (d) VMBE 762, (e) VMBE 788, (f) VMBE 787. The thermally activated resonance is indicated by the label X. 112

5.8 (a) The thermally activated $n = 1$ subband critical alignment resonance peak current with increasing temperature for the range of seven VMBE TBRTS samples. (b) The thermally activated $n = 1$ subband critical alignment resonance valley current with increasing temperature for the range of seven VMBE TBRTS samples. The discontinuities in VMBE 788 are due to a sudden switch in the voltage at which the valley current occurs, shown in figure 5.10(b) with the origin of the switch still unclear at the time of writing. 114

5.9 (a) A schematic of the conduction band potential profile for a symmetric TBRTS under zero bias showing the energy difference between the $n = 1$ subband and the conduction band edge, ΔE and the probability density of the confined states (red). (b) A schematic of the conduction band potential profile for an asymmetric TBRTS with voltage applied across the device which is sufficient to energetically align the quantum well confined states and form an $n = 1$ subband. The energy difference between the $n = 1$ subband and the conduction band edge is less than in (a) due to the bias required to align the quantum well states. 115

5.10 (a) The calculated peak-to-valley ratio against sample temperature for the series of TBRTS with varying quantum well asymmetry. The discontinuity observed in the PVCR for VMBE 788 is a result of a sharp change in valley current voltage, which results in a lower valley current and is shown in figure 5.10(b). (b) The I(V) characteristic for VMBE 788 between 85K and 95K with characteristics for every 2K shown. At temperatures 85K and below, and 135K and above the valley current for the resonance is located at approximately 230 mV. A shift in the valley current voltage out to approximately 470 mV occurs between 87K and 133K where there are no longer two distinct resonances, as the NDR region merges across both. 116

5.11 The maximum peak-to-valley current ratio (PVCR) against ratio of quantum well widths (Emitter:Collector) which is a measure of the asymmetry of the triple barrier resonant tunnelling structures. Below a QW ratio of 1.425 there is a good fit to linear function for the maximum PVCR, however for the most asymmetric structure which has a QW ratio of 1.4375 this point no longer fits the trend as there is a dramatic increase in PVCR. 117

5.12 A conduction band potential schematic showing the critically aligned $n = 1$ subband quantum well states (red) and the activation energy, $\mathrm{E_a}$, which is the difference between the Fermi Energy and the energy of the $n = 1$ subband states. 118

5.13 (a) The experimentally extracted Arrhenius plots for the series of seven VMBE TBRTS devices between 83K and 250K. Straight line fits to extract the gradient are made to each with the determined activation energies shown in figure 5.14. (b) The theoretically calculated Arrhenius plots for the series of seven VMBE TBRTS devices between 83K and 250K. Straight line fits to extract the gradient are made to each with the determined activation energies shown in figure 5.14. 120

5.14 The experimentally determined (red diamonds) and theroretically calculated (blue circles) activation energies against quantum well width ratio (emitter:collector) for the $n = 1$ subband critical alignment current resonance. There is good agreement between the experimental and theoretical data with a straight line fit made to the experimental results. 121

6.1 The extracted peak to valley current (ΔI) from the series resistance adjusted I(V) characteristics for the current resonance attributed to the $n = 1$ critical subband alignment for the series of VMBE TBRTS devices against sample temperature. Only every fifth data point is shown for clarity. 128

6.2 The extracted peak to valley voltage (ΔV) from the series resistance adjusted I(V) characteristics for the current resonance attributed to the $n = 1$ critical subband alignment for the series of VMBE TBRTS devices against sample temperature. Only every fifth data point is shown for clarity. 129

6.3 The calculated average negative differential conductance, G, using equation (6.4), plotted against sample temperature for the series of VMBE TBRTS devices. Only every fifth data point is shown for clarity. 130

6.4 The calculated steady state maximum output power from equation (6.5) for the series of VMBE devices against sample temperature. 131

6.5 The maximum output power density against sample temperature calculated from equation (6.5) using values extracted from I(V) characteristics for series of VMBE devices with approximate mesa areas of 3480 $\mu\mathrm{m}^2$. 131

6.6 The calculated maximum oscillation frequency (blue circles) from equation (6.3) and frequency dependent maximum output power (black squares) from equation (6.7) for the most asymmetric TBRTS device, VMBE 787. The device has an active mesa area of ≈ 3480 μm^{-2}. 132

6.7 The extracted peak to valley current difference, ΔI, for the most asymmetric TBRTS, VMBE 787 for a device with mesa area ≈ 3480 μm^{-2}. Two clear regions with different dependency on temperature can be seen and exponential fits are made to both of these regions. 133

6.8 The extracted peak to valley voltage difference, ΔV, for the most asymmetric TBRTS, VMBE 787 for a device with mesa area ≈ 3480 μm^{-2}. Two clear regions with different dependency on temperature can be seen and exponential fits are made to both of these regions. A fit to the high temperature region above the sharp discontinuity which can be seen is also made. 134

6.9 The experimentally measured I(V) characteristic for the most asymmetric sample VMBE 787 at 3K (solid blue) and 293K (solid red) with the position of the extracted “hidden valley” indicated by a red cross. The I(V) characteristic for the second most asymmetric structure VMBE 788 is also shown (dashed blue) along with line of average negative differential conductance from the resonance peak current to the hidden valley and from the hidden valley to the observed valley (dotted black). 135

6.10 The experimentally measured I(V) characteristic for the most asymmetric sample VMBE 787 at 3K (solid blue) and an illustrated estimation of the steady state I(V) characteristic in the negative differential region (dotted blue). The combination of two separate resonances can form a “shoulder” in the NDR region, thus resulting in two regions with significantly different mean negative differential conductances. 136

6.11 The calculated maximum oscillation frequency (blue circles) from equation (6.3) and frequency dependent maximum output power (black squares) from equation (6.7) for the region G_1 using the fits I_2 and V_3 for a device which has an active mesa area of ≈ 3480 μm^{-2}. Polynomial fits to both oscillation frequency and maximum output power are also shown. 137

6.12 The calculated maximum oscillation frequency (blue circles) and frequency dependent maximum output power (black squares) in the region G_2 for a device which has an active mesa area of ≈ 3480 μm^{-2}. The values of ΔI and ΔV used in equations (6.3) and (6.7) were calculated from equations (6.8) and (6.9). Polynomial fits to both oscillation frequency and maximum output power are also shown. 137

6.13 The polynomial fits to the maximum oscillation frequency (blue) and frequency dependent maximum output power (black) in both NDC regions, G_1 (solid lines) and G_2 (dash-dotted lines) for a device which has an active mesa area of ≈ 3480 μm^{-2}. 138

6.14 The calculated maximum oscillation frequency (blue circles) from equation (6.3) and frequency dependent maximum output power (black squares) from equation (6.7) for VMBE 788. Polynomial fits to both the maximum oscillation frequency and maximum output power are also shown. 139

6.15 (a) The simulated current density against applied voltage for the structure reported by Kanaya et al. [14]. There is very good agreement between the simulated and experimentally measured values for a 12nm collector, shown in figure 6.15(b). (b) The experimentally measured current density against voltage from [14]. 141
6.16 The simulated current density against voltage characteristics for the structures detailed in table 6.3 with a quantum well width ratio, R (emitter:collector), of (a) R $\geq$ 1, (b) R $\leq$ 1. The simulated structure reported in [14] and shown in figure 6.15 are also given. 143
6.17 The calculated mean negative differential conductance, G (open circles) and steady state output power density (open squares) against the degree of quantum well width asymmetry (emitter:collector). The dotted and dashed line represent the calculated mean negative differential conductance and steady state output power density values respectively for the Kanaya et al. double barrier structure, whilst the dash-dotted box indicates those structures that offer the best negative differential resistance and output power density. 144
6.18 The simulated current density against voltage characteristics for the structures detailed in table 6.4 for varying middle barrier widths. The simulated structure reported in [14] and shown in figure 6.15 are also given. 146
6.19 The calculated mean negative differential conductance, G (open circles) and steady state output power density (open squares) against the width of the middle barrier. The dotted and dashed line represent the calculated mean negative differential conductance and steady state output power density values respectively for the Kanaya et al. double barrier structure. 146
6.20 The calculated output to input ratio based on the figure of merit by Baba et al. [23] (open crosses) and the extracted peak resonance voltage (open diamonds) against the width of the middle barrier. The dotted and dashed line represent the peak resonance voltage and calculated input to output power ratio values respectively for the Kanaya et al. double barrier structure. 147
6.21 The simulated current density against voltage characteristics for the structures detailed in table 6.5 for varying middle barrier widths. The simulated structure reported in [14] and shown in figure 6.15 are also given. 149
6.22 The calculated mean negative differential conductance, G (open circles) and steady state output power density (open squares) against the width of the emitter barrier. The dotted and dashed line represent the calculated mean negative differential conductance and steady state output power density values respectively for the Kanaya et al. double barrier structure. The red circle and square are included as a reference and represent the mean negative differential conductance and output power density respectively for the structure ALL 4.6, which is not strain compensated. 149
6.23 The calculated output to input ratio based on the figure of merit by Baba et al. [23] (open crosses) and the extracted peak resonance voltage (open diamonds) against the width of the emitter barrier. The dotted and dashed line represent the peak resonance voltage and calculated input to output power ratio values respectively for the Kanaya et al. double barrier structure. 150

6.24 The simulated current density against voltage characteristics for the structure design ALL 4.6c given in table 6.5 where charge accumulation in the emitter quantum well is allowed and forbidden. The simulated structure reported in [14] and shown in figure 6.15 are also given. 151

6.25 The calculated mean negative differential conductance, G, plotted against the varied width of the collector quantum well for the In53A (open circles), In53B (open diamonds), In53C (open squares) and In53X (open crosses) design variations detailed in tables 6.7 to 6.10. Third order polynomial fits to each data set are also shown whilst the dashed line represents the calculated mean negative differential conductance for the Kanaya et al. double barrier structure. 155

6.26 The calculated steady state output power density plotted against the varied width of the collector quantum well for the In53A (open circles), In53B (open diamonds), In53C (open squares) and In53X (open crosses) design variations detailed in tables 6.7 to 6.10. Third order polynomial fits to each data set are also shown whilst the dashed line represents the calculated steady state output power density for the Kanaya et al. double barrier structure. 155

6.27 The extracted resonance peak voltage plotted against the varied width of the collector quantum well for the In53A (open circles), In53B (open diamonds), In53C (open squares) and In53X (open crosses) design variations detailed in tables 6.7 to 6.10. Third order polynomial fits to each data set are also shown whilst the dashed line represents the extracted resonance peak voltage for the Kanaya et al. double barrier structure. 156

6.28 The calculated input to output power efficiency plotted against the varied width of the collector quantum well for the In53A (open circles), In53B (open diamonds), In53C (open squares) and In53X (open crosses) design variations detailed in tables 6.7 to 6.10. Third order polynomial fits to each data set are also shown whilst the dashed line represents the calculated input to output power efficiency for the Kanaya et al. double barrier structure. 156

6.29 The calculated frequency dependent output power density for the optimised double barrier structure by Kanaya et al. [14], and improved triple barrier resonant tunnelling structure designs In53B.1 and In53B.6. 158

A.1 Numerically obtained wavefunctions for an electron in a conduction band potential profile (solid black line) for a 67Å wide GaAs quantum well with $\mathrm{Al}_{0.33}\mathrm{Ga}_{0.67}\mathrm{As}$ barriers of height 0.264 eV. The true n = 1 steady state solution is shown (solid blue line) at $E = -53.6414160$meV. Wavefunctions (dashed green lines) ±0.1neV the energy of the true solution are also shown diverging to $+\infty$ to $-\infty$. 177

A.2 Numerically obtained conduction band potential profile (black) for a 67Å wide n-type doped GaAs quantum well with doping density $1 \times 10^{19} cm^{-3}$ between two $\mathrm{Al}_{0.33}\mathrm{Ga}_{0.67}\mathrm{As}$ undoped barrier regions with barrier height 0.264V. The probability distribution of the n=1 confined solution is also shown (red). 180

List of Tables

2.1 A summary of important material parameters at 300K for GaAs and $Al_{0.33}Ga_{0.67}As$. 24

3.1 The measured quantum well widths by photoluminescence excitation (PLE) for the series of VMBE samples grown by MBE at The University of Manchester. For details of these measurements see appendix C. 40

3.2 The ratio of the expected and measured quantum well widths for wells A to B for the series of VMBE samples. 41

4.1 The required voltage to align the $n = 1$ confined states of the nominally symmetric triple barrier resonant tunnelling structure with the conduction band edge E_{CB} in the simple linear voltage drop model. 68

4.2 A summary of the origin of each of the features seen in the current density against voltage characteristics for the nominally symmetric TBRTS, figures 4.15(a), 4.15(b) and 4.24. 76

4.3 The measured quantum well width ratio and $n = 1$ confined state energies calculated from a a self-consistent Schrödinger-Poisson model (appendix A) for the series of seven samples studied in this section. 78

4.4 The measured quantum well width ratio and $n = 2$ confined state energies $E_{2_{W1}}$ and $E_{2_{W2}}$ calculated from a a self-consistent Schrödinger-Poisson model for the series of seven samples studied in this section. 81

4.5 The measured mesa wet etch depth for the series of seven VMBE samples. The increased etch depth of VMBE 760 has introduced a small but significant extra series resistance which can not be removed from the measurement circuit. 82

4.6 The nominal and measured square mesa side lengths used in the perimeter vs area analysis for samples VMBE 755 and VMBE 787 where the mesa side wall length was measured to be nominally the same for both samples. The calculated perimeter and area values for each size are also given. 85

4.7 A summary of the dominant current origin, whether via mesa perimeter or mesa area for the current resonances via two different methods: (a) extracting the maximum peak current and minimum valley current and (b) correcting the data for an apparent change in series resistance and extracting the current at a single voltage. 92

6.1 A summary of the comparisons between the important parameters for THz frequency emitters for the most asymmetric $GaAs/Al_{0.33}Ga_{0.67}As$ Triple Barrier Tunnelling Structures studied in this chapter against those of the state of the art InGaAs/AlAs double barrier structures extracted from [14, 17] 140

6.2 The WinGreen input parameters for the double barrier resonant tunnelling structure reported by Kanaya et al. [14]. These parameters are used throughout the simulations presented in this section, with only the layer thickness and material being altered. 142
6.3 The widths of the active region layers simulated for a series of triple barrier resonant tunnelling structures, with Aluminium Arsenide (AlAs) barrier layers and $In_{0.90}Ga_{0.10}As$ quantum well layers. 143
6.4 The widths of the active region layers simulated for a series of triple barrier resonant tunnelling structures, with Aluminium Arsenide (AlAs) barrier layers and $In_{0.90}Ga_{0.10}As$ quantum well layers. The width of the middle barrier, B_{MB} has been varied by a monolayer between each structure. . . . 145
6.5 The widths of the active region layers simulated for a series of triple barrier resonant tunnelling structures, with Aluminium Arsenide (AlAs) barrier layers and $In_{0.90}Ga_{0.10}As$ quantum well layers. The width of the middle barrier, B_{MB} is kept constant at 6 ml whilst the emitter and collector barrier layers are varied between each structure. The total ratio of $In_{0.90}Ga_{0.10}As$ to AlAs material is also kept constant at 19 ml to 14 ml, which is a strain compensated system. 148
6.6 The widths of the active region layers of the starting structures for a series of triple barrier resonant tunnelling structures in which there is reduced charge accumulation in the emitter quantum well. All four structures are strain approximately strain compensated, utilising AlAs barriers and an $In_{0.53}Ga_{0.47}As$ collector quantum well. The alloy composition of the emitter quantum well for designs In53A.1, In53B.1 and In53C.1 is $In_{0.90}Ga_{0.10}As$, whilst a $In_{0.80}Ga_{0.20}As$ is used in the In53X.1 design. 152
6.7 The widths of the active region layers for a series of triple barrier resonant tunnelling structures in which there is reduced charge accumulation in the emitter quantum well. These designs are based on the staring structure In53A.1 in table 6.6 which has an $In_{0.90}Ga_{0.10}As$ emitter quantum well. Only the width of the $In_{0.53}Ga_{0.47}As$ collector quantum well is varied across each different design. 153
6.8 The widths of the active region layers for a series of triple barrier resonant tunnelling structures in which there is reduced charge accumulation in the emitter quantum well. These designs are based on the staring structure In53B.1 in table 6.6 which has an $In_{0.90}Ga_{0.10}As$ emitter quantum well. Only the width of the $In_{0.53}Ga_{0.47}As$ collector quantum well is varied across each different design. 154
6.9 The widths of the active region layers for a series of triple barrier resonant tunnelling structures in which there is reduced charge accumulation in the emitter quantum well. These designs are based on the staring structure In53C.1 in table 6.6 which has an $In_{0.90}Ga_{0.10}As$ emitter quantum well. Only the width of the $In_{0.53}Ga_{0.47}As$ collector quantum well is varied across each different design. 154
6.10 The widths of the active region layers for a series of triple barrier resonant tunnelling structures in which there is reduced charge accumulation in the emitter quantum well. These designs are based on the staring structure In53X.1 in table 6.6 which has an $In_{0.80}Ga_{0.20}As$ emitter quantum well. Only the width of the $In_{0.53}Ga_{0.47}As$ collector quantum well is varied across each different design. 154

B.1 The WinGreen input parameters for the double barrier resonant tunnelling structure simulations shown in section 4.3.1. 185
B.2 The WinGreen input parameters for the double barrier resonant tunnelling structure simulations shown in section 4.3.1. 185

Abbreviations

DBRTS	**D**ouble **B**arrier **R**esonant **T**unnelling **S**tructure
DUT	**D**evice **U**nder **T**est
EMA	**E**ffective **M**ass **A**pproximation
I(V)	**C**urrent **V**oltage
LDOS	**L**ocal **D**ensity **O**f **S**tates
MBE	**M**olecular **B**eam **E**pitaxy
ml	**M**ono**L**ayer
NDC	**N**egative **D**ifferential **C**onducatance
NDR	**N**egative **D**ifferential **R**esistance
PL	**P**hotoluminescence
PLE	**P**hotoluminescence **E**xcitation
PVCR	**P**eak to **V**alley **C**urrent **R**atio
RTA	**R**apid **T**hermal **A**nnealing
RTD	**R**esonant **T**unnelling **D**iode
SEM	**S**canning **E**lectron **M**icroscope
TBRTS	**T**riple **B**arrier **R**esonant **T**unnelling **S**tructure
QW	**Q**uantum **W**ell
WKB	**W**entzel-**K**ramers-**B**rillouin

Dedicated to all of my family, friends, colleagues and teachers, without whom, this journey would not have been possible.

Chapter 1

Introduction

1.1 Motivation

The frequency range from 300 GHz to 10 THz, known as the terahertz region of the electromagnetic spectrum, is of great interest. Radiation in this frequency band offers many different applications such as enhanced security imaging [1] which exploits the unique "terahertz fingerprints" of many non-conducting materials to identify hidden objects, ultra-fast wireless communications for short range high-capacity line of sight communication [2] and non-invasive highly sensitive medical imaging due to the non-ionising nature of the terahertz radiation.

The lack of practical and coherent THz radiation sources has lead to the term "terahertz gap" [3] being used to describe this frequency range. Therefore, there is high demand to develop practical compact, coherent and efficient emitter devices which can operate at these frequencies and are suitable for integration into modern electronic circuitry. Optical terahertz sources have been developed but are challenged by difficulties in obtaining suitably low energy band-to-band transitions and the need for cryogenic cooling to operate [4] at THz frequencies. Solid state sources however are limited in operating frequency by the carrier transit time, which is often too long for devices to operate in the THz band [5].

Resonant tunnelling devices utilise quantum mechanical tunnelling, which is inherently a fast process and so are recognised as promising candidates to fulfil the need for compact and coherent terahertz emitters which operate at room temperature. These structures however still suffer from difficulties with monolayer precision growth required across entire wafers before they can be developed into a low cost manufacturable technology.

Conventional double barrier resonant tunnelling structures which are well understood are used in the current state of the art devices studied in this field [6]. Resonant tunnelling devices which utilise the more complex and less studied triple barrier structure designs have the potential to operate at higher frequencies and with more output power than conventional double barrier structures. However, due to the increased degree of complexity of these structures a thorough understanding of the behaviour of triple barrier structures is needed. Low temperature analysis of such structures will allow for understanding of the fundamental processes occurring in the devices, whilst studies at room temperature will facilitate the design of efficient structures for practical applications.

1.2 Historical Perspective

In 1958 a new diode which exhibited "negative resistance" was reported by Leo Esaki [7] which exploits the effect of quantum mechanical tunnelling. Esaki's pioneering work in electron tunnelling in semiconductor materials earned the 1973 Nobel Prize in physics [8] in conjunction with Giaever and Josephson.

In 1970 Esaki and Tsu reported the first observations of a new tunnelling phenomenon called "resonant tunnelling" in superlattices [9, 10] and the first observations of resonant tunnelling in GaAs/AlGaAs semiconductor double barrier structures were made by Chang et al. in 1974 [11]. A significant amount of research on resonant tunnelling devices has been carried out in the intervening period, with most of the work focusing on conventional double barrier structures. Investigations have been carried out on both fundamental tunnelling processes [12–22] and electronic and optoelectronic applications [23–25], with the most noteworthy device development being that of the "quantum cascade laser" [26–28], first reported in the early 1990's. Coupled quantum well systems have also proved a very rich area for the study of physical phenomena associated with quantum interference and coherent electron oscillations [29–31].

The first report of resonant tunnelling in triple barrier heterostructures was made by Nakagawa et al. in 1986 [32] where resonances in the devices current-voltage (I(V)) characteristics were observed. The current resonances were attributed to tunnelling of electrons from the ground state of the emitter quantum well to the first and second excited states in the collector quantum well and although a resonance that could be attributed to tunnelling between the emitter ground state and collector ground state is observed in the I(V) characteristics it was not studied in detail in this publication.

In 1983 Sollner et al. [33] reported the first observation of resonant tunnelling at room temperature in double barrier structures and demonstrated that the charge transport in resonant tunnelling structures can be very fast by comparing the dc I(V) curves with the I(V) curves at 2.5 THz. The agreement between the two curves was sufficient to show the charge transport mechanism is at least as fast as the angular period of 2.5 THz ($\approx$60 fs), thus indicating that resonant tunnelling structures were suitable for high speed oscillator applications.

Oscillations from double barrier structures were first observed by Sollner et al. in 1984 [34] at 18 GHz albeit at 200K. In 1987 Sollner et al. reported observations of oscillations upto 56 GHz at room temperature and considered some theoretical limitations of the ultimate frequency limits of double barrier resonant tunnelling structures. Previous limits of oscillations formed by WKB (Wentzel-Kramers-Brillouin) analysis of such structures consistently underestimated the frequency limits, with frequencies greater than the WKB limits already experimentally observed. Sollner et al. concluded that the upper limits were of the order of several hundred GHz when considering the lifetimes of electrons in the depletion region and transit through the quantum well, where the tunnelling time was best described by the lifetime of the resonant state given by the uncertainty relation $\tau = \frac{\hbar}{\Delta E}$ where ΔE is extracted from the width of the transmission resonance calculated using a method similar to Tsu and Esaki [10].

Work on improving the maximum frequency of oscillation of double barrier resonant tunnelling structures continued with various different material systems investigated due to advances in compound semiconductor growth techniques. Brown et al. reported fundamental oscillations up to 200 GHz and furthered estimates of their maximum oscillation frequency to exceed 600 GHz in 1988 [35]. Brown et al. also reported oscillations up to 420 GHz a year later [36] in GaAs/AlAs structures and 712 GHz at room temperature in InAs/AlSb resonant tunnelling diodes in 1991 [37] which exhibited 50 times larger power density at 360 GHz than GaAs/AlAs structures.

Double barrier resonant tunnelling structures were also demonstrated in the InAs/AlSb material system by Söderström et al. [38] with a peak current density of 3.7 x 10^5 Acm^{-2} and a peak to valley ratio of 3.2 at room temperature. The InGaAs/AlAs system was also investigated by Broekaert et al. [39] who reported peak to valley current ratios of as high as 30 at room temperature with thick AlAs potential barriers.

Other material systems such as InSb/AlInSb were briefly explored for double barrier structures due to the high mobility of InSb which was thought could provide a reduced device access resistance and thus improve the ultimate oscillation frequency [40]. However, due to the lack of a lattice matched substrate there are many difficulties in growing high quality InSb/AlInSb structures and there have been no reports of significant work on these structures since.

Various different designs have been reported to improve the peak to valley current ratio and output power density of resonant tunnelling structures since the early 1990's, however significant progress has been limited. Innovative proposals to use triple barrier resonant tunnelling structures as THz radiation sources as have been reported [41, 42] with various studies carried out on similar structures of this design [43–45].

1.3 Recent Developments

The InGaAs/AlAs/InP material system has become extremely popular in recent resonant tunnelling device research efforts due to the large current densities and peak to valley current ratios obtainable. The $In_{0.53}Ga_{0.47}As$ alloy composition has been of particular interest due to the lattice matching with InP, high electron mobility in the order of 10,000 $cm^2V^{-1}s^{-1}$ for low access resistance and a low electron effective mass of ≈ 0.041 at room temperature. As such this material system has been used to design the fastest reported measured oscillation frequency to date of 1.92 THz [46].

The evolution of this work can be traced back to 2005 where Orihashi et al. reported a 1.02 THz third harmonic component of the fundamental oscillation of 342 GHz with an output power of around 23 μW [47]. The continuation of this work has greatly improved the fundamental frequency of oscillation up to 831 GHz [48], 1 THz [49], 1.1 THz [50], 1.31 THz [51], 1.42 THz [52], 1.55 THz [6] and the most recent report of 1.92 THz [46] over the subsequent years by improving the resonant tunnelling double barrier structure design and the attached resonant circuit.

However, despite improvements in the operational frequency of the double barrier resonant tunnelling diode devices (RTDs), the low output power of a single device still remains a problem for practical applications where output powers of the order of ≈ 1 mW are required. Reddy et al. demonstrated in 1997 the use of an oscillator array to produce coherent oscillations [53], since which several attempts have been made during the intervening period to increase the output power using similar methods [54–58].

Triple barrier resonant tunnelling structures have been scarcely studied for the application of high speed oscillators although it is accepted that such structures offer some benefits for the peak to valley current ratio due to a suppression of the off resonant background current. This suppression of the background current allows for increased negative differential conductance, thus increasing the fundamental frequency of oscillation and improving output power densities. With proper structure design it is expected that triple barrier resonant tunnelling structures can replace the double barrier structures currently used in state of the art THz RTD oscillators.

1.4 Outline of Thesis

This thesis describes the work carried out on a series of triple barrier resonant tunnelling structures which have historically been less studied than the conventional double barrier structures. Consisting of three potential barriers and two quantum wells the triple barrier structures are an example of a heterostructure which exploits the phenomenon of quantum mechanical tunnelling to produce current-voltage characteristics with a region of negative differential resistance, which can be utilised as high frequency oscillators. The strong coupling between the two quantum wells results in a structure in which the transmission coefficient is highly dependent on the energetic alignment of the quasi-bound carrier states. Thus as a result the negative differential resistance regions observed in the I(V) characteristics of triple barrier resonant tunnelling structures (TBRTS) are more sensitive to changes in voltage than the conventional double barrier structures.

Chapter 3 describes the epitaxial layers of the series of resonant tunnelling structures studied in this thesis along with the device fabrication processes used. The electrical measurement and variable temperature system set up are also described here.

The process of quantum mechanical tunnelling is described in chapter 4 as well as the phenomenon known as "resonant tunnelling". In this chapter the differences between tunnelling in single, double and multi (> 3) barrier heterostructures are discussed and the effects of series resistance on the experimentally observed I(V) characteristics are considered. A nominally symmetric GaAs/$Al_{0.33}Ga_{0.67}As$ TBRTS is studied in detail in both forward and reverse bias directions at low temperature (3K) with several current resonances observed in the measured I(V) characteristics. These resonances are attributed to energetic alignment of the quasi-bound quantum well states and the conduction band edge. A simple model has also been developed to predict and compare the voltages at which these resonances occur. A more complex model has been used to simulate the I(V) characteristic of the nominally symmetric TBRTS in the forward bias direction and explore the role of charge accumulation in the emitter quantum well in this device.

A series of asymmetric TBRTS with decreasing collector quantum well width are also studied in chapter 4 and the evolution of the current resonances examined as a function of increasing quantum well width asymmetry. The peak to valley current ratio of the resonances observed in the I(V) characteristics of the nominally symmetric and asymmetric structures is calculated and compared against the degree of quantum well width asymmetry.

Perimeter versus area analysis has also been performed on devices with varying mesa area for the nominally symmetric and most asymmetric triple barrier structures and the effect of device self heating and charge accumulation probed using pulsed voltage measurements.

Chapter 5 describes how the measured I(V) characteristics of the triple barrier resonant tunnelling structures vary with increasing sample temperature between 3K and 293K. A resonant feature not observed at low temperature emerges with increasing sample temperature and the origin of this is discussed. Experimentally determined and theoretically calculated activation energies for the novel current resonance for the nominally symmetric and asymmetric structures are extracted from Arrhenius plots and are in excellent agreement.

The series of triple barrier resonant tunnelling structures studied are examined in detail as to their potential to be utilised as THz radiation sources in chapter 6. The maximum frequency of oscillation and maximum output power are calculated for the series of 60 μm x 60 μm GaAs/$Al_{0.33}Ga_{0.67}As$ devices and compared to state of the art $In_{0.90}Ga_{0.10}As$/AlAs structures currently reported. An improved TBRTS which does not suffer from charge accumulation in the emitter quantum well has been developed. Calculations from the simulated I(V) characteristics for such a devices shows it improves on the standard double barrier structure used in the current state of the art oscillators in both frequency of oscillation and output power density.

Chapter 7 summarises the results obtained from the research undertaken in this thesis and briefly discusses future possible research areas. Appendices are included at the end of the thesis in which relevant addition details are provided for the simulations performed in this thesis. Additional background information on photoluminescence and photoluminescence excitation measurements performed prior to the work carried out in this thesis to determine the widths of the quantum wells is also given in the appendices.

1.5 Contributions to the Field

The work carried out in this thesis was aimed at advancing high frequency resonant tunnelling oscillator devices in the terahertz frequency range utilising triple barrier resonant tunnelling structures rather than the conventionally studied double barrier structures. In order to achieve this a thorough understanding of the behaviour of simple triple barrier resonant tunnelling structures at low and room temperatures was required to aid in the development of a triple barrier structure design which out performs the current state of the art double barrier structures in both oscillation frequency and output power density.

In this work it has been demonstrated that triple barrier resonant tunnelling structures have much more complex resonant tunnelling behaviour than double barrier structures and the origin of the current resonances observed in experimentally measured current-voltage characteristics explored. It has been shown that charge accumulation in the emitter quantum well of the structures plays an important role in the behaviour of these devices, and is detrimental to the maximum frequency of oscillation due to increased device capacitance.

A novel resonant tunnelling mechanism through energetically aligned $n = 1$ subband states has been identified and studied for a series of symmetric and asymmetric triple barrier structures. It has been shown that this resonance increases in magnitude with increasing sample temperature which is rare behaviour in a system where quantum mechanical effects dominate. This resonant tunnelling mechanism can possibly be

exploited for low voltage, room temperature current resonances with an enhanced peak to valley current ratio in comparison to double barrier structures.
Finally, an improved triple barrier resonant tunnelling structure has been carefully designed to avoid charge accumulation in the emitter quantum well. Simulations of the current-voltage characteristics of this structure have been shown to indicate a higher frequency of oscillation and output power density than the state of the art double barrier structures at room temperature.

1.6 List of Publications

[1] C P Allford, R E Legg, R A O'Donnell, P Dawson, M Missous and P D Buckle. 'Thermally activated resonant tunnelling in GaAs/AlGaAs triple barrier heterostructures'. In: Semiconductor Science and Technology 30.10 (2015), p. 105035.

[2] C P Allford and P D Buckle. '$In_{0.53}Ga_{0.47}As$/AlAS triple barrier resonant tunnelling structures for improved THz emitters.' In preparation (2016).

1.7 Conference Presentations

[1] C P Allford, R E Legg, R A O'Donnell, P Dawson, M Missous and P D Buckle. 'Thermally activated resonant tunnelling in GaAs/AlGaAs triple barrier heterostructures'. UK Semiconductors 2014, Sheffield Hallam University, July 2014.

[2] C P Allford, P D Buckle and M Missous. 'Critical state alignment and charge accumulation in triple barrier resonant tunnelling structures'. The 39$^{\text{th}}$ Workshop on Compound Semiconductor Devices and Integrated Circuits (WOCSDICE 2015), Smolenice Castle, Slovakia, June 2015

Bibliography

[1] *http://terasense.com/applications/homeland-security/*. URL. Terasense Group, Inc, USA, 2016.

[2] Ho-Jin Song and T. Nagatsuma. 'Present and Future of Terahertz Communications'. In: *Terahertz Science and Technology, IEEE Transactions on* 1.1 (Sept. 2011), pp. 256–263. ISSN: 2156-342X. DOI: 10.1109/TTHZ.2011.2159552.

[3] T. Nagatsuma. 'Generating millimeter and terahertz waves'. In: *IEEE, Microwave Magazine* 10.4 (2009), pp. 64–74. ISSN: 1527-3342. DOI: 10.1109/MMM.2009.932283.

[4] Martin Brandstetter, Christoph Deutsch, Michael Krall, Hermann Detz, Donald C. MacFarland, Tobias Zederbauer, Aaron M. Andrews, Werner Schrenk, Gottfried Strasser and Karl Unterrainer. 'High power terahertz quantum cascade lasers with symmetric wafer bonded active regions'. In: *Applied Physics Letters* 103.17, 171113 (2013). DOI: http://dx.doi.org/10.1063/1.4826943.

[5] S. M. Sze and K. K. Ng. *Physics of Semicondcutor Devices. Third Edition*. John Wiley & Sons, 2007.

[6] T. Maekawa, H. Kanaya, S. Suzuki and M. Asada. 'Frequency increase in terahertz oscillation of resonant tunnelling diode up to 1.55 THz by reduced slot-antenna length'. In: *Electronics Letters* 50.17 (Aug. 2014), pp. 1214–1216. ISSN: 0013-5194. DOI: 10.1049/el.2014.2362.

[7] Leo Esaki. 'New Phenomenon in Narrow Germanium $p-n$ Junctions'. In: *Phys. Rev.* 109 (2 Jan. 1958), pp. 603–604. DOI: 10.1103/PhysRev.109.603.

[8] L. Esaki. 'Nobel Lectures in Physics 1971-1980'. In: ed. by S Lundqvist. World Scientific Publishing Co., 1992. Chap. A Long Journey into Tunneling, pp. 116–133. ISBN: 978-981-02-0727-4.

[9] L. Esaki and R. Tsu. 'Superlattice and Negative Differential Conductivity in Semiconductors'. In: *IBM Journal of Research and Development* 14.1 (Jan. 1970), pp. 61–65. ISSN: 0018-8646. DOI: 10.1147/rd.141.0061.

[10] R. Tsu and L. Esaki. 'Tunneling in a finite superlattice'. In: *Applied Physics Letters* 22.11 (1973), pp. 562–564. DOI: http://dx.doi.org/10.1063/1.1654509.

[11] L. L. Chang, L. Esaki and R. Tsu. ‘Resonant tunneling in semiconductor double barriers’. In: *Applied Physics Letters* 24.12 (1974), pp. 593–595. DOI: `http://dx.doi.org/10.1063/1.1655067`.

[12] B. Ricco and M.Ya. Azbel. ‘Physics of resonant tunneling: the one-dimensional double-barrier case’. In: *Physical Review B* 29.4 (1984), pp. 1970–1981. DOI: `10.1103/PhysRevB.29.1970`.

[13] A.S. Vengurlekar, F. Capasso, S. Sen, A.L. Hutchinson, S.N.G. Chu, D. Sivco and A.Y. Cho. ‘Quasi-ballistic resonant tunneling of minority electrons into the excited states of a quantum well’. In: *Applied Physics Letters* 55.24 (1989), pp. 2529–2531. DOI: `10.1063/1.101972`.

[14] P. Guéret, C. Rossel, W. Schlup and H.P. Meier. ‘Investigations on resonant tunneling in III-V heterostructures: Comparison between experimental data and model calculations’. In: *Journal of Applied Physics* 66.9 (1989), pp. 4312–4316. DOI: `10.1063/1.343977`.

[15] P. Guéret, C. Rossel, E. Marclay and H. Meier. ‘Investigations on resonant tunneling in III-V heterostructures’. In: *Journal of Applied Physics* 66.1 (1989), pp. 278–285.

[16] M.S. Skolnick, D.G. Hayes, P.E. Simmonds, A.W. Higgs, G.W. Smith, H.J. Hutchinson, C.R. Whitehouse, L. Eaves, M. Henini, O.H. Hughes, M.L. Leadbeater and D.P. Halliday. ‘Electronic processes in double-barrier resonant-tunneling structures studied by photoluminescence spectroscopy in zero and finite magnetic fields’. In: *Physical Review B* 41.15 (1990), pp. 10754–10766. DOI: `10.1103/PhysRevB.41.10754`.

[17] J. Leo and A.H. MacDonald. ‘Disorder-assisted tunneling through a double-barrier structure’. In: *Physical Review Letters* 64.8 (1990), pp. 817–820. DOI: `10.1103/PhysRevLett.64.817`.

[18] J. Leo and A.H. MacDonald. ‘Disorder-assisted tunneling through a double-barrier resonant-tunneling structure’. In: *Physical Review B* 43.12 (1991), pp. 9763–9771. DOI: `10.1103/PhysRevB.43.9763`.

[19] D. Bertram, H. Lage, H.T. Grahn and K. Ploog. ‘Electroluminescence spectroscopy of resonantly coupled GaAs-AlAs superlattices’. In: *Applied Physics Letters* 64.8 (1994), pp. 1012–1014. DOI: `10.1063/1.110954`.

[20] J.J. Finley, R.J. Teissier, M.S. Skolnick, J.W. Cockburn, R. Grey, G. Hill and M.A. Pate. ‘An optical and electrical study of tunnelling mechanisms through indirect gap single barrier GaAs/AlAs/GaAs heterostructures’. In: *Surface Science* 361-362 (1996), pp. 197–200. DOI: `10.1016/0039-6028(96)00383-4`.

[21] S. Ozaki, J.M. Feng, J.H. Park, S.-I. Osako, H. Kubo, M. Morifuji, N. Mori and C. Hamaguchi. 'Observation of resonant optical-phonon assisted tunneling in asymmetric double quantum wells'. In: *Journal of Applied Physics* 83.2 (1998), pp. 962–965.

[22] A.M. Malik, M.J. Godfrey and P. Dawson. 'Tunneling of heavy holes in semiconductor microstructures'. In: *Physical Review B - Condensed Matter and Materials Physics* 59.4 (1999), pp. 2861–2866.

[23] Hiroshi Mizuta, T. Tanoue and S. Takahashi. 'A new triple-well resonant tunneling diode with controllable double-negative resistance'. In: *IEEE Transactions on Electrons Devices* ED-35 (1988), pp. 1951–1956.

[24] T. Tanoue, H. Mizuta and S. Takahashi. 'Triple-well resonant tunneling diode for multiple-valued logic application.' In: *Electron device letters* 9.8 (1988), pp. 365–367.

[25] T. Waho, K.J. Chen and M. Yamamoto. 'A novel multiple-valued logic gate using resonant tunneling devices'. In: *IEEE Electron Device Letters* 17.5 (1996), pp. 223–225.

[26] J. Faist, F. Capasso, C. Sirtori, D.L. Sivco, A.L. Hutchinson, S.N.G. Chu and A.Y. Cho. 'Quantum-well intersub-band electroluminescent diode at $\lambda = 5\mu\text{m}$'. In: *Electronics Letters* 29.25 (1993), pp. 2230–2231.

[27] J. Faist, F. Capasso, D.L. Sivco, C. Sirtori, A.L. Hutchinson and A.Y. Cho. 'Quantum cascade laser'. In: *Science* 264.5158 (1994), pp. 553–556.

[28] J. Faist, F. Capasso, C. Sirtori, D.L. Sivco, A.L. Hutchinson, M.S. Hybertsen and A.Y. Cho. 'Quantum cascade lasers without intersubband population inversion'. In: *Physical Review Letters* 76.3 (1996), pp. 411–414.

[29] J. Faist, F. Capasso, A.L. Hutchinson, L. Pfeiffer and K.W. West. 'Suppression of optical absorption by electric-field-induced quantum interference in coupled potential wells'. In: *Physical Review Letters* 71.21 (1993), pp. 3573–3576.

[30] H.G. Roskos, M.C. Nuss, J. Shah, K. Leo, D.A.B. Miller, A.M. Fox, S. Schmitt-Rink and K. Köhler. 'Coherent submillimeter-wave emission from charge oscillations in a double-well potential'. In: *Physical Review Letters* 68.14 (1992), pp. 2216–2219.

[31] T. Strutz and Y. Shiraki. 'Room-temperature quantum interference in an asymmetric triple-barrier resonant-tunnelling diode'. In: *Semiconductor Science and Technology* 11.1 (1996), pp. 103–106.

[32] T. Nakagawa, H. Imamoto, T. Kojima and K. Ohta. 'Observation of resonant tunneling in AlGaAs/GaAs triple barrier diodes'. In: *Applied Physics Letters* 49.2 (1986), pp. 73–75.

[33] T. C. L. G. Sollner, W. D. Goodhue, P. E. Tannenwald, C. D. Parker and D. D. Peck. ‘Resonant tunneling through quantum wells at frequencies up to 2.5 THz’. In: *Applied Physics Letters* 43.6 (1983), pp. 588–590. DOI: http://dx.doi.org/10.1063/1.94434.

[34] T. C. L. G. Sollner, P. E. Tannenwald, D. D. Peck and W. D. Goodhue. ‘Quantum well oscillators’. In: *Applied Physics Letters* 45.12 (1984), pp. 1319–1321. DOI: http://dx.doi.org/10.1063/1.95134.

[35] E. R. Brown, W. D. Goodhue and T. C. L. G. Sollner. ‘Fundamental oscillations up to 200 GHz in resonant tunneling diodes and new estimates of their maximum oscillation frequency from stationary-state tunneling theory’. In: *Journal of Applied Physics* 64.3 (1988), pp. 1519–1529. DOI: http://dx.doi.org/10.1063/1.341827.

[36] E. R. Brown, T. C. L. G. Sollner, C. D. Parker, W. D. Goodhue and C. L. Chen. ‘Oscillations up to 420 GHz in GaAs/AlAs resonant tunneling diodes’. In: *Applied Physics Letters* 55.17 (1989), pp. 1777–1779. DOI: http://dx.doi.org/10.1063/1.102190.

[37] E. R. Brown, J. R. Soderstrom, C. D. Parker, L. J. Mahoney, K. M. Molvar and T. C. McGill. ‘Oscillations up to 712 GHz in InAs/AlSb resonant−−tunneling diodes’. In: *Applied Physics Letters* 58.20 (1991), pp. 2291–2293.

[38] J. R. Söderström, E. R. Brown, C. D. Parker, L. J. Mahoney, J. Y. Yao, T. G. Andersson and T. C. McGill. ‘Growth and characterization of high current density, high-speed InAs/AlSb resonant tunneling diodes’. In: *Applied Physics Letters* 58.3 (1991), pp. 275–277. DOI: http://dx.doi.org/10.1063/1.104659.

[39] T. P. E. Broekaert, W. Lee and C. G. Fonstad. ‘Pseudomorphic In$_0$.53Ga$_0$.47As/AlAs/InAs resonant tunneling diodes with peak-to-valley current ratios of 30 at room temperature’. In: *Applied Physics Letters* 53.16 (1988), pp. 1545–1547. DOI: http://dx.doi.org/10.1063/1.99951.

[40] J. R. Soderstrom, J. Y. Yao and T. G. Andersson. ‘Observation of resonant tunneling in InSb/AlInSb doublebarrier structures’. In: *Applied Physics Letters* 58.7 (1991), pp. 708–710.

[41] W.S. Truscott. ‘Wave functions in the presence of a time-dependent field: Exact solutions and their application to tunneling’. In: *Physical Review Letters* 70.13 (1993), pp. 1900–1903.

[42] W.S. Truscott. ‘Negative conductance at THz frequencies in multi-well structures’. In: *Solid-State Electronics* 37.4-6 (1994), pp. 1235–1238.

[43] P.D. Buckle, P. Dawson, M. Missous and W.S. Truscott. 'Full wafer optical characterisation of resonant tunnelling structures using photoluminescence excitation spectroscopy'. In: *Journal of Crystal Growth* 175-176.PART 2 (1997), pp. 1299–1302.

[44] P.D. Buckle, P. Dawson, C.Y. Kuo, A.H. Roberts, W.S. Truscott, M. Lynch and M. Missous. 'Charge accumulation in GaAs/AIGaAs triple barrier resonant tunneling structures'. In: *Journal of Applied Physics* 83.2 (1998), pp. 882–887.

[45] P.D. Buckle, P. Dawson, M.A Lynch, Chun-Yi Kuo, Mohammed Missous and W.S. Truscott. 'An inter-subband device with terahertz applications'. In: *Microwave Theory and Techniques, IEEE Transactions on* 48.4 (Apr. 2000), pp. 632–638.

[46] Takeru Maekawa, Hidetoshi Kanaya, Safumi Suzuki and Masahiro Asada. 'Oscillation up to 1.92 THz in resonant tunneling diode by reduced conduction loss'. In: *Applied Physics Express* 9.2 (2016), p. 024101.

[47] N. Orihashi, S. Suzuki and M. Asada. 'One THz harmonic oscillation of resonant tunneling diodes'. In: *Applied Physics Letters* 87.23 (2005). DOI: `http://dx.doi.org/10.1063/1.2139850`.

[48] Safumi Suzuki, Atsushi Teranishi, Kensuke Hinata, Masahiro Asada, Hiroki Sugiyama and Haruki Yokoyama. 'Fundamental Oscillation of up to 831 GHz in GaInAs/AlAs Resonant Tunneling Diode'. In: *Applied Physics Express* 2.5 (2009), p. 054501.

[49] Safumi Suzuki, Masahiro Asada, Atsushi Teranishi, Hiroki Sugiyama and Haruki Yokoyama. 'Fundamental oscillation of resonant tunneling diodes above 1 THz at room temperature'. In: *Applied Physics Letters* 97.24 (2010). DOI: `http://dx.doi.org/10.1063/1.3525834`.

[50] Michael Feiginov, Cezary Sydlo, Oleg Cojocari and Peter Meissner. 'Resonant-tunnelling-diode oscillators operating at frequencies above 1.1THz'. In: *Applied Physics Letters* 99.23 (2011). DOI: `http://dx.doi.org/10.1063/1.3667191`.

[51] Hidetoshi Kanaya, Hirotaka Shibayama, Riku Sogabe, Safumi Suzuki and Masahiro Asada. 'Fundamental Oscillation up to 1.31 THz in Resonant Tunneling Diodes with Thin Well and Barriers'. In: *Applied Physics Express* 5.12 (2012), p. 122401.

[52] Hidetoshi Kanaya, Riku Sogabe, Takeru Maekawa, Safumi Suzuki and Masahiro Asada. 'Fundamental Oscillation up to 1.42 THz in Resonant Tunneling Diodes by Optimized Collector Spacer Thickness'. In: *Journal of Infrared, Millimeter, and Terahertz Waves* 35.5 (2014), pp. 425–431. ISSN: 1866-6906. DOI: `10.1007/s10762-014-0058-z`.

[53] M. Reddy, S. C. Martin, A. C. Molnar, R. E. Muller, R. P. Smith, P. H. Siegel, M. J. Mondry, M. J. W. Rodwell, H. Kroemer and S. J. Allen. 'Monolithic Schottky-collector resonant tunnel diode oscillator arrays to 650 GHz'. In: *IEEE Electron Device Letters* 18.5 (May 1997), pp. 218–221. ISSN: 0741-3106. DOI: 10.1109/55.568771.

[54] H. I. Cantu and W. S. Truscott. 'Injection-locking and power combining with double barrier resonant tunnelling diodes'. In: *Electronics Letters* 37.20 (Sept. 2001), pp. 1264–1265. ISSN: 0013-5194.

[55] Safumi Suzuki, Naoyuki Orihashi and Masahiro Asada. 'Mutual Injection Locking between Sub-THz Oscillating Resonant Tunneling Diodes'. In: *Japanese Journal of Applied Physics* 44.11L (2005), p. L1439.

[56] Safumi Suzuki and Masahiro Asada. 'Coherent Power Combination in Highly Integrated Resonant Tunneling Diode Oscillators with Slot Antennas'. In: *Japanese Journal of Applied Physics* 46.12L (2007), p. L1108.

[57] Safumi Suzuki, Kenta Urayama and Masahiro Asada. 'Coherent Power Combination in Multi-Element Sub-Terahertz Resonant Tunneling Diode Oscillators Coupled with Metal–Insulator–Metal Stub Structure'. In: *Applied Physics Express* 1.9 (2008), p. 093001.

[58] M. Asada and S. Suzuki. 'Theoretical analysis of coupled oscillator array using resonant tunneling diodes in subterahertz and terahertz range'. In: *Journal of Applied Physics* 103.12, 124514 (2008). DOI: http://dx.doi.org/10.1063/1.2947600.

Chapter 2

GaAs and Semiconductor Heterostructures

Semiconductors that consist of a single element fall into the category elemental semiconductors and may consist of a single group four element, for example silicon (Si) or a single group six element, for example tellurium (Te). Semiconducting materials that consist of elements from two or more groups of the periodic table are given the name compound semiconductors and include binary compounds such as indium antimonide (InSb), zinc sulphide (ZnS) and gallium arsenide (GaAs). Compound semiconductors that derive from elements from group three and group five of the periodic table (e.g. gallium and arsenide) are known as III-V semiconductors, where similarly those that derive from group two and group six elements (e.g. cadmium and tellurium) are known as II-VI semiconductors.

Traditionally the most important and widely used semiconducting material was Si, with it generally being favoured due its abundance in nature, the ability to grow high quality crystals with a low defect density and the ease at which a high quality native oxide (SiO_2) can be introduced to its surface. In part it is these properties that have allowed for the growth in the silicon semiconductor industry which now produces a vast quantity of silicon based electronics utilised in modern day technologies. However, compound semiconductors are becoming of increasing importance due to the advancements that have been made in modern growth techniques. The need for a material with optical properties deriving from a direct band-gap, a property which Si does not exhibit, initially drove improvement in III-V growth quality and high quality compound semiconductor crystals of the scale necessary for commercial fabrication are now becoming a reality.

The properties of increasingly exotic semiconductor material systems are now being investigated as it is accepted that, although the production of silicon electronics is well established not only may compound semiconductor devices be capable of out performing their silicon counterparts, but may also give rise to novel semiconductor devices due to superior properties they exhibit. Therefore it is essential to ensure that the basic structure and properties of these materials are fully understood.

2.1 Basic Properties of GaAs

Historically, gallium arsenide (GaAs) is the most studied of the III-V compound semiconductors as it was used a prototype material in studies of molecular beam epitaxy (MBE) performed in the 1960's and 1970's [1–5] due to the excellent lattice matching between GaAs and it's alloy aluminium gallium arsenide, $\mathrm{Al}_x\mathrm{Ga}_{(1-x)}\mathrm{As}$. As a result of this work the properties of GaAs, and those of $\mathrm{Al}_x\mathrm{Ga}_{(1-x)}\mathrm{As}$ are very well known.

2.1.1 Crystal Structure

An ideal crystal is one that is constructed by the infinite consecutive repetition of identical groups of atoms in space and in many elemental materials this is simply just the constituent atom repeated in a regular 3D lattice. In more complex materials it is necessary to define a *lattice*, and a *basis set* of atoms to describe the crystal structure. The crystal lattice is an array of points on which each basis set is located, with the basis set defined as the group of atoms at each lattice point. Each point on the lattice can be described by an integer translation of three vectors (**a**,**b**,**c**) from any other lattice point and there are many different sets of vectors for which this is possible. The volume of a cell is defined by these vectors and the set of vectors which describe the smallest cell

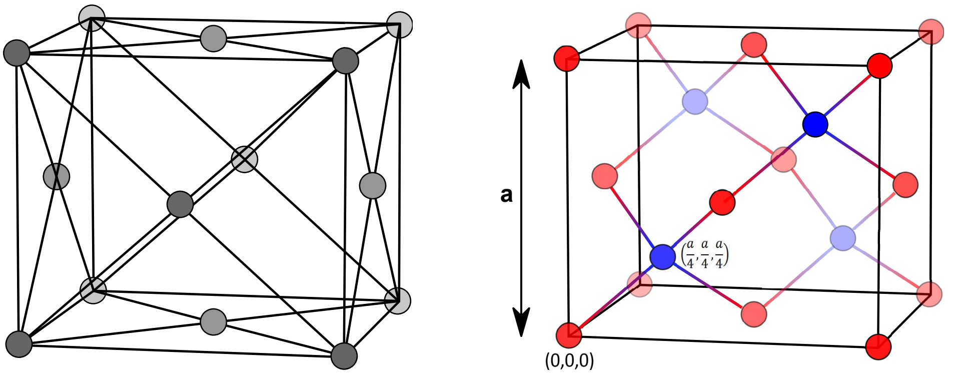

(a) (b)

FIGURE 2.1: (a) The face centred cubic (fcc) Bravais lattice. Atoms are located at each of the eight verticies, with additional atoms located at each of the six faces of cube. (b) Zincblende structure of GaAs which shows two interpenetrating fcc sublattices of Ga (red spheres) and As (blue spheres). Covalent bonding between the four nearest neighbour atoms in a tetrahedral structure are shown (blue-red gradient lines).

volume are known as the *primitive vectors* and this cell defined as the *primitive unit cell*. There are fourteen different types of lattice, *the Bravais lattices*, by which every known crystal structure can be described, with most elements crystallising into hexagonal or cubic structures. There are two cubic structures, where the length of each vector is equal ($a = b = c$) and the angles between them are equal (90°), the body centred cubic (bcc) and face centred cubic (fcc). Figure 2.1(a) shows the face centred cubic structure, with an atom at all eight vertices, and additional atoms at the centre of each of the six faces of the cube.

Nearly all III-V compound semiconductors, which includes GaAs, crystallise into the zincblende structure, shown in figure 2.1(b). The zincblende structure is closely related to the diamond crystalline structure and consists of two interpenetrating face centred cubic Bravais lattices. Each fcc lattice consists of a single constituent atom (in this case Ga or As) offset from each other by $(a/4, a/4, a/4)$. Covalent bonds are made between each atom and its four equally spaced nearest neighbour atoms in a tetrahedral arrangement. In reality however, the final crystalline structure of the material is then determined by the forces that act on each individual atom (including any impurities or vacancies), such that the free energy of the crystal is minimised.

The lattice is defined in real space, but it is also beneficial to consider the reciprocal lattice in momentum (or k-) space. The reciprocal lattice defines allowed k states of the crystal structure in question, and as with a direct lattice, a reciprocal lattice can be defined by a unit cell. Since the reciprocal lattice is also periodic, the first Brillouin zone contains all the necessary information to define the entire crystal structure and therefore the behaviour of any electrons propagating through the lattice. The Wigner-Seitz unit

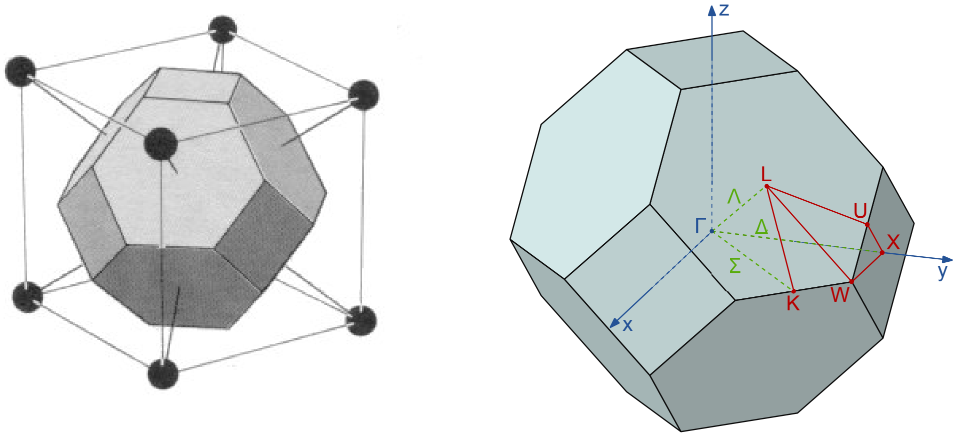

(a) (b)

FIGURE 2.2: (a) The Wigner-Seitz unit cell of a body centred cubic lattice (bcc), the bcc is the reciprocal lattice of the face centred cubic (fcc) direct lattice, and as such the Wigner-Seitz unit cell defines the first Brillouin zone of a fcc structure. (b) The first Brillouin zone of a face centred cubic direct lattice shown with a number of high-symmetry points.

cell [6] is therefore generally used to describe reciprocal lattices, as to the region of k-space occupied by the Wigner-Seitz unit cell constitutes the first Brillouin zone. Therefore it is possible to equate any point in the reciprocal lattice to a point in the first Brillouin zone. The reciprocal lattice of a face centred cubic structure is the body centred cubic lattice, for which the Wigner-Seitz unit cell is shown in figure 2.2(a) (i.e. the first Brillouin zone of the fcc direct lattice).

A number of high symmetry points are shown in the first Brillouin zone of the face centred cubic direct lattice, figure 2.2(b). The high symmetry points are directions and points in the reciprocal lattice that are invariant under various rotations and reflections about the zone centre, Γ. The Δ axes follow both positive and negative [100], [010] and [001] crystallographic plane directions to one of the six X points at the edge of the zone, where as the Σ axes follow the [110] directions to the K points (one of four) at the zone edge. The Λ axes run along the [111] directions to the L points (one of eight) and given that the reciprocal lattice is periodic the properties at one high-symmetry point are identical for all equivalent points in the crystal lattice.

2.1.2 Electron Behaviour in GaAs

As with all semiconductors, metals, semi-metals and insulators the electronic transport properties of these materials are determined by the distribution, in energy, of the available electronic states. Despite the success of the *free electron model* at explaining many properties of metals, it fails to explain the behaviour of semiconductors, semi-metals and insulators. An extension to the free electron model must therefore be made and the resulting model is known as the *nearly free electron model*.

The nearly free electron model differs from the free electron model by taking into account the fact that the positive ions in the crystal structure do not produce a uniform attractive field, but one which has strong negative peaks at the ion lattice sites, an example of which is given in figure 2.3. With the introduction of this concept, regions in energy

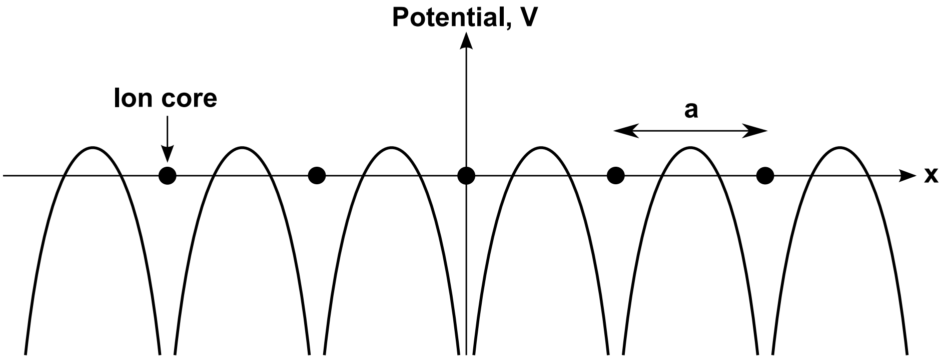

Figure 2.3: A one dimensional periodic potential associated with a chain of idential equally spaces ions. The ion cores are seperated by a distance, a.

where no electronic states exist are formed, and are known as energy gaps or *band gaps*. Since the electrical transport properties of solids are determined by the distribution in energy of the available electronic states the band gap is a major factor in determining these properties. It is therefore essential to understand the the origin of energy bands, the nearly free electron model and origin of energy bands are treated in great detail in references [6–9].

The band structure, or distribution of electron energy as a function of wavenumber (E vs k diagram) of a solid can simply be considered by solving Schrödinger's equation for a

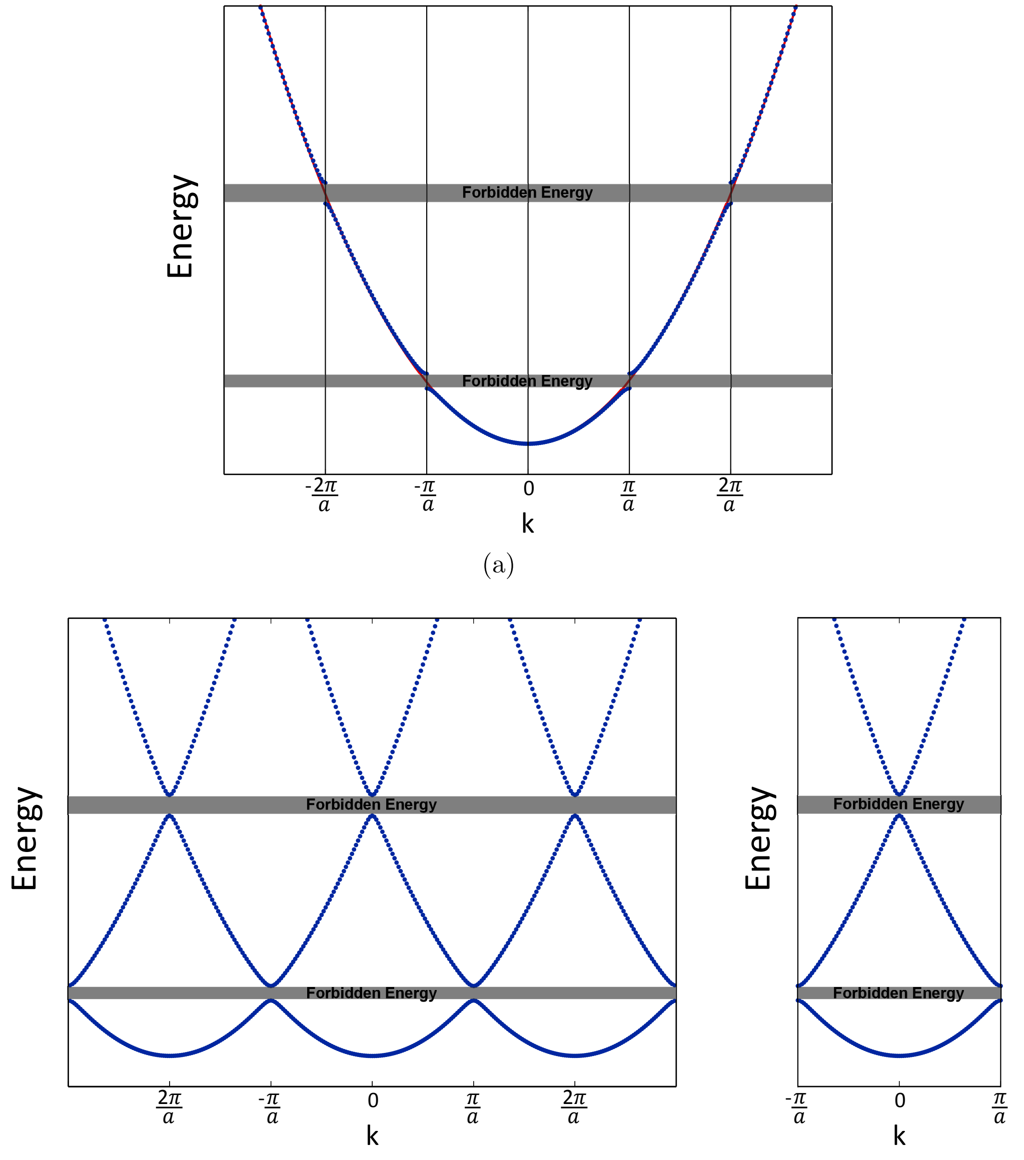

(a)

(b)

(c)

FIGURE 2.4: (a) The band structure for a monatomic lattice in a weak periodic potential with a perodicity, a (blue dots). The red line shows the E vs k relationship for a free electron. (b) The band structure for a periodic array of atoms, known as the "periodic zone scheme". (c) The band structure in the first Brillouin zone only, the "reduced zone scheme".

single electron in the nearly free electron model.

$$\left(\frac{-\hbar^2}{2m^*}\nabla^2 + V(\mathbf{r})\right)\psi_k(\mathbf{r}) = E_k\psi_k(\mathbf{r}) \tag{2.1}$$

Bloch's theorem states that the solutions of Schrödinger's equation for a periodic potential is given by the product of a plane wave, as in the free electron case, and a periodic Bloch function, $U_k(\mathbf{r})$,

$$\psi_k(\mathbf{r}) = U_k(\mathbf{r})\exp(i\mathbf{k}\cdot\mathbf{r}) \tag{2.2}$$

where the periodicity of $V(\mathbf{r})$ and $U_k(\mathbf{r})$ is equal to the periodicity of the crystal lattice and $U_k(\mathbf{r}) = U_k(\mathbf{r} + \mathbf{T})$. Here $\mathbf{T}$ is the translation vector of the lattice (the vector through which an electron is required to move such that it is in the same place in the next unit cell). The case for a monatomic lattice in a weak periodic potential is considered here and shown in figure 2.4(a) and it can be seen that the inclusion of a periodic potential results in the formation of energy gaps at multiples of $k = \frac{\pi}{a}$, where a is the periodicity of the lattice potential. The continuous parts of the function form the allowed bands and due to the periodic nature of the lattice the function is repeated at every lattice point, shown in figure 2.4(b), and is known as the "periodic zone scheme". Figure 2.4(c) shows the "reduced zone scheme" which only considers the band structure in the first Brillouin zone, $-\frac{\pi}{a} \leq k \leq \frac{\pi}{a}$. As any point in the reciprocal lattice can be equated a point in the first Brillouin zone only the band structure in the first Brillouin zone needs be considered.

The nearly free electron model is useful to demonstrate the effects that a periodic potential has on the behaviour of electrons in a crystal, however to accurately describe the band structure of a real semiconductors a more complex model that takes into account several bands is required. Details on more comprehensive methods such as the $\mathbf{k}\cdot\mathbf{p}$ theory [10, 11] and the pseudo-potential technique [10, 12] can be found in their respective references and will not be detailed in this thesis.

2.1.3 Bandstructure of GaAs

Crystals of the zincblende structure have a valence band that consists of four sub bands (if spin splitting is ignored), 3 of which are degenerate at $k = 0$. The conduction band consists of a number of sub bands, for which the minima occurs at the gamma point, Γ in GaAs, resulting in a direct band gap (where the valence band maxima and conduction band minima occur at the same value of k). If we consider this region only (indicated by the blue box shown in figure 2.5(a)), then the band structure of GaAs can be considered using only these four bands, a single parabolic conduction band, a valence band consisting of a light and heavy hole sub bands and the split-off sub band, illustrated in figure 2.5(b).

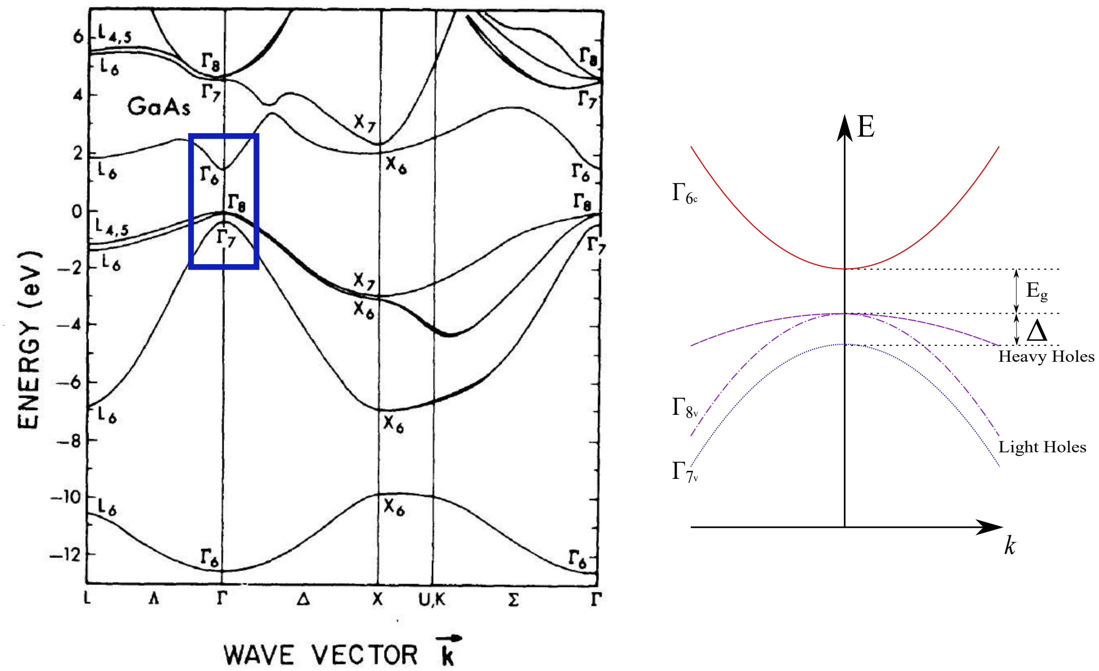

(a) (b)

Figure 2.5: (a) Band structure for GaAs calculated by Chelikowsy and Cohen in 1976 [12]. A direct bandgap of 1.51eV is calculated at the zone centre, Γ ($k = 0$), the region indicated by the blue box. (b) Schematic of the region around the band gap at the Γ point (indicated by the blue box). The conduction band (solid red line), light hole (purple dashed line), heavy hole (purple dashed-dotted line) and split off (dotted blue line) valence bands are shown. E_g is the fundamental bandgap, where Δ is the split off energy.

The band gap of bulk GaAs at the Γ point is 1.424 eV at 300K, with the temperature, T, dependence of the band gap for bulk GaAs according to [13] given by,

$$E_g = \left[1.519 - \frac{5.41T^2 \times 10^{-4}}{T + 204}\right] eV \tag{2.3}$$

To simplify the band structure and allow a comparison of the behaviour of electrons in a periodic potential to that of a free electron the *effective mass approximation* (EMA) is used. For a simple parabolic band (such as the conduction band at low values of k) solving Schrödinger's equation with the EMA Hamlitonian gives solutions:

$$E_c(\mathbf{k}) = E_n + \frac{\hbar^2 k_\perp^2}{2m^*_{cb\perp}} \tag{2.4}$$

where $E_c(\mathbf{k})$ is the energy of an electron at wavevector $\mathbf{k}$ in that sub band. E_n is the energy of the bottom of the n^{th} sub band, which for the conduction band is set to zero. $m^*_{cb\perp}$ is the in-plane effective mass of the electron at the conduction band edge, and is energy independent for parabolic bands. The effective mass of a sub band is dependent on its curvature [6, 8], and is described by the equation:

$$\frac{1}{m^{*}_{cb\perp}} = \frac{1}{\hbar^{2}} \frac{\partial^{2} E}{\partial k^{2}_{\perp}} \tag{2.5}$$

For small values of k the simple parabolic band model is an accurate representation of the conduction band, however with increasing value of k the conduction band becomes less parabolic and therefore a non-parabolic approximation must be made. Band non-parabolicity is beyond the scope of this thesis, however the effects of non-parabolicity are described in references [14–16].

2.2 Semiconductor Heterostructure Engineering

The ability to tailor the electronic properties of a wide range of semiconductors is fundamental to modern day semiconductor physics research and electrical engineering, with many novel electronic devices having been engineered in this way. Generally, to artificially engineer the electrical properties of a semiconductor such as its band gap, E_g, a third element (in the case of binary compound semiconductors) is introduced to the crystal structure in a process known as alloying.

2.2.1 Semiconductor Alloying

If we consider the diatomic semiconductor, gallium arsenide (GaAs), which has a direct band gap of 1.424 eV at 300K, it may be desirable to increase or reduce the width of the band gap to suit specific electronic device requirements. Should we wish to engineer a device with a marginally larger band gap, then alloying GaAs with aluminium (Al) would be an appropriate way to proceed.

The introduction of aluminium atoms during growth results in the substitution of gallium atoms with aluminium atoms in the crystal lattice. Where this occurs the electronic properties of the material are no longer those of a pure GaAs crystal, but a transition between those of GaAs and AlAs (aluminium arsenide). As AlAs has a larger band gap, 2.17 eV, than GaAs, then the introduction of Al results in an increased band gap in the alloy material. The exact electrical properties of the alloy depend on the ratio of Ga to Al atoms in the lattice, commonly known as the alloy fraction, x. Semiconductor alloys are often described using the notation, $\mathrm{Al}_x\mathrm{Ga}_{(1-x)}\mathrm{As}$, and to a first approximation, the variation of properties such as lattice constant, band gap and dielectric constant in alloy materials follow Vergard's law [10], i.e. the variation is linear with x. However, it is often required to engineer the material's properties to a high level of accuracy and therefore material systems such as GaAs and AlGaAs have been extensively studied. The

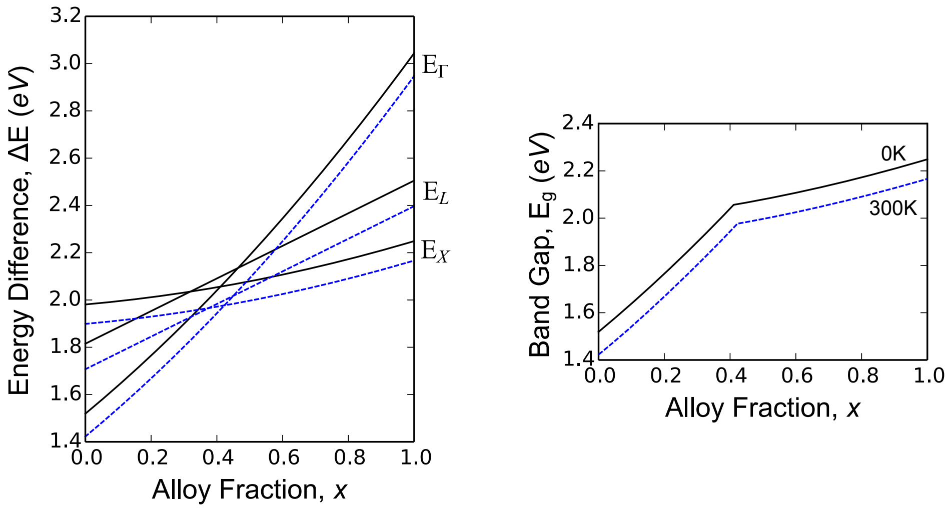

(a) (b)

FIGURE 2.6: (a) The calculated energy difference between the top of the valence band and bottom of the Γ, X and L valley minima at 0K (solid black line) and 300K (dashed blue line) for $\mathrm{Al}_x\mathrm{Ga}_{(1-x)}\mathrm{As}$ with increasing alloy fraction. A cross over occurs where the smallest energy difference (band gap) switches from the Γ-valley to the X-valley minima. (b) The band gap for $\mathrm{Al}_x\mathrm{Ga}_{(1-x)}\mathrm{As}$ as a function of alloy fraction at 0K (solid black line) and 300K (dashed blue line).

energy difference between the top of the valence band and the Γ point of $\mathrm{Al}_x\mathrm{Ga}_{(1-x)}\mathrm{As}$ at T = 0K [17] is given by,

$$E_\Gamma(0) = \left[1.519 + 1.155x + 0.37x^2\right] eV \tag{2.6}$$

and the temperature dependence of this given by:

$$E_\Gamma(T) = \left[E_\Gamma(0) - \frac{5.41T^2 \times 10^{-4}}{T + 204}\right] eV \tag{2.7}$$

However it is important to note that although GaAs is a direct band gap material, AlAs is an *indirect* band gap material with a conduction band minima at the X-valley minima. Therefore between an alloy fraction of approximately $x = 0.41$ and $x = 0.45$ (dependent on the temperature considered) the minima of the conduction band switches from the Γ-valley to the X-valley minima and so $\mathrm{Al}_x\mathrm{Ga}_{(1-x)}\mathrm{As}$ transitions from a direct to an indirect band gap semiconductor. It is therefore no longer appropriate to use equations (2.6) and (2.7) to calculate the band gap of of $\mathrm{Al}_x\mathrm{Ga}_{(1-x)}\mathrm{As}$ as the energy difference between the top of the valence band and the minima in the X-valley must be considered,

$$E_X(0) = \left[1.981 + 0.124x + 0.144x^2\right] eV \tag{2.8}$$

with the temperature dependence of the X-valley conduction band minima given by:

$$E_X(T) = \left[E_X(0) - \frac{4.60T^2 \times 10^{-4}}{T + 204} \right] eV \tag{2.9}$$

Similarly, the L-valley conduction band minima at T = 0K and temperature dependence of this minima are given by:

$$E_L(0) = [1.815 + 0.69x]\, eV \tag{2.10}$$

$$E_L(T) = \left[E_L(0) - \frac{6.05T^2 \times 10^{-4}}{T + 204} \right] eV \tag{2.11}$$

Calculated values from equations (2.6) to (2.11) for energy differences between the top of the valence band and the X, Γ and L valley minima against alloy fraction, x for temperatures of 0K (solid black line) and 300K (dashed blue line) are shown in figure 2.6(a). There is a clear cross over point at which the minimum energy difference (i.e. the band gap) switches from the E_Γ valley minima to the E_X valley minima for both temperatures. Figure 2.6(b) shows the band gap energy in eV against alloy fraction, the discontinuity in the line occurs at the alloy fraction for which the switch between a direct and indirect band gap occurs.

For most modern commercial electronic applications the operation and performance at room temperature (approximately 300K) is vitally important, therefore the approximate band gap of $\mathrm{Al}_x\mathrm{Ga}_{(1-x)}$ at 300K is more generally given by: equations (2.12) and (2.13),

$$E_g = 1.424 + 1.155x + 0.37x^2 \ \ (eV) \qquad \text{for,} \ \ x < 0.43 \tag{2.12}$$

$$E_g = 1.900 + 0.125x + 0.143x^2 \ \ (eV) \qquad \text{for,} \ \ x \geq 0.43 \tag{2.13}$$

Due to the $\mathrm{Al}_x\mathrm{Ga}_{(1-x)}\mathrm{As}$ material band gap becoming indirect, the majority of device structures use a composition with an alloy fraction of less than ≈ 0.35, as close to the direct and indirect semiconductor transition the alloy suffers from problems relating to a deep level, called the *D-X centre* [10]. It is believed that this centre is related to the merging of the Γ, X and L valleys in energy and has been an intense area of research, however this is beyond the scope of this thesis.

Table 2.1: A summary of important material parameters at 300K for GaAs and $\mathrm{Al}_{0.33}\mathrm{Ga}_{0.67}\mathrm{As}$.

Material	**Bandgap at 300K (eV)**	**Effective Mass (m^*)**	**Relative Permittivity (ε_r)**
GaAs	1.424	0.0630	12.90
$\mathrm{Al}_{0.33}\mathrm{Ga}_{0.67}\mathrm{As}$	1.854	0.0904	11.96

The alloying of a semiconductor also has an effect on other material parameters, such as the effective mass, m^* and relative permittivity ε_r, which also determine the overall electrical properties of the compound. A summary of the material parameters for GaAs and $Al_{0.33}Ga_{0.67}As$ can be found in table 2.1, with a substantial review of the properties of the $Al_xGa_{(1-x)}As$ alloy found in the article by Adachi [18].

Generally the alloying of semiconductors is far more complex and difficult for material systems other than $Al_xGa_{(1-x)}As$. Figure 2.7 shows the band gap energy and lattice constant of various III-V semiconductors at room temperature, where the transition between binary compound materials via alloying is represented by solid lines for regions with a direct bandgap and dashed lines for an indirect bandgap. It can be seen that GaAs (5.653Å) and AlAs (5.660Å) are near perfectly lattice matched, with only a 0.007Å (0.00124%) mismatch at 300K, and so it is possible to grow high quality $Al_xGa_{(1-x)}As$ crystals, with a low defect density on commonly available GaAs substrates without introducing large amounts of strain into the crystal lattice.

Alloys such as $In_xGa_{(1-x)}As$ (Indium Gallium Arsenide) or even binary compounds like InSb (Indium Antimonide), which are desirable for many reasons, are much more difficult to grow due to the lack of lattice matched, readily available, substrates on which to grow. Due to the mismatch in lattice constant between the substrate used and the III-V compound a significant amount of strain is introduced into the crystal lattice. This strain

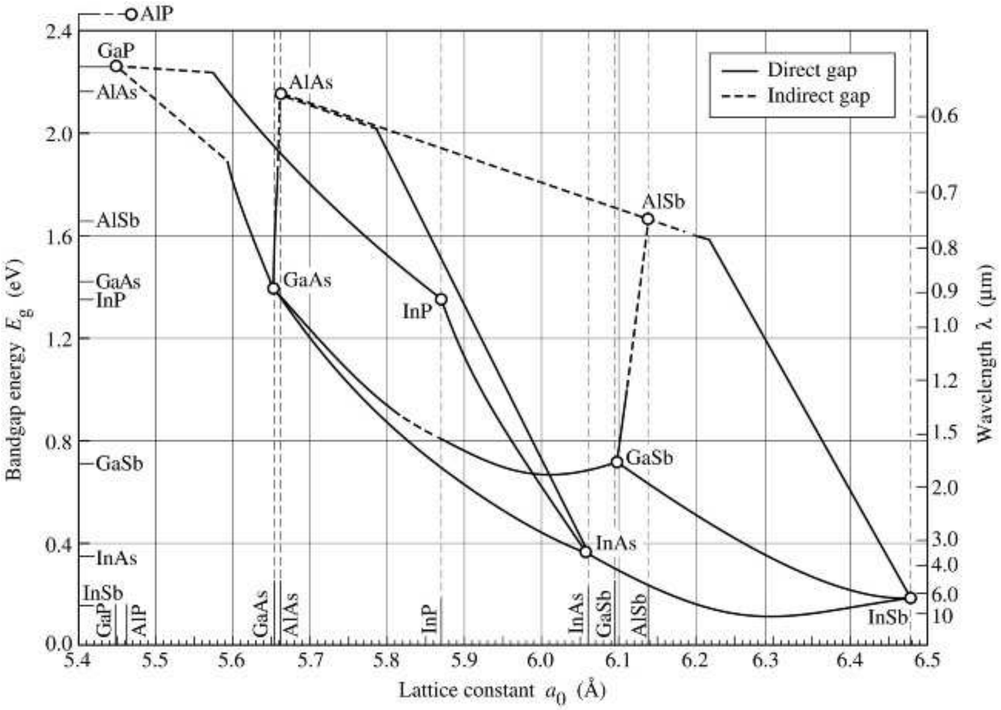

FIGURE 2.7: The bandgap energy, E_g (eV) versus lattice constant, a_0, (Å) for several III-V compound semiconductors and their alloys at 300K. The alloy transitions between binary compounds are indicated by solid lines, representing a direct bandgap, and dashed lines, representing an indirect bandgap.

can cause dislocation defects to occur, where an extra atom is included (or even omitted) from the periodic lattice to reduce the amount on strain in the crystal, which modifies the electrical, or optical properties of the material. It is therefore extremely important to consider the practical growth aspects when engineering any semiconductor material.

2.2.2 Heterojunctions and Heterostructures

The artificial engineering of semiconductor band structures has allowed for the creation of a vast range of novel devices, which utilise the properties of the interface which occurs between two layers of dissimilar crystalline semiconductors, known as heterojunctions. Several layers of dissimilar crystalline semiconductors, consisting of many heterojunctions, are known as heterostructures and this technology is utilised in many semiconductor devices which exploit quantum mechanical effects.

2.2.2.1 Heterojunctions

As the bandgap of different semiconducting materials is naturally different, it is reasonable to assume, that when creating an heterojunction of dissimilar materials, the conduction and valence bands will not necessarily be aligned at the same energy for the two different materials. This misalignment results in discontinuities in the structure of the valence and conduction bands and the resultant heterojunctions can be categorised into three distinct types, which are shown in figure 2.8.

Type I heterojunctions, or straddling gap heterojunctions, are formed by the joining of

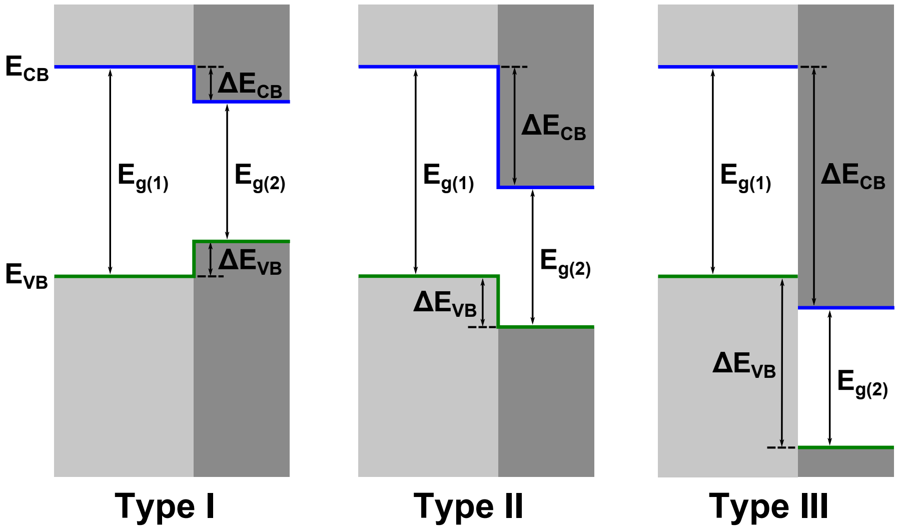

FIGURE 2.8: The three types of heterojunctions, type I or straddling gap, type II or staggered gap and type III the broken gap, formed at the interface of two dissimilar materials.

two dissimilar semiconducting materials, where one material has a wider bandgap, $E_{g(1)}$, and the other a narrower bandgap, $E_{g(2)}$. The energy of the conduction band, E_{CB}, and valence band E_{VB}, of the narrower bandgap material both lay within the bandgap of the wider bandgap material. An example of this type of heterojunction is the interface between a layer of $\mathrm{Al}_x\mathrm{Ga}_{(1-x)}\mathrm{As}$ where $x > 0$, which has a wider bandgap than a layer of GaAs.

A staggered gap, or type II heterojunction, occurs in the situation where the conduction band energy, E_{CB} of one material lays within the bandgap of the other, but the valence band energy, E_{VB} of the material lays within the valence band of the other. A heterojunction between InAs (Indium Arsenide) and AlSb (Aluminium Antimonide) exhibits this type of behaviour. Finally, an interface between a layer of InAs and GaSb (Gallium Antimonide) leads to the situation where neither the conduction band energy, E_{CB}, or valence band energy, E_{VB}, of either material lay within the band gap of the other and this is known as a broken gap, or type III heterojunction.

Therefore, when we consider heterojunctions, it not sufficient to simply specify the bandgaps, $E_{g(1)}$ and $E_{g(2)}$ of the materials, extra information is required in the form of the difference in energy between either the conduction band, ΔE_{CB} or valence band, ΔE_{VB} edges of the materials [19].

The conduction band, E_{CB} and valence band, E_{VB} edge offsets for $\mathrm{Al}_x\mathrm{Ga}_{(1-x)}\mathrm{As}$ with respect to GaAs [17] at 300K are given by:

$$\Delta E_{CB} = 0.79x \ \ (eV) \qquad \text{for, } \ x < 0.43 \tag{2.14}$$

$$\Delta E_{CB} = 0.475 - 0.335x + 0.143x^2 \ \ (eV) \qquad \text{for, } \ x \geq 0.43 \tag{2.15}$$

$$\Delta E_{VB} = -0.46x \ \ (eV) \tag{2.16}$$

2.2.2.2 Heterostructures

A construction of several consecutive heterojunctions forms what is known as a heterostructure, which can take many different forms. The most common and important two type of heterostructures are the formation of a potential barrier or potential well in the conduction or valence band of the semiconductor band structure.

A potential barrier is formed at the conduction and valence band edges (for type I heterojunctions) by the inclusion of a wider band gap material between two layers of narrower bandgap material, figure 2.9(a). Charge carriers (electrons in the conduction band and holes in the valence band) with less energy than that of the potential barrier would classically be unable to overcome the barrier, and as such their movement through the semiconductor crystal in the growth direction, z halted. Quantum mechanically

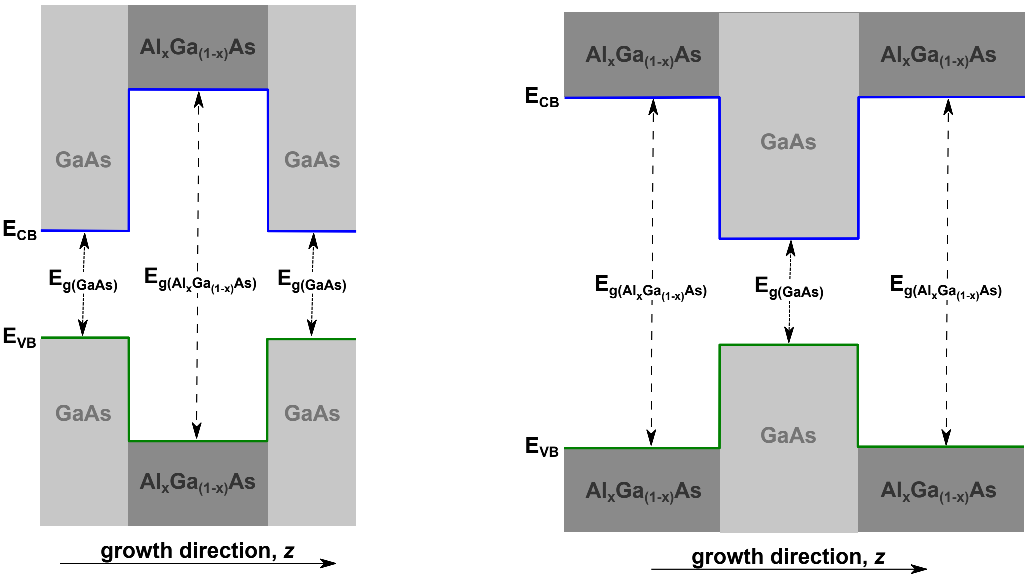
$Al_xGa_{(1-x)}As$
GaAs
GaAs
E_{CB}
$E_{g(GaAs)}$
$E_{g(Al_xGa_{(1-x)}As)}$
$E_{g(GaAs)}$
E_{VB}
GaAs
GaAs
$Al_xGa_{(1-x)}As$
growth direction, z
$Al_xGa_{(1-x)}As$
$Al_xGa_{(1-x)}As$
E_{CB}
GaAs
$E_{g(Al_xGa_{(1-x)}As)}$
$E_{g(GaAs)}$
$E_{g(Al_xGa_{(1-x)}As)}$
E_{VB}
GaAs
$Al_xGa_{(1-x)}As$
$Al_xGa_{(1-x)}As$
growth direction, z

(a) (b)

FIGURE 2.9: Two different forms of heterostructures created by two type I heterojunctions. (a) The inclusion of a wider bandgap material ($Al_xGa_{(1-x)}As$) between two layers of narrower band gap material produces a potential barrier in the conduction and valence band edges. (b) Engineering a layer of narrower bandgap material (GaAs) between two layers of wider bandgap material ($Al_xGa_{(1-x)}As$) results in the formation of a potential well.

however, passage through the crystal structure for charge carriers with less energy than that of the potential barrier is possible, and is treated in more detail in section 4.1. Figure 2.9(b) shows the result of engineering a layer of narrower bandgap material between two layers of wider bandgap material (all with type I heterojunctions). A potential well is formed in the conduction and valence band edges, and charge carriers with energy less than the depth of the potential well are unable to escape. If the width

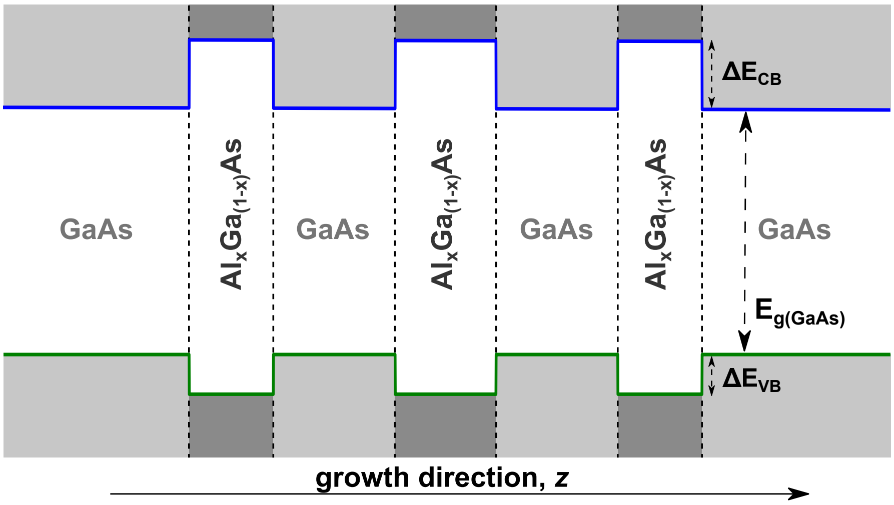
ΔE_{CB}
GaAs
$Al_xGa_{(1-x)}As$
GaAs
$Al_xGa_{(1-x)}As$
GaAs
$Al_xGa_{(1-x)}As$
GaAs
$E_{g(GaAs)}$
ΔE_{VB}
growth direction, z

FIGURE 2.10: A schematic of a triple barrier, double quantum well heterostructure created by alternating layers of GaAs and $Al_xGa_{(1-x)}As$ in the growth direction z.

of the potential well layer is of the order of the thermal deBroglie wavelength of the charge carrier then quantum mechanical effects take hold within the well region, which are described in section 2.2.3

Combining further layers of wider and narrower bandgap materials allows for the construction of even more complex heterostructures. The structures studied in this thesis are formed by incorporating three layers of wider bandgap material ($\mathrm{Al}_x\mathrm{Ga}_{(1-x)}\mathrm{As}$), between which layers of a narrower bandgap material (GaAs) are sandwiched. This combination results in the formation of three potential barriers and two potential wells in the conduction and valence band edges and is known as a triple barrier heterostructure. A schematic of the resulting band profile is shown in figure 2.10.

2.2.3 Quantum Wells

The quantum well is is one of the simplest heterostructures that takes advantage of an artificially engineered band structure, and is formed when the width of a potential well is of the order of the thermal deBroglie wavelength of the charge carriers:

$$\lambda = \frac{h}{\sqrt{2mk_BT}} \tag{2.17}$$

where h is Planck's constant, m is the mass of the particle, k_B is Boltzmann's constant and T is temperature. It is at these length scales where the charge carriers allowable energy states within the quantum well becomes quantised, and as such the charges in this region are only able to move freely in the two dimensions perpendicular to the growth direction. The behaviour of the carriers in the quantum well can be described by using a simple quantum mechanical picture of confinement in a one dimensional finite quantum well.

2.2.3.1 The Finite Quantum Well

A quantum well with a finite barrier of height V_0 can be described by in the effective mass approximation by the time-independent Schrödinger equation [20]

$$\left[-\frac{\hbar^2}{2m^*}\frac{\partial}{\partial z^2} + V(z)\right]\Psi(z) = E\Psi(z) \tag{2.18}$$

where the potential, $V(z) = V_0$ in the barrier regions and $V(z) = 0$ in the quantum well region, m^* is the particle effective mass, $\Psi(z)$ is the particle wavefunction and E is the energy. Since the barrier potential is not infinite the wavefunction is non-zero at the well interfaces. The wavefunction penetrates into the barrier regions and therefore this must be taken into account when considering the solutions to equation (2.18).

The wavefunctions in the quantum well region can take the form

$$\Psi_n(z) = A\cos k_z z \qquad \text{when n is odd} \tag{2.19}$$

$$\Psi_n(z) = A\sin k_z z \qquad \text{when n is even} \tag{2.20}$$

where n is the quantum number and $n = 1, 2, 3...etc.$ The wavefunction of the particle in the barrier regions can be expressed as

$$\Psi_b(z) = Be^{\pm\kappa z} \tag{2.21}$$

and the wavenumbers k_z and κ_z are given by:

$$k_z = \left[\frac{2m_w^* E}{\hbar^2}\right]^{\frac{1}{2}} \tag{2.22}$$

$$\kappa_z = \left[\frac{2m_b^*\left(V_0 - E\right)}{\hbar^2}\right]^{\frac{1}{2}} \tag{2.23}$$

The particle effective mass in the well and barrier regions of the quantum well are given by m_w^* and m_b^* respectively.

It is important to note that since the wavefunction in the barrier regions is non-zero, and that the probability, $P(z)$ of finding a particle is

$$P(z) = |\Psi(z)|^2 \tag{2.24}$$

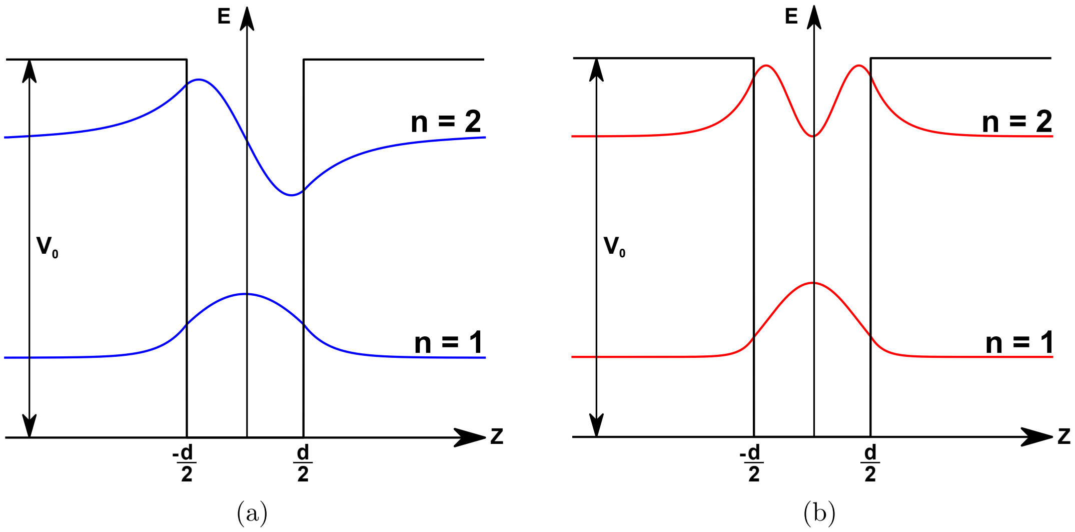

FIGURE 2.11: Schematics of a qunatum well of width d and barrier height V_0. (a) The particle wavefunctions for the $n = 1$ and $n = 2$ confined states are shown in blue. (b) The particle probability density for the $n = 1$ and $n = 2$ confined states are shown in red.

there is a finite probability that the particle can be present in the barrier regions. This is an important quantum mechanical phenomenon, which contradicts with our understanding from classical mechanics, where the presence of the particle in the barrier region is forbidden. It is this phenomenon which gives rise to the possibility of quantum mechanical tunnelling, a concept which is discussed in section 4.1. Schematics for a finite potential well are shown in figure 2.11, with the particle wavefunction for two confined states shown in figure 2.11(a) and the particle probability density shown in figure 2.11(b). To solve the solutions for the finite quantum well, the boundary conditions at the interfaces between the well and barrier regions require that

$$\Psi_{LHS} = \Psi_{RHS} \tag{2.25}$$

$$\frac{1}{m^*_{LHS}} \frac{\partial \Psi}{\partial z}\Big|_{LHS} = \frac{1}{m^*_{RHS}} \frac{\partial \Psi}{\partial z}\Big|_{RHS} \tag{2.26}$$

where Ψ_{LHS} and Ψ_{RHS} are the wavefunctions and m^*_{LHS} and m^*_{RHS} the effective masses of the particles at the left-hand and right-hand side of the interface respectively.

Equation (2.26) is subtly different to that of an ideal potential step for various reasons, however the main consideration is that it is not only the conduction band edge potential that is effectively discontinuous, but also the effective mass [21]. The application of equations (2.25) and (2.26) to equations (2.19) and (2.20) for a quantum well of width d, results in:

$$\frac{k_z}{\kappa} \tan\left(k_z \frac{\mathrm{d}}{2}\right) = \frac{m^*_w}{m^*_b} \qquad \text{when n is odd} \tag{2.27}$$

$$\frac{\kappa}{k_z} \tan\left(k_z \frac{\mathrm{d}}{2}\right) = -\frac{m^*_b}{m^*_w} \qquad \text{when n is even} \tag{2.28}$$

for which solutions of equations (2.27) and (2.28) can only be obtained by graphical or numerical analysis.

It is important to remember that this confinement of particles is only in one direction for a quantum well, the z-direction, and hence that it is only k_z that is quantised. The particle is free within the plane of the quantum well and as such there are still numerous values that k_x and k_y can take. Hence, the total energy of a particle in the quantum well region is given by

$$E = E_n + \frac{\hbar^2}{2m^*_w}\left(k_x^2 + k_y^2\right) \tag{2.29}$$

where E is the total energy of the particle, E_n is the quantised energy of the particle in the z direction and m^*_w is the effective mass in the quantum well region.

2.2.4 Density of States in Three and Two Dimensions

To calculate the concentrations of electrons and holes in the conduction and valence bands, respectively, then the number of allowable energy states per unit energy per unit volume must be known. This quantity is known as the density of states and will be discussed in the following sections.

2.2.4.1 Three Dimensions

For a three dimensional (3D) structure, where we can consider the electrons in the structure as not confined in any direction, we know from the *effective mass approximation* (equation (2.4)) that,

$$E = \frac{\hbar^2 \boldsymbol{k}^2}{2m^*} = \frac{\hbar^2}{2m^*}(k_x^2 + k_y^2 + k_z^2) \tag{2.30}$$

and so the electron wavefunctions must satisfy Schrödinger's equation, with solutions of the form:

$$\psi_k(\mathbf{r}) = U_k(\mathbf{r})\exp(i\mathbf{k}\cdot\mathbf{r}) \tag{2.31}$$

Due to energy degeneracy with $\boldsymbol{k} = k_x^2 + k_y^2 + k_z^2$, for a cube of material with side length L,

$$k_x = \frac{2\pi n_x}{L}, \quad k_y = \frac{2\pi n_y}{L}, \quad k_x = \frac{2\pi n_y}{L} \tag{2.32}$$

where n_x, n_y, n_z are integers, So if we now wish to consider the number of allowable values of $\boldsymbol{k}$ in k-space, then we must first consider the volume between two shells of radii, $\boldsymbol{k}$ and $\boldsymbol{k} + d\boldsymbol{k}$, as shown in figure 2.12. In three dimensions, the volume is given by:

$$V_{\text{shell}}\ \mathrm{d}\boldsymbol{k} = 4\pi|\boldsymbol{k}|^2 d\boldsymbol{k} \tag{2.33}$$

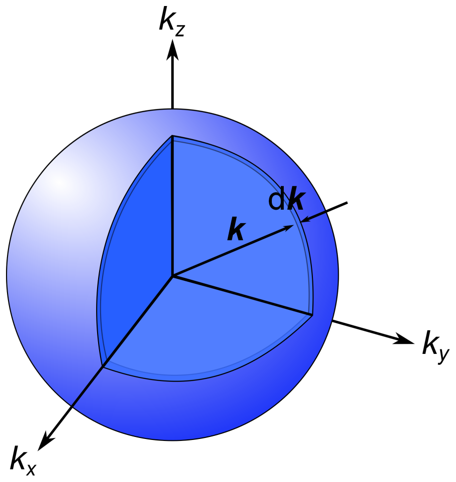

FIGURE 2.12: Spheres in k-space of radius $\boldsymbol{k}$ and $\boldsymbol{k} + \mathrm{d}\boldsymbol{k}$. The volume of a shell of thickness d$\boldsymbol{k}$ is given by subtracting the volume of one sphere from the other.

The number of states is therefore given by dividing the volume of a shell, equation (2.33) by the volume of a single energy state,

$$V_{\text{state}} = \left(\frac{2\pi}{L}\right)^3 \tag{2.34}$$

and introducing a factor of two, which accounts for the electron spin states, resulting in:

$$g(\boldsymbol{k})\ \mathrm{d}\boldsymbol{k} = \frac{|\boldsymbol{k}^2| d\boldsymbol{k} L^3}{\pi^2} \tag{2.35}$$

It is then trivial to show, by rearranging equation (2.30) and substituting into equation (2.35) that:

$$g(E)_{3D}\ \mathrm{d}E = \frac{1}{2\pi^2}\left(\frac{2m}{\hbar^2}\right)^{\frac{3}{2}} E^{\frac{1}{2}}\ \mathrm{d}E \tag{2.36}$$

Which is known as the density of states per unit volume per unit energy, and by integration between two different energies, can be used to calculate the number of allowable states per unit volume.

2.2.4.2 Two Dimensions

Similarly to section 2.2.4.1, it can be shown that when confined in one direction, as in a quantum well, that the volume of a single energy state in k-space:

$$V_{\text{state}} = \left(\frac{2\pi}{L}\right)^2 \tag{2.37}$$

and the volume of an annulus of allowed k-space states is given by:

$$V_{\text{shell}}\ \mathrm{d}\boldsymbol{k} = 2\pi|\boldsymbol{k}|\ \mathrm{d}\boldsymbol{k} \tag{2.38}$$

The density of states in two dimensions can therefore be shown to be:

$$g(E)_{2D}\ \mathrm{d}E = \frac{m^*}{\pi\hbar^2}\ \mathrm{d}E \tag{2.39}$$

It is significant to note that the two-dimensional density of states does not depend on energy, and as such there are a significant number of states immediately available[*]. Figure 2.13 shows the density of states for a three and two dimensional system, to take into account the other energy levels in the quantum well, the density of states equation must be modified,

$$g(E)_{2D}\ \mathrm{d}E = \frac{m^*}{\pi\hbar^2}\sum_i \Theta(E - E_i)\ \mathrm{d}E \tag{2.40}$$

---

[*] Which is a very important property for laser structures, where there are a large number of states at the lasing energy.

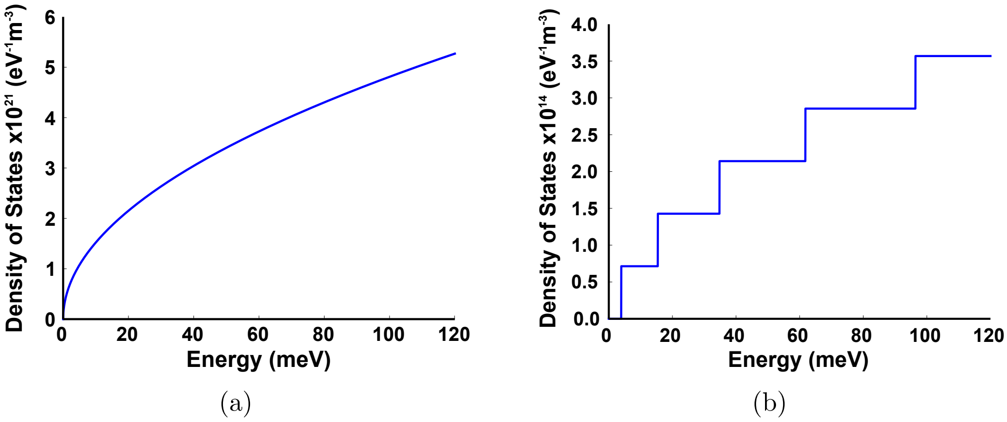

(a)

(b)

FIGURE 2.13: The calculated density of states (DoS) for: (a) Bulk GaAs, using equation (2.36) (b) A GaAs quantum well of well width 350nm using equation (2.39). For a two-dimensional system the lowest available energy state is no longer at zero, but has been shifted to a higher energy due to the quantum confinement. The spacing in energy of the allowed quantum levels is proportional to $\mathrm{E}^{\frac{1}{2}}$ and hence the 2D DoS fits within the 3D Dos. In the limit where the spacing between the energy levels in a 2D system tends to zero, the 3D DoS and 2D DoS are equivilent.

where $\Theta(E - E_i)$ is the Heavyside function and takes the value of zero when $E < E_i$ and one when $E \geq E_i$ when $E_{i]}$ is the energy of the ith level within the quantum well.

Bibliography

[1] John E. Davey and Titus Pankey. 'Epitaxial GaAs Films Deposited by Vacuum Evaporation'. In: *Journal of Applied Physics* 39.4 (1968), pp. 1941–1948. DOI: `http://dx.doi.org/10.1063/1.1656467`.

[2] J. R. Arthur and J. J. LePore. 'GaAs, GaP, and GaAs$_x$P$_{1-x}$ Epitaxial Films Grown by Molecular Beam Deposition'. In: *Journal of Vacuum Science & Technology* 6.4 (1969), pp. 545–548. DOI: `http://dx.doi.org/10.1116/1.1315677`.

[3] A. Y. Cho. 'Film Deposition by Molecular-Beam Techniques'. In: *Journal of Vacuum Science & Technology* 8.5 (1971), S31–S38. DOI: `http://dx.doi.org/10.1116/1.1316387`.

[4] A. Y. Cho. 'GaAs Epitaxy by a Molecular Beam Method: Observations of Surface Structure on the (001) Face'. In: *Journal of Applied Physics* 42.5 (1971), pp. 2074–2081. DOI: `http://dx.doi.org/10.1063/1.1660490`.

[5] A.C. Gossard. 'Growth of microstructures by molecular beam epitaxy'. In: *Quantum Electronics, IEEE Journal of* 22.9 (1986), pp. 1649–1655. ISSN: 0018-9197. DOI: `10.1109/JQE.1986.1073165`.

[6] C Kittel. *Introduction to Solid State Physics*. Eigth. John Wiley & Sons, Ltd, 2005.

[7] N. W. Ashcroft and N. D. Mermin. *Solid State Physics*. Saunders College Publishing, 1976.

[8] J. R. Hook and H. E. Hall. *Solid State Physics*. Second. John Wiley & Sons, Ltd, 2004.

[9] H. Ibach and H. Luth. *Solid State Physics. An Introduction to Principles of Materials Science*. Springer, 2009.

[10] J. Singh. *Physics of Semiconductors and their Heterostructures*. First. McGraw-Hill, Inc, 1993.

[11] P.Y. Yu and M. Cardona. *Fundamentals of Semiconductors*. Fourth. Springer, 2010.

[12] James R. Chelikowsky and Marvin L. Cohen. ‘Nonlocal pseudopotential calculations for the electronic structure of eleven diamond and zinc-blende semiconductors’. In: *Phys. Rev. B* 14 (2 July 1976), pp. 556–582. DOI: `10.1103/PhysRevB.14.556`.

[13] *http://www.ioffe.ru/SVA/NSM/Semicond/GaAs/bandstr.html.* URL. Ioffe Institue, St. Petersburg, Russion Federation, 2015.

[14] O. Kane Evan. ‘Band structure of indium antimonide’. In: *Journal of Physics and Chemistry of Solids* 1.4 (1957), pp. 249–261. ISSN: 0022-3697. DOI: `http://dx.doi.org/10.1016/0022-3697(57)90013-6`.

[15] P. Pfeffer and W. Zawadzki. ‘Conduction electrons in GaAs: Five-level $k{\cdot}p$ theory and polaron effects’. In: *Phys. Rev. B* 41 (3 Jan. 1990), pp. 1561–1576. DOI: `10.1103/PhysRevB.41.1561`.

[16] A. M. Gilbertson. ‘Spin and Magnetotransport Properties of Narrow Gap Semiconductors’. PhD thesis. University of London, Imperial College London, 2009.

[17] *http://www.ioffe.ru/SVA/NSM/Semicond/AlGaAs/bandstr.html.* URL. Ioffe Institue, St. Petersburg, Russion Federation, 2015.

[18] Sadao Adachi. ‘GaAs, AlAs, and AlxGa1-xAs: Material parameters for use in research and device applications’. In: *Journal of Applied Physics* 58.3 (1985), R1–R29. DOI: `http://dx.doi.org/10.1063/1.336070`.

[19] M Razeghi. *Fundamentals of Solid State Engineering.* Springer US, 2009.

[20] M Fox. *Optical Properties of Solids.* Oxford University Press, 2010.

[21] K. Barnham and D. Vvedensky. *Low-dimensional semicondcutor structures.* Cambridge University Press, 2001.

Chapter 3

Practical Realisation of Heterostructure Devices and Experimental Details

3.1 Practical Realisation of Heterostructure Devices

The practical realisation of heterostructures is an area which has been subject to extensive research for over 40 years, and has resulted in various techniques being developed to achieve high quality semiconductor crystal growth. The techniques described in the following sections give only a brief overview of these approaches where they are applicable to this thesis.

The term epitaxial growth refers to the deposition of new thin films of material, via reactions between thermal energy molecular (or atomic) beams and the surface of a substrate crystal onto which the new layers are grown. The substrate is held at a precisely controlled temperature, that encourages specific growth characteristics of the material, whilst in an ultra-high vacuum. In depth descriptions of growth techniques such as molecular beam epitaxy (MBE) and metalorganic chemical vapor deposition (MOCVD) are given in references [1–4].

3.1.1 Molecular Beam Epitaxy (MBE)

MBE is distinguished from previous vacuum deposition techniques by the precise control of growth conditions, which allows for atomic layer precision in the growth of epitaxial structures. The growth of the epitaxial layers is governed mainly by the kinetics of the processes occurring on the substrate surface. The MBE process uses a technique by

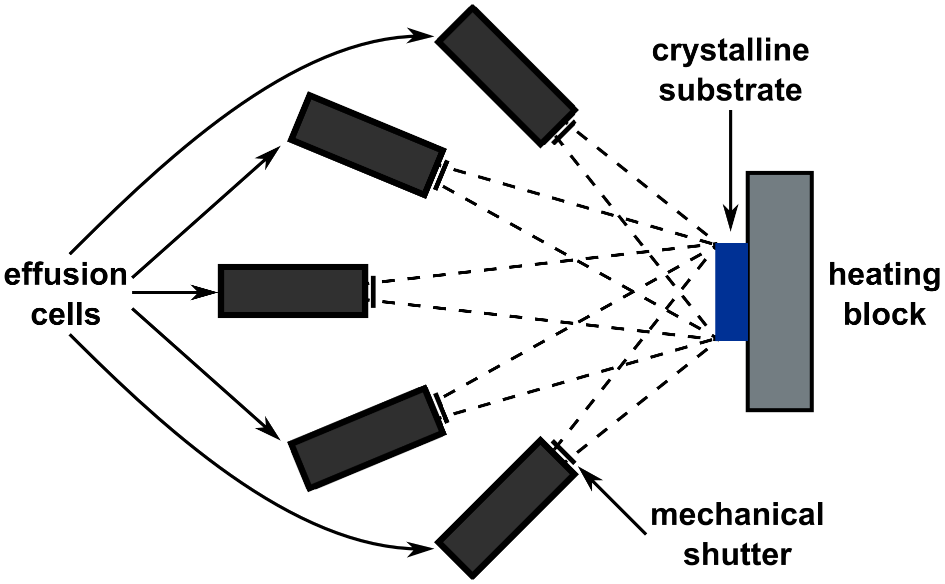

FIGURE 3.1: A simple schematic showing the main components under ultra-high vacuum required for molecular beam epitaxy growth. Several effusion cells of different elements are located such that an evaporated beam of molecules is targeted at a crystalline substrate on a heating block, with mechanical shutters controling which elements are incident on the substrate.

.

which high purity materials are evaporated at the target substrate, for which the rate at which the material incident onto the substrate surface is accurately controlled by the temperature of the solid source cells (often Knudsen-effusion-cell). The use of simple mechanical shutters to impede the beam fluxes, and so interrupt material deposition on the surface allows for sharp interfaces between dissimilar molecular compositions.

Figure 3.1 shows a simple schematic of the MBE growth technique. Effusion cells of different elements are heated such that the material evaporates in a beam towards the crystalline substrate which is rotated on a heating block. The mechanical shutters at each cell are individually opened or closed to allow a desired composition of elements to be incident on the substrate surface, so epitaxial growth can take place.

The incorporation of impurity atoms into the crystal structure during growth, allows for the intentional altering of the electrical properties of the material. This process is known as doping and is commonly used to increase the conductivity of the grown material. Two types of doping exist, *n-type* where the inclusion of an impurity atom has the possibility of donating an extra electron, and *p-type*, which leads to the possibility of an extra hole. Regions of semiconductor material that have been heavily doped, such that they are highly conductive are referred to as *n+* and *p+* for heavily doped *n-type* and *p-type* materials respectively. An in depth look at the effects of doping in III-V semiconductors by Schubert can be found in reference [5].

3.1.2 GaAs/AlGaAs Wafer Design

The structures studied in this thesis were grown by solid source molecular beam epitaxy at The University of Manchester and grown on semi-insulating gallium arsenide (GaAs) substrates. The growth layers of the structures are as follows:

i) 1 µm n+ (n=7x10^{18} cm^{-3}) GaAs buffer layer,

ii) 100Å doped (n=3x10^{17} cm^{-3}) GaAs layer,

iii) 100Å undoped GaAs spacer layer,

iv) 45Å $Al_{0.33}Ga_{0.67}As$ barrier,

v) Nominally 23 monolayers undoped GaAs quantum well A,

vi) 54Å $Al_{0.33}Ga_{0.67}As$ barrier,

vii) Undoped GaAs quantum well B,

viii) 45Å $Al_{0.33}Ga_{0.67}As$ barrier,

ix) 200Å GaAs space layer,

x) n=5x10^{12} cm^{-2} Si δ-doped layer,

xi) 0.4 µm n+ (n=7x10^{18} cm^{-3}) contact layer.

A schematic of the layer structure is shown in figure 3.2 and the resultant conduction and valence band structure with zero applied electric field is shown in figure 3.3. The growth of this layer structure results in the formation of three potential barriers ($Al_{0.33}Ga_{0.67}As$ layers), which in turn form two GaAs quantum wells. The layer of δ-doping is introduced to act as a fulcrum and create a fixed point about which the band bending, when a

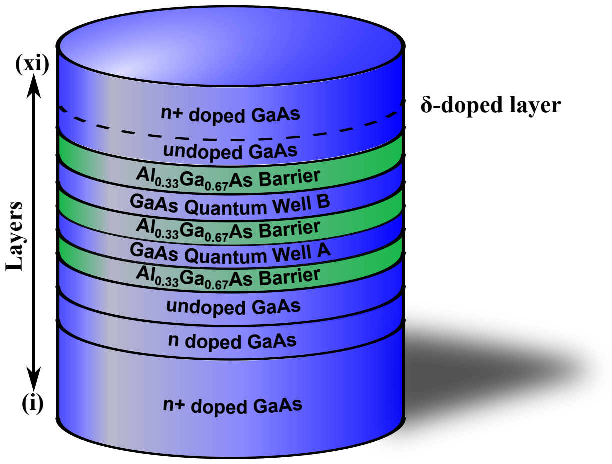
(xi)
n+ doped GaAs
δ-doped layer
undoped GaAs
Al0.33Ga0.67As Barrier
GaAs Quantum Well B
Al0.33Ga0.67As Barrier
GaAs Quantum Well A
Al0.33Ga0.67As Barrier
undoped GaAs
n doped GaAs
Layers
(i)
n+ doped GaAs

FIGURE 3.2: A schematic of the triple barrier resonant tunnelling layer structure, which consists of n-type doped contact layers, undoped spacers layers of GaAs and an active region of three $Al_{0.33}Ga_{0.67}As$ barrier layers, alternating with two GaAs quantum well layers.

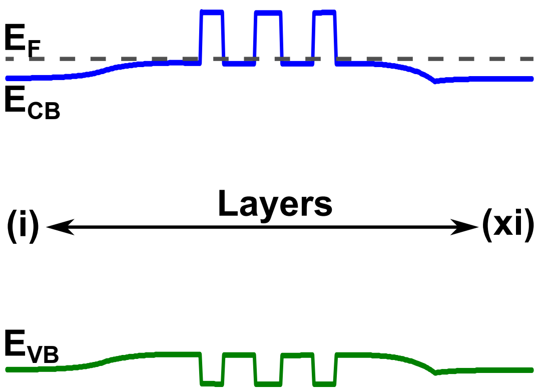

FIGURE 3.3: A calculated energy band diagram using the model described in appendix B, for a triple barrier resonant tunnelling structure described in section 3.1.2. The valence band edge, E_{VB} and conduction band edge, E_{CB} are shown, along with the calculated Fermi level, E_F, which lays within the conduction band.

voltage is applied, takes place and so results in the depletion region in the emitter side of the device becoming fixed.

A series of seven triple barrier structures were studied, with the width of quantum well (QW) B varied by approximately one monolayer (ml) between each sample. Previous work carried out on these samples had experimentally determined the quantum well widths by measurements from photoluminescence excitation (PLE). The expected growth widths for quantum wells A and B, as well as the experimentally determined well widths are shown in table 3.1 and for more details of these measurements and well width extraction see reference [6].

The range of samples were initially designed such that they varied from a structure with symmetric quantum wells, to one with a high degree of asymmetry. The ratio of quantum well A to quantum well B is therefore considered as an important measure of

TABLE 3.1: The measured quantum well widths by photoluminescence excitation (PLE) [6] for the series of VMBE samples grown by MBE at The University of Manchester. For details of these measurements see appendix C.

Sample	**Expected Quantum Well A Width (ml)**	**Measured Quantum Well A Width (ml)**	**Expected Quantum Well B Width (ml)**	**Measured Quantum Well B Width (ml)**
VMBE 755	23.0	23.8	23.0	23.1
VMBE 757	23.0	24.9	22.0	23.3
VMBE 760	23.0	23.3	20.0	21.1
VMBE 761	23.0	23.8	19.0	20.3
VMBE 762	23.0	24.4	18.0	18.4
VMBE 787	23.0	23.0	16.0	16.0
VMBE 788	23.0	22.6	17.0	16.0

Table 3.2: The ratio of the expected and measured quantum well widths for wells A to B for the series of VMBE samples.

Sample	**Expected Quantum Well Ratio A:B**	**Measured Quantum Well Ratio A:B**
VMBE 755	1.000	1.030
VMBE 757	1.045	1.069
VMBE 760	1.150	1.104
VMBE 761	1.211	1.172
VMBE 762	1.278	1.326
VMBE 787	1.438	1.438
VMBE 788	1.353	1.413

the structural asymmetry in the sample and is shown for the expected and measured quantum well widths in table 3.2.

3.1.3 Device Fabrication

Fabrication of the triple barrier resonant tunnelling structure devices detailed here was carried out using conventional semiconductor processing techniques at the Cardiff University, School of Physics and Astronomy cleanroom. The devices were fabricated from the as-grown wafers described in section 3.1.2 via combinations of conventional photolithograpy, chemical etching and metal deposition. The fabrication process for devices measured in chapters 4 and 5 is detailed in the following sections.

3.1.3.1 Photolithography

The technique of photolithography, which is also known as optical lithograpy is used to pattern semiconductor substrates during device fabrication. The process usually involves the transferring of a desired pattern from a "mask" (usually a clear glass tile, with a metallic opaque pattern) onto a polymer film, known as a photoresist. The photoresist is deposited onto the semiconductor substrate, initially in liquid form, and distributed into an even layer across the surface by the use of a mechanical spin coater, figure 3.4(a). The evenly spun resist is then baked on a hot plate to evaporate the solvents, forming a solid, hard plastic polymer. The photoresists used in the fabrication of the triple barrier resonant tunnelling structure devices were *Microposit* S1813 and *PMGI* SF6, both of which are positive tone. The thickness of the photoresist layer is dependent upon the speed at which the sample is spun, however typically the samples were spun for 10 seconds at 5000rpm, resulting in a thickness once baked of 1.5μm and 600nm for the S1813 and SF6 resists respectively, with a typical bake temperature of 95°C for 5

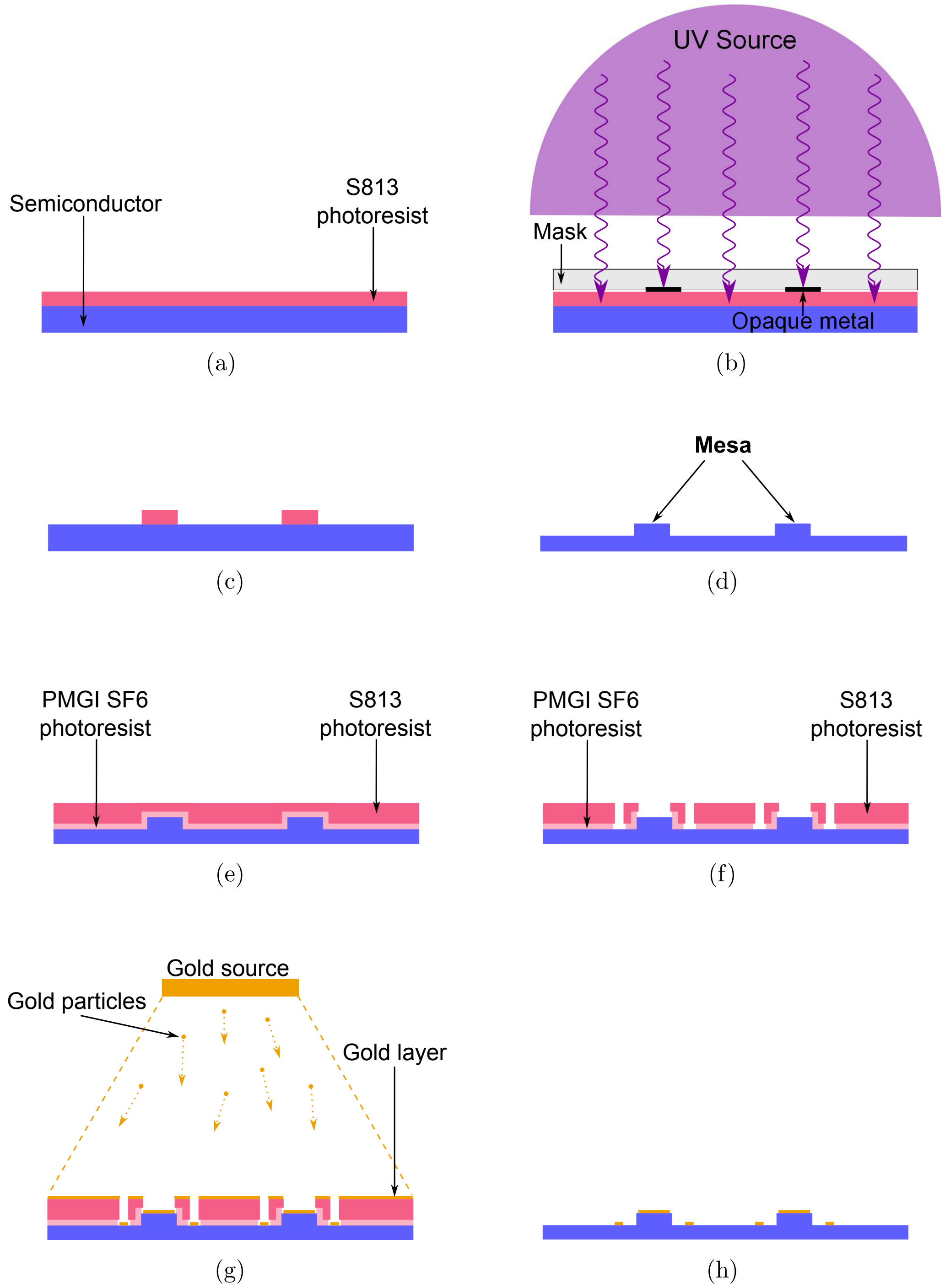
Semiconductor
S813 photoresist
UV Source
Mask
Opaque metal
Mesa
PMGI SF6 photoresist
S813 photoresist
PMGI SF6 photoresist
S813 photoresist
Gold source
Gold particles
Gold layer

(a) (b) (c) (d) (e) (f) (g) (h)

FIGURE 3.4: Schematics of the main processing steps in the fabrication of triple barrier resonant tunnelling structure devices. (a) Application of S1813 photoresist to the semiconductor substrate. (b) Exposure of the photoresist using ultraviolet radiation and a glass mask patterned with opaque metal. (c) The resultant resist profile after development of exposed resist to be used as an etch mask. (d) The mesa profiles once chemical etching of the substrate has taken place and resist etch maks removed. (e) Application of two layers of resis in a bi-layer process, SF6 and S1813. (f) The resultant resist profile after exposure of the resist to UV radiation and development, an undercut feature can be seen in the SF6 layer. (g) Thermal evaporation from a gold source where a film of metal is deopsited onto the substrate and resist surfaces. (h) The remaining gold contants and mesa profile after removal of the unwanted resist and metal.

minutes.

Once the photoresist has been applied, the mask is brought into very close proximity to the semiconductor substrate, and the mask and substrate combination is exposed to ultraviolet (UV) radiation. The areas of opaque metal on the mask block the UV radiation from reaching the photoresist underneath on the surface of the substrate, figure 3.4(b). The exposure of the resist to UV radiation alters its chemical make up, such that when immersed in a developer solution the exposed photoresist (for a positive tone resist) or unexposed (for a negative tone resist) is removed. The alignment of the mask to the semiconductor substrate, and exposure to UV radiation was performed by using a *Karl Suss Contact Mask Aligner*, with the sample exposed for 6.5 seconds and developed in *Microposit* MF319 developer for approximately 40 seconds. The remaining pattern of unexposed S1813 resist, matches the pattern of the opaque metal on the mask, figure 3.4(c), and can be used as protection for the surface of the semiconductor for metal deposition, or as a mask for a dry or wet chemical etch.

When used as a mask for chemical etching a single layer of photoresist such as S1813 is used, however, for deposition of metal (or dielectric material also) a bi-layer (SF6 and S1813) resist process is used. This process is described futher in section 3.1.3.3.

3.1.3.2 Chemical Etching

Chemical etching is a technique that allows for the removal of unwanted areas of semiconductor and is often used to electrically isolate regions of material from each other in a desired pattern or expose certain epitaxial layers of the substrate, for example. Two forms of chemical etching exist, the first of which is *dry etching*, which uses a plasma to bombard the substrate surface with ions that remove part of the exposed material. Various different dry etching techniques are in use, and for a more detailed look at dry etching technology see [1].

The other is *wet etching*, which has been used to fabricate the devices studied in this thesis and is used extensively in general semiconductor processing. Immersion wet etching involves submerging the sample wafer into a solution of etchant. The process of wet etching works by three vital steps, the reactants in the solution are transported to the substrate surface via diffusion, chemical reactions occur at the surface of the substrate and the products of these reactions are carried away via diffusion. The etch rate, which is the amount of material removed per unit time can vary with etchant temperature and the agitation of the sample within the etchant solution.

The wet etching process used for GaAs used a solution of de-ionised water, Ammonia and Hydrogen Peroxide in a ratio of 20:1:1, with an etch rate of $\approx 600\,\mathrm{nm/min}$. The samples were etched to a mesa depth of $\approx 0.65\,\mu\mathrm{m}$, to isolate the active region of each resonant tunnelling device and the resist protecting the mesa removed. The resulting surface profile appears similar to that shown in figure 3.4(d) and the etch depth was monitored and recorded by performing line scans on a *Dektak Stylus Profiler*.

3.1.3.3 Ohmic Contact Processing

To electrically contact, and therefore provide the ability to manipulate the electric field across the active region of the resonant tunnelling structures, contacts to the highly doped contact layers (epitaxial layers i and xi) were required. Ohmic contacts on top of the mesa, and on the etched surface of the substrate were patterned using photolithography in a similar process to that described in section 3.1.3.1, however two layers of resist spun onto the substrate, figure 3.4(e). The first layer of resist (SF6) was applied using the standard spin recipe of 5000rpm for 10s, and then baked at 95°C, but on this occasion for 10 minutes. The second layer of resist (S1813) was also applied with the standard spin recipe, but baked at the lower temperature of 80°C for 5 minutes. The resist layers were then exposed to UV radiation with the desired contact mask pattern for 4.5s and developed in MF319 for 8s, figure 3.4(f).

Each of the resists have different exposure/development properties and these are exploited to create a resist profile, where the resist removed from the second layer (SF6) undercuts the top layer (S1813). To achieve this the desired areas of the top layer of resist (S1813) are exposed to UV radiation as per standard contact photolithography, the difference however comes from the development process. For the S1813 layer, the exposed resist is removed via the developer fluid as usual, but the SF6 underneath also comes into contact with the developer once the top layer of resist is removed. The SF6 resist which is contacted by the developer is therefore also removed, as it does not require the need for exposure to UV radiation. This results in a region of resist with an undercut in the SF6 resist, which can be seen in figure 3.4(f). Resist profiles which exhibit an undercut are extremely useful as they reduce the possibility of creating a continuous film of metal across the surface of the sample, which can be problematic when attempting to remove the unwanted metal.

The metal is deposited onto the surface of the sample by a process known as *thermal evaporation*, and this process works on a simple basis where the samples are placed into a chamber in which a vacuum is created. A crucible of metal, which is targeted at the surface of the samples, is heated until metal atoms evaporate from the metal source, providing a beam of metal which is deposited into the target area. A thickness monitor placed close to the samples within the target area measures the rate and thickness of the metal deposition and simple mechanical shutter across the metal source is used to control when the deposition can take place. The energy of the metal atoms which reach the target surface, and the rate at which they do so is controlled by the temperature of the metal source.

The top (on top of the mesa) and bottom (at the base of the mesa on the etched semiconductor surface) contacts were made by depositing AuGe/Ni/Au (gold-germanium, nickel, gold) layers onto the surface of thickness 100 nm, 28 nm and 300 nm respectively (figure 3.4(g)). Once removed from the thermal evaporator the unwanted metal on the surface of the sample (on top of the resist layers) was removed by removing the resist, resulting in patterned sample surface of mesas and contacts (figure 3.4(h)). To create a good ohmic contact between the metal and the semiconductor, the contacts are then alloyed by *Rapid Thermal Annealing*, (RTA) at 390°C for 30s.

3.1.4 Device Packaging and Design Evolution

To perform the electrical measurements described in chapters 4 and 5 the fabricated samples were mounted into 20-way ceramic packages, which have an inner recess of 3.6 mm by 3.6 mm for sample mounting, an example of which is shown in figure 3.5. The fabricated samples were cleaved into smaller sections with dimensions less than 3.6 mm by 3.6 mm and mounted into the 20-way ceramic packages using *Low Temperature GE Varnish*, which has excellent bonding properties and good thermal conductivity down to low temperatures.

Electrical bonds between the ceramic package pin contacts, highlighted in figure 3.5 and the desired contact pad on the semiconductor device were made by a *West Bond 7400A wedge-wedge wire bonder*, which had been modified for fine gold wire of diameter 12.5 μm. The wire bond were made via process called *wedge bonding* in which a force and heat are

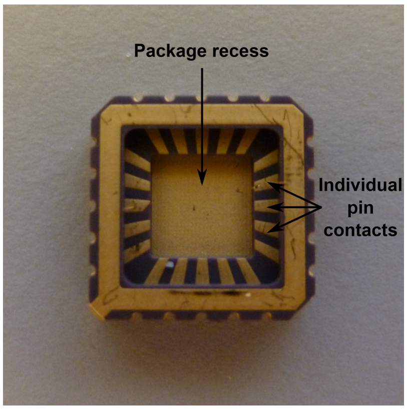

FIGURE 3.5: An optical image of a typical 20-way ceramic package used for sample mounting. The diced up sample chip is mounted into the package recess using low temperature GE varnish. Electrical bonds are made between the contacts on the semiconductor substrate and the individual pin contacts on the package via a gold wire using a wedge bonding technique.

.

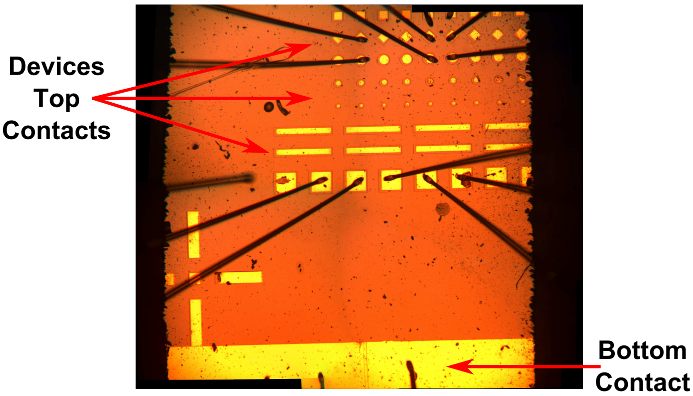

FIGURE 3.6: An optical microscope image of a V1.0 triple barrier resonant tunnelling structure chip. Bond wires can be seen making contacting the gold top of various size mesa structures and the gold bottom contact. The large distance between the device mesas and bottom contact introduces a large series resistance in the measurement circuit and is problematic for resonant tunnelling structure measurements.

.

applied on the wire and contact pad to form the bond. Often ultrasonic power is used to assist in making the bonds, however this has not been applied to the devices studied in this thesis.

Three versions of the triple barrier resonant tunnelling structure (TBRTS) devices were fabricated following the processes described in section 3.1.3. The first generation of devices, V1.0, figure 3.6 consisted of devices which varied in size (50 μm to 200 μm) and shape (circular and square) and a large single bottom contact. Although the remaining GaAs substrate is highly doped, and therefore relatively conductive, the large distance ($\approx$2-3 mm) between the device mesas and the bottom contact introduced a series resistance into the measurement circuit, which is problematic for measurement of resonant tunnelling devices. A full explanation of the problems caused by series resistance in the measurement circuit can be found in section 4.3.4.

In an attempt to reduce the series resistance in the measurement circuit a second version

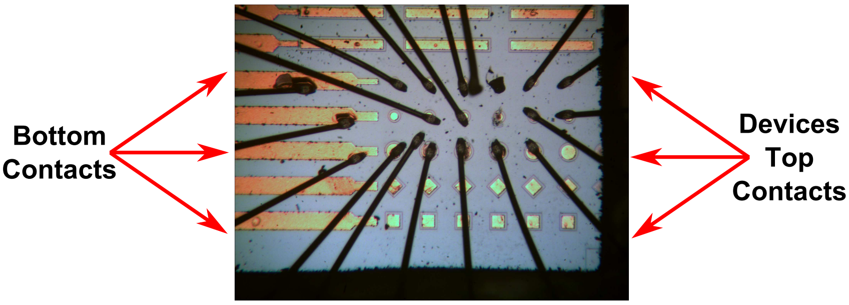

FIGURE 3.7: An optical microscope image of a V2.0 triple barrier resonant tunnelling structure chip. Bond wires can be seen making contacting the gold top of various size mesa structures and the gold bottom contacts, which are now much closer ($\approx$ 50-500μm) to the devices. This resulted in a reduction of the series resistance introduced into the measurement circuit.

.

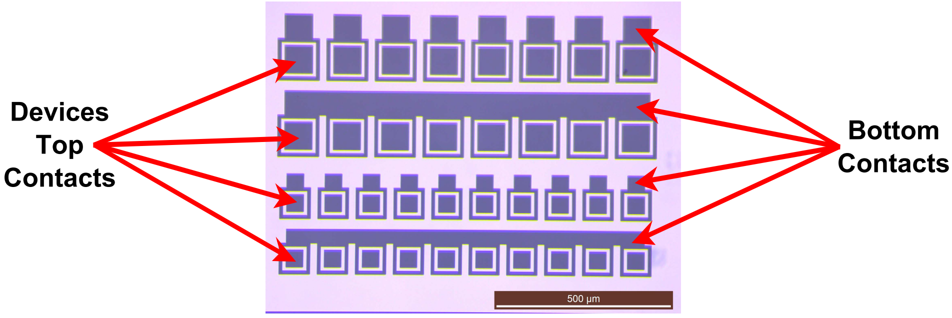

FIGURE 3.8: An optical microscope image of the V3.0 design contact mask. The bottom contact surrounds the top contact and is placed such that it will be in very close proximity to the mesa side wall.

.

of samples, V2.0 were fabricated, which consisted of the same variation of size and shape devices as V1.0. The difference between these two version however was the placement of the bottom contact such that it was significantly closer than the previous devices. Figure 3.7 shows an optical microscope image of a V2.0 device where it can be seen that the bottom contact is now within ≈ 50-500 μm of the devices, which significantly reduced the amount of series resistance introduced into the measurement circuit.
Figure 3.8 shows an optical microscope image of part of the mask set that was designed to further reduce the series resistance as it was clear that further improvements could be made. In this design the bottom contact surrounds the top contact, such that it is very close to the mesa edge wall (≈ 5 μm) with devices which have individual, or common bottom contacts. A variety of different size mesa devices were designed, ranging from the smallest of 60 μm x 60 μm to the largest of 200 μm x 200 μm. The reported measurements in chapters 4 and 5 were taken from the V3.0 design devices and a scanning electron microscope (SEM) image of a fabricated V3.0 60 μm x 60 μm mesa device is shown in figure 3.9.

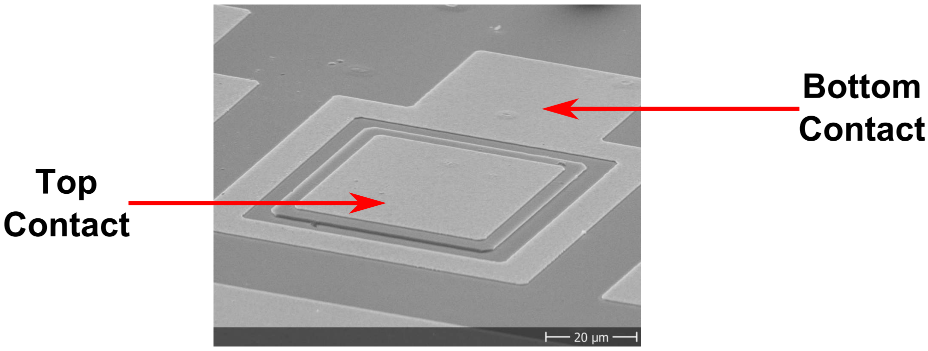

FIGURE 3.9: A scanning electron microscope image of a 60 μm x 60 μm mesa V3.0 device. The top contact on the top of the mesa and bottom contact, surrounding the mesa can clearly be seen, with the distance between the bottom contact and the mesa sidewall being approximately 5 μm.

.

3.2 Experimental Details

The electrical, current-voltage (I(V)) measurements described in chapters 4 and 5 were carried out at Cardiff University in a closed cycle helium pulse tube cryostat with the ability to vary temperature between 2.8K and 310K.

3.2.1 Variable Temperature Measurement System

For measurement the 20-way ceramic packages were mounted into a package holder on the cold-finger of an *Oxford Instruments* Optistat AC-V12 system, which consists of a *Cryomech, Inc* PT403 cold head, *Cryomech, Inc* CP830 helium gas compressor which is water cooled and an *Oxford Instruments* Mercury iTC temperature controller. This system is capable of cooling samples to 2.8K without the need for liquid cryogens significantly improving the running costs and ease of use. The sample space of the PT403 cold head is held in a vacuum, produced by a *œrlikon leybold vacuum* turbolab 80 basic turbomolecular pump system with a dry compressing backing pump. A simplified schematic of the main components of a pulse tube refrigerator is shown in figure 3.10.

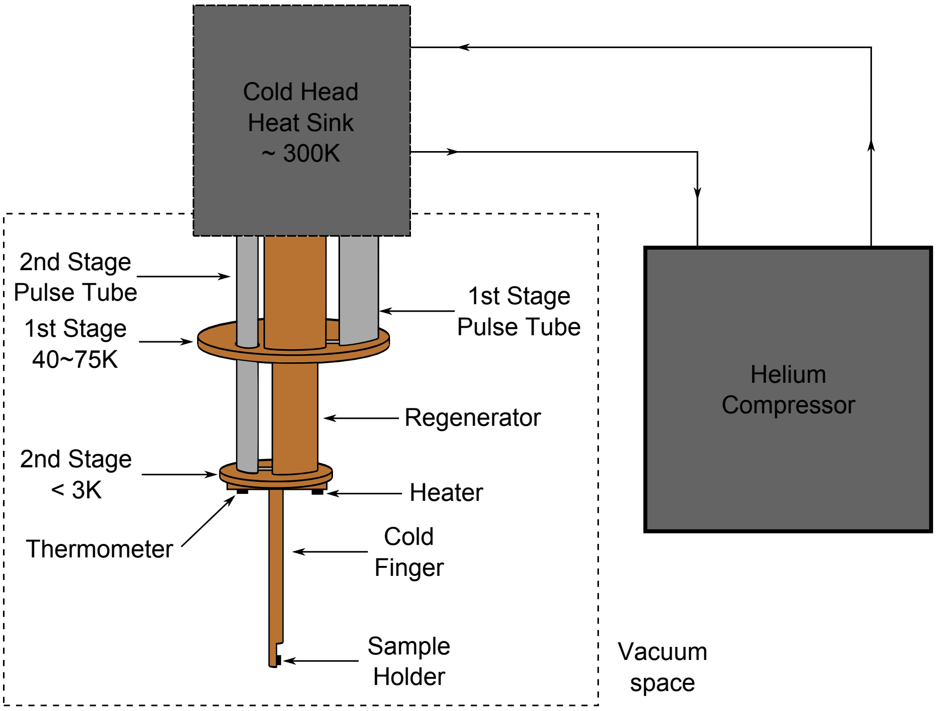
Cold Head
Heat Sink
~ 300K
2nd Stage
Pulse Tube
1st Stage
40~75K
1st Stage
Pulse Tube
Regenerator
2nd Stage
< 3K
Heater
Thermometer
Cold
Finger
Sample
Holder
Vacuum
space
Helium
Compressor

FIGURE 3.10: A simplified schematic of the main components in a pulse tube cryostat. A helium compressor generates an oscillating pressure, which in turn generates an oscillating gas flow. The expansion of helium gas in the pulse tubes reduces the temperature of the first and second stages. The pulse tubes and temperature stages are held in vacuum and thermally shielded to minimise any heat conduction between outside of the cryostat and the low temperature stages.

.

The main advantage of pulse tube cryorefrigerators over a Gifford-McMahon cryocooler (about which more information can be found in [7, 8]) is that they have no moving parts in the low temperature region, and as such vibrations within this region are significantly reduced. Pulse tube cryorefrigerators use an oscillating pressure at the compressor to generate an oscillating gas flow within the rest of the system, with the cooling power provided by the expansion of helium gas within two pulse tubes. The first pulse tube is thermally anchored to the first stage cold plate which provides cooling power between 40K to 75K and the second anchored to the second stage cold plate which achieves temperatures as low as 2.8K. A regenerator, which is a kind of heat exchanger cools incoming gas to the pulse tubes and warms outgoing gas to ambient temperatures. A copper cold finger, onto which the samples are mounted is attached to the second cold plate, along with a resistive heater and a Rhodium-Iron thermometer which have been calibrated to control the sample temperature attached to the end of the cold finger. For more information on pulse tube refrigerators see [9, 10].

The Mercury iTC Temperature Controller is programmable via a USB interface and is controlled by a bespoke computer program written in the Python programming language, allowing for fully automated temperature sweeps over the whole temperature range. When the temperature of the sample is changed a time delay is introduced before electrical measurements are performed to ensure that the sample is in thermal equilibrium with the cold finger and thermometer due to the distance between the sample at the end of the cold finger, and the thermometer and heater at the top of the cold finger. The wires that provide electrical access to the sample holder at the base of the cold finger and the are thermally anchored to the heat exchanger and cold finger in order to minimise the heat conducted to the sample along the wires and exit the cryostat on the cold head via 10 pin Fischer connectors.

3.2.2 Current-Voltage (I(V)) Measurement Set Up

The current-voltage measurements described in chapters 4 and 5 were carried out using an *Agilent Technologies* B1505A Power Device Analyzer/Curve Tracer controlled via a GPIB interface using a bespoke computer program written in the Python programming language. The B1505A Curve Tracer was equipped with two *Agilent Technologies* B1510A High Power Source Monitor Unit (HPSMU), an *Agilent Technologies* B1512A High Current Source Monitor (HCSMU) and an *Agilent Technologies* B1513B High Voltage Source Monitor Unit (HVSMU).

Two of the B1505A plug-in modules were used in the measurements described in this thesis; The B1512A HCSMU was utilised for to provide voltage pulses of down to 500 μs pulse width in the 10 μA to 1 A range, which, due to the high current density of TBRTS devices, was essential when measuring the large area devices examined in sections 4.6 and 4.7. A single B1510A HPSMU was used to maintain the bottom contact of the device at ground (0.0 V) as it too could handle currents up to 1 A, which was again necessary for sections 4.6 and 4.7.

A four-wire measurement technique was used to eliminate the series resistance due to the lead resistances from the measurement circuit by bonding two wires to each of the top and bottom contacts of the devices. The HCSMU and HPSMU plug-in modules both have two channels, known as the *force* and *sense*. The force channel sets the desired voltage output, whilst the sense channel measures the voltage, V_{M} in this case, between the voltage output ($V_{Sense\ +}$) and ground ($V_{Sense\ -}$) sides of the device under test (DUT). Due to the resistance of the leads ($R_{Lead\ 1}$ and $R_{Lead\ 4}$) the voltage across the DUT is less than is the desired voltage, $V_{Desired}$, therefore the voltage between the output, $V_{Out\ +}$ and ground, $V_{Out\ -}$ is increased until $V_{Desired}$ is equal to V_{M} and current in the circuit is then measured. This technique ensures that the only series resistance, R_{S}, (not due to variable resistance, R_{RTD} of the resonant tunnelling diode) is due to the ohmic contacts and the semiconductor substrate between the bottom of the mesa and the bottom contact. Figure 3.11 shows a circuit diagram for the four-wire measurement technique described.

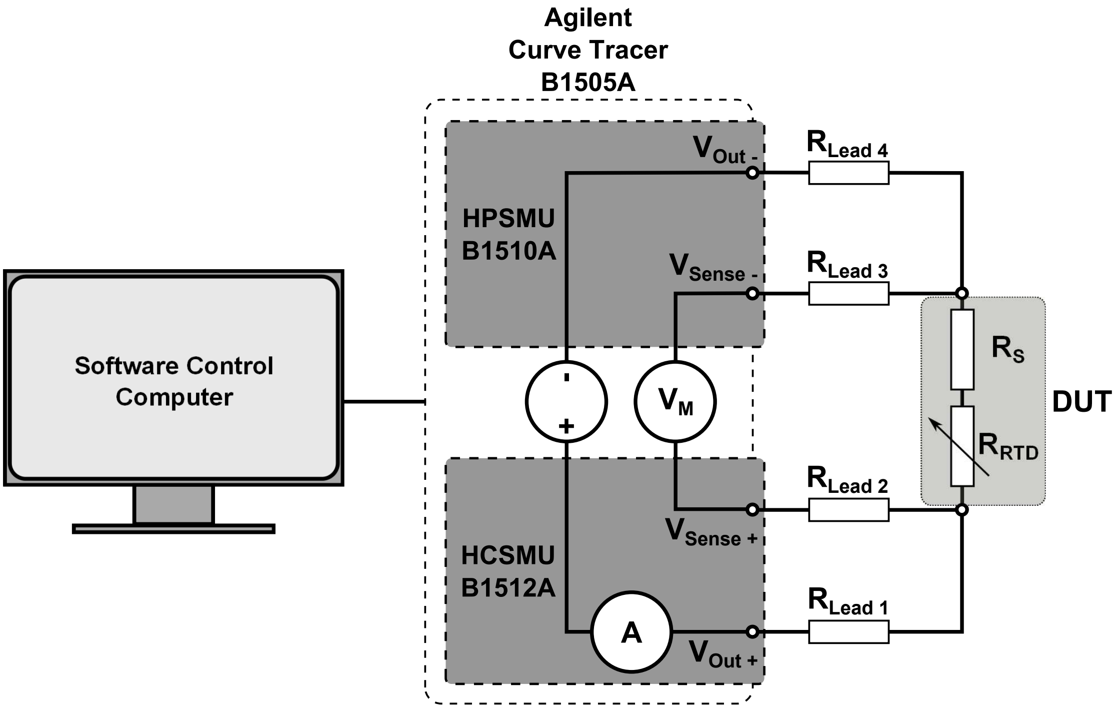

FIGURE 3.11: A schematic showing the circuit for the current-votlage measurements discussed in chapters 4 and 5. The measurement hardware and four-wire technique used down the device under test (DUT) are explained in the main body text.

.

Bibliography

[1] S. M. Sze and M. Lee. *Semiconductor Devices: Physics and Technology, International Student Version*. John Wiley & Sons Singapore Pte, Ltd, 2012.

[2] M. A. Harman and H. Sitter. *Molecular Beam Epitaxy; Fundamentals and Current Status*. Springer-Verlag Berlin Geidelberg, 1989.

[3] E. H. C. Parker. *The Technology and Physics of Molecular Beam Epitaxy*. Plenum Press, 1985.

[4] A. C. Jones and M. L. Hitchman. *Chemical Vapour Deposition: Precursors, Processes and Applications*. Royal Society of Chemistry, 2008.

[5] E. F. Schubert. *Doping in III-V Semiconductors*. Cambridge Books Online. Cambridge University Press, 1993. ISBN: 9780511599828.

[6] P.D. Buckle, P. Dawson, M. Missous and W.S. Truscott. 'Full wafer optical characterisation of resonant tunnelling structures using photoluminescence excitation spectroscopy'. In: *Journal of Crystal Growth* 175-176.PART 2 (1997), pp. 1299–1302.

[7] H.O. McMahon and W.E. Gifford. 'A New Low-Temperature Gas Expansion Cycle'. English. In: *Advances in Cryogenic Engineering*. Ed. by K.D. Timmerhaus. Vol. 5. Advances in Cryogenic Engineering. Springer US, 1960, pp. 354–367. DOI: `10.1007/978-1-4757-0537-9_43`.

[8] W.E. Gifford. 'The Gifford-McMahon Cycle'. English. In: *Advances in Cryogenic Engineering*. Ed. by K.D. Timmerhaus. Vol. 11. Advances in Cryogenic Engineering. Springer US, 1966, pp. 152–159. DOI: `10.1007/978-1-4757-0522-5_16`.

[9] E.I. Mikulin, A.A. Tarasov and M.P. Shkrebyonock. 'Low-Temperature Expansion Pulse Tubes'. In: *Advances in Cryogenic Engineering*. Ed. by R.W. Fast. Vol. 29. Advances in Cryogenic Engineering. Springer US, 1984, pp. 629–637. ISBN: 978-1-4613-9867-7. DOI: `10.1007/978-1-4613-9865-3_72`.

[10] John Wheatley, T. Hofler, G. W. Swift and A. Migliori. ‘Understanding some simple phenomena in thermoacoustics with applications to acoustical heat engines’. In: *American Journal of Physics* 53.2 (1985), pp. 147–162. DOI: `http://dx.doi.org/10.1119/1.14100`.

Chapter 4

Tunnelling in Triple Barrier Resonant Tunnelling Structures

The physics of resonant tunnelling structures has been studied for over 45 years, since they were first proposed by Esaki and Tsu in 1970 [1, 2]. Such devices exploit the phenomenon known as quantum mechanical tunnelling to produce resonant current peaks and an associated negative differential resistance (NDR) region. Many exciting applications, as described in section 1.1, have been developed based on these principles and a basic theoretical explanation of quantum mechanical tunnelling and results from characterisation of devices described in chapter 3 are presented in this chapter.

4.1 Quantum Mechanical Tunnelling

When length scales are reduced to those of the order of the thermal deBroglie wavelength (equation (2.17)), it is quantum mechanics and therefore the wavefunction of the charge carriers which dominate their behaviour. If we consider the case of a single electron state and potential barrier, as shown in figure 4.1, then classically, if the electron has an energy, E_1, which is less than that of the potential barrier, V_0, then an electron travelling from the left (region I) towards the right (region III) would be blocked by the potential barrier (region II) and its motion reflected.

However, as briefly mentioned in section 2.2.3.1, part of the electron wavefunction penetrates into the classically "forbidden" potential barrier region and decays exponentially towards zero. If the potential barrier is thin, such that the electron state wavefunction does not decay to zero[*], then the wavefunction continues to propagate on the other

---

[*] The wavefunction only truly collapses to zero at infinity, and as such there is always the possibility of tunnelling no matter the length or height of the potential barrier.

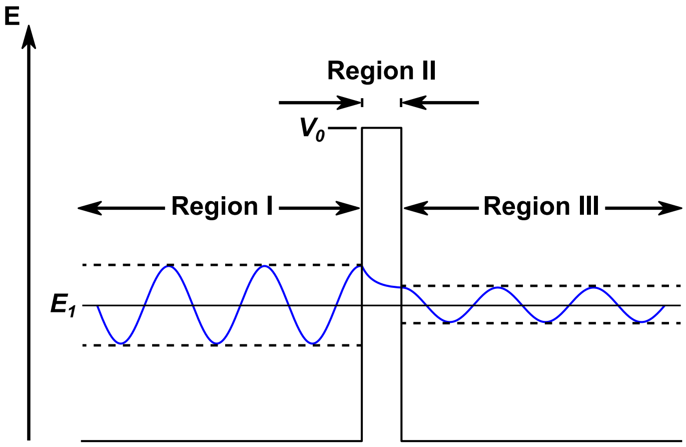

FIGURE 4.1: A schematic showing a single potential barrier, of height V_0. The wavefunction of a state with less energy than V_0 propagates from the left-hand side of the barrier (region I) and penetrates into the clasically forbidden barrier, region II. The wavefunction decays exponentially in the barrier region, but does not decay totally to zero, it then continues to propagate on the right-hand side of the barrier (region III) with a smaller amplitude than region I.

.

side of the potential barrier. This therefore allows for the possibility that any electrons which occupy such states have a finite probability (equation (2.24)) of being transmitted through the potential barrier, and it is this process which is known as *quantum mechanical tunnelling*.

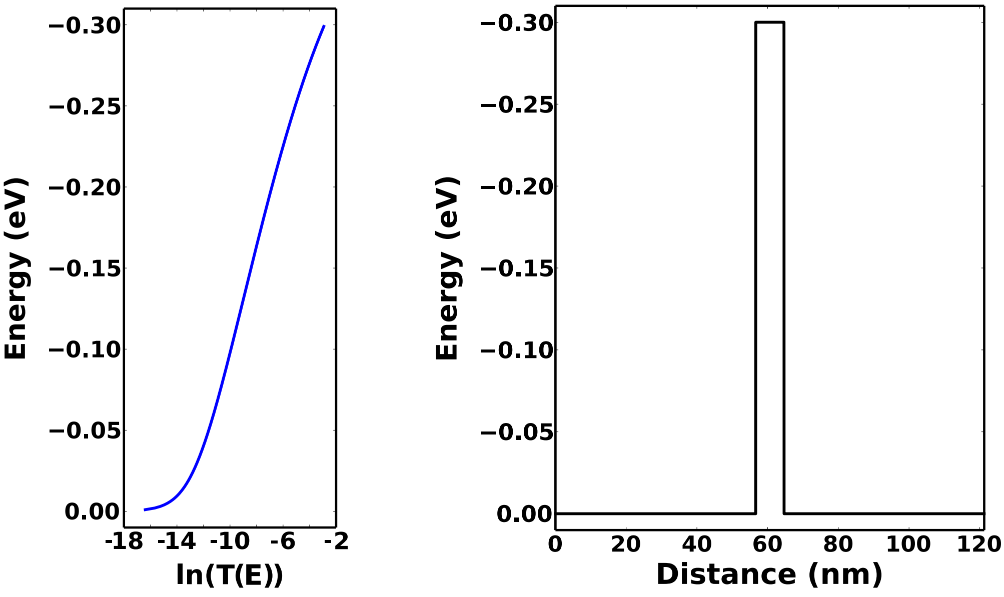

(a) (b)

FIGURE 4.2: (a) The calculated transmission probability $T(E)$ as a function of energy for the single potential barrier shown in figure 4.2(b), the method for calculation is based on that described in [3]. (b) A single potential barrier of energy 0.3eV and width 8nm. The effective masses used in the calculation of figure 4.2(a) for the barrier and outer regions are $0.09439m_e$ and $0.067m_e$ respectively, where m_e is the electron rest mass.

The probability that an electron incident on the potential barrier will be able to tunnel and emerge on the other side is known as the *transmission coefficient* and varies as a function of energy, *T(E)*. A variety of different theories for calculating the transmission coefficient have been developed [2, 4–7], with the accuracy of each theory dependent upon the potential profile being examined. An important development in this field were the calculations performed by Ando and Ito in 1986 for the calculation of transmission probability across arbitrary potential barriers. Their method uses a simple multi-step potential approximation which is applicable to various potential barriers and wells, which include continuous variations of potential and effective mass. Figure 4.2(a) shows the calculated transmission probability as a function of energy for the potential barrier shown in figure 4.2(b), the method used to calculate the transmission probability is based on those performed by Ando and Ito [3].

Figure 4.2(a) allows us to see that for a potential barrier of the type shown in figure 4.2(b), that there is a finite, but small probability that any electrons incident on the barrier (travelling left to right, or similarly for right to left) will tunnel through. The probability of tunnelling is not only highly dependent upon the energy of the electrons in the given direction, but is also depends highly on the width of the tunnelling barrier, reducing exponentially with increasing barrier width and it is this principle on which the *scanning tunnelling microscope* (STM) is based.

4.2 Tunnelling in Multi-Barrier Heterostructures

For multi-barrier heterostructures, where there are 2 or more potential barriers between which a quantum well is formed, the tunnelling probability changes dramatically, at first glance, in a non-intuitive way. From section 4.1 it would be reasonable to assume that the introduction of a second, or subsequent potential barriers would reduce the possibility of tunnelling further, for all energies, however this is not the case, as can be seen from figure 4.3(a) which shows the calculated transmission probability $T(E)$, for a double barrier, single quantum well.

With the addition of a second potential barrier, the transmission probability significantly decreases for the majority of values of energy as one would naturally expect. However, if the second potential barrier is in close enough proximity to the first such that a quantum well is formed, then the behaviour of the transmission probability at energies near to and equal to those of the confined states in the quantum well dramatically increases. Figure 4.3(b) shows the $n = 1$ and $n = 2$ quantum well states, and at energies in close proximity to those of these confined states the probability of transmission through the structure rapidly increases, with a peak in probability occurring at the energy equal to that of the confined state. The magnitude of this peak in tunnelling probability is

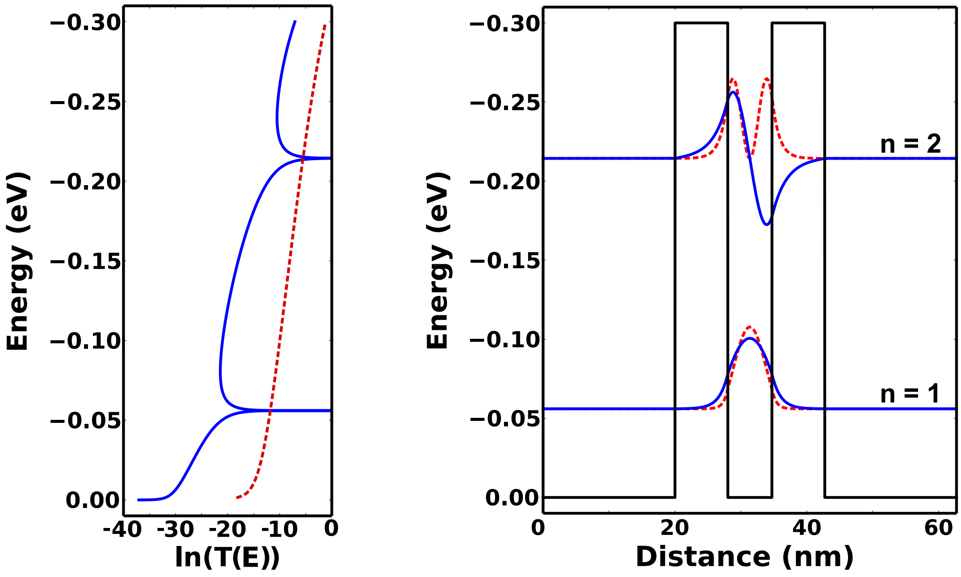

(a) (b)

FIGURE 4.3: (a) The calculated transmission probability $T(E)$, for the double potential barrier single quantum well heterostructure shown in figure 4.3(b) (solid blue line) and the single potential barrier (dotted red line) from figure 4.2. Clear resonant peaks in the tunnelling probability can be seen at energies equal to those of the confined states shown in figure 4.3(b). (b) The potential profile and associated confined state wavefunction (solid blue line) and probability density (dotted red line) for a double barrier single quantum well heterostructure with well width 67Å and barrier widths 8nm. In this structure $n = 1$ and $n = 2$ quantum well states are formed, with the wavefunction only calculated for the barrier and quantum well regions.

dependent on the symmetry of the structure in question, and for a totally symmetric structure, as shown in figure 4.3(b) the maximum probability of unity occurs. Therefore, for charge carriers at the correct energy the structure is transparent, and in the ideal case of zero scattering centres, their motion is unaffected by the structure.

A similar effect is seen in the transmission probability with the addition of a third potential barrier to form a triple barrier, double quantum well heterostructure which is the basis of the devices studied in this thesis. Figure 4.4(a) shows the tunnelling probability of such a structure, with the potential profile shown in figure 4.4(b). The formation of two quantum wells now results in not only a single $n = 1$ state localised to each quantum well such as in figure 4.3(b), but a doublet pair which consists of a symmetric and anti-symmetric (about the middle barrier) which are coupled if the middle barrier is thin. Peaks in the tunnelling probability are seen for the $n = 1$ and $n = 2$ doublet states and for a totally symmetric structure the tunnelling probability is once again unity.

If a fourth potential barrier is added to the structure, then the $n = 1$ and $n = 2$ states form a triplet pair, and so on with the addition of further barriers with the number of states for each $n = 1, 2, 3...$ level given by a $N_{\text{states}} = N_{\text{Barriers}} - 1$. Heterostructures which consists of many barriers forming many quantum wells are known as superlattices

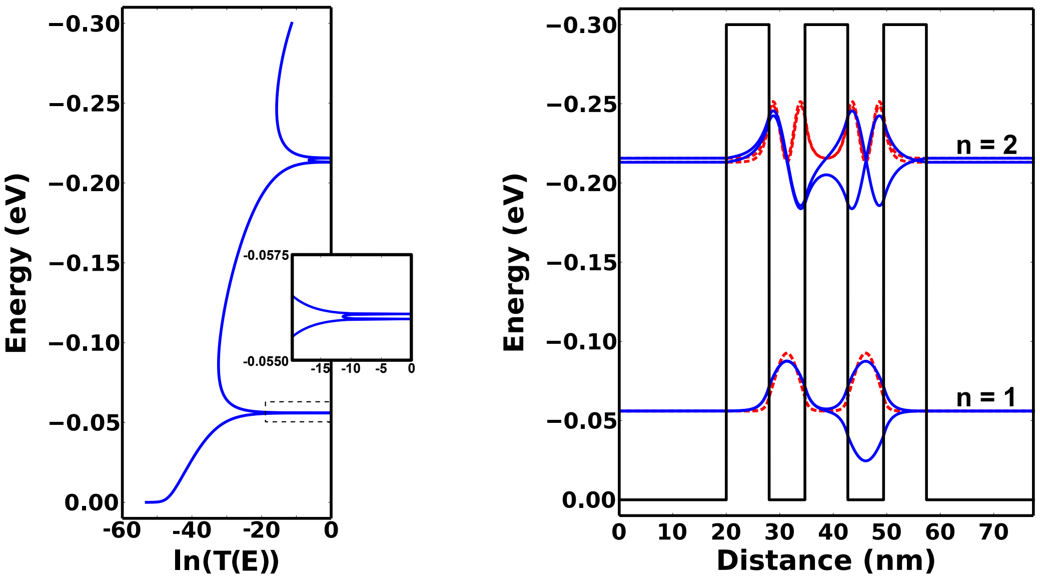

(a) (b)

Figure 4.4: (a) The calculated transmission probability $T(E)$, for the triple potential barrier double quantum well heterostructure shown in figure 4.4(b). Four resonant peaks in the tunnelling probability can be seen at energies equal to those of the four confined states shown in figure 4.4(b). A close up of the region indicated by the dashed box shows that although very close together, there are two distinct peaks for the $n = 1$ level. (b) The potential profile and associated confined state wavefunction (solid blue line) and probability density (dotted red line) for a triple barrier double quantum well heterostructure with well widths 67Å and barrier widths 8nm. In this structure two $n = 1$ and two $n = 2$ sub-band quantum well states are formed, with the wavefunction only calculated for the barrier and quantum well regions.

and the states for each $n = 1, 2, 3...$ level are collectively referred to as a minibands. The superlattice is the basic structure on which the Quantum Cascade Laser was developed [8].

4.3 Resonant Tunnelling

Resonant tunnelling refers to the tunnelling of charge carriers (most commonly electrons) due to the sharp resonant peaks in the tunnelling probability around certain energies as described in section 4.2. This section aims to explain the mechanism of resonant tunnelling firstly in the simpler, more studied, double barrier resonant tunnelling structure and secondly in the more complex triple barrier resonant tunnelling structure (TBRTS).

4.3.1 Double Barrier Resonant Tunnelling Structures

Figure 4.5 shows a simulated current density vs voltage plot at 3K for a double barrier resonant tunnelling structure similar to those discussed in section 4.2. The plot shows

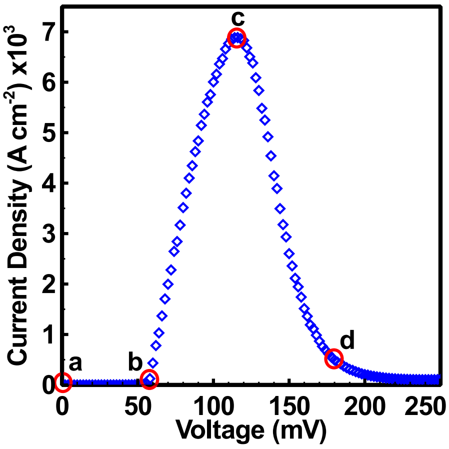

Figure 4.5: A simulated current density vs voltage plot for a double barrier resonant tunnelling structure showing a resonant current peak followed by a region of negative differential resistance. The labels a,b,c and d refer to figures 4.6(a) to 4.6(d) respectively which show the conduction band potential profile, local density of states (LDOS) and tunnelling probability (T(E)) at each point.

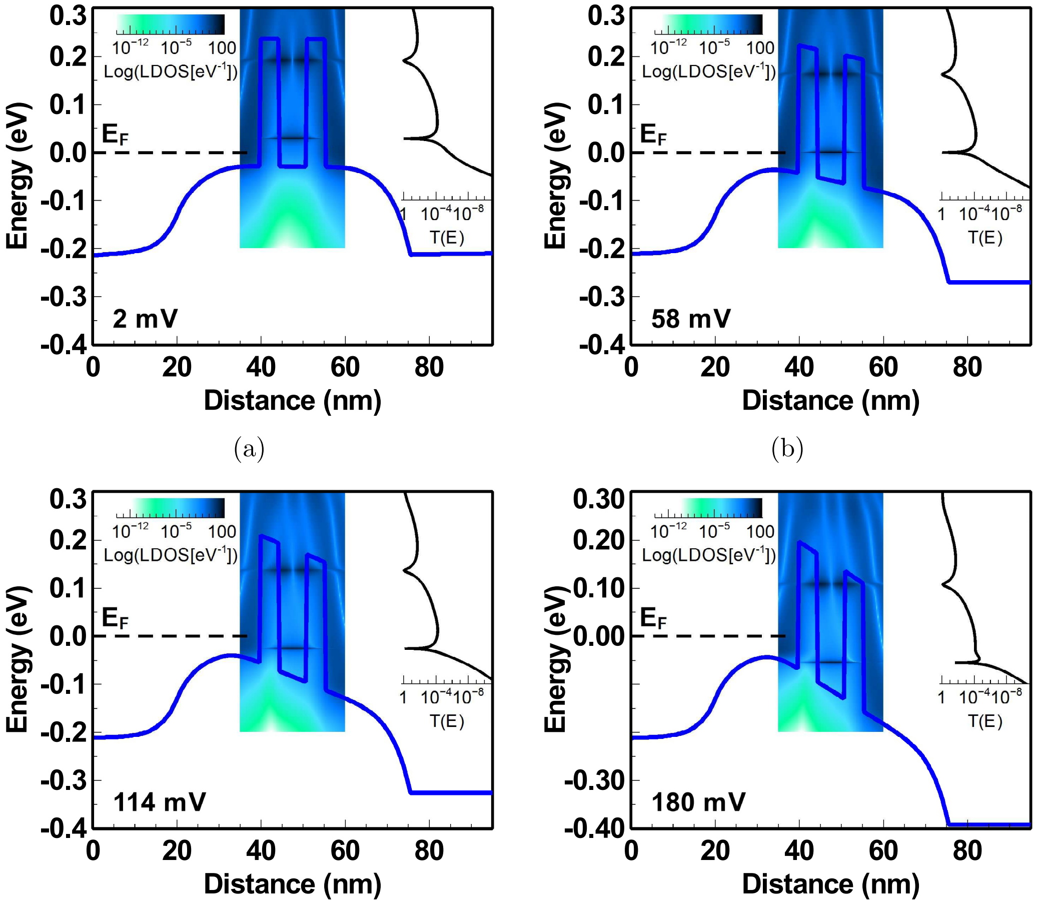

(a) (b)

(c) (d)

Figure 4.6: The simulated (details of which can be found in appendix B) conduction band potential profile, local density of states (LDOS) and tunnelling probability for a double barrier resonant tunnelling structure for applied voltages of: (a) 2 mV, (b) 58 mV, (c) 114 mV and (d) 180 mV.

typical resonant tunnelling diode behaviour, with a rapid switch on, an increasing current which peaks and is then followed by a region of negative differential resistance (NDR). The conduction band potential, local density of states (LDOS) and tunnelling probability, T(E), for various voltages are shown in figures 4.6(a) to 4.6(d). When the structure is under very low bias (figure 4.6(a)), between 0 mV and ≈50 mV, the device is highly resistive and very little current flows. This is due to the fact that although there are energies at which the tunnelling probability is near unity ($\approx 28\,\mathrm{meV}$ for figure 4.6(a)), there is also a well defined Fermi level, $\mathrm{E_F}$ (at $\approx 0.0\,\mathrm{eV}$) below which almost all of the occupied electron states lay. Therefore as the "resonant state" energy in the quantum well is greater than $\mathrm{E_F}$ there are very few electrons available at the appropriate energy to resonantly tunnel and as such a very low current flows.

Once enough voltage has been applied the resonant confined quantum well state starts to energetically align with that of the Fermi level in the emitter region of the device, figure 4.6(b). As there are now many electrons that have the same energy as the confined state, and still a near unitary tunnelling probability at these energies, there is a rapid increase in the net current through the device.

With further increase in voltage the current continues to increase and reaches maximum where the confined resonant state is nearly energetically equal to that of the conduction band edge, as can be seen from figure 4.6(c). The increase in current as the energy of the confined state approaches that of the three dimensional emitter conduction band edge at first may seem counter-intuitive, but is described in detail in section 4.3.3.

The current through the RTD then begins to decrease with the application of higher voltages and results in a region of negative differential resistance (NDR), which is shown in figure 4.5. The decrease in current with increasing voltage occurs due to a decrease in the tunnelling probability, which is caused by the confined state energy dropping below the conduction band edge and so a reduction in the number of carriers energetically aligned with the confined state. Figure 4.6(d) shows such a situation and it can clearly be seen that the tunnelling probability is now far from unity, although there are still many carriers available to tunnel in the far left of the emitter region.

It is therefore important to note that for a DBRTS it is the energetic alignment of the resonant confined state with the charge carriers in the emitter region of the device that dominates the net current flow.

4.3.2 Triple Barrier Resonant Tunnelling Structures

For triple barrier resonant tunnelling structures (TBRTS) the resonant tunnelling behaviour is similar to that described in section 4.3.1, however there are subtle differences. For a TBRTS, as in a DBRTS, the device remains highly transparent to charge carriers which have energies equal to and around the resonant peaks in the tunnelling probability, and very opaque to all other carriers with energies less than the confining barrier potentials. The tunnelling probability for a TBRTS under zero bias is shown in figure 4.7(a), in which four resonant peaks with maximum tunnelling probability equal to one can be seen, as explained in section 4.2.

At low temperatures there is still a well defined Fermi level, E_F in a TBRTS device, and so the energetic alignment of the confined state resonant peaks in the tunnelling probability with the emitter electron distribution still remains important, however, there is an added layer of complexity. As there are two quantum wells in the structure, doublet pair subbands for the $n = 1$ and $n = 2$ levels form (as described in section 4.2). If the middle potential barrier is thin, then there is strong coupling between the states in the first and second quantum wells, and so the electron wavefunction is equally localised between them, as seen in figures 4.4(b) and 4.8(a). For these states, the electron wavefunction extends across the entire structure (from the emitter to the collector), which results in electrons, which are energetically aligned to these states being able to tunnel with a high (unity for a perfectly symmetric structure) probability.

However, with the application of an external voltage across the structure, such as in figure 4.8(b), the shape of the confining potential and relative energy of each quantum well changes. This results in a change in the energy of the wells confined states, but more importantly, the wavefunctions of each of these states now become more localised to a

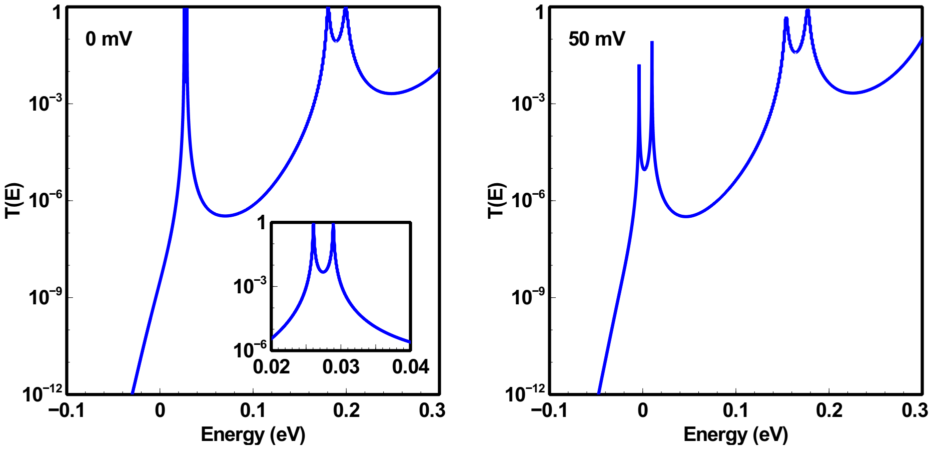

(a) (b)

FIGURE 4.7: (a) The calculated tunnelling probability, T(E), for a triple barrier resonant tunnelling structure under zero bias, as seen in figure 4.8(a). Two resonant peaks for each quantum well subband can be seen, with the tunnelling probability at the resonant peaks being unity. A magnified look at the $n = 1$ subband resonant peaks is shown inset. (b) The calculated tunnelling probability, T(E), for the structure seen in figure 4.8(b) which has an applied voltage of 50 mV. A dramatic decrease in the tunnelling probability for the $n = 1$ subband resonances can be seen, caused by the energetic misalignment of the subband states. A decrease is also seen in the tunnelling probability for the $n = 2$ subband states, however this is smaller as these states are still partially energetically aligned.

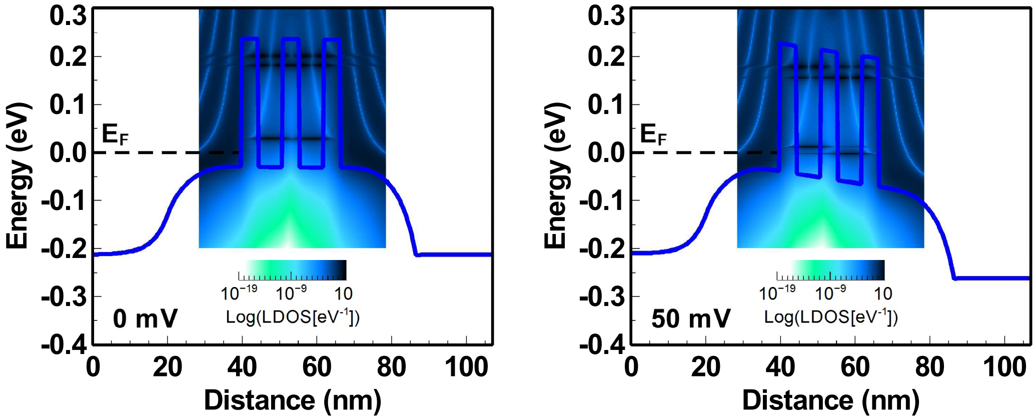

(a)

(b)

FIGURE 4.8: The simulated (details of which can be found in appendix B) conduction band potential profile and local density of states for a triple barrier resonant tunnelling structure for applied voltages of: (a) 0 mV, (b) 50 mV. The tunnelling probability for (a) and (b) are shown in figures 4.7(a) and 4.7(b).

specific well (figure 4.9) and as such the wavefunctions no longer penetrate as far into the collector or emitter regions (dependent on whether the state is localised more to the emitter or collector quantum well respectively). This therefore reduces the probability that electrons at the confined state energies will tunnel through the entire structure and is reflected in the dramatic decrease (by over a factor of 50) in the maximum value of

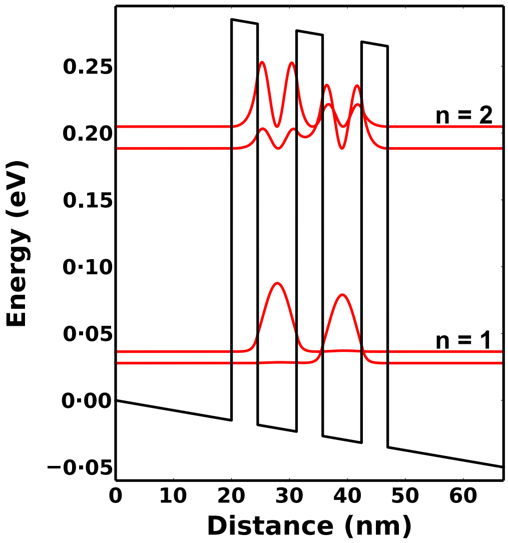

FIGURE 4.9: The potential profile and associated probability density (red line) for a triple barrier double quantum well heterostructure with a voltage of 50 mV applied in a linear potential drop model. In this structure two $n = 1$ and two $n = 2$ sub-band quantum well states are formed, however, due to the applied voltage the $n = 1$ states are highly localised to a specific quantum well, which results in a decrease in the tunnelling probability for these energies (as can be seen in figure 4.7(b)). The $n = 2$ states also become more localised to a specific quantum well, however the effect is not as strong. The wavefunctions in this simulation are only calculated for the barrier and quantum well regions.

the tunnelling probability at the resonant energies, which is shown in figure 4.7(b). The flow of charge carriers through a triple barrier structure therefore is not only controlled by the energetic alignment with the emitter electron distribution, but also the energetic alignment of the quantum well states with each other. As a result, TBRTS are far more complex than the more studied and conventional DBRTS with current-voltage characteristics that have not only one, but several current resonances and associated regions of negative differential resistance. Other effects such as accumulation of charge in the quantum wells and a switch between a 3D to 2D emitter state are more profound in TBRTS and so the design for the optimisation of such structures must therefore be carefully considered and tailored to specific applications, as has been done in chapter 6.

4.3.3 Three Dimensional to Two Dimensional Tunnelling

The discussion of resonant tunnelling has thus far only focused on the energetic alignment of the confined quantum well (QW) states with that of the emitter charge carrier distribution. Therefore it may seem counter-intuitive that the maximum current through a resonant tunnelling device (particularly for a DBRTS) often occurs when the QW states are aligned with, or just above the conduction band edge in energy.

As figure 4.10 shows, for a degenerately doped semiconductor, the Fermi level, E_F in the 3D emitter, lays within the conduction band and for low temperatures there is a well defined electron distribution. The maximum carrier density therefore occurs just below the Fermi level, and as such should provide the largest number of carriers able to resonantly tunnel, hence creating the largest current flow. However, this is not the case

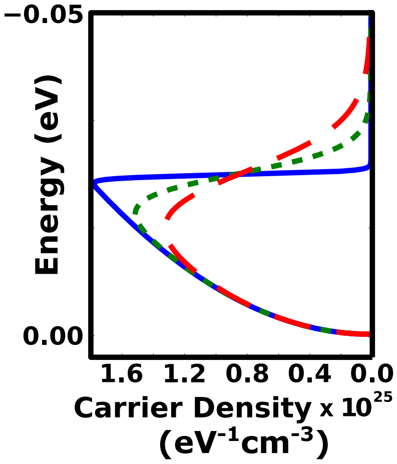

Figure 4.10: The electron distribution in the conduction band of a degenerately doped three dimensional semiconductor region, such as the emitter in a resonant tunnelling structure. The distributions are shown for low temperatures of 3K (solid blue), 24K (dotted green) and 45K (dashed red) and it can be seen the maximum carrier density is seen well above the conduction band edge (0.0 eV).

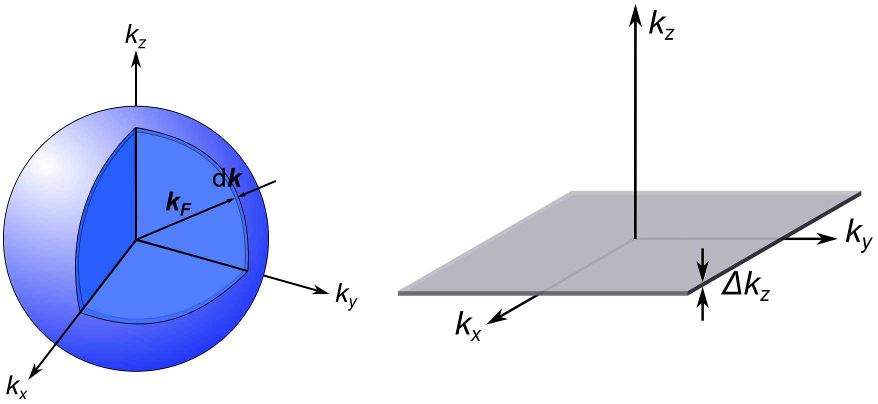

(a) (b)

FIGURE 4.11: (a) The distribution of occupied states for three dimensions in reciprocal space, this solid sphere at 0K is known as the Fermi sphere. (b) A two dimensional system, confined in the k_z direction. For this state the allowable wavevectors are given by an infinite sheet in the k_x and k_y directions, with thickness Δk_z.

as charge carriers which are able to tunnel through the structure must not only fulfil the requirements of the conservation of energy, but momentum must be conserved also. i.e. The wavevector of the charge carriers in the confined direction, must be equal to that of the confined state.

Figure 4.11(a) shows the distribution of occupied electron states in three dimensions (k_x,k_y,k_z) in reciprocal space. At 0K this known as the Fermi sphere, where all states whose wavevector is less than the radius of the sphere, k_F are occupied. For a two dimensional system, such as the confined quantum well states, where there are only two free directions (k_x and k_y), which may take any value and a well defined k_z. Therefore the allowable wavevectors for the confined state form an infinite sheet in the k_x and ky direction, of thickness Δk_z, as illustrated in figure 4.11(b).

For carriers wishing to tunnel between a 3D system into a 2D system, the wavevectors

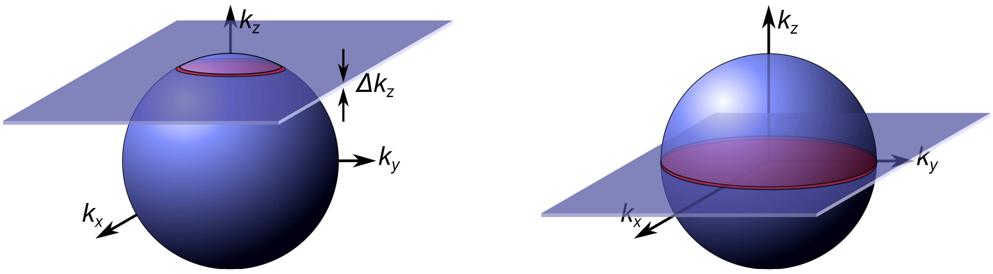

(a) (b)

FIGURE 4.12: The intersection of a three dimensional and two dimensional (confined in the k_z direction) allowable wavevectors in reciprocal space, for: (a) A small energy (or wavevector, k_z) below the surface of the Fermi sphere. (b) At the equator (in k_z of the Fermi sphere), i.e. the conduction band edge. The wavevectors which fulfil the conservation of momentum and energy requirements for 3D to 2D tunnelling are shown by the formation of a disc of thickness Δk_z where the Fermi sphere and infite sheet overlap (shaded in red).

which match these conditions and so are able to tunnel, are given by the intersection of the two dimensional infinite sheet and the three dimensional Fermi sphere, as shown in figures 4.12(a) and 4.12(b). This intersection, and therefore number of tunnelling charge carriers reaches a maximum at, or just above the equator of the Fermi sphere, where k_z in the conduction band is approximately zero, i.e. the conduction band edge.

4.3.4 The Effects of Series Resistance

As briefly mentioned in section 3.1.4, any series resistance in the measurement circuit has a drastic effect on the I(V) characteristics measured. For an ideal resonant tunnelling structure, such as the one simulated in figure 4.5, the series resistance would be zero. However, in practice this is not achievable and so every effort must be made to minimise the series resistance in the circuit when measuring any device which exhibits regions of negative differential resistance. Figure 4.13 shows the simulated ideal characteristic for a double barrier resonant tunnelling structure with zero series resistance (blue diamonds), and the same characteristic modified for a simulated series resistance of 1.5x10^{-6} Ωcm^2, which is equivalent to ≈ 42 mΩ for a 60 μm × 60 μm diode (red circles and black crosses). With the introduction of a series resistance into the measurement circuit, simulated via equation (4.1),

$$V_{\text{Total}} = V_{\text{DUT}} \left(\frac{R_{\text{DUT}} + R_{\text{Series}}}{R_{\text{DUT}}} \right) \tag{4.1}$$

it is possible to see that when the series resistance, R_{Series} is small compared to the resistance of the DUT, R_{DUT}, (V < 50mV and V > 200 mV in figure 4.13) then there is

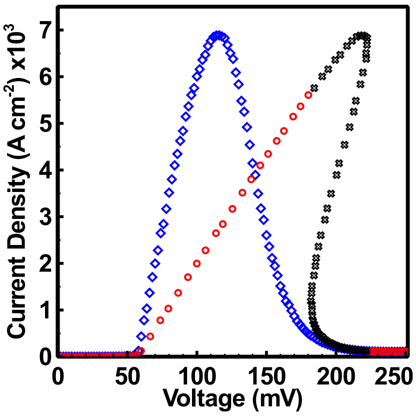

FIGURE 4.13: A simulated current density vs voltage plot for a double barrier resonant tunnelling structure as previously shown in figure 4.5, the blue diamonds indicate the ideal characteristic with no simulated series resistance. A series resistance of 1.5x10^{-6} Ωcm^2 (equivalent to ≈ 42 mΩ for a 60 μm × 60 μm diode) has been simulated and added to the ideal I(V) characteristic and is indicated by the plot of red circles and black crosses. The black crosses indicate the data points which could possibly be "lost" by a conventional I(V) measurement circuit.

little effect on the measured characteristic in this region, because the majority of the applied voltage is still dropped across the DUT. However, where the R_{Series} is similar in magnitude or greater than R_{DUT}, (50 mV $<$ V $<$ 200 mV) then the majority of the voltage is now dropped across the series resistance and as such a large voltage must be sourced to drop the desired amount across the DUT. This has the effect of shifting the low DUT resistance region of the curve (i.e. high current values in the resonant peak) out to higher voltages, whilst the high DUT resistance regions remain the same.

As there are now two values of current which occur at the same voltage a bistable region is formed, where the device may switch between the high and low current stable states. This bistable region can often be seen in the difference between measurements performed in the forward (zero to finite voltage) and backwards (finite voltage to zero) directions as a hysteresis in the I(V) characteristic, as shown in figure 4.14. The voltage at which the measurement switches between the high and low current states is dependent on the characteristics of the measurement circuit, and as such the data plotted by black crosses in figure 4.13 show the data points which may be lost.

A measurement circuit was designed by Martin et al. [9] to probe this region of bistability utilising an active circuit to modify the measurement load line from a conventional one with a positive slope, to one with a negative output resistance. Although these measurements were important in the proof that this bistability is intrinsic, for practical devices it is much simpler to minimise the series resistance by making alterations to the device design and fabrication process, as well as having the beneficial effects of reduced power consumption and device heating.

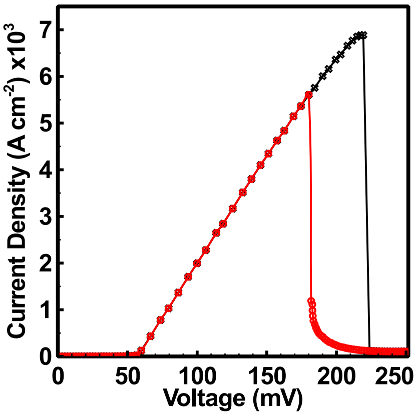

FIGURE 4.14: Simulated current density vs voltage plot for a double barrier resonant tunnelling structure with a simulated series resistance. A bistable region forms due to the introduction of a series resistance, which can lead to a hysteresis in the forward and backwards measured directions. The forward measured direction plot is shown by the black crosses, where the DUT remains in the high current stable state in the bistable region where as the red circles show the backwards measurement direction where the DUT remains in the low current state.

4.4 The Symmetric Triple Barrier Resonant Tunnelling Structure

In this section the current-voltage (I(V)) characteristic for the nominally symmetric triple barrier resonant tunnelling structure (TBRTS), VMBE 755, at low temperature are presented. Details of the measurement technique, sample structure and device fabrication can be found in chapter 3.

4.4.1 Positive Bias Characteristic

The positive bias I(V) characteristic in the forwards and backwards sweep directions for the nominally symmetric TBRTS at 3K are shown in figure 4.15(a). There are three main features of interest, labelled F1, F2 and F3, each of which exhibits a region of negative differential (NDR) resistance which is characteristic of the resonant tunnelling process as explained in section 4.3. The origin of the low voltage features F1 and F2 can be explained by modelling the application of an external voltage across the nominally symmetric TBRTS in a simple linear drop model across the undoped region, as illustrated in figure 4.16. The model is only valid for low voltages and loses accuracy with increasing voltage as it makes several assumptions to simplify the situation and predict the voltages at which the resonance peaks (i.e. alignment of a confined level with the conduction band edge) occur. The main assumptions made are:

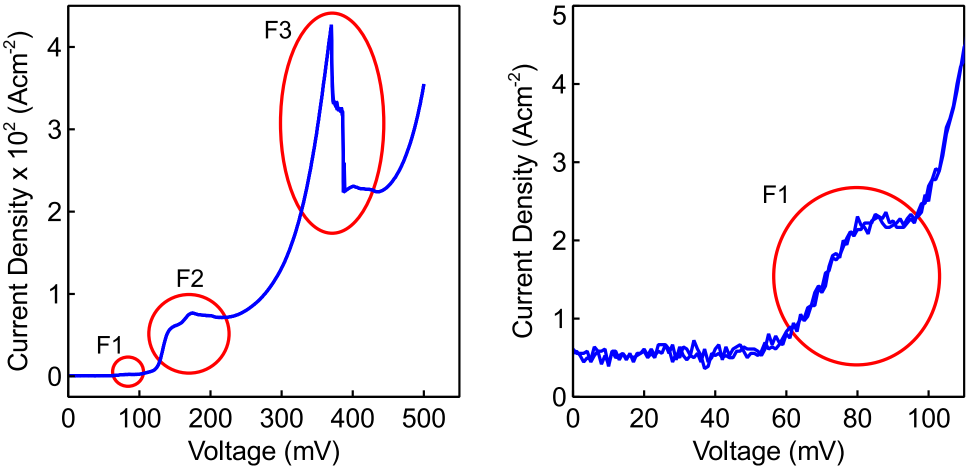

(a) (b)

FIGURE 4.15: (a) The positive bias, forward and backward direction, Current Density vs Voltage characteristic for a 60 μm x 60 μm nominally symmetric TBRTS. Three main features of interest are visible, with each indicated by a red ellipse and labelled F1, F2 and F3 respectively. (b) An enlarged plot of the feature, F1 from figure 4.15(a). Each of the features, F1, F2 and F3 show a region of negative differential resistance which is characteristic of the resonant tunnelling process.

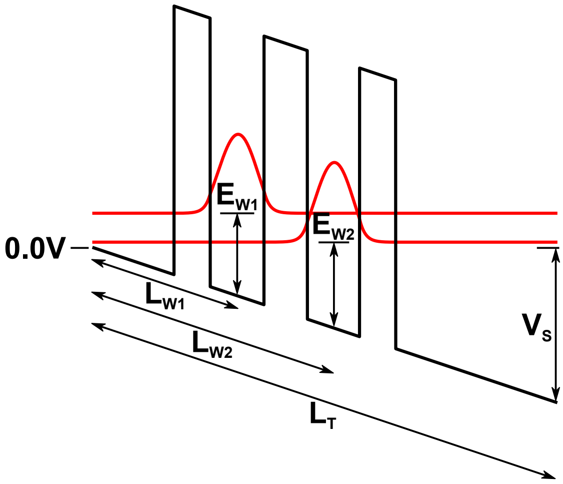

FIGURE 4.16: A schematic of the conduction band edge potential profile for a simple linear voltage drop model, with a voltage of V_s applied. The energy of the first and second QW confined states, E_{W1} and E_{W2} are assumed to be shifted in energy by the same amount as a point in the middle of their respective QW. Only the length of the undoped spacers and the active region of the device, L_T are considered, whilst the distance to the centre of the first and second QWs are L_{W1} and L_{W2} respectively.

i) The voltage is dropped linearly across only the length of the undoped spacer layers and the active triple barrier region of the device.

ii) Only the ground ($n = 1$) states of the quantum wells contribute to the resonances and any charge accumulation in the quantum wells is neglected.

iii) The energies of the ground states are shifted by the same amount as a point in the middle of their respective quantum well.

iv) The distance, L_{state} over which the amount of voltage required to align the state is dropped is taken to be the distance from the point held at 0.0 V to the centre of the respective quantum well.

v) Any confined states in the triangular well in the emitter region are neglected.

The expression for the voltage required, V_s, to align a confined state with the conduction band edge can therefore be shown to be:

$$V_s = \frac{E_{\text{state}}}{q}\left(\frac{L_T}{L_{\text{state}}}\right) \tag{4.2}$$

where only the energy of the confined state, E_{state}, distance to the centre of the states respective quantum well from the point held a 0.0 V, L_{state}, the total length of the linear voltage drop region, L_T and the carrier charge, q, need to be known.

It is worth noting that at the maximum applied voltage of 0.5 V in these structures, if entire voltage drop is across the region described by the simple linear model then the calculated $\frac{1}{F_{Electric}}$ value is $\approx 1.2 \times 10^{-6}$ cmV^{-1}. This falls below the applied electric field at which impact ionisation becomes significant in GaAs [10] and so impact ionisation in these structures is considered to be negligible.

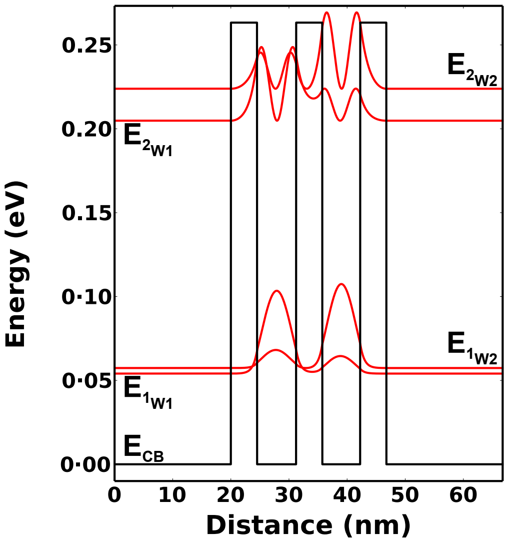

Figure 4.17: The calculated conduction band potential profile (black line) and electron probability density (red lines) output from a self-consistent Schrödinger-Poisson model for the nominally symmetric TBRTS. Due to a slight asymmetry in the widths of the first (W1) and second (W2) quantum wells, the electron probability densities are more localised to a specific QW. The states more localised to W1 are known as $E_{1_{W1}}$ and $E_{2_{W1}}$, where similarly for W2 the $n = 1$ and $n = 2$ states are $E_{1_{W2}}$ and $E_{2_{W2}}$.

Figure 4.17 shows the zero applied electric field conduction band potential profile (black line) and quantum well confined state probability density (red lines) for the nominally symmetric structure. Although nominally symmetric, there is a the slight asymmetry in the measured quantum well widths (table 3.1), thus the wavefunctions of the confined states, and therefore the probability density also, are more localised to one quantum well than the other. The energy of the $n = 1$ state more localised to the emitter quantum well, $E_{1_{W1}}$, and the state more localised to the collector quantum well, $E_{1_{W2}}$, were calculated from a self-consistent Schrödinger-Poisson model (appendix A) to be 54.1 meV and 57.4 meV above the conduction band edge, E_{CB}, respectively. The distances to the middle of the quantum well for each state, L_{states} and total distance, L_T were calculated from the known layer structure, allowing the voltage required to align each state with the conduction band edge to be calculated, the results of which are given in table 4.1.

Table 4.1: The required voltage to align the $n = 1$ confined states of the nominally symmetric triple barrier resonant tunnelling structure with the conduction band edge E_{CB} in the simple linear voltage drop model.

Confined State Energy (meV)	**Voltage Required to Align to E_{CB} (mV)**
54.1	91.5
57.4	144.3

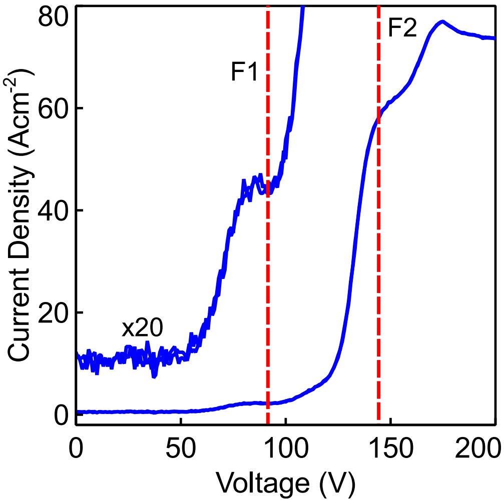

FIGURE 4.18: The low voltage (< 200 mV) current-density vs voltage (blue lines) for the nominally symmetric triple barrier resonant tunnelling structure with the current scaled by ×1 and ×20. The red dashed lines indicate the predicted voltages at which the resonances associated with the alignment of the $n = 1$ subband states and the conduction band edge should occur. There is excellent agreement between the theoretical and experimental results.

Figure 4.18 shows the low voltage (< 200 mV) characteristic, and the predicted resonant peak voltages (red dashed lines) for the nominally symmetric TBRTS. There is excellent agreement between the simple linear voltage drop model predictions and the measured peak resonance values and as such the feature F1 can be attributed to the alignment of the collector quantum well confined state and the conduction band edge, $\mathrm{E}_{1_{\mathrm{W2}}}\mathrm{E}_{\mathrm{CB}}$. Where as the feature F2 is attributed to the alignment of the emitter quantum well confined state and the conduction band edge $\mathrm{E}_{1_{\mathrm{W1}}}\mathrm{E}_{\mathrm{CB}}$.

However, on closer inspection of the feature F2, it is possible to see from figures 4.15(a) and 4.18 that there is some structure in this resonance that the simple model fails to predict. The structure in the feature is thought to be combination of two overlaying resonant peaks as illustrated in figure 4.19 and it is thought that the first peak in this feature is due to the alignment of the emitter quantum well confined state $\mathrm{E}_{1_{\mathrm{W1}}}$, with the conduction band edge E_{CB} as predicted by the simple model.

The second proposed resonant peak in F2 is thought to be caused by the formation of a two dimensional state in the triangular well of the emitter region when sufficient voltage is applied across the device. Formation of a confined state in this region allows for a further resonance condition of the energetic alignment of the emitter quantum well state, $\mathrm{E}_{1_{\mathrm{W1}}}$ and the two dimensional triangular emitter state $\mathrm{E}_{\mathrm{M_{2D}}}$.

To model this situation a freely available simulation package WinGreen V2.1 developed by K. M. Indlekofer and J. Malindretos [11] was used. The simulated I(V) characteristic for the nominally symmetric TBRTS is shown in figures 4.20(a) and 4.20(b), and gives good agreement for the voltage at which features F1 and F3 occur, however feature F2

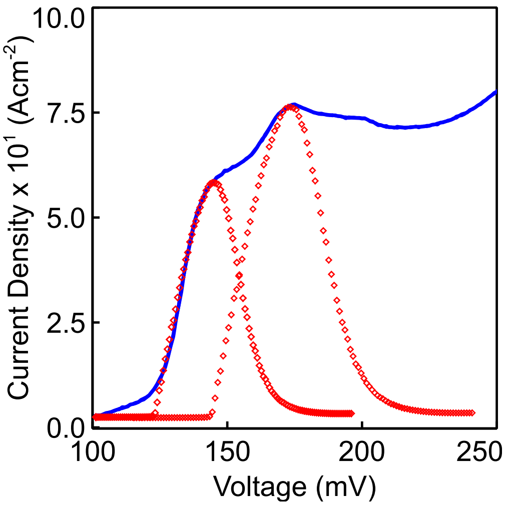

FIGURE 4.19: The I(V) characteristic (blue solid line) for the nominally symmetric TBRTS centred on the feature F2. Two typical current resonances are overlayed (red diamonds) to illustrate the possibility of that the feature is a construct of two separate resonances, spaced closely in voltage, with the smaller, lower voltage resonance attributed to the energetic alignment of $E_{1_{W1}}$ and E_{CB}, and the second larger resonance attributed to the alignment of a two-dimensional state in the triangular potential of the emitter region, $E_{M_{2D}}$.

does not appear to be present in these simulations.

This suppression of a major resonant feature in the simulated results is unexpected, however its absence can be explained by carefully considering how the conduction band edge potential profile changes with increasing bias. When voltage is applied across the device, when the $n = 1$ confined state, which is localised to the first quantum well, $E_{1_{W1}}$

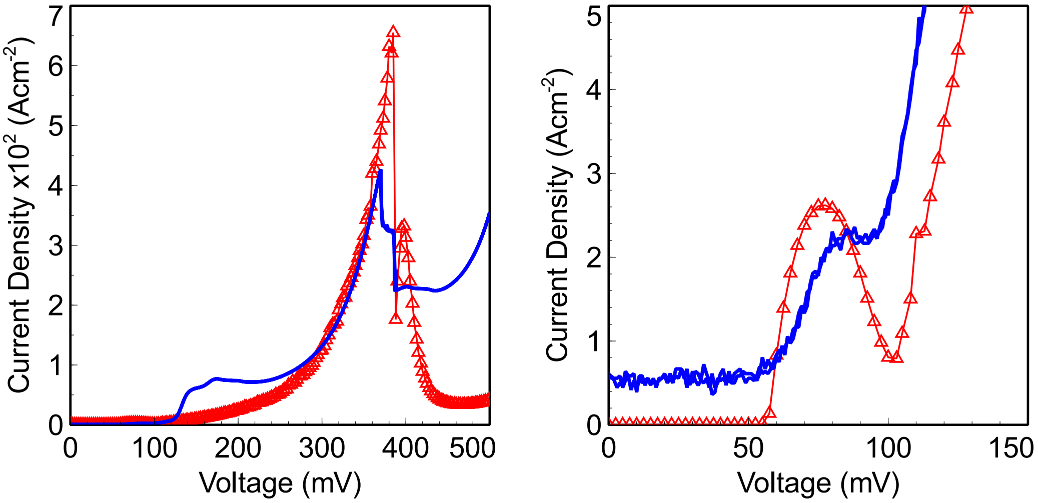

(a) (b)

FIGURE 4.20: (a) The experimental (blue line) and simulated (red triangles) forward bias characteristic for the nominally symmetric TBRTS. (b) The low voltage region of the forward bias experimental (blue) and simulated (red) characteristic for the nominally symmetric structure. There is good agreement between the experimental and simulated voltages at which the resonant peaks occur for features F1 and F3.

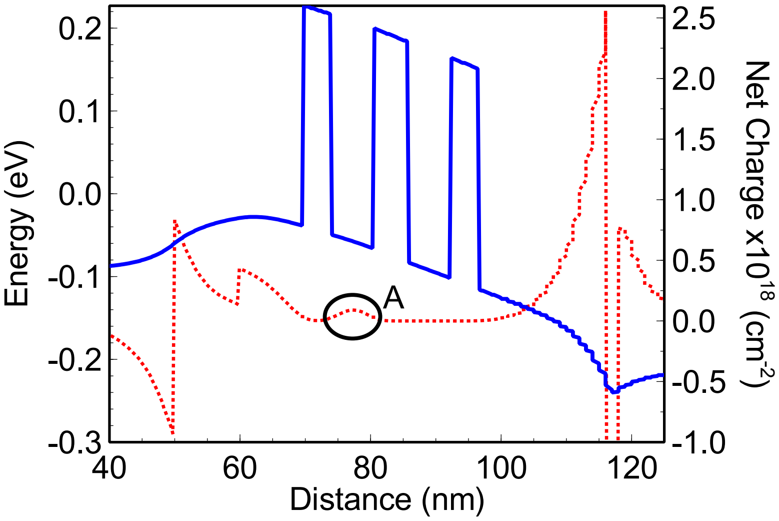

(a)

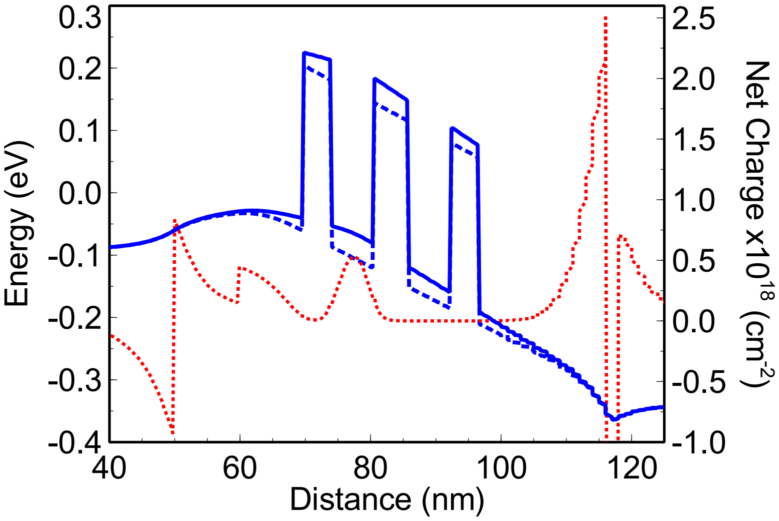

(b)

FIGURE 4.21: (a) The calculated conduction band potential profile (blue solid line) and net charge distribution (red dotted line) for the nominally symmetric structure with 0.125V applied. A positive net charge (which represents an excess of electrons) can be seen in the first quantum well which is circled and labelled point A. (b) The calculated conduction band potential profiles with 0.25V applied for the case with (solid blue line) and without (dashed blue line) charge accumulation. In the situation where charge accumulates in the first quantum well the conduction band edge is held high and results in a pinning of the first QW confined state, $E_{1_{W1}}$ in energeteic alignment with the emitter electron distribution. Where the accumlation of charge in the first quantum well is forbidden $E_{1_{W1}}$ drops below the conduction band edge and so the resonant tunnelling current diminishes. The net charge destribution (red dotted line) for the case with charge accumulation is also shown.

begins to energetically align with the Fermi level, E_F, a significant amount of charge accumulates in the first quantum well state, as shown in figure 4.21(a). This region of the conduction band is therefore held high, with respect to the non-charge accumulating case and the electric field is redistributed across the structure as necessary. Any further application of voltage results in more charge accumulation in the confined quantum well state such to balance out the increase in bias, figure 4.21(b), and so the localised QW state is effectively pinned on resonance.

The structure will remain pinned on resonance with increasing bias until the electron tunnelling probability out of the first quantum well becomes equal to the probability of electrons tunnelling into the well (e.g. when the $E_{2_{W2}}$ states comes into alignment with the $E_{1_{W1}}$ state), or there are no longer any available states for electrons to tunnel into and occupy in the well. At this point the accumulated charge is ejected from the well and the conduction band potential redistributes, this process of charge accumulation and pinning is attributed to the feature F3 in figure 4.15(a), and is replicated in the simulated characteristic shown in figure 4.20(a). The observation of charge accumulation and pinning of the emitter quantum well state on resonance in the measured I(V) characteristics confirms the observations made by Buckle et al. in these structures by photoluminescence and photoluminescence excitation spectroscopy techniques [12].

It is also this process of pinning of the resonant state which appears to suppress the feature F2 in the simulated data. Analysis of the calculated tunnelling probability shows the state localised to the first quantum well, $E_{1_{W1}}$, remains pinned at a higher energy due to the charge accumulation (figure 4.22) and therefore the confined state does not

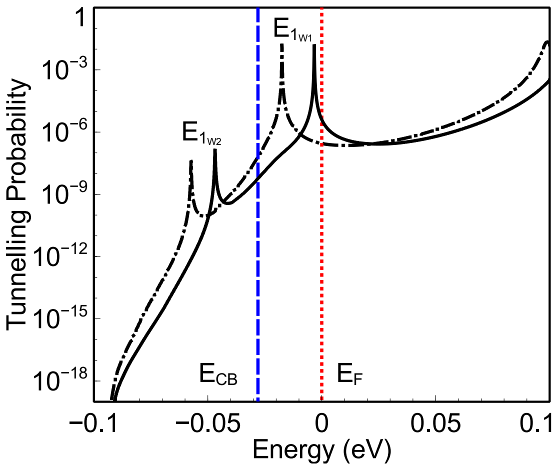

Figure 4.22: The calculated tunnelling probability for the nominally symmetric TBRTS with 0.15V applied for the situations where charge is allowed (solid black line) and forbidden (dash-dotted black line) to accumulate in the first quantum well are shown. The peaks in the tunnelling probability associated with the $E_{1_{W1}}$ and $E_{1_{W2}}$ confined states are at a higher energy when charge is allowed to accumulate, than when charge accumulation is forbidden. The energy of the conduction band edge, E_{CB} (dashed blue) and Fermi level, E_F (dotted red) are also shown.

pass through the emitter electron distribution, to its maximum near the conduction band edge as would normally be expected to form a resonance as seen in figure 4.18.

It is believed that the charge accumulation in the quantum wells when modelling these devices is potentially overestimated and as such the pinning of the $\mathrm{E}_{1_{\mathrm{W1}}}$ state occurs at a lower voltage than in the experimental data. The two proposed resonances in the feature F2 therefore do not form in the simulated results. The overestimation of charge accumulation is thought to occur due to model being an effective one-dimensional problem, which eliminates the lateral degrees of freedom (k_x and k_y) and as such the requirement of matching k-states when tunnelling into the quantum well is ignored.

Figures 4.23(a) and 4.23(b) show plots of the tunnelling probability against voltage at energies equal to the conduction band edge, E_{CB} and Fermi level, E_{F} for the cases where charge is allowed and not allowed to accumulate in the first quantum well. Several peaks in the tunnelling probabilities can be seen in these figures which occur at the voltages where the confined energy levels pass through the Fermi level and conduction band edge. The lowest voltage peak in the tunnelling probability for the E_{F} and E_{CB} plots in figure 4.23(a) is associated with the $\mathrm{E}_{1_{\mathrm{W2}}}$ confined state and occurs at a lower voltage for the Fermi level than the conduction band edge as is expected. The second peak in the E_{F} plot of figure 4.23(a) is associated with the $\mathrm{E}_{1_{\mathrm{W1}}}$ state and does not occur in the conduction band edge (CB) plot of figure 4.23(a), where charge is permitted to accumulate in the first quantum well, but does appear in figure 4.23(b) where charge accumulation is forbidden. The omission of this peak is therefore evidence to suggest that when charge accumulates in the quantum well the $\mathrm{E}_{1_{\mathrm{W1}}}$ state is pinned well above

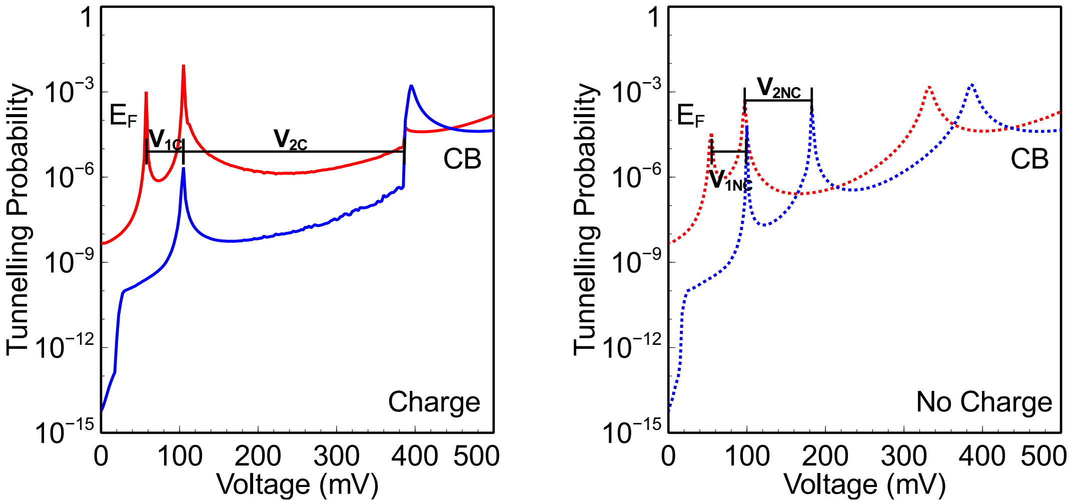

(a) (b)

FIGURE 4.23: The calculated tunneling probability against applied voltage for the nominally symmetric TBRTS at the Fermi level, E_{F} (red solid line) and conduction band, E_{CB} (blue solid line) for (a) the case where charge is allowed to accumulate in the first quantum and (b) where charge is forbidden to accumulate in the first quantum well.

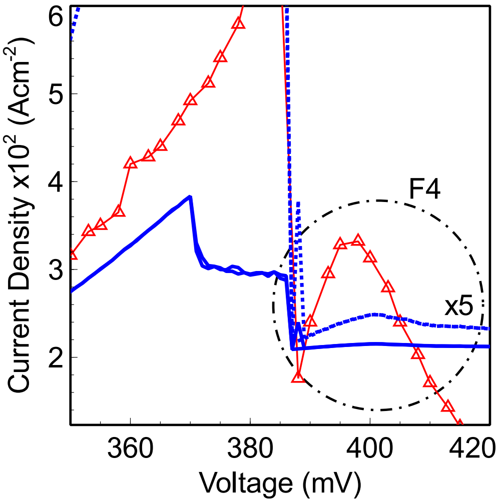

FIGURE 4.24: The experimental forward bias characteristic at x1 (solid blue) and x5 (dotted blue) scales. The simulated characteristic for the nominally symmetric structure is also shown (red triangles) from which it is clear to see another current density resonance feature, F4. This feature is associated with the energetic alignment of the $E_{2_{W2}}$ localised state with the emitter electron distribution.

the conduction band edge, and hence suppresses the expected resonance associated with this state.

The sharp discontinuity seen in figure 4.23(a) at around 380 mV occurs at the point where no further charge can accumulate and as such the charge is ejected from the well and the field across the structure redistributed. It is at this voltage where coincidentally, once the charge has been ejected that the $E_{2_{W2}}$ state energetically aligns with the emitter electron distribution. This alignment therefore causes another resonance in the I(V) characteristic which has previously not been identified as it was easily masked by feature F3. This resonance can clearly be seen in the simulated results, and is highlighted in figure 4.24.

The difference in voltage, for example, V_{1C}, between a peak in the tunnelling probability at the Fermi level, and one in the conduction band edge which are associated with a specific confined state can be used as a good estimate of the width in voltage of the resonant current peak. This is possible due to the fact there is a well defined Fermi level at low temperatures and so the emitter reservoir electrons only occupy states between the Fermi level and the conduction band edge. Only energetic alignment of a resonant state between these two energies will therefore allow for any substantial resonant tunnelling current to flow. The widths in voltage of the resonances associated with the $E_{1_{W2}}$ and $E_{1_{W1}}$ states for the charge and non-charge accumulating cases are shown on figures 4.25(a) and 4.25(b) respectively.

The estimated width of the resonances in voltage for the case where charge accumulation is permitted, V_{1C} and V_{2C} show good agreement with experimental results. However, it is also interesting that in the case where charge accumulation is forbidden, V_{1NC} gives

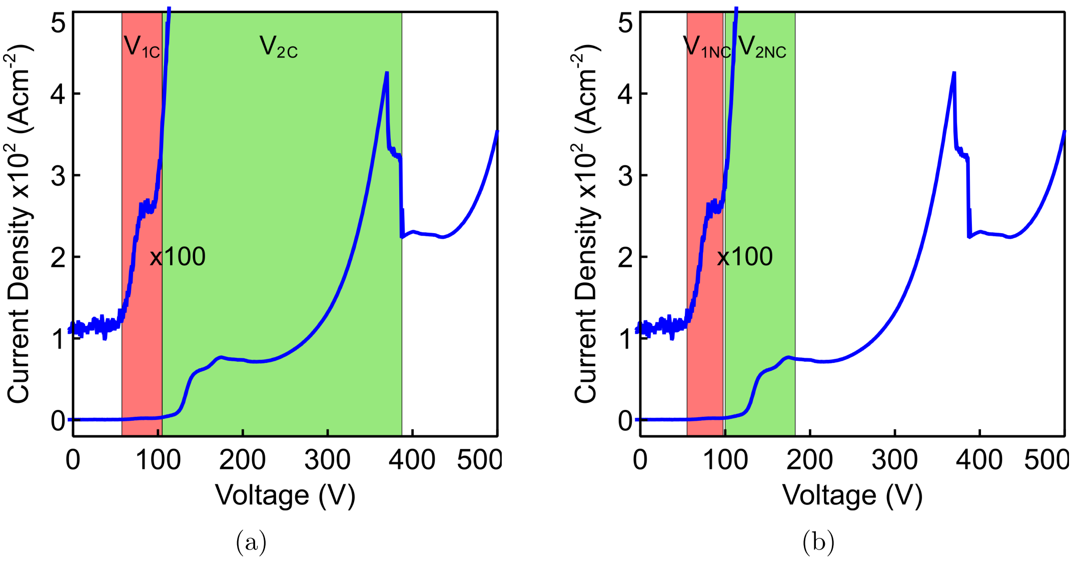

(a)

(b)

FIGURE 4.25: The experimental current density vs voltage characteristic for the nominally symmetric TBRTS. An estimate of the widths in voltage of the resonances associated with the $E_{1_{W2}}$ and $E_{1_{W1}}$ confined states from simulated results (figures 4.23(a) and 4.23(b) are shown for: (a) The case where charge accumulation in the first quantum well is allowed, V_{1C} and V_{2C}; (b) The case where charge accumulation in the first quantum well is forbidden, V_{1NC} and V_{2NC}.

good agreement for the resonance associated with $E_{1_{W2}}$ and although not for the entirety of feature F2, V_{2C} does give good agreement for the first small resonance of feature F2. Further inspection of the simulated results for the non-charge accumulating case show that a two dimensional state in the triangular well of the emitter has indeed formed with 170 mV applied across the structure, as shown in figure 4.26. As such it is plausible that the second small peak seen in feature F2 may well indeed be caused due to a transition

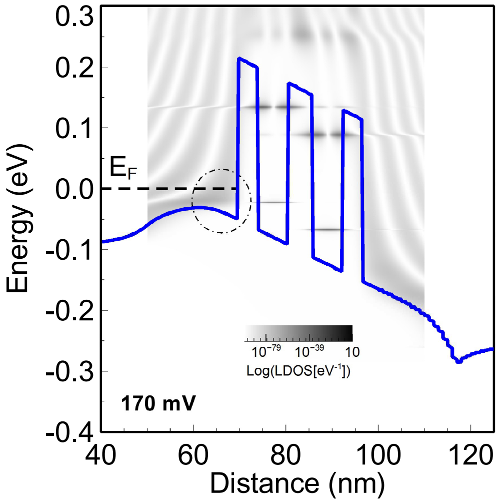

FIGURE 4.26: The calculated conduction band potential (solid blue line) and local density of states (LDOS) for the nominally symmetric TBRTS with 170 mV external voltage applied. Charge accumulation in the first quantum well is forbidden in this case, where a 2D state forms in the triangular well region of the emitter (circled).

between an emitter which is three dimensional in nature, to one which is two dimensional. Any subsequent pinning of the $E_{1_{W1}}$ state on resonance would then also be strong as the requirements of tunnelling for matching k-states is already fulfilled as the emitter is now also two dimensional.

A summary of the origin of each of the current resonances seen in the forward bias characteristic is given in table 4.2

TABLE 4.2: A summary of the origin of each of the features seen in the current density against voltage characteristics for the nominally symmetric TBRTS, figures 4.15(a), 4.15(b) and 4.24.

Feature	**Origin**
F1	The energetic alignment of the confined state localised to the second quantum well, $E_{1_{W2}}$, with the 3D emitter electron distribution.
F2-1	The energetic alignment of the confined state localised to the first quantum well, $E_{1_{W1}}$, with the 3D emitter electron distribution.
F2-2	The energetic alignment of the confined state localised to the first quantum well, $E_{1_{W1}}$, with a 2D state formed in the triangular well of the emitter region.
F3	Charge accumulation in the first quantum well results in the confined state $E_{1_{W1}}$ pinning on resonance with a 2D state formed in the triangular well. The state remains on resonance until no further charge can accumulate in the first quantum well, where there is a sharp drop off as the electric field across the structure redistributes.
F4	Coincidental to the field across the structure redistributing (caused by F3), the $E_{2_{W2}}$ confined state energetically aligns with the emitter electron distribution.

4.4.2 Negative Bias Characteristic

For a perfectly symmetric TBRTS, the forward and reverse bias characteristics should be identical. However, it is already known from previous experimental results (table 3.1) that there is a slight asymmetry in the widths of the two quantum wells in this structure, and as such we should expect a near, but not completely identical characteristic in both bias directions. Figure 4.27(a) shows the forward and reverse current-voltage I(V) characteristic for the nominally symmetric structure, from which it is possible to see that indeed there are striking similarities between the forward and reverse bias directions.

The resonance features in the reverse bias characteristic are similar in magnitude and voltage as those seen in the forward bias direction, and as such in general have the same

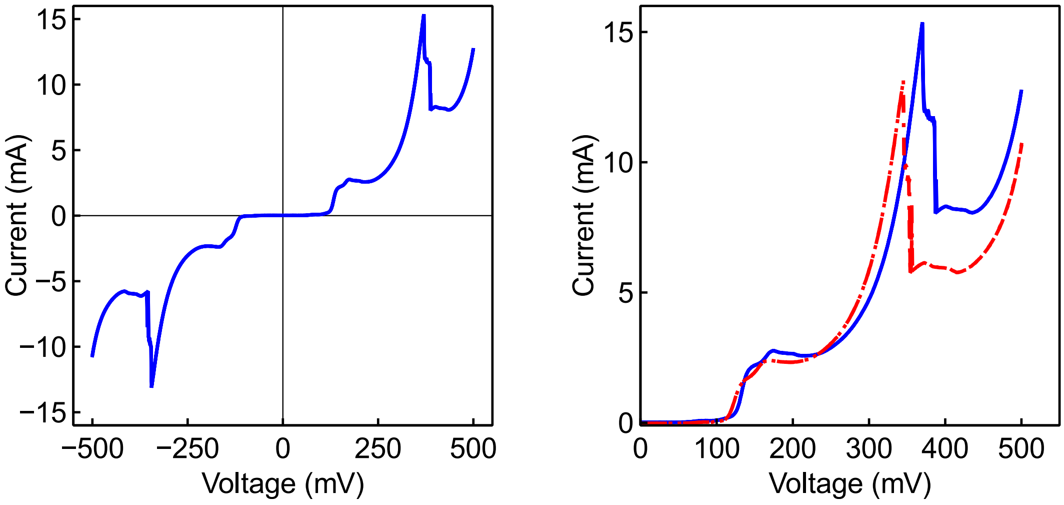

(a) (b)

FIGURE 4.27: (a) The full experimental current-voltage (I(V) characteristic in the forward and reverse bias directions for the nominally symmetric TBRTS at 3K in which it can be seen that there are striking similarities between the forward and reverse bias directions. (b) The forward (solid blue) and reverse (dashed red) I(V) characteristics overlain on the same axis for the nominally symmetric TBRTS at 3K. The small unintentional asymmetry in the two quantum wells and intended asymmetry due to the inclusion of a δ-doped layer in the structure results in the difference between the two characteristics.

origin and explanation as those described in section 4.4.1, but with the subtlety that the order in voltage at which the resonances associated with the respective quantum well states ($E_{1_{W1}}$ and $E_{1_{W2}}$)[†] occur is now reversed. Due to the slight asymmetry in the width of the quantum wells[‡] and the change in order in which they occur with respect to the emitter the voltage at which each resonance occurs and the magnitude of the current of each resonance will be changed. The effect of intentionally altering the quantum well asymmetry is studied in more detail in section 4.5.

Although described as nominally symmetric, this is only strictly applicable to the active region of the triple barrier structure. Within the outer layers of the device there is an inbuilt asymmetry due to the inclusion of a δ-doped layer in one side of the structure and asymmetric doping in either side of the active region (layers ii, iii, ix and x in section 3.1.2). This asymmetry results in different carrier injection properties into the active region of the TBRTS due to differences in the resistance and carrier dwell time and so subtlety different emitter and collector regions depending on the direction of bias. Closer examination of figure 4.27(b) suggests that there is the possibility that the series resistance in the reverse bias direction may be lower than that of the forward bias direction as the forward bias characteristic appears to be slightly shifted. However, there is also a decrease in the maximum current attained in the reverse bias direction compared to that of the forward characteristic, and so less carriers resonantly tunnel through the structure. Detailed studies of these points, although interesting and warranting of further investigation are currently beyond the scope of this thesis.

[†] Where the notation is consistent with the physical quantum wells given in figure 4.17, but a negative sign introduced to indicate the reverse bias.

[‡] Hence also a change in the energy of the localised confined states

4.5 Asymmetric Triple Barrier Resonant Tunnelling Structures

The current-voltage (I(V)) characteristic for the range of asymmetric triple barrier resonant tunnelling structures (table 3.1) are presented at low temperature and compared to the symmetric structure studied in section 4.4. Full details of the measurement technique, sample structure and device fabrication can be found in chapter 3.

4.5.1 Reducing the Collector Quantum Well Width

As described in section 3.1.2, a series of seven TBRTS with varying degrees of asymmetry are studied with the width of the collector quantum well reduced by approximately one monolayer between each sample from symmetric through to highly asymmetric. In the infinite well approximation the confinement energy is given by,

$$\mathrm{E_n} = \frac{\hbar^2 n^2 \pi^2}{2mL^2} \tag{4.3}$$

and so the energy of the confined states in the well, $\mathrm{E_n} \propto \frac{1}{L^2}$. A decrease in the width of the quantum well will therefore result in an increase in the energy of the confined states in that well.

Table 4.3: The measured quantum well width ratio and $n = 1$ confined state energies calculated from a a self-consistent Schrödinger-Poisson model (appendix A) for the series of seven samples studied in this section.

Sample	**Measured Quantum Well Ratio A:B**	$\mathbf{E_{1_{W_1}}}$ **(meV)**	$\mathbf{E_{1_{W_2}}}$ **(meV)**
VMBE 755	1.030	54.1	57.4
VMBE 757	1.069	51.3	56.4
VMBE 760	1.104	55.9	63.8
VMBE 761	1.172	54.5	66.8
VMBE 762	1.326	52.8	74.8
VMBE 787	1.438	56.9	87.5
VMBE 788	1.413	58.2	87.5

The energy of the $n = 1$ state more localised to the emitter quantum well, $E_{1_{W1}}$, and the state more localised to the collector quantum well, $E_{1_{W2}}$, for each of the seven samples were calculated using the measured quantum well widths (table 3.1) from a self-consistent Schrödinger-Poisson model (appendix A) and are shown, along with the measured quantum well width ratio in table 4.3.

Utilising these confined state energies, the known layer structure and the simple linear voltage drop model described in section 4.4.1 it is possible to predict the voltage at which each of the current resonances associated with the $E_{1_{W1}}$ and $E_{1_{W2}}$ states occur, and how this changes with increasing quantum well asymmetry.

The predicted resonance voltages for the $E_{1_{W1}}$ and $E_{1_{W2}}$ states in the forward and reverse bias directions against measured quantum well asymmetry are shown in figure 4.28. In the reverse bias direction these resonances diverge in voltage with increasing quantum well asymmetry, however the resonances in the forward bias direction, $E_{1_{W1}}$ and $E_{1_{W2}}$ converge to a crossing point, and in the most asymmetric structure, VMBE 787 these resonances nearly occur coincidentally with the conduction band edge.

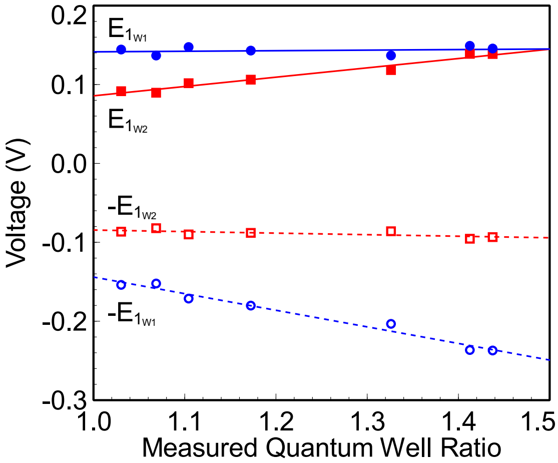

FIGURE 4.28: The predicted voltages at which the current resonances will occur for the $n = 1$ localised confined states in the forward bias, $E_{1_{W1}}$ (solid circle) and $E_{1_{W2}}$ (solid square), and reverse bias, $-E_{1_{W2}}$ (open square) and $-E_{1_{W1}}$ (open circle) directions. With the increase in quantum well asymmetry it can be seen that in the forward bias direction resonances converge, whilst the reverse bias direction resonances diverge.

This is significant as the maximum tunnelling current through a resonant state occurs when it is energetically aligned near or equal to the conduction band edge. Also, as explained in sections 4.2 and 4.3.2 the maximum tunnelling probability through a triple barrier resonant tunnelling structure occurs when the confined states are energetically aligned with each other. Therefore the peak tunnelling current through a structure which coincidentally energetically aligns the confined states with each other and the conduction band edge is expected to be very large.

Figure 4.29 shows the unmodified current-voltage characteristics at 3K for the series of VMBE samples with increasing quantum well asymmetry (table 4.3) with each of the

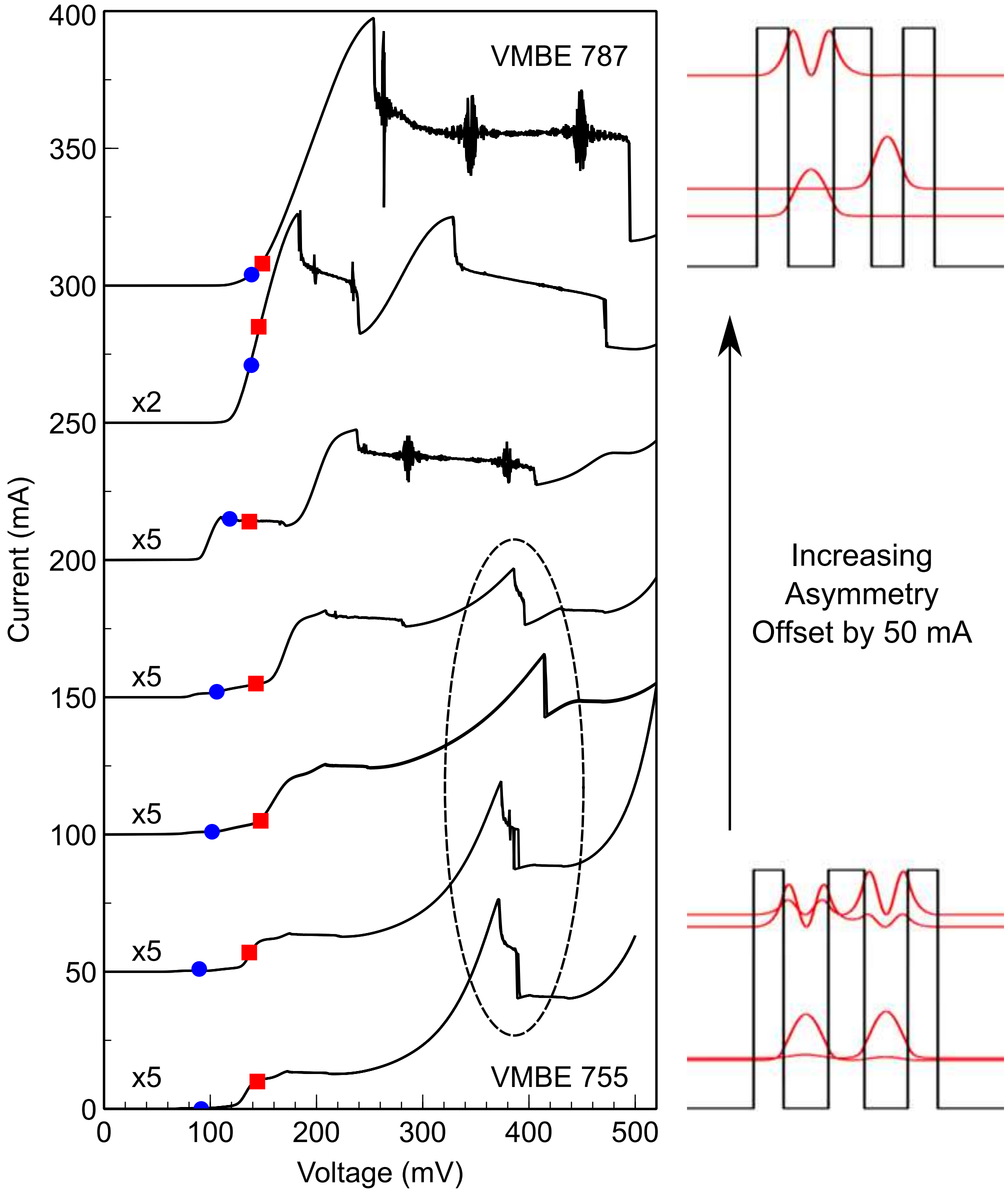

FIGURE 4.29: The raw current-voltage (I(V)) characteristics for the series of VMBE samples with increasing quantum well asymmetry at 3K. The characteristics for each different structure are offset by 50 mA for clarity and are given in increasing asymmetry order (most symmetric at the bottom, most asymmetric at the top). The forward bias simple model predicted current resonance voltages for the $E_{1_{W1}}$ (blue solid circle) and $E_{1_{W2}}$ (red solid square) are also shown. A very large single resonance is seen in the most asymmetric structure which is attributed to the coincidental energetic alignment of the quantum well confined states with each other and conduction band edge.

characteristics offset by 50 mA for clarity. The samples with a low degree of asymmetry (< 1.2) have similar features to those of the nominally symmetric structure described in section 4.4, however in the samples which have a larger degree of quantum well asymmetry (> 1.3) there are clear differences in the number and appearance of the resonant current features.

The feature F3 (table 4.2 and circled in figure 4.29), which is present in the low quantum well asymmetry samples is no longer present in the characteristics of the devices with a high degree of asymmetry. This is believed to be caused by the reduction in the width of the collector quantum well, which in turn results in an increase in the energy of the confined quantum well states and as such for the more asymmetric structures the $E_{2_{W2}}$ confined state no longer resides in the quantum well. The $E_{2_{W2}}$ confined state can therefore no longer provide a mechanism of escape for any charge which has accumulated in the emitter quantum well, and so the sharp drop off of the resonant feature seen in the low well asymmetry structures is no longer present.

The magnitude of this peak is also reduced with increasing quantum well asymmetry as a result of a reduction in the amount of charge allowed to accumulate in the emitter QW. Due to the exponential dependence of the tunnelling probability [3] on the width of the tunnelling barrier, a small decrease in the the width of the "effective" potential barrier (i.e. middle barrier, forbidden regions in the collector QW and collector barrier) results in a significant increase in the tunnelling probability and therefore the tunnelling rate of electrons out of the emitter quantum well. This increase in tunnelling probability in turn reduces the total amount of charge accumulation in the emitter quantum well as it is this rate which determines the amount of charge accumulation in the quasi-equilibrium state.

Table 4.4 shows the energies of the $E_{2_{W2}}$ confined states for the series of VMBE samples as calculated from a self-consistent Schrödinger-Poisson model. For the three most asymmetric structures, VMBE 762, 787 and 788 the model predicts that there is no longer a $E_{2_{W2}}$ state confined in the collector quantum well.

TABLE 4.4: The measured quantum well width ratio and $n = 2$ confined state energies $E_{2_{W_1}}$ and $E_{2_{W_2}}$ calculated from a a self-consistent Schrödinger-Poisson model for the series of seven samples studied in this section.

Sample	**Measured Quantum Well Ratio A:B**	**$E_{2_{W_1}}$ (meV)**	**$E_{2_{W_2}}$ (meV)**
VMBE 755	1.030	204.8	223.9
VMBE 757	1.069	196.4	219.1
VMBE 760	1.104	212.3	243.8
VMBE 761	1.172	208.4	252.2
VMBE 762	1.326	203.4	No state
VMBE 787	1.438	217.6	No state
VMBE 788	1.413	222.0	No state

The most striking difference between the more symmetric and most asymmetric structures however is the transition from an I(V) characteristic in which several small resonant features occur, to one in which there is one prominent resonant feature (VMBE 787), which is large in magnitude and has an extensive region of negative differential resistance. This single resonant feature is thought to occur due to the coincidental energetic alignment of the $n = 1$ confined states with each other, near to or at the conduction band edge. It is here where the number of charge carriers in the three dimensional emitter distribution that have k-state values which match those of the 2D confined states is very large (section 4.3.3) and so this combined with a large tunnelling probability through the structure results in a large tunnelling current through the device.

Although a four-wire measurement technique (which is described in section 3.2.2) was used there is still some minor series resistance which is affecting the characteristics shown in figure 4.29, with the series resistance also varying between each sample. These variations are believed to be caused by: a) minor differences in the samples growth parameters, which has affected the series resistance of the doped contact layers, and undoped spacer layers and b) variations in the sample fabrication process, especially the wet etch phase where each sample was etched separately and so the depth of the etch (and hence depth of the bottom contact) varies between each sample, with sample VMBE 760 seeming to be the worst affected.

Table 4.5 shows the measured wet etch depth for each of the series of samples, and as can be seen sample VMBE 760 has been etched considerably deeper than the other samples. The bottom contact layer for VMBE 760 is therefore much further from the active region of the device than was intended, and although the contact layer is very conductive a small, but significant extra series resistance has been introduced.

Table 4.5: The measured mesa wet etch depth for the series of seven VMBE samples. The increased etch depth of VMBE 760 has introduced a small but significant extra series resistance which can not be removed from the measurement circuit.

Sample	**Etch Depth (μm)**
VMBE 755	0.65
VMBE 757	0.62
VMBE 760	1.21
VMBE 761	0.68
VMBE 762	0.66
VMBE 787	0.63
VMBE 788	0.65

A small series resistance still remains in all of the samples due to the $\approx 5\mu$m region of doped contact layer between the bottom edge of the mesa and the bottom contact of the device, as well as the $0.4\,\mu$m length of top contact layer and $\approx 0.2\,\mu$m (for most samples) bottom contact layer region the electrons have to travel through before reaching (or after passing through) the active triple barrier region of the device. Figure 4.30 shows the I(V) characteristics for the series of seven samples after small corrections for series resistance have been made using equation (4.1) where the value of the series resistance has been extracted from the high voltage region where the series resistance dominates.

Although not a complete measure of the effectiveness of a device (for more information see chapter 6), the peak-to-valley current ratio or PVCR is a conventional way of measuring the scale of a current resonance and can give an indication of the potential efficiency of a device which may utilise a current resonance as a binary operator i.e. a device which for a small voltage change can switch between a high current "on" state and a low current

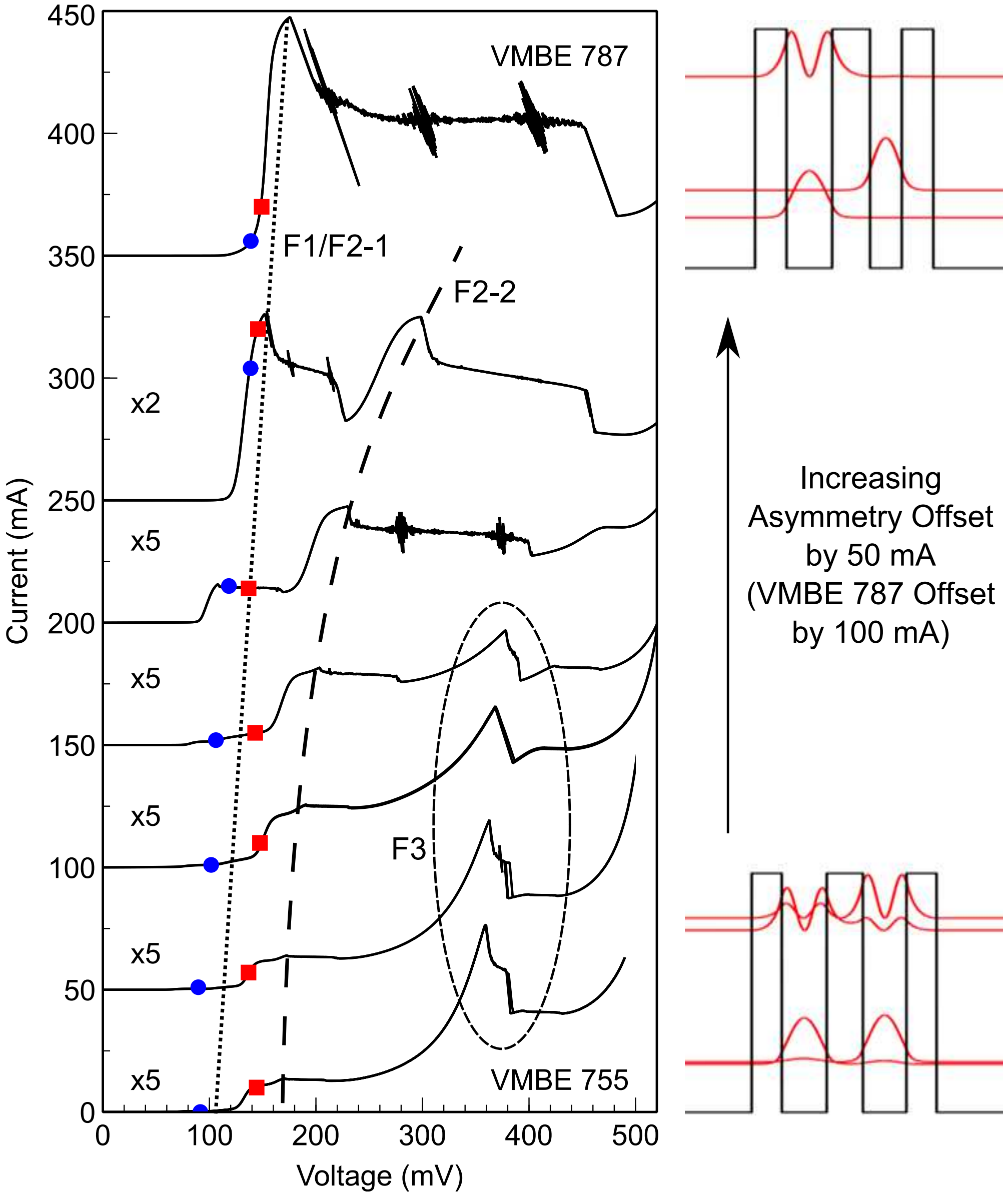

FIGURE 4.30: The series-resistance adjusted current-voltage (I(V)) characteristics at 3K, an effective resistance of 0.8 Ω has been removed for all characteristics except VMBE 760 (third from bottom) which has had 3.5 Ω removed. Each characteristic is offset by 50 mA from the previous for clarity (for VMBE 787 there is a 100 mA offset) with the most symmetric at the bottom and most asymmetric at the top. The forward bias simple model predicted current resonance voltages for the $E_{1_{W_1}}$ (blue solid circle) and $E_{1_{W_2}}$ (red solid square) are given and lines to guide the eye to the evolution of the features F1/F2-1, F2-2 and F3 are also shown.

"off" state. The peak-to-valley current ratio is given by,

$$\mathrm{PVCR} = \frac{\text{Peak Current}}{\text{Valley Current}} \tag{4.4}$$

where the resonance peak current is the maximum current value and the valley current is the minimum current value following the peaks NDR region as shown in figure 4.31(a). The calculated peak-to-valley current ratios for the features F1/F2-1, F2-2 and F3 (table 4.2) with a discernible negative differential resistance region against quantum well asymmetry are shown in figure 4.31(b).

From this it is clear to see that with increasing quantum well asymmetry the formation of a single resonant feature not only increases the maximum (peak) resonance current, but the peak-to-valley ratio also dramatically increases as the valley current remains low. As such the most asymmetric device design, VMBE 787, where the energetic alignment of the confined quantum well states with each other and the conduction band edge occurs coincidentally is very interesting and a good starting point from which to begin considering ways in which to improve peak resonant current magnitude and minimise the valley current in the TBRTS. This optimisation of the triple barrier resonant structure design is the subject of chapter 6 and so will not be discussed further here. A detailed analysis of the effect of device area on the leakage (valley) current through the most asymmetric and nominally symmetric structures however is presented in section 4.6.

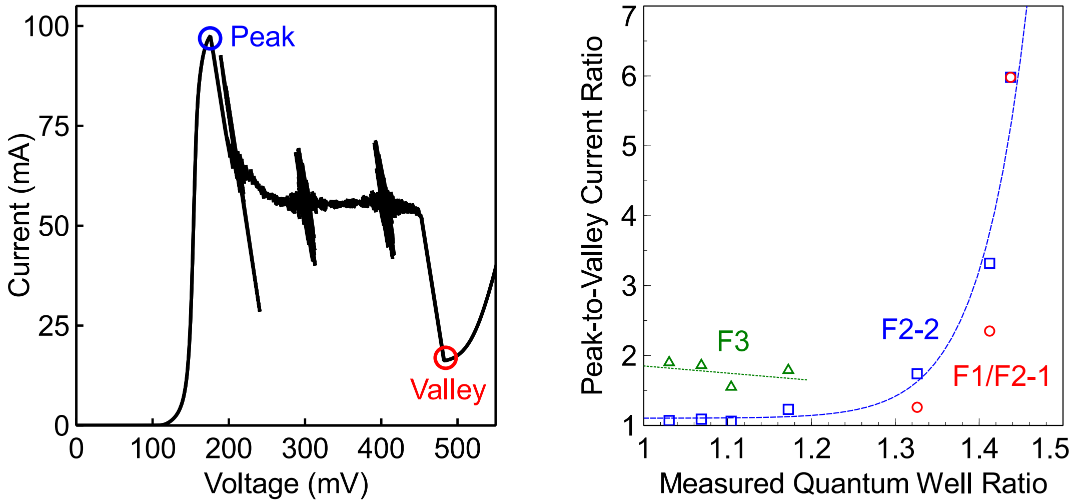

(a) (b)

FIGURE 4.31: (a) The series resistance adjusted I(V) characteristic for the most asymmetric structure, VMBE 787. The peak (blue) and valley (red) currents of the large single resonance are circled, with the peak-to-valley current ratio of this resonance calculated to be ≈ 6. (b) The calculated peak-to-valley current ratio for the features F1/F2-1, F2-2 and F3 which have discernible NDR regions against quantum well asymmetry.

4.6 Perimeter vs Area Analysis

The nominally symmetric (VMBE 755) and most asymmetric (VMBE 787) structures were chosen to be studied to investigate the affect of the physical mesa dimensions on the TBRTS device properties at low temperature (3K) and whether the varying TBRTS design altered the dominant current flow. Four wire current-voltage (I(V)) measurements (as described in section 3.2.2) were performed on five square devices of varying mesa area, all of which were contained on a single 3.6mm x 3.6mm section of cleaved wafer mounted into a 20-way ceramic package (as shown in section 3.1.4). The dimensions of the five different devices measured for each wafer are given in table 4.6.

Table 4.6: The nominal and measured square mesa side lengths used in the perimeter vs area analysis for samples VMBE 755 and VMBE 787 where the mesa side wall length was measured to be nominally the same for both samples. The calculated perimeter and area values for each size are also given.

Nominal Mesa Side Length (μm)	**Measured Mesa Side Length (μm)**	**Calculated Mesa Perimeter (μm)**	**Calculated Mesa Area (μm^2)**
60	59	236	3481
90	89	356	7921
110	109	436	11881
130	129	516	16641
160	159	636	25281

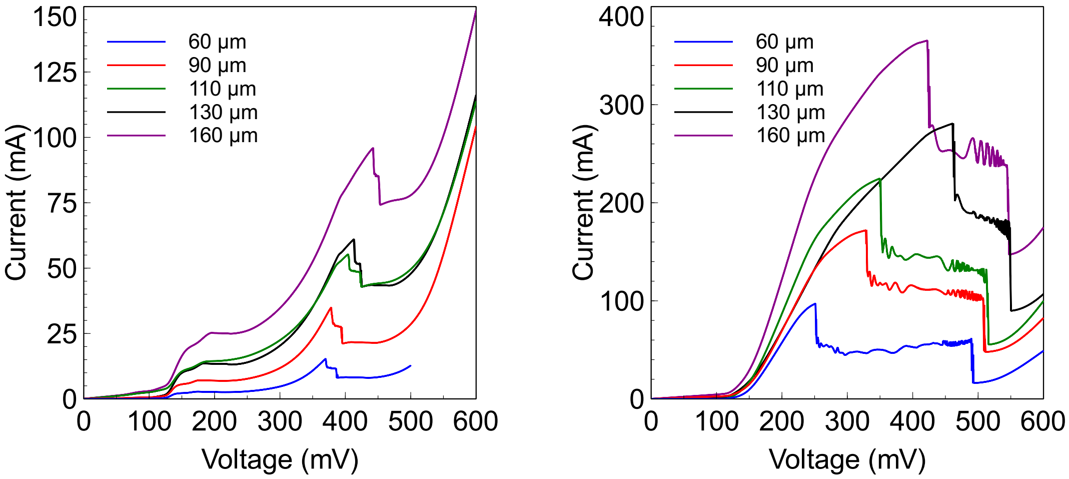

(a) (b)

Figure 4.32: The measured current-voltage characteristics of five different devices varying in mesa side wall length for (a) the nominally symmetric structure and (b) the most asymmetric structure. A general trend of increasing current magnitude with increasing mesa size is observed.

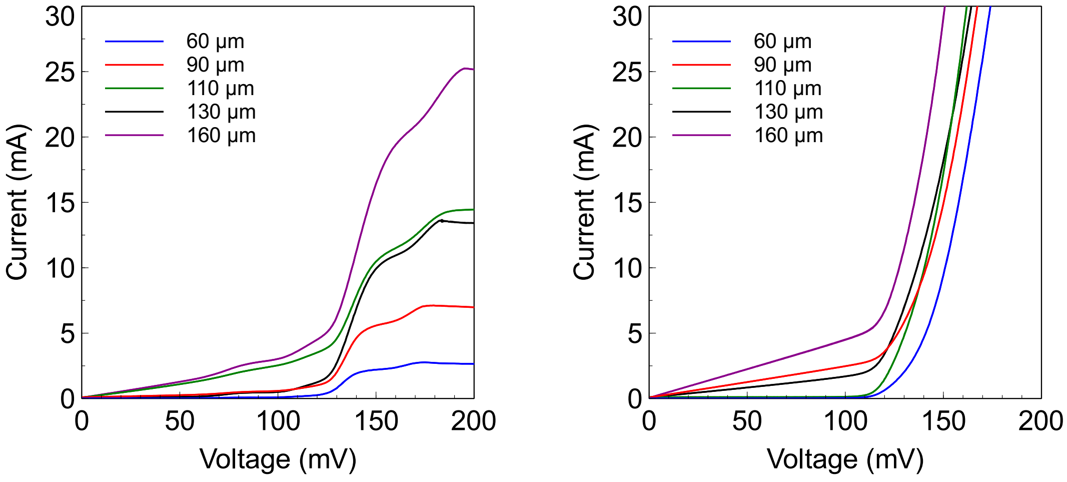

(a) (b)

FIGURE 4.33: The low voltage measured current-voltage characteristics of five different devices varying in mesa side wall length for (a) the nominally symmetric structure and (b) the most asymmetric structure. In both samples the low voltage region current does not follow this general trend with the magnitude of the current appearing to be random with device size.

The measured I(V) characteristics for the nominally symmetric and most asymmetric structure devices are shown in figures 4.32(a) and 4.32(b) respectively and as expected the magnitude of the current generally increases with increasing device size. However there are a few devices which do not follow this general trend across the whole voltage range, particularly in the low voltage region.

Figures 4.33(a) and 4.33(b) show the low voltage regions of samples VMBE 755 and VMBE 787 respectively, in which it can be seen that there appears a small, but significant contribution to the overall device current which fluctuates between device sizes. In the low voltage (<50 mV) region both of the triple barrier resonant tunnelling structures studied here are highly resistive due to the misalignment of all the confined quantum states with the emitter electron distribution, therefore any current which flows at these voltages is expected to be due to a parallel, lower resistance mechanism.

To investigate the nature of this lower resistance parallel current path, and confirm that it does not scale linearly with device perimeter or area the current at a single voltage for each of the different device sizes were plotted against device perimeter and device area. The current-perimeter and current-area plots for VMBE 755 and VMBE 787 are shown in figures 4.34(a) and 4.34(b) respectively.

There is no clear correlation between the measured current values at 50 mV and either the calculated mesa perimeter or calculated mesa area and so this leakage current neither scales with perimeter or area. It therefore can not attributed to general leakage through the potential barriers of the TBRTS due to alloy fluctuations or small defects (which would be area dominated), or general mesa side wall leakage (which would be perimeter

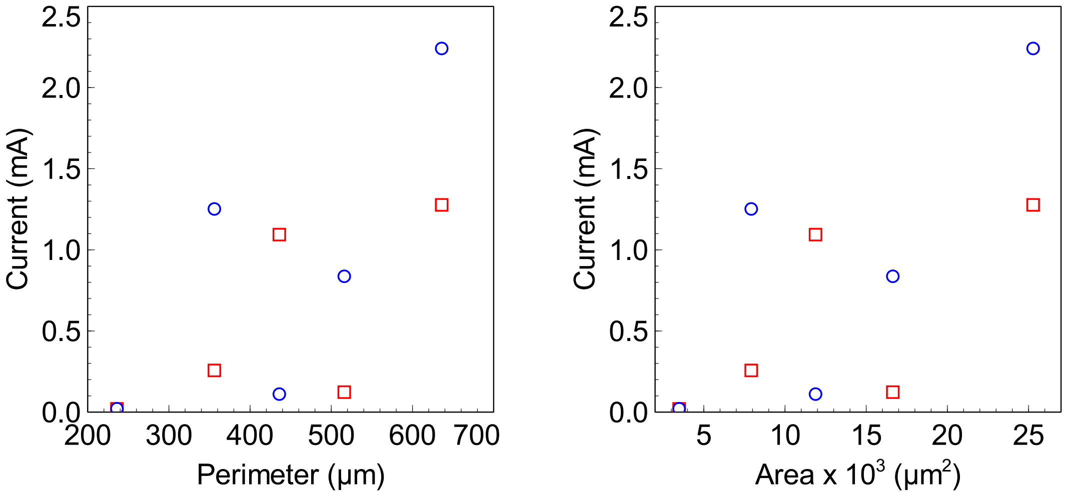

(a) (b)

FIGURE 4.34: The current values at 50 mV for devices with varying size mesa sizes. (a) The 50 mV current values against the measured device mesa perimeter for the nominally symmetric (red squares) and most asymmetric (blue circles) triple barrier resonant tunnelling structures. There is no clear correlation between the measured current and either calculated perimeter or calculated mesa area.

dominated). There are many other processes which may potentially cause this low parallel resistance path that varies between devices such as large defects in the crystal structure which completely penetrate the active region of the TBRTS, a side wall defect which bypasses the active TBRTS region or a short circuit (which bypasses the TBRTS active region) caused by the metal deposition fabrication process or device bonding. Without further analysis, and a much large sample of devices it is not possible to determine the root cause of this parallel conduction path.

The parallel conduction leakage current is therefore removed from the I(V) characteristics by fitting a second order polynomial to the low voltage (0 to 50 mV) region and subtracting the associated current across the entire voltage range. Figures 4.35(a) and 4.35(a) show the parallel conduction corrected data for VMBE 755 and VMBE 787 respectively in which it can be seen the general trend of increasing current magnitude with increasing device size is now followed across the entire voltage range.

There are however still some differences between the I(V) characteristics of the different size mesas besides that of the scaling of the magnitude of the current. In particular it is observed that with increasing device size the series resistance of each device also appears to increase, and has the most significant effect on the 110 μm device in figure 4.35(a) and 130 μm device in figure 4.35(b). Initially this seems to be the opposite effect to what would be expected with increasing mesa size (and therefore area), but can easily be explained by considering the total resistance of the device under test.

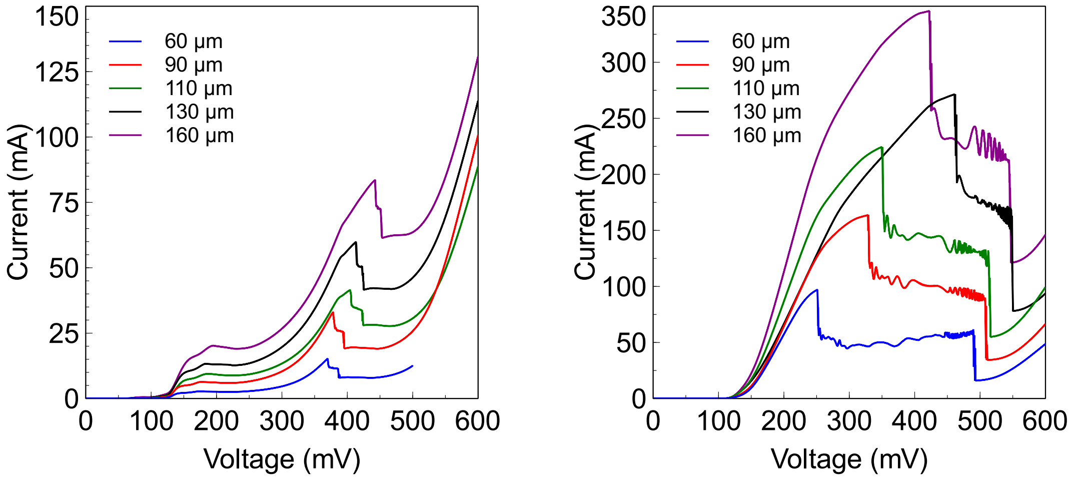

(a) (b)

FIGURE 4.35: The parallel conduction adjusted I(V) characteristics of TBRTS devices with varying mesa size for (a) the nominally symmetric structure and (b) the most asymmetric structure.

It is well known that the resistance, R of a material of area A and length L with a resistivity ρ can be expressed as,

$$R = \frac{\rho L}{A} \tag{4.5}$$

and as such any increase in area reduces the resistance. In the measurement circuit of a device under test (DUT) with a resistance $\mathrm{R_{DUT}}$ (which is described by equation (4.5)) and series resistance $\mathrm{R_S}$, the total resistance, $\mathrm{R_T}$ is given by,

$$\mathrm{R_T} = \mathrm{R_S} + \mathrm{R_{DUT}} \tag{4.6}$$

and the total voltage applied, $\mathrm{V_T}$ is the sum of the voltages, $\mathrm{V_S}$ and $\mathrm{V_{DUT}}$, dropped across the respective resistances. The measurement circuit therefore can be thought of as a simple potential divider in which the ratio of the resistances is equal to the ratio of the voltages dropped across those resistances:

$$\frac{\mathrm{R_{DUT}}}{\mathrm{R_S}} = \frac{\mathrm{V_{DUT}}}{\mathrm{V_S}} \tag{4.7}$$

With simple rearrangement and substitution of equation (4.6) into equation (4.7) it can be shown that,

$$\mathrm{V_{DUT}} = \frac{\mathrm{V_T}}{1 + \left[\dfrac{A}{\rho L}\right] \mathrm{R_S}} \tag{4.8}$$

Equation (4.8) therefore shows that for a constant bias and series resistance an increase in the area of the DUT (and so a reduction in the DUT resistance) results in a decrease in the amount of bias dropped across the DUT. This has the effect of shifting the features in the I(V) characteristics of the largest area devices out to higher voltages than where they are identified in the I(V) characteristics of the smallest area devices, as seen in figures 4.35(a) and 4.35(a). It is important to note that this is therefore not a change in the series resistance associated with device size (as this is nominally constant and dominated by the 5 μm gap between the bottom of the mesa edge and the bottom contact), but a change in device resistance relative to the constant series resistance.

To account for this the parallel conduction adjusted I(V) characteristics can be modified by the use of equation (4.1), where an estimate of the series resistance is made by calculating the resistance in the high voltage region and extrapolating the data to a point where this resistance becomes constant, this is then taken as the series resistance value.

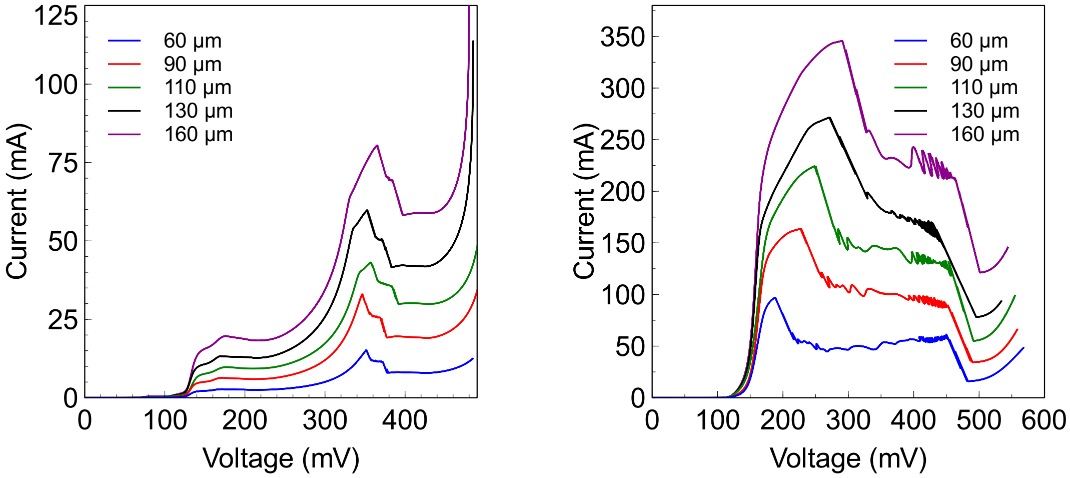

(a) (b)

FIGURE 4.36: The measured I(V) characteristics for (a) the nominally symmetric TBRTS and (b) the most asymmetric TBRTS after adjustment to the voltage to take into account the change of the device resistance relative to the constant series resistance.

Figures 4.36(a) and 4.36(b) show the modified I(V) characteristics for the nominally symmetric and most asymmetric structures respectively from which it can be seen that the 110 μm device in figure 4.35(a) and 130 μm device in figure 4.35(b) now clearly follow the trend of the other the device characteristics, being very similar in appearance but with increasing magnitude. As these characteristics are now so similar with respect to the voltage applied it is now possible to analyse the current against mesa perimeter and mesa area for a single voltage which is common for each device.

Figures 4.37(a) and 4.37(b) show the valley current at 420 mV for VMBE 755 and 520 mV for VMBE 787 plotted against mesa perimeter and area respectively with a second order polynomial fit made to each data set. From figure 4.37(a) it is possible to see that neither the valley current for VMBE 755 nor VMBE 787 is proportional to the mesa perimeter, however in figure 4.37(b) the current appear to scale more linearly with area, although there still appears to be a degree of curvature for VMBE 755. This therefore suggests that the valley current for the most asymmetric structures is dominated by a

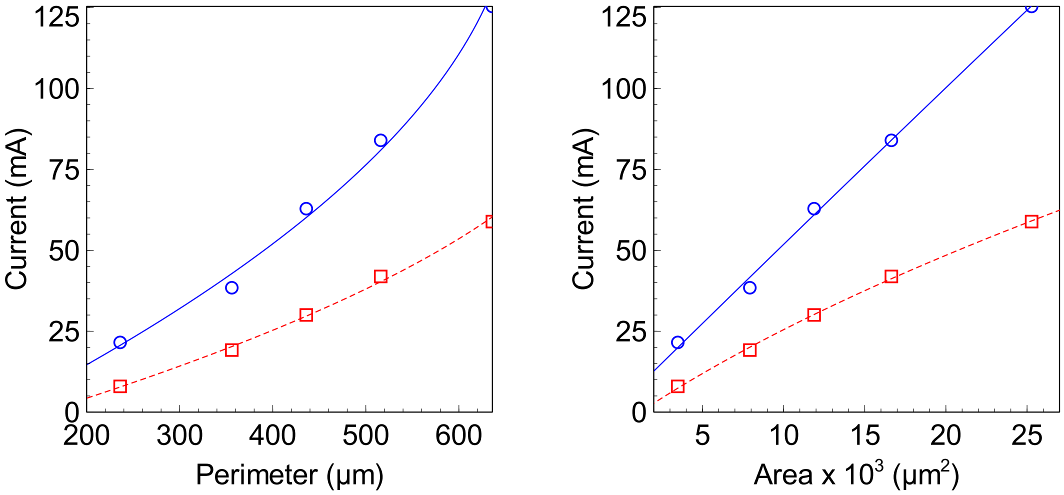

(a) (b)

FIGURE 4.37: The valley current at 420 mV for VMBE 755 (red squares) and 520 mV for VMBE 787 (blue circles) plotted against (a) calculated mesa perimeter and (b)calculated mesa area. Second order polynomial fits are made to each data to explore the linearity of each.

mechanism which scales with area, and so should we wish to reduce the valley current then this can simply be achieved by reducing the mesa area. Whilst the origin of the valley current in VMBE 755 however is still not clear.

The current-perimeter and current-area plots for a resonance peak at 340 mV for the nominally symmetric structure (F3) and 180 mV for the most asymmetric structure are shown in figures 4.38(a) and 4.38(b) respectively. In contrast to the valley current these

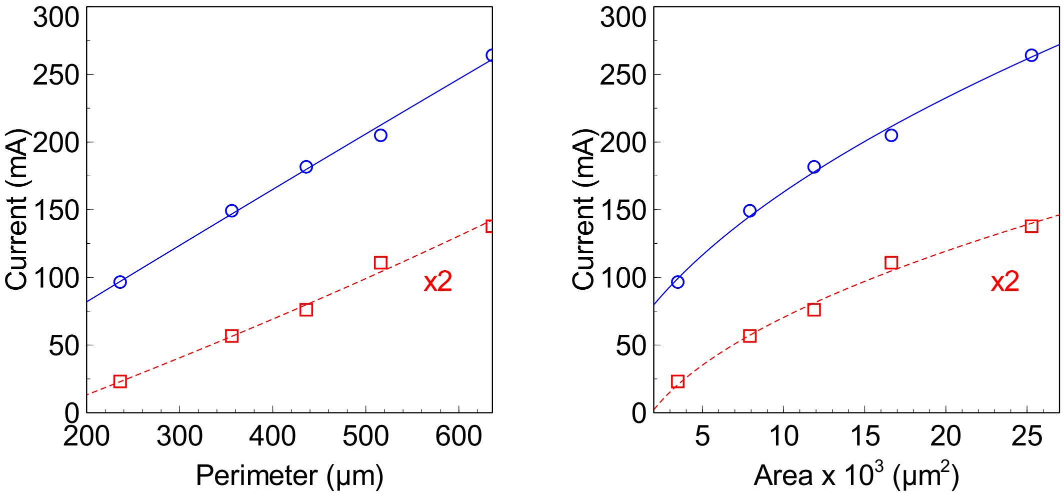

(a) (b)

FIGURE 4.38: The peak current at 340 mV for VMBE 755 (red squares) and 180 mV for VMBE 787 (blue circles) plotted against (a) calculated mesa perimeter and (b) calculated mesa area. Second order polynomial fits are made to each data set and show that the current scales more linearly with perimeter than area, which is an unexpected result.

resonant peaks appear to be dominated by a process which scales more linearly with perimeter than area, indicating that the majority of the current path is along the edge of the mesa rather than the entire mesa area. This is an unexpected result, particularly as the resonant features have been attributed to the coincidental energetic alignment of the confined quantum well states with each other and the emitter electron distribution, which one would expected to be an area dominated process.

From figures 4.36(a) and 4.36(b) it is possible to see that although an adjustment has been made to correct for the apparent change in series resistance with increasing device area, the voltages at which the features in the I(V) characteristics occur do still shift slightly between each device size. These small shifts mean that although selecting a single

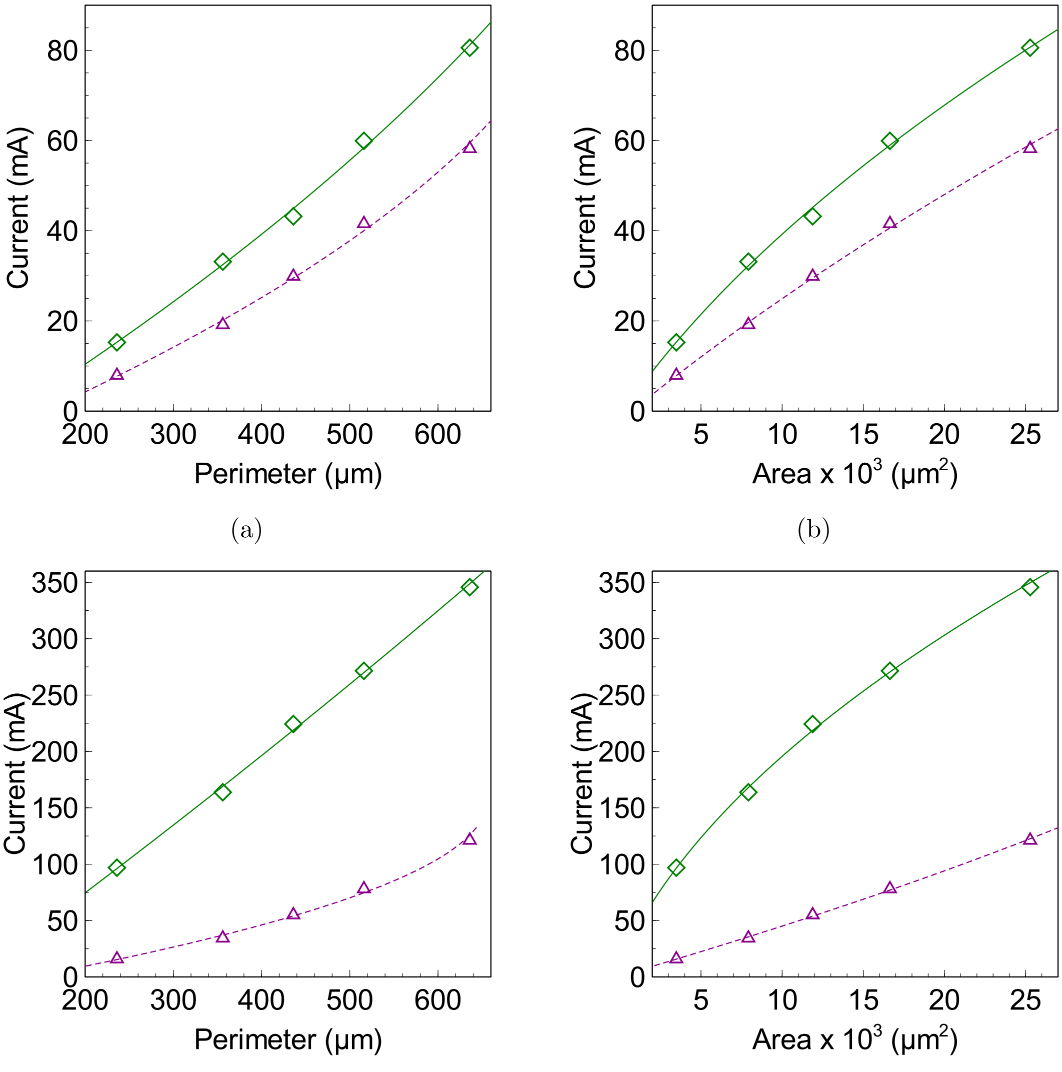

(a) (b) (c) (d)

FIGURE 4.39: The peak (green diamonds) and valley (magenta triangles) currents against (a) mesa perimeter and (b) mesa area for the feature F3 in the nominally symmetric triple barrier resonant tunnelling structure I(V) characteristic and (c) mesa perimeter and (d) mesa area for the large single resonance feature in the most asymmetric structure VMBE 787.

voltage at which to perform the perimeter vs area analysis initially appears a sensible approach the variations may affect the results. The amount to adjust the data to account for the change in apparent series resistance can also be subjective as the value for the series resistance which is extracted from the high voltage region of the characteristic is often tending to, but has not yet reached a single value and so there may be some uncertainty in the final value of series resistance that is extracted.

To explore whether these adjustments have had an affect on the results obtained the unadjusted peak and valley currents are plotted against mesa perimeter and area for each device and are shown in figures 4.39(a) and 4.39(b) for the same resonance, F3 as was studied in figures 4.37(a) and 4.37(b) for VMBE 755. The peak and valley current for the large single resonance in the I(V) characteristic for VMBE 787 against mesa perimeter and area are also plotted in figures 4.39(c) and 4.39(d).

From these plots is it once again clear to see that the peak current for the VMBE 787 resonance scales more linearly with perimeter than area, whilst the valley current is more linear with area than perimeter. The results for VMBE 755 however are more difficult to interpret as both do not appear to clearly scale linearly with either perimeter or area, which may indicate that the peak current of feature F3 is a result of contributions from both the area and perimeter of the mesa where neither contribution dominates. These results however do still agree with those obtained when the current at a single voltage of the series resistance modified I(V) characteristics was studied (which are summarised in table 4.7) and so are evidence to suggest that this a true trend and not a result of the data being adjusted to account for the apparent change in series resistance with increasing mesa size.

Table 4.7: A summary of the dominant current origin, whether via mesa perimeter or mesa area for the current resonances via two different methods: (a) extracting the maximum peak current and minimum valley current and (b) correcting the data for an apparent change in series resistance and extracting the current at a single voltage.

Sample (Resonance)	**Maximum Current Peak**	**Minimum Current Valley**	**Single Voltage Peak**	**Single Voltage Valley**
VMBE 755 (F3)	Unclear	Unclear	Perimeter	Unclear
VMBE 787 (F1/F2-1)	Perimeter	Area	Perimeter	Area

Using the extracted peak and valley currents from the I(V) characteristics of VMBE 755 and VMBE 787 the peak-to-valley ratio (PVCR) of the resonant features F3 and F1/F2-1 are calculated using equation (4.4) and plotted against mesa perimeter and area in figures 4.40(a) and 4.40(b) respectively. As one may expect considering the peak current of these features is perimeter dominated and the valley current is area dominated for VMBE 787 the PVCR is neither linear with area or voltage, but does increase with

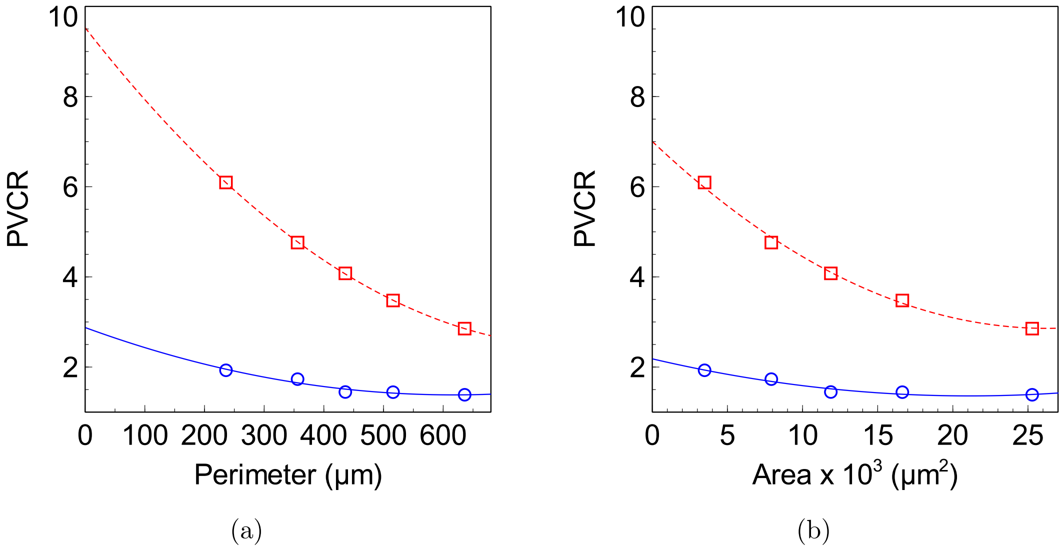

(a)

(b)

FIGURE 4.40: The calculated peak-to-valley current ratio for the extracted peak and valley currents for the features VMBE 755 F3 (blue circles) and VMBE 787 F1/F2-1 (red squares) against (a) mesa perimeter and (b) mesa area. Second order polynomial fits to the data are also shown.

both reducing area and perimeter. This trend is also seen for the feature F3 in VMBE 755, however the affect is less pronounced. Second order polynomial fits are made to both PVCR-perimeter and PVCR-area plots and are shown in figures 4.40(a) and 4.40(b), where the fit in the PVCR-perimeter plot appears to be marginally better. The intercepts of the PVCR-perimeter and PVCR-area fits are found to be 9.5 and 7.0 respectively for the VMBE 787 F1/F2-1 resonance and 2.8 and 2.2 for the VMBE 755 F3 resonance, which therefore give an estimate of the maximum obtainable PVCR for these resonances with small dimension devices.

Whether the current flow through the TBRTS devices is perimeter or area dominated has only been explored for two isolated resonances thus far, but as has been shown by the differences between the peak and valley measurements this mechanism has the potential to change across the entire measured voltage range. Therefore in order to analyse the entire measured voltage range another approach has been taken, with the full I(V) characteristics for all VMBE 755 and VMBE 787 devices scaled with mesa perimeter, which results in a one-dimensional current density (Acm^{-1}) and scaled with mesa area which results in a two-dimensional current density (Acm^{-2}). The scaled curent values are plotted against voltage for the nominally symmetric structure in figures 4.41(a) and 4.41(b) and for the most asymmetric structure in figures 4.42(a) and 4.42(b) respectively.

The regions where the one or two dimensional current density-voltage plots for each of the different size devices overlay indicates regions where the current is dominated (and therefore scales linearly) by a perimeter or area dominated process respectively. As a result figure 4.41(b) shows that over the majority of the voltage range the current flow is

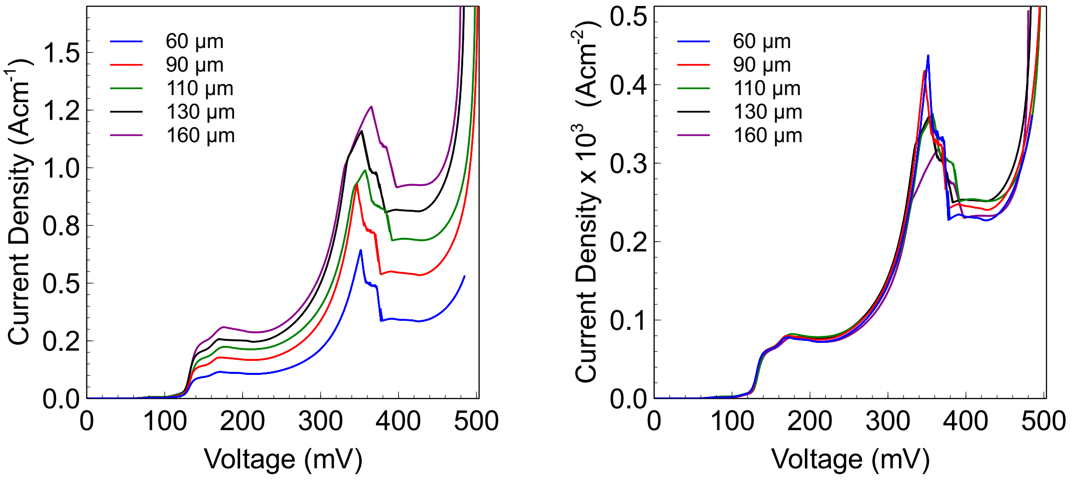

(a) (b)

FIGURE 4.41: (a) The one dimensional current density-voltage characteristic for the nominally symmetric TBRTS after adjustment for the apparent change in series resistance with mesa size. (b) The one dimensional current density-voltage characteristic for the nominally symmetric TBRTS after adjustment for the apparent change in series resistance with mesa size.

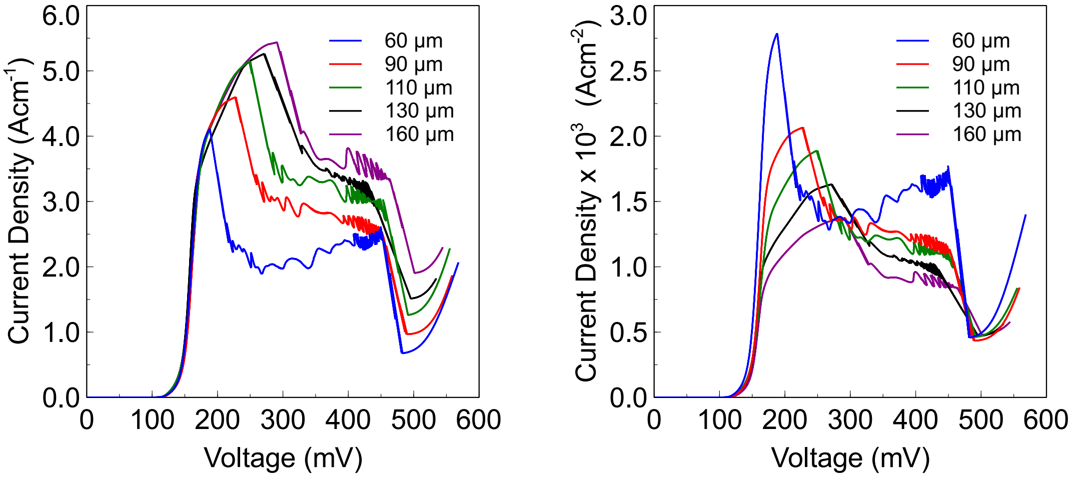

(a) (b)

FIGURE 4.42: (a) The one dimensional current density-voltage characteristic for the most asymmetric TBRTS after adjustment for the apparent change in series resistance with mesa size. (b) The one dimensional current density-voltage characteristic for the most asymmetric TBRTS after adjustment for the apparent change in series resistance with mesa size.

dominated by the mesa area, however, the peak current-density for feature F3 do not overlay. This indicates that the peak current is not an area dominated process which agrees with the previous results of this section, which suggest it is perimeter dominated. The peak current-densities for feature F3 in figure 4.41(a) however do not overlay when scaled for perimeter either, which suggests that the peak current flow must be a combination of an area and perimeter driven process, where neither contribution dominates. However, as the majority of the current flow across the voltage range is area dominated, it suggests the possibility that the peak resonant current is a perimeter dominated process, but with a significant contribution from a background area driven process.

Figures 4.42(a) and 4.42(b) however show that for the most asymmetric structure the peak resonance current is quite clearly a perimeter dominated process, with the valley current equally as unmistakably an area dominated process.

To understand why the on resonance current flow is perimeter dominated, but the off resonance current flow area dominated the current flow through the TBRTS devices is considered and illustrated in figure 4.43. Here it is shown that under positive bias the current flows from the top contact through the TBRTS active layers, which has a resistance R_{TBRTS} to the bottom contact which is 5 μm from the bottom of the mesa edge. The series resistance, R_S is dependent on the path taken by the current, where a longer path results in a higher series resistance.

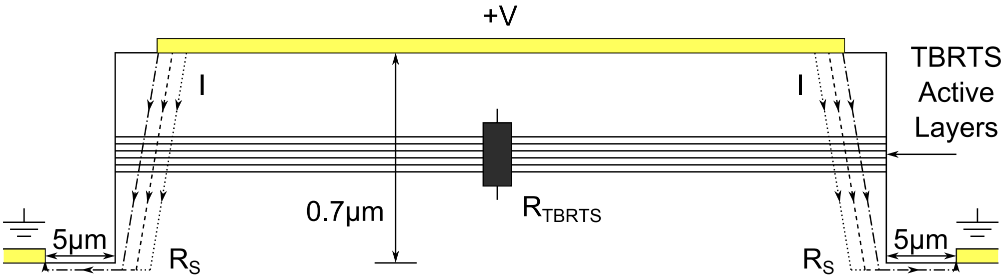

FIGURE 4.43: An illustration of a TBRTS device under a positive bias V. The current flows from the top contact through the TBRTS active layers, which has a resistance R_{TBRTS} to the bottom contact which is 5 μm from the bottom of the mesa edge. The resistance associated with the GaAs layers (all layers excluding the TBRTS active layers) is given by R_S, which varies and is dependent on the path taken by the current (i.e. the long path, the higher resistance)

.

When the device is off resonance the TBRTS active layers are high resistance and so it is R_{TBRTS} which dominates and is the limiting resistance to the current i.e. the current spreads more evenly across the entire area of the mesa as the variations in R_S by taking a longer path are small compared to R_{TBRTS}. However, when the device is on resonance the TBRTS active layers are transparent and so the resistance is much lower. In this situation the series resistance dominates and so the majority of the current flows via the path of least resistance, i.e. where there is the shortest path. Since the bottom contact surrounds the mesa then the shortest path is down the perimeter of the mesa and directly to the bottom contact.

To visualise this effect a simple model has been created of which the results are shown in figures 4.44(a) to 4.44(f). The model simply assumes that the series resistance between a point on the top of the mesa and nearest bottom contact, R_S is proportional to the distance between those two points, whilst the TBRTS active layer resistance R_{TBRTS} is

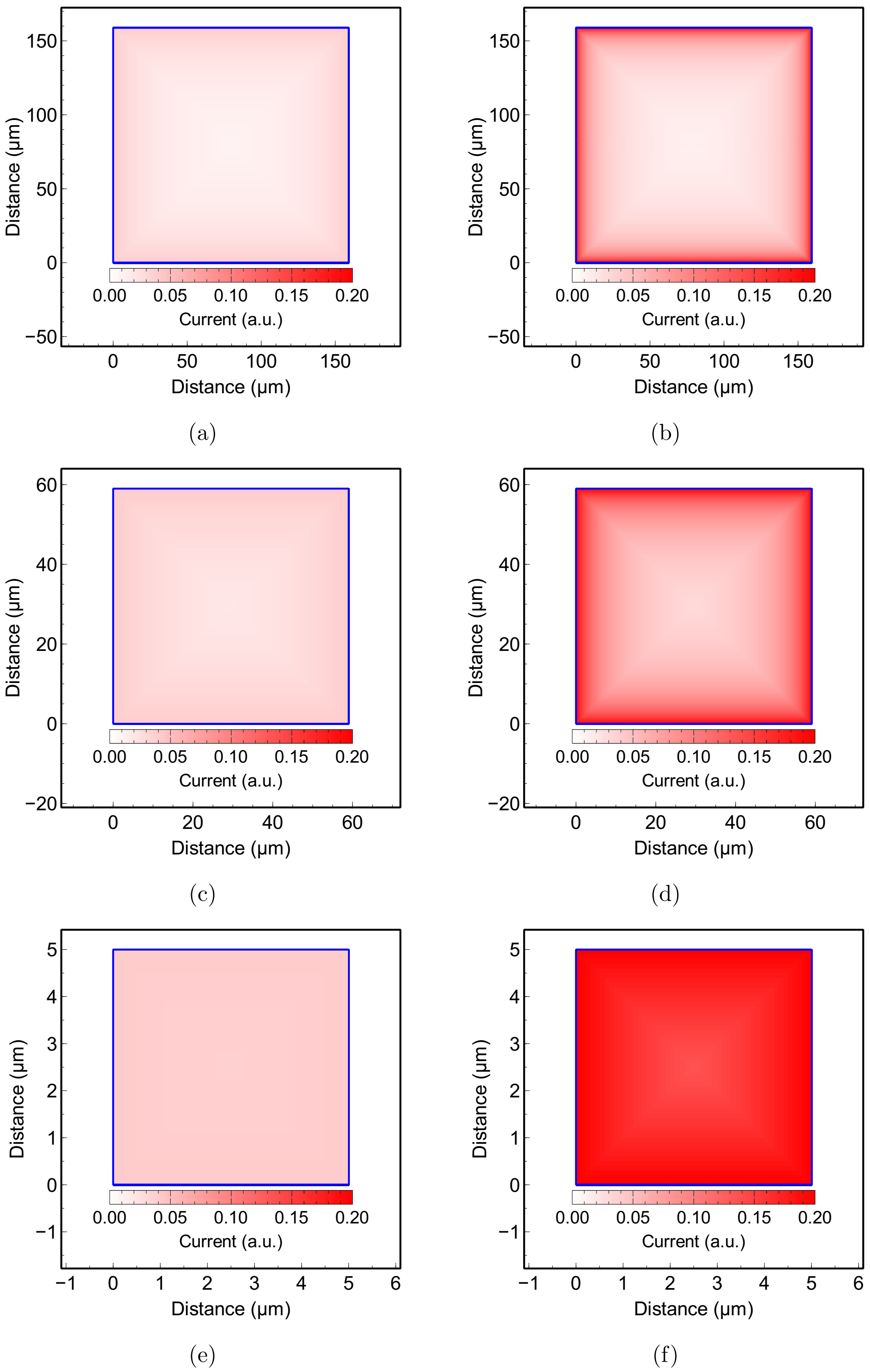

(a) (b)

(c) (d)

(e) (f)

FIGURE 4.44: The simulated current distribution in arbitrary units for TBRTS devices which are off resonance (a) 159 x 159 μm (c) 59 x 59 μm (e) 5 x 5 μm. The simulated current distribution for on resonance TBRTS are also shown for (b) 159 x 159 μm (d) 59 x 59 μm (f) 5 x 5 μm devices.

constant across the entire mesa (high when off resonance, low when on resonance). A simple calculation of the total resistance for each point, $R_T = R_S + R_{TBRTS}$ and the fact that the total resistance is inversely proportional to current allows for the calculation of an arbitrary current for each point on the mesa area.

Figures 4.44(a), 4.44(c) and 4.44(e) show that when the device is off resonance, the current is very uniform across the entire mesa area, as observed from experimental results where the non-resonant current is area dominated. Whilst figures 4.44(b), 4.44(d) and 4.44(f) clearly show that when the device is on resonance, the current is not uniform across the entire mesa area but localised to the mesa perimeter where the path of least resistance is, which again agrees with the experimental data given in figure 4.42(a). The inconclusive nature of the results from feature F3 in figures 4.41(a) and 4.41(a) where there is no clear linear dependence of the current with area or perimeter can also be explained from the these simple considerations.

Where the feature F3 is attributed to the energetic alignment of a single confined quantum well state with the conduction band edge, resulting in an increase in transparency of the TBRTS active region, it is not as significant as the increase in transparency of the feature studied in VMBE 787. The coincidental alignment of the quantum well states with each other and the conduction band edge results in a much larger increase in transparency than the feature F3 and so the reduction in resistance associated with the active region, R_{TBRTS}, is much more significant in VMBE 787 than VMBE 755. The current is therefore much more perimeter dominated in VMBE 787 than VBME 755 where the current is not dominated by perimeter or area which suggests the series and TBRTS active region contributions to the total resistance of the device are similar in magnitude.

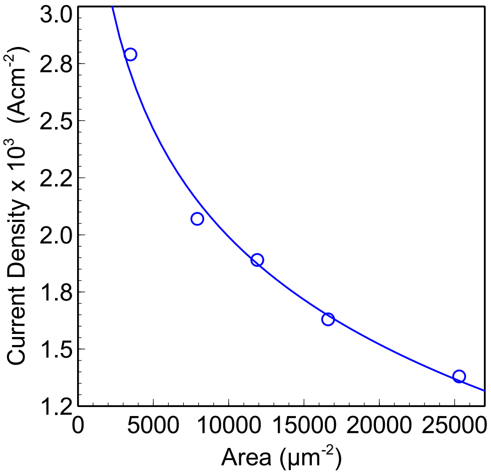

FIGURE 4.45: The peak areal current density against mesa area for VMBE 787, the most asymmetric structure. With decreasing mesa area the maximum current density increases due to the current path distribution becoming more uniform over the full mesa area as explained by the model in figures 4.43 and 4.44.

The origin of the increase in current density (Acm^{-2}) with reduction in mesa area seen in figures 4.41(b) and 4.42(b) is shown against mesa area in figure 4.45 and can also be explained by this model. For large devices the majority of current flows within a set distance (which depends on the conductivity of the semiconducting spacer and doped layers) from the perimeter of the device and hence the average areal current density is low as the majority of the device area is not conducting. If the dimensions of the mesa are reduced then the highly conductive region within the set distance of the perimeter remains fixed but the area of the less conducting material reduces which leads to an increase in the ratio of the highly conducting material to the less conducting material and hence the average areal current density increases. The areal current density will continue to increase with further reduction in mesa size until it plateaus as the maximum path length from the top to the bottom contact approaches the electron mean free path, beyond which there there is no further increase in current density.

4.7 Device Self Heating and Charge Accumulation

In sections 4.4 to 4.6 it has been shown that throughout the range of the varying quantum well asymmetry triple barrier resonant tunnelling structures there are regions of charge accumulation and high power dissipation in their respective I(V) characteristics. To investigate if a time-scale for any charging behaviour could be established and whether the power dissipation within the TBRTS resulted in any self heating effects a series of pulsed voltage measurements were performed.

As described in section 3.2.2 the *Agilent Technologies* B1505A Power Device Analyzer/-Curve Tracer mainframe was used to provide voltage pulses of pulse widths 500μs and a pulse period (the time from the start of one pulse to the start of the next) of 5 ms, resulting in a 10% duty cycle. Between each pulse the base voltage was held at 0.0V to allow for any accumulated charge to escape and the sample to cool should there be any self heating affects. Pulsed I(V) characteristics were taken for the 60 μm nominally symmetric TBRTS, where the charge accumulation is most pronounced, and for the most asymmetric structure, which had the highest power dissipation and compared to continuous wave (CW) measurements.

Figures 4.46(a) and 4.46(b) show the CW I(V) characteristics (solid black), with the pulsed voltage I(V) characteristics (dotted red) overlayed for the nominally symmetric and most asymmetric TBRTS respectively. The difference between the pulsed and CW measurement currents, ΔI are also shown (green solid line) from which it can be seen for both VMBE 755 and VMBE 787 that although there are no large differences there are some small variations in the currents measured. These variations, where the pulsed voltage current is greater than the CW current, suggest a slight reduction in the device

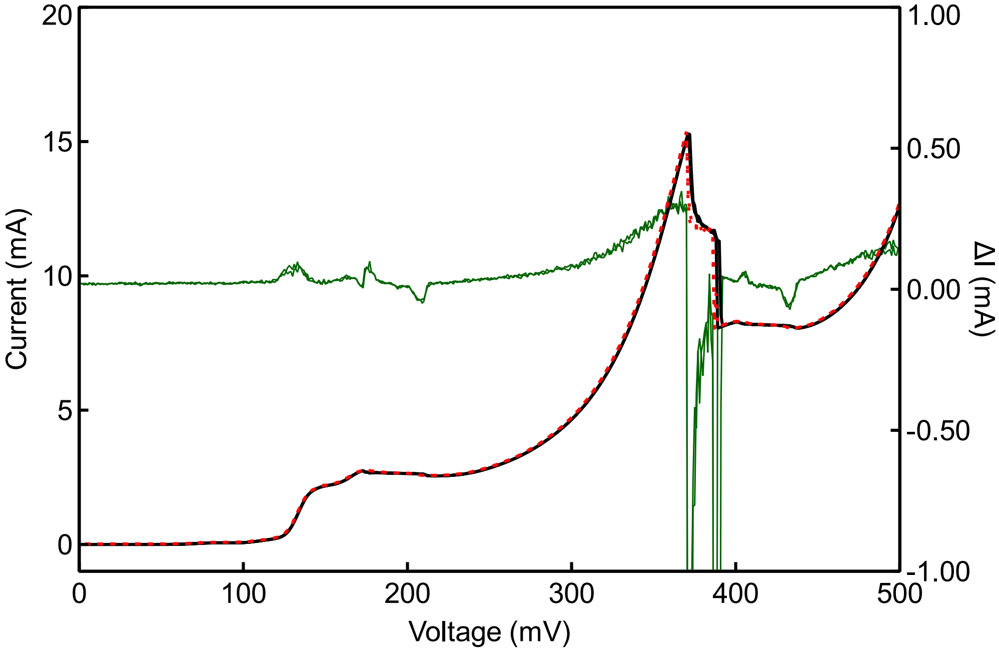

(a)

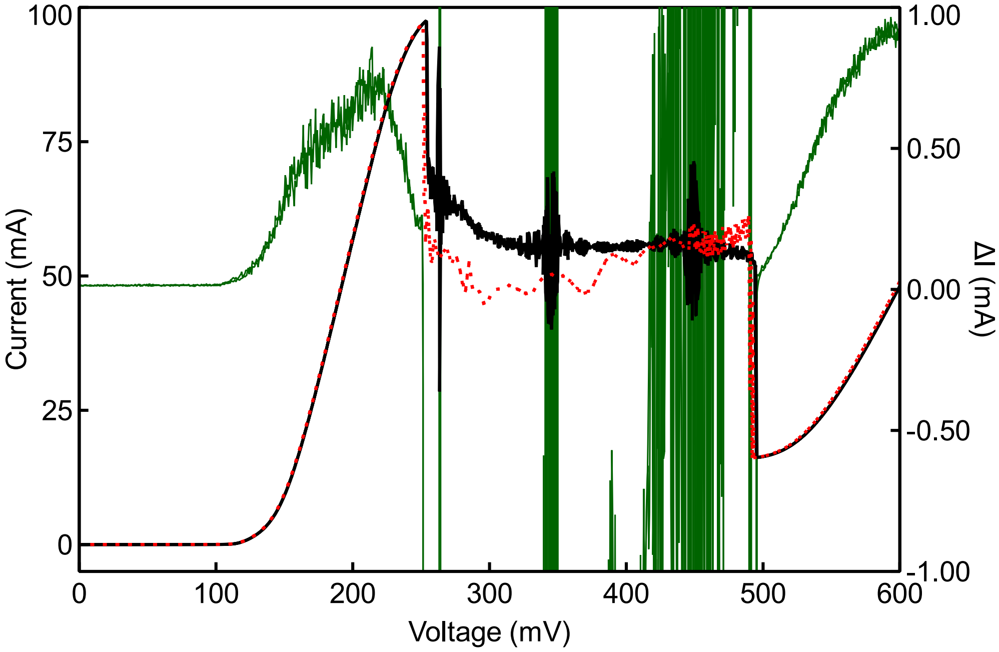

(b)

FIGURE 4.46: The continuous wave (CW) (solid black) and pulsed voltage (dotted red) I(V) characteristics at 3K for (a) the nominally symmetric TBRTS and (b) the most asymmetric TBRTS. The calculated difference between the puled voltage and CW current for each structure is also shown (solid green), focusing on regions of the I(V) characteristic where the device is in a stable (non NDR) state.

(and series combination) resistance and are of greatest magnitude at the current resonances where the power dissipation is considerable. However, these variations between the CW and pulsed voltage measurements only result in approximately 1-2% change in the overall current, which indicates that any self-heating effects in these devices are minimal and so have little affect on the device characteristics.

There also appears to be little difference in the I(V) characteristics in the regions of applied voltage ($\approx$ 200 mV to 350 mV for VMBE 755) which are attributed to charge accumulation in the emitter quantum well. From this it can only be concluded that any charging affects in these devices are on a faster time scale than 500 μs and for any further I(V) investigation of these charge affects a system capable of examining the device characteristics on a much smaller time scale is required.

4.8 Summary

In this chapter a series of triple barrier resonant tunnelling structures (TBRTS) have been studied at low temperature. The main differences between double barrier tunnelling structures and triple barrier tunnelling structures have been explained and the importance of series resistance on device measurement illustrated. The forward and reverse bias I(V) characteristics of a nominally symmetric TBRTS has been studied, with several current resonances observed.

A simple linear voltage drop model has been developed and utilised to predict and confirm the origin of the current resonances which have been attributed to the coincidental energetic alignment of the quasi-bound quantum well states with the emitter conduction band edge. A more complex model using the WinGreen modelling package has also been utilised to explain the shape of the I(V) characteristic at low temperature and the affect of charge accumulation in the emitter quantum well.

Triple barrier resonant tunnelling structures with varying collector quantum well widths have also been investigated. Predictions of a merging of the individual current resonances observed in the nominally symmetric structure with increasing quantum well width asymmetry have been compared with experimental data and it has been found that in the most asymmetric structure studied an extremely large single resonance is observed.

The peak to valley current ratio for each of the TBRTS devices for the different current resonances has been calculated and perimeter versus area analysis for square devices of varying mesa areas has been conducted. From this study it has been found that the off resonance valley current is an area dominated process, whilst the on resonance peak current flows via the device perimeter, which was unexpected. A simple model has been developed to explain this result and this behaviour is attributed to non-uniform current distribution when the triple barrier structure is highly transparent (on resonance) caused by the comparatively large resistivity of the doped contact epitaxy layer.

The affect of device self heating due to the high current densities has been explored and found to have a negligible affect on device performance, whilst it has been determined that the charge accumulation in the emitter quantum well occurs on a much shorter time scale than is examinable with short voltage pulses.

Bibliography

[1] L. Esaki and R. Tsu. ‘Superlattice and Negative Differential Conductivity in Semiconductors’. In: *IBM Journal of Research and Development* 14.1 (Jan. 1970), pp. 61–65. ISSN: 0018-8646. DOI: `10.1147/rd.141.0061`.

[2] R. Tsu and L. Esaki. ‘Tunneling in a finite superlattice’. In: *Applied Physics Letters* 22.11 (1973), pp. 562–564. DOI: `http://dx.doi.org/10.1063/1.1654509`.

[3] Yuji Ando and Tomohiro Itoh. ‘Calculation of transmission tunneling current across arbitrary potential barriers’. In: *Journal of Applied Physics* 61.4 (1987), pp. 1497–1502. DOI: `http://dx.doi.org/10.1063/1.338082`.

[4] Amitabh Chandra and Lester F. Eastman. ‘Quantum mechanical reflection at triangular ’planar-doped’ potential barriers for transistors’. In: *Journal of Applied Physics* 53.12 (1982), pp. 9165–9169. DOI: `http://dx.doi.org/10.1063/1.330428`.

[5] K.H. Gundlach. ‘Zur berechnung des tunnelstroms durch eine trapezformige potentialstufe’. In: *Solid-State Electronics* 9.10 (1966), pp. 949–957. ISSN: 0038-1101. DOI: `http://dx.doi.org/10.1016/0038-1101(66)90071-2`.

[6] D.N. Christodoulides, A.G. Andreou, R.I. Joseph and C.R. Westgate. ‘Analytical calculation of the quantum-mechanical transmission coefficient for a triangular, planar-doped potential barrier’. In: *Solid-State Electronics* 28.8 (1985), pp. 821–822. ISSN: 0038-1101. DOI: `http://dx.doi.org/10.1016/0038-1101(85)90069-3`.

[7] Wayne W. Lui and Masao Fukuma. ‘Exact solution of the Schrodinger equation across an arbitrary one-dimensional piecewise-linear potential barrier’. In: *Journal of Applied Physics* 60.5 (1986), pp. 1555–1559. DOI: `http://dx.doi.org/10.1063/1.337788`.

[8] J. Faist, F. Capasso, D.L. Sivco, C. Sirtori, A.L. Hutchinson and A.Y. Cho. ‘Quantum cascade laser’. In: *Science* 264.5158 (1994), pp. 553–556.

[9] A. D. Martin, M. L. F. Lerch, P. E. Simmonds and L. Eaves. ‘Observation of intrinsic tristability in a resonant tunneling structure’. In: *Applied Physics Letters* 64.10 (1994), pp. 1248–1250. DOI: `http://dx.doi.org/10.1063/1.110854`.

[10] Thomas P. Pearsall, Federico Capasso, Robert E. Nahory, Martin A. Pollack and James R. Chelikowsky. 'The band structure dependence of impact ionization by hot carriers in semiconductors: GaAs'. In: *Solid-State Electronics* 21.1 (1978), pp. 297–302. DOI: http://dx.doi.org/10.1016/0038-1101(78)90151-X.

[11] *https://www.hs-rm.de/en/faculty-of-engineering/about-us/people/personen-im-fb-ing/michael-indlekofer/research-and-development/nanoelectronics/index.html.* URL. Hochschule RheinMain, University of Applied Sciences, Faculty of Engineering, 2015.

[12] P.D. Buckle, P. Dawson, C.Y. Kuo, A.H. Roberts, W.S. Truscott, M. Lynch and M. Missous. 'Charge accumulation in GaAs/AIGaAs triple barrier resonant tunneling structures'. In: *Journal of Applied Physics* 83.2 (1998), pp. 882–887.

Chapter 5

Thermally Activated Resonant Tunnelling in Triple Barrier Structures

For real world applications devices which require expensive and bulky cryogenic cooling systems for routine operation are nigh on impossible to integrate into the miniature nature of today's existing technology. As such, the widespread commercialisation and application of triple barrier resonant tunnelling structure (TBRTS) devices beyond those of specialist equipment requires that the devices have the capacity to operate reliably and efficiently at and above room temperature.

Chapter 4 describes the study of the electrical properties of a series of seven GaAs/AlGaAs TBRTS with varying degrees of quantum well asymmetry at low temperatures (3K). In this chapter a study of the TBRTS over a large temperature range from 3K to 293K is presented and builds on work published in [1]. The nature of a thermally activated resonant tunnelling feature observed in the current-voltage I(V) characteristics of these devices is explored where the thermally activated feature increases in magnitude with increasing sample temperature. This is rare behaviour in systems where quantum mechanics dominates and may prove useful for practical applications of tunnelling devices at high temperature.

The details of the measurement technique, variable temperature measurement system, sample structure and device fabrication can be found in chapter 3.

5.1 Thermally Activated Resonant Tunnelling - Symmetric Structure

In this section the nominally symmetric triple barrier resonant tunnelling structure, VMBE 755, current-voltage (I(V)) characteristics from 3K to 293K are presented. Figures 5.1(a) and 5.1(b) show the I(V) characteristic for the nominally symmetric structure, VMBE 755, at various temperatures from 3K to 293K. The low temperature characteristics remain very similar to the 3K characteristic, however once the sample temperature is raised to 103K a new resonant feature, F0 has emerged in the very low bias (<20 mV) region. This feature exhibits a region of negative differential resistance and associated time-averaged oscillation which is characteristic of a resonant tunnelling process and continues to increase in magnitude as the sample temperature is raised further, with the feature still clearly discernible at 293K.

The increase in tunnelling current with increasing temperature is extremely interesting and quite rare behaviour in systems which are dominated by quantum mechanical affects. As can be seen from figure 5.1(a) the features identified in section 4.4, (F1, F2 and F3) all exhibit the opposite behaviour, reducing in strength and becoming enveloped in a background current of exponential form as the sample temperature is increased. The behaviour of feature F0 is therefore quite unique and so hints at an origin other than the energetic alignment of the quantum well confined states with the conduction band edge for which have been attributed to features F1, F2 and F3 previously.

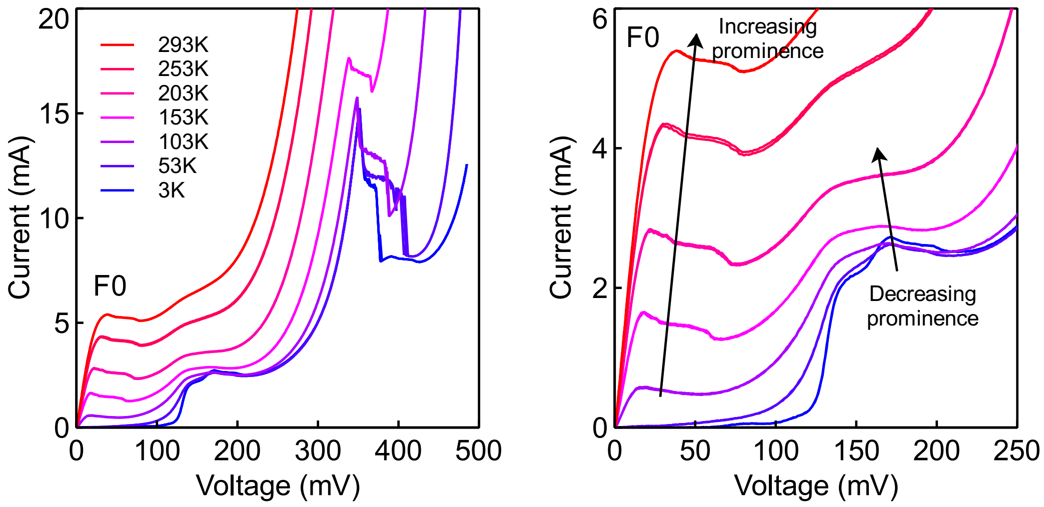

(a) (b)

FIGURE 5.1: The positive bias, forward and backward direction, current-voltage characteristic for a 60 μm x 60 μm nominally symmetric TBRTS at various temperatures (only every 50K shown for clarity). A resonant feature which is not visible at low temperatures, F0, emerges as the sample temperature is increased. (b) An enlarged plot of the emerging resonant feature which exhibits a region of negative differential resistance which is still discernible at 293K.

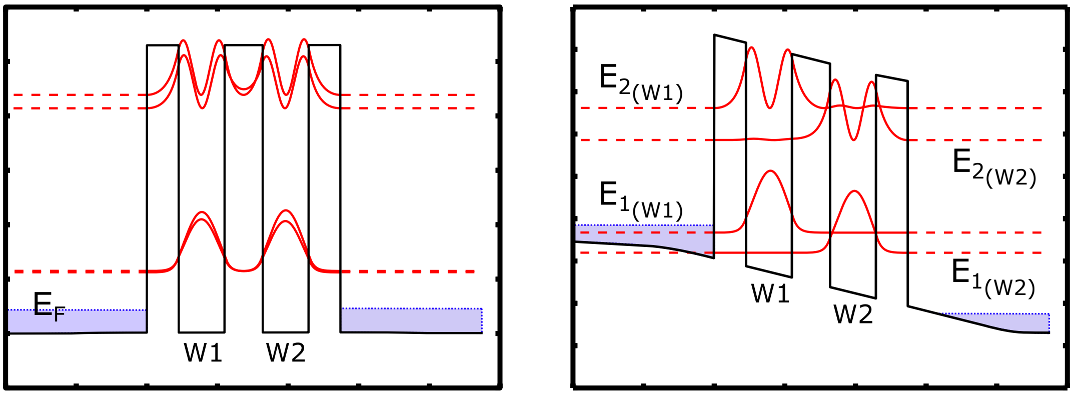

(a)

(b)

FIGURE 5.2: (a) A schematic of the conduction band potential profile for a totally symmetric TBRTS under zero bias. The electron probability density is also shown (red) and is equally distributed between each of the quantum wells (W1 and W2) and extends across the entire structure, resulting in a high tunnelling probability for charge carriers at these energies. (b) A schematic of the conduction band potential profile for a totally symmetric TBRTS with voltage applied across the device. The electron probability distribution is now localised to a specific quantum well, which dramatically decreases the tunnelling probability of charge carriers at each of the specific quantum well state energies.

If we consider a totally symmetric structure at zero bias then as illustrated in figure 5.2(a) the electron probability density is equally distributed between both the emitter and collector quantum wells (W1 and W2) forming a $n = 1$ subband which extends across the entire active region. When the quantum well states are not localised to a specific quantum well we take the states to be energetically aligned and so electrons which are incident on the emitter barrier whose energy are equal to that of the aligned quantum well states have a high theoretical probability of tunnelling through the TBRTS active region. Conventionally, to instigate net electron tunnelling a voltage must be applied across the structure, however in doing so the symmetry and alignment of the quantum well states is broken with the states becoming more localised to a specific quantum well resulting in a decrease in the overall tunnelling probability.

Figures 5.3(a) and 5.3(b) show the conduction band potential profile for a symmetric structure at zero bias along with the emitter electron distribution at various temperatures. At low temperatures it can be seen that there are very few electrons at energies equal to the energetically aligned quantum well states and so despite the high transmission probability no current flows. If however the sample temperature is raised then a significant number of electrons are promoted to energies equal to the $n = 1$ subband energies. On application of a very small forward bias, such that there is negligible perturbation in the alignment of the quantum well states then the electrons can tunnel through the TBRTS structure resulting in a net current flow. As the sample temperature is increased further then an increasing number of electrons are promoted to energies equal to the $n = 1$ subband and so the magnitude of the tunnelling current increases.

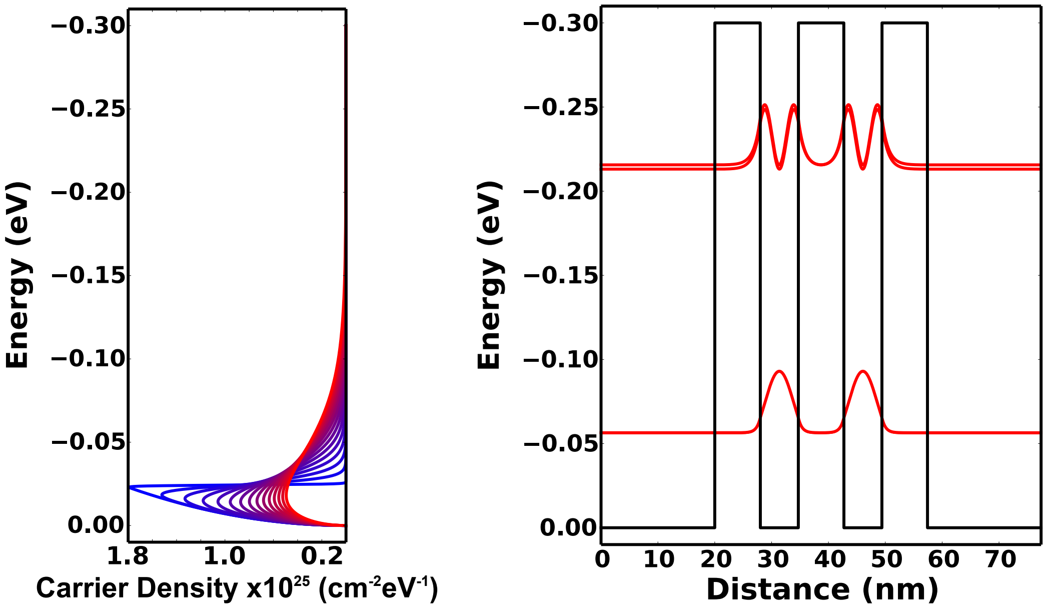

(a) (b)

FIGURE 5.3: (a) The 3D emitter carrier density distribution at various temperatures from 3K (blue) where there is a sharp, well defined distribution to 293K (red) where the carriers are now distributed over many different energies. (b) The conduction band potential profile for a totally symmetric triple barrier resonant tunnelling structure, the electron probability distribution (shown in red) is equally distributed between the emitter and collector quantum wells.

Increasing the bias across the device forces the quantum well states out of energetic alignment with each other and localises each state to a specific quantum well as shown in figure 5.2(b). This dramatically decreases the tunnelling probability through the structure and results in the region of negative differential resistance seen in figures 5.1(a) and 5.1(b). It is important to stress that this is very different behaviour to the conventional double barrier resonant tunnelling structure which remains transparent to an increasing number of electrons as the bias is increased and the quantum well state is moved lower in energy relative to the emitter electron distribution. As this behaviour is a result of the energetic alignment of two quantum well states then it is purely associated with multiple (≥ 3) barrier structures where the application of an electric field alters the transmission properties of the structure and not just the effective incident electron energies.

A reasonable estimate of the voltage required to energetically misalign the quantum well $n = 1$ subband states can be calculated from the broadening of the quantum well $n = 1$ subband using a simple transmission coefficient calculation by a transfer matrix method, as a function of energy based on the approach by Ando and Itoh [2]. The full-width half maximum of the $n = 1$ subband peaks were taken as the broadening of the states and the linear voltage drop model (described in section 4.4.1) applied to calculate the amount of bias required to misalign the states, which in the case of a completely symmetric TBRTS

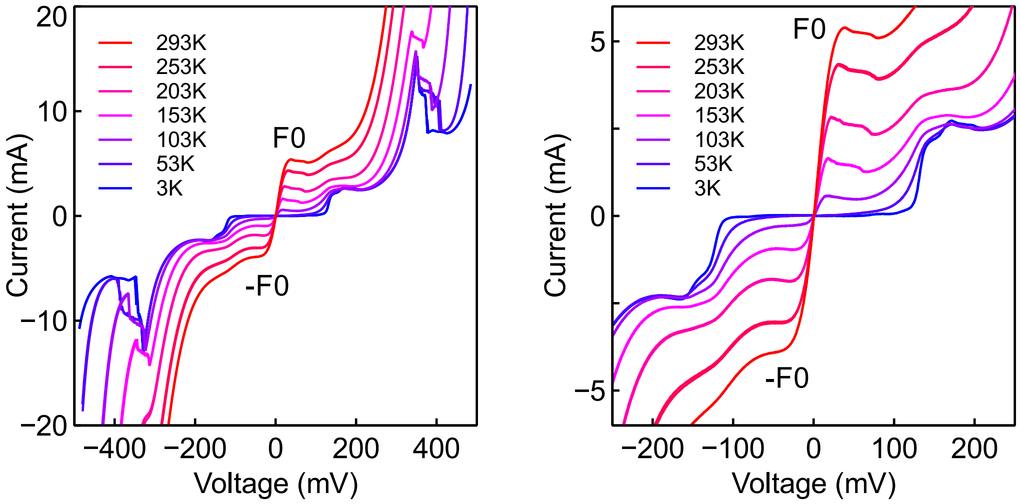

(a) (b)

FIGURE 5.4: The positive and negative bias, forward and backward direction, I(V) characteristic for a 60 μm x 60 μm nominally symmetric TBRTS at various temperatures (only every 50K shown for clarity). A resonant feature which is not visible at low temperatures, F0 (or -F0 in the negative bias direction), emerges as the sample temperature is increased. (b) An enlarged plot of the emerging resonant feature which exhibits a region of negative differential resistance which is still discernible at 293K.

was found to be 12.5 mV.

This gives reasonable agreement with what is observed in figure 5.1(b), however it is already known from photoluminescence (PL) and photoluminescence excitation (PLE) measurements of the quantum well widths (table 3.1) that there is a small degree of asymmetry in the quantum wells of the nominally symmetric structure. Therefore the amount of bias required to misalign the $n = 1$ subband states using these measured well widths is found to be 16.3 mV.

In the nominally symmetric structure the thermally activated current peak is seen in the forward and reverse bias as shown in figures 5.4(a) and 5.4(b), but is stronger in the positive bias direction. This observation agrees with the measured quantum well widths (table 3.1), as in the forward bias direction it is the narrower quantum well, B, which is the collector well. As this quantum well is narrower, its associated confined states are at a slightly higher energy than that of the emitter quantum well and so a small positive voltage must be applied across the structure to completely align the $n = 1$ subband states. This can be seen in the I(V) characteristic shown in figure 5.4(b) where the peak of the thermally activated resonant feature (F0) is at a slightly higher voltage and current in the positive bias direction, than in the negative bias direction (-F0).

As the triple barrier resonant tunnelling structure is very transparent at energies equal to those of the energetically aligned quantum well states then the device current is significant at extremely low bias. Combining this with the nature of the dramatic decrease in tunnelling probability with the application of further bias to misalign the quantum well

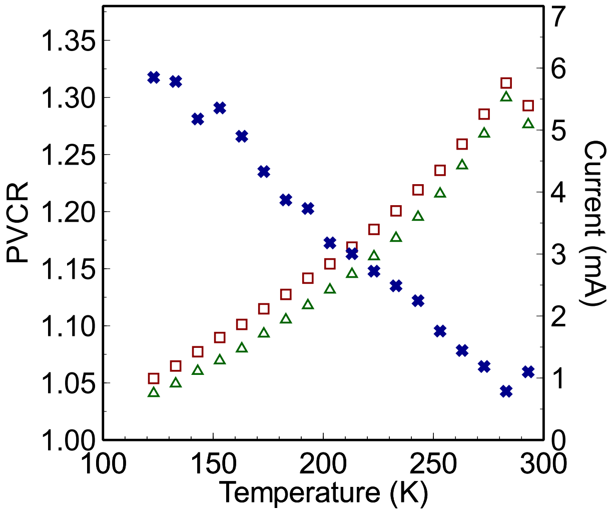

FIGURE 5.5: The extracted peak (red squares) and valley (green triangles) currents from the series resistance adjusted I(V) characteristic for the nominally symmetric TBRTS at various temperatures. The calculated peak-to-valley current ratio (PVCR) is also shown (solid blue crosses).

.

states results in a resonance of this nature having the potential for a large peak-to-valley current ratio.

Figure 5.5 shows the extracted peak and valley currents for the nominally symmetric TBRTS between 121K and 293K, where the maximum peak and minimum valley currents are clearly discernible. The peak and valley current both increase with increasing temperature almost proportionally, therefore the calculated peak-to-valley ratio, which is also shown, for the thermally activated resonance decreases with increasing temperature. Although this resonant alignment condition has the potential to produce a current resonance with a large peak to valley ratio, the valley current (as well as the peak current, as has already been shown) is highly dependent on the emitter electron distribution.

As previously discussed, the promotion of electrons to higher energies (figure 5.3(a)) with increasing temperatures results in an increasing number of electrons at energies equal to that of the highly transparent aligned quantum well states. However, this also results in an increased number of electrons with the ability to be transmitted through the active region via other mechanisms, which with respect to the aligned $n = 1$ quantum well states are leakage mechanisms. Some potential leakage mechanism which are likely to contribute to the valley current are:

i) Tunnelling through the now misaligned $n = 1$ states, which although has much less probability of occurring than when the states are aligned, still remains significant due to the large number of electrons available at the correct energy.

ii) Tunnelling through the $n = 2$ quantum well states, which are still partially aligned, and therefore have a large tunnelling probability*.

iii) Electrons which have sufficient energy may pass completely over the top of the potential barriers.

5.2 Thermally Activated Resonant Tunnelling - Asymmetric Quantum Well Structures

In section 5.1 a thermally activated current resonance, which increased in magnitude with increasing temperature was identified in the I(V) characteristic of the nominally symmetric triple barrier resonant tunnelling structure. In the following section the I(V) characteristics for the series of seven TBRTS with varying degrees of quantum well asymmetry are presented over a range of temperatures from 3K to 293K.

The thermally activated resonant tunnelling current peak described in section 5.1 assumes that the $n = 1$ quantum well states are energetically aligned at zero bias, which for a nominally symmetric structure is true (figure 5.2(a)). However in an asymmetric structure where the quantum wells are different widths this is not the case as, shown in figure 5.6(a). For an asymmetric structure, where one quantum well is narrower than the other, the narrower well confined states are at a higher energy, which in the infinite

---

*The partial alignment of the $n = 2$ states after the $n = 1$ states have misaligned is illustrated in figure 4.9 and caused due to the increased broadening in energy of these states as they are less well confined

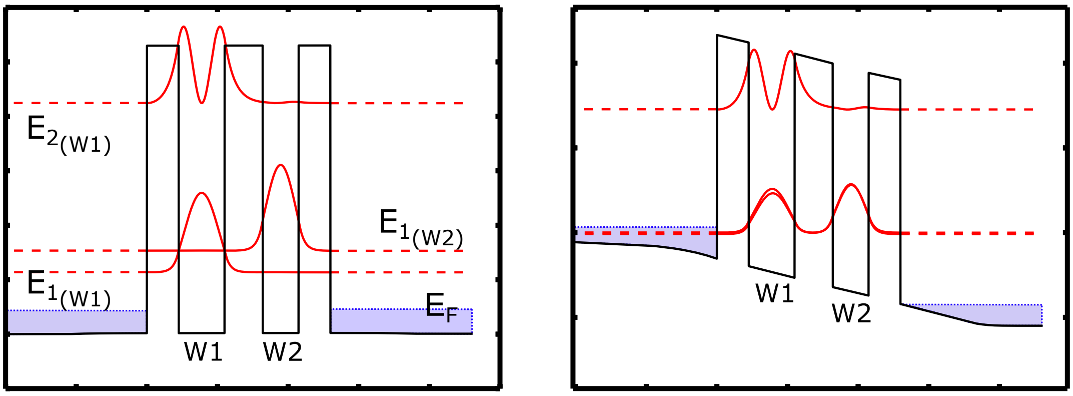

(a) (b)

FIGURE 5.6: (a) A schematic of the conduction band potential profile for a asymmetric TBRTS under zero bias. The electron probability density is also shown (red) and is localised to a specific quantum well (W1 or W2) (b) A schematic of the conduction band potential profile for an asymmetric TBRTS with voltage applied across the device which is sufficient to energetically align the quantum well confined states and form an $n = 1$ subband. The electron probability distribution extends across the entire structure resulting in a high transmission probability for charge carriers energetically aligned to this subband.

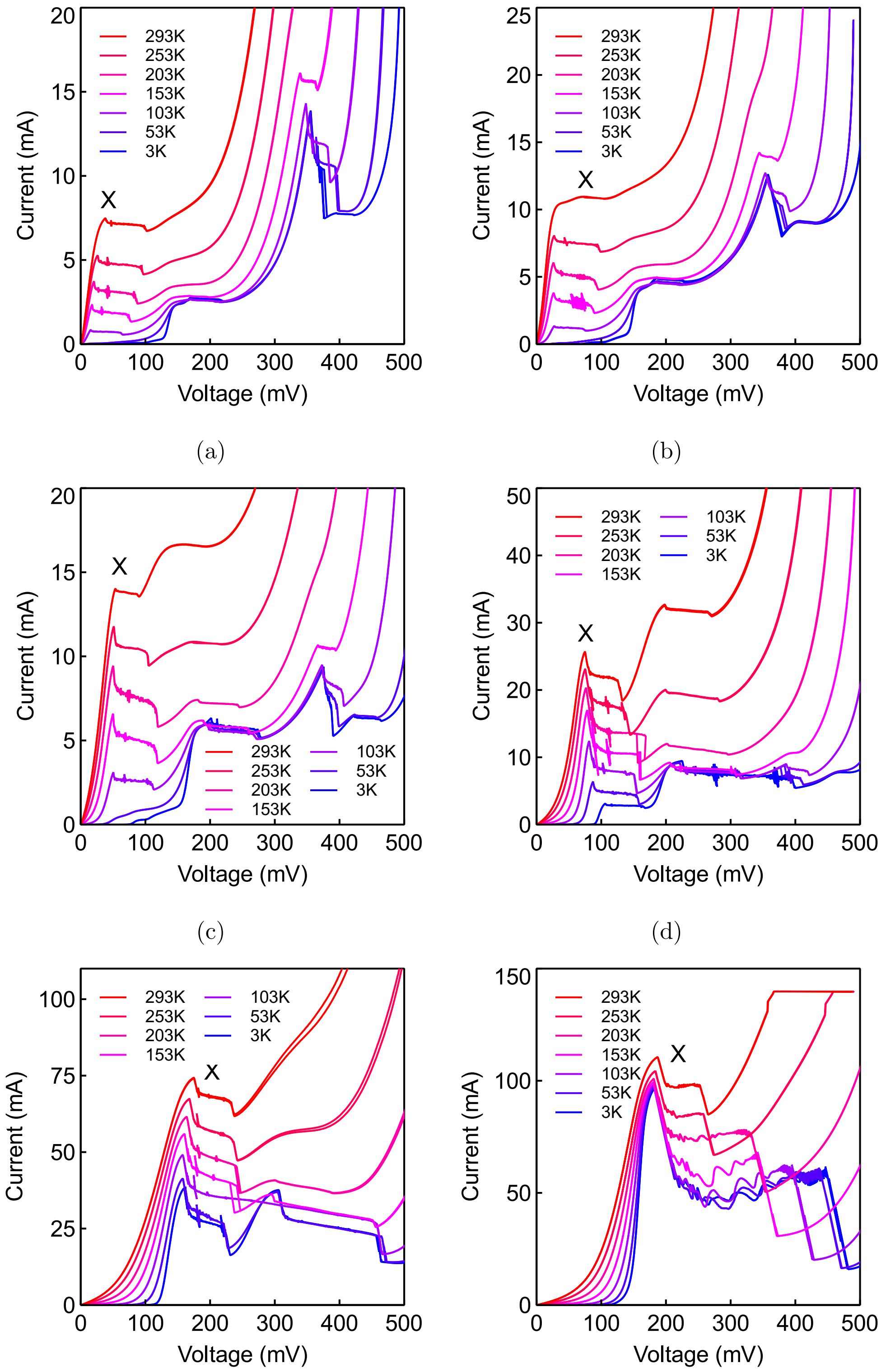

(a)

(b)

(c)

(d)

(e)

(f)

FIGURE 5.7: The positive bias, forward and backwards direction I(V) characteristics at various temperatures for the series of asymmetric TBRTS: (a) VMBE 757, (b) VMBE 760, (c) VMBE 761, (d) VMBE 762, (e) VMBE 788, (f) VMBE 787. The thermally activated resonance is indicated by the label X.

well approximation is given by equation (4.3).

Therefore in order to energetically align the $n = 1$ states of an asymmetric triple barrier resonant tunnelling structure an appropriate voltage must be applied across the device, as illustrated in figure 5.6(b). The amount of bias required is dependent on the difference in energy between the two localised $n = 1$ states and so increases with increasing quantum well asymmetry where the collector quantum well is narrower than the emitter quantum well. However, if the emitter quantum well is narrower than the collector quantum well, i.e. in the negative bias direction, then the $n = 1$ localised states of the emitter and collector quantum wells never align.

Figures 5.7(a) to 5.7(f) show the I(V) characteristics of the six asymmetric VMBE samples in increasing degree of quantum well asymmetry. In the low quantum well asymmetry structures (figures 5.7(a) and 5.7(b)) as in the nominally symmetric structure, a current resonance feature which is not present at low temperature appears as the sample temperature is raised and continues to increase in magnitude with increasing temperature.

Figure 5.7(c) shows the I(V) characteristic for VMBE 761, which has a quantum well ratio of 1.172. As the temperature of this sample increases the temperature dependent current peak once again emerges, however in this structure it appears to emerge from, or near, a feature which is observed at 3K. This is further emphasised in figure 5.7(d) which clearly shows that in this structure the temperature dependent current peak is an enhancement of the first large resonance observed in the I(V) characteristics at 3K and is also observed in the most asymmetric structures shown in figures 5.7(e) and 5.7(f).

In this thesis the application mainly considered for these devices is high frequency emitters. However, it is interesting to note that due to the highly non-linear nature of the current with voltage at the temperature dependent resonance peak, these structures may also have applications as high-frequency receivers. The detected power, P, can be expressed (in the case of a 50 Ω load) as [3]:

$$P = \frac{1}{50}\left[\frac{\frac{A^2}{4}f^{(2)}(V_{\text{Bias}}) + \frac{A^4}{64}f^{(4)}(V_{\text{Bias}})}{f^{(1)}}\right]^2 \tag{5.1}$$

where $f(V)$ is the I(V) characteristic, $f^{(1)}$, $f^{(2)}$, $f^{(4)}$ the derivatives of $f(V)$ with respect to V and A is the input radio frequency (RF) voltage which is applied to the resonant tunnelling diode.

Therefore from equation (5.1) it can be seen that a large second differential, $f^{(2)}$, is beneficial for device responsivity. Thus the sharp energetic misalignment of the $n = 1$ subband states, which causes the sharp drop in tunnelling current associated with the temperature dependent resonance, as can be seen in figures 5.7(a) to 5.7(f), may warrant further investigation. The study of these devices as potential receivers, or transceivers, where the resonant tunnelling structure operates as both emitter and receiver is not continued in this thesis, however further information on such devices can be found in [3, 4].

5.2.1 Resonant Current Temperature Dependence

The enhancement of the resonance feature with temperature and magnitude of the peak and valley currents for each sample appear to vary with quantum well asymmetry. The temperature dependence of peak and valley currents and peak-to-valley current ratio of the thermally activated current resonance for the series of asymmetric quantum well structures and the nominally symmetric structure are shown in figures 5.8(a) and 5.8(b) respectively.

The thermally activated resonance peak current is plotted on a logarithmic scale against increasing temperature for the series of VMBE triple barrier resonant tunnelling structures and it can be seen that with increasing quantum well asymmetry the peak current increases across the entire temperature range. There is a significant difference between the peak current of the nominally symmetric and most asymmetric structure resonance at some temperatures, with a difference of over three decades observed.

To understand this dramatic increase in peak resonance current we must consider that the triple barrier structure is at its most transparent, with a transmission probability

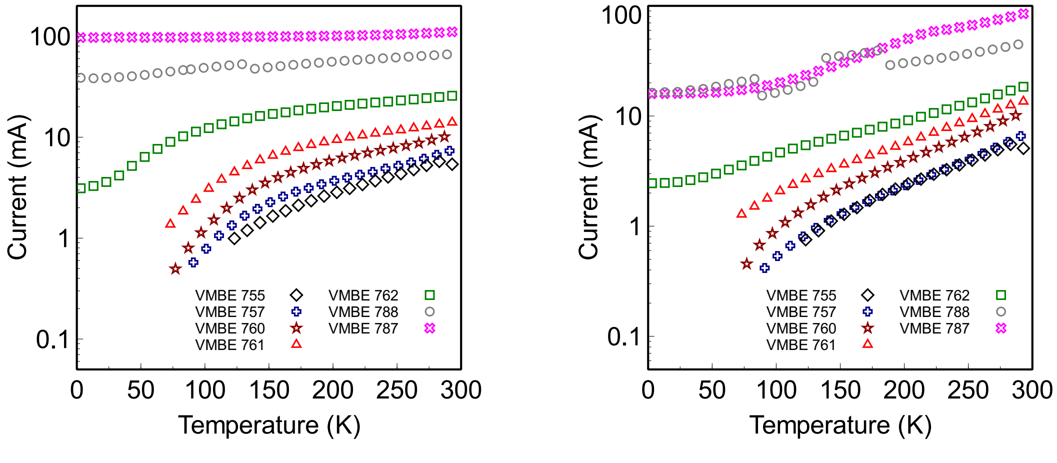

(a) (b)

FIGURE 5.8: (a) The thermally activated $n = 1$ subband critical alignment resonance peak current with increasing temperature for the range of seven VMBE TBRTS samples. (b) The thermally activated $n = 1$ subband critical alignment resonance valley current with increasing temperature for the range of seven VMBE TBRTS samples. The discontinuities in VMBE 788 are due to a sudden switch in the voltage at which the valley current occurs, shown in figure 5.10(b) with the origin of the switch still unclear at the time of writing.

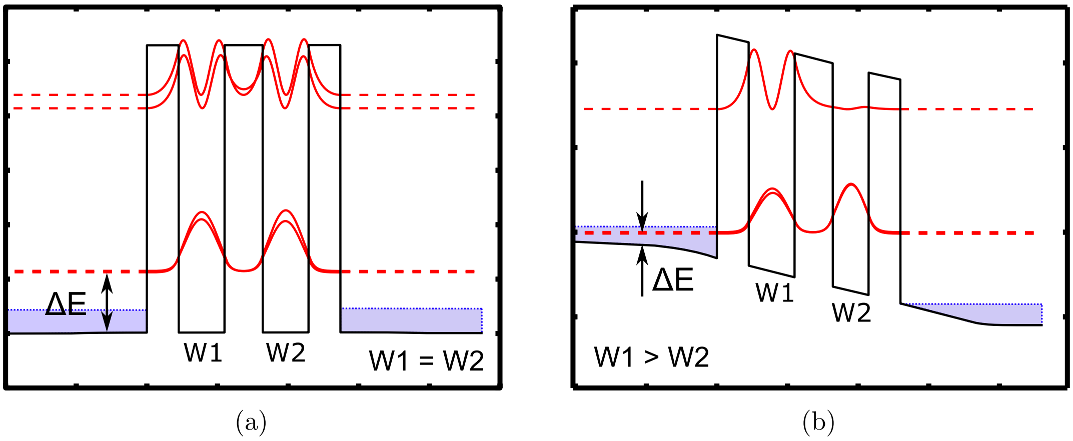

(a) (b)

Figure 5.9: (a) A schematic of the conduction band potential profile for a symmetric TBRTS under zero bias showing the energy difference between the $n = 1$ subband and the conduction band edge, ΔE and the probability density of the confined states (red). (b) A schematic of the conduction band potential profile for an asymmetric TBRTS with voltage applied across the device which is sufficient to energetically align the quantum well confined states and form an $n = 1$ subband. The energy difference between the $n = 1$ subband and the conduction band edge is less than in (a) due to the bias required to align the quantum well states.

very close to one at the confined state energies when the $n = 1$ subband quantum well states are energetically aligned. As this alignment occurs under the correct amount of bias in each of the TBRTS studied then the increase in magnitude of the peak resonance current is not specifically due to any differences in the alignments between the $n = 1$ subband in structure, and therefore must be due to $n = 1$ subband alignment relative to the emitter charge carrier distribution.

As has previously been discussed, the bias required to energetically align the $n = 1$ confined quantum well states with each other increases as the quantum well asymmetry increases and therefore with more bias across the device the critical $n = 1$ subband alignment occurs at lower energies relative to the conduction band edge. The difference in energy, ΔE between the $n = 1$ subband and the conduction band edge therefore reduces with increasing quantum well asymmetry and is illustrated in figures 5.9(a) and 5.9(b). For a degenerately doped TBRTS, where the Fermi Energy, E_F is within the conduction band (as the emitter and collector regions of the series of VMBE samples are) even at 0K the electron states at the bottom of the conduction band are occupied. Therefore at low temperature if the $n = 1$ subband energetic alignment occurs close to, or below the Fermi Energy then there are a large number of electrons readily available to tunnel through the aligned subband states, thus creating a large current resonance.

At this resonance peak the current is large for the highly asymmetric structures, increasing the bias across the structure to misalign the $n = 1$ subband states and localise them to a specific quantum well should result in the TBRTS becoming more opaque and so a much lower valley current in comparison to the peak. This can be seen in figure 5.8(b), where

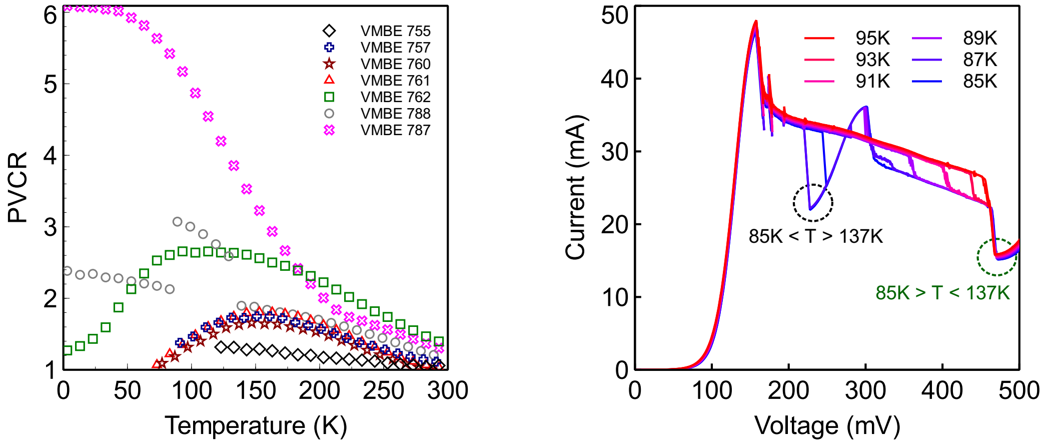

(a) (b)

FIGURE 5.10: (a) The calculated peak-to-valley ratio against sample temperature for the series of TBRTS with varying quantum well asymmetry. The discontinuity observed in the PVCR for VMBE 788 is a result of a sharp change in valley current voltage, which results in a lower valley current and is shown in figure 5.10(b). (b) The I(V) characteristic for VMBE 788 between 85K and 95K with characteristics for every 2K shown. At temperatures 85K and below, and 135K and above the valley current for the resonance is located at approximately 230 mV. A shift in the valley current voltage out to approximately 470 mV occurs between 87K and 133K where there are no longer two distinct resonances, as the NDR region merges across both.

for the most asymmetric structure, VMBE 787 there is a significant difference between the peak and valley currents.

The calculated peak-to-valley current ratio of the thermally activated resonant tunnelling peak for each of the triple barrier tunnelling structures is shown in figure 5.10(a) where it can be seen there is a general trend of increasing PVCR with structure asymmetry.

The PVCR for VMBE 787 remains relatively high at temperatures up to ≈ 100K in comparison to the less asymmetric TBRTS, which hints at a resonance which, with some optimisation, may lead to a high room temperature PVCR. Interestingly however, the second highest PVCR is not displayed by the second most asymmetric structure VMBE 788, but by VMBE 762, which has a moderate degree of quantum well asymmetry. This is thought to be due to the difference between the conduction band potential profiles at the bias of the valley current of the two samples. The valley current for the most asymmetric structure is measured at a bias of ≈ 480 mV, whereas the valley current for VMBE 762 occurs at ≈ 230 mV. As the most asymmetric structure is under much higher bias, the potential barriers on the collector side of the active region are much lower in energy compared to those of VMBE 762, resulting in a higher transmission probability at energies approaching the top of the potential barriers for VMBE 787 than VMBE 762. Therefore as the sample temperature increases the dependency of the leakage valley current on temperature for each structure also differs and is much stronger for the most asymmetric structure, thus resulting in a larger growth in leakage valley current (and hence lower PVCR) with increasing temperature for VMBE 787. However, with optimisation of the TBRTS design such that the critical $n = 1$ subband energetic alignment occurs and is coincident with the electron distribution, but at a lower bias, this effect can be reduced.

The maximum PVCR for each structure is plotted against quantum well asymmetry and shown in figure 5.11 where a linear fit to the maximum PVCR gives good agreement for the majority of the TBRTS devices below a quantum well width ratio of 1.425, however interestingly there is a dramatic increase in the maximum PVCR for the most asymmetric structure, which rises to a PVCR of ≈ 6. In the lower asymmetry structures, the first resonance peak, F0, is attributed to the critical $n = 1$ subband alignment, and there is a clear valley associated with this resonance. However, as the quantum well asymmetry increases the valley current begins to merge with the feature F2-2 which is attributed to the formation of a two-dimensional emitter, and as such the valley current for the resonance increases.

In the most asymmetric structure however only a single large resonance with a single NDR region is observed in the I(V) characteristics. It is also worth noting that the valley current voltage has shifted from approximately 230 mV in VMBE 788 to approximately 480 mV (at 3K) for VMBE 787 and as such the associated resonance valley current is much lower. This switch between two valley current voltages is also observed in the I(V) characteristic of VBME 788 between 85K and 95K, and is shown in figure 5.10(b). Thus the valley current for VMBE 787 and between 83K and 137K for VMBE 788 is more accurately described as the valley current of the combined current resonances than the

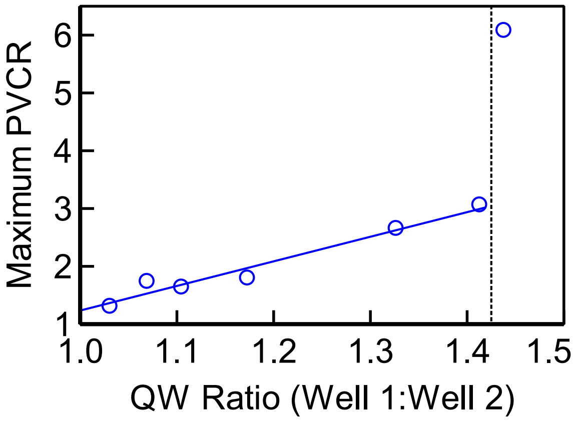

FIGURE 5.11: The maximum peak-to-valley current ratio (PVCR) against ratio of quantum well widths (Emitter:Collector) which is a measure of the asymmetry of the triple barrier resonant tunnelling structures. Below a QW ratio of 1.425 there is a good fit to linear function for the maximum PVCR, however for the most asymmetric structure which has a QW ratio of 1.4375 this point no longer fits the trend as there is a dramatic increase in PVCR.

.

valley associated with the feature F0. The origin of the switch in valley current voltage is discussed in section 6.2.3.

5.2.2 Critical Alignment Activation Energy

As previously explained in section 5.2.1, with increasing quantum well asymmetry the $n = 1$ subband energetic alignment occurs at energies closer to the Fermi Energy, $\mathrm{E_F}$, which is well defined at 3K. Therefore the energy required to promote electrons to energies equal to the $n = 1$ subband states also decreases and hence the thermally activated current resonance emerges in the I(V) characteristic at lower and lower temperatures with increasing quantum well asymmetry.
For a process which is dependent on temperature, Arrhenius plots are often used to analyse the effect of temperature and determine the activation energy, $\mathrm{E_a}$ of the process. The analysis is based on the assumption that the temperature dependencies of the semiconductor band gap, and Fermi level are linear over the temperature range. Therefore for the thermally activated resonance the activation energy, which is a measure of the amount of energy required to promote electrons from the Fermi Energy (which is a linear extrapolation to T = 0K, for more information see [5]) to the energetically aligned $n = 1$ subband states (figure 5.12), can be determined from Arrhenius plots governed by the Arrhenius equation:

$$\mathrm{I_{Peak}} = \mathrm{A}\exp\left(\frac{-\mathrm{E_a}}{\mathrm{K_b}}\frac{1}{\mathrm{T}}\right) \tag{5.2}$$

Where $\mathrm{I_{Peak}}$ is the thermally activated peak resonance current, $\mathrm{K_b}$ is the Boltzmann constant, T is temperature and A is a constant. Simple rearrangement results in,

$$\ln\left(\mathrm{I_{Peak}}\right) = \frac{-\mathrm{E_a}}{\mathrm{K_b}}\frac{1}{\mathrm{T}} + \ln\left(\mathrm{A}\right) \tag{5.3}$$

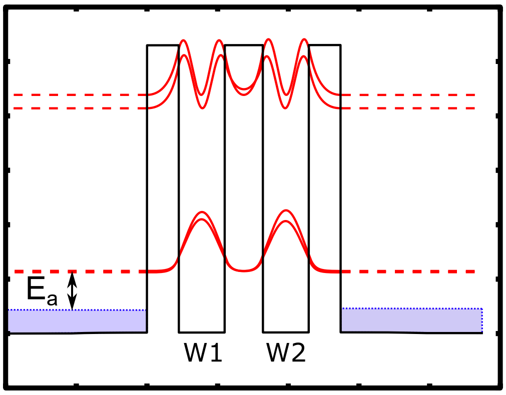

FIGURE 5.12: A conduction band potential schematic showing the critically aligned $n = 1$ subband quantum well states (red) and the activation energy, $\mathrm{E_a}$, which is the difference between the Fermi Energy and the energy of the $n = 1$ subband states.

and so a simple plot of $\ln\left(\mathrm{I_{Peak}}\right)$ against $\frac{1}{\mathrm{T}}$ yields $\frac{-\mathrm{E_a}}{\mathrm{K_b}}$ allowing for the extraction of the activation energy for each sample.

Figures 5.13(a) and 5.13(b) show the experimental and theoretical Arrhenius plots respectively for the critical $n = 1$ subband current resonance of the seven VMBE triple barrier resonant tunnelling structures between 83K and 250K, with only every 5th data point shown for clarity. Data is only plotted for this range as below 83K the $n = 1$ subband alignment is not discernible for several of the low quantum well asymmetry samples and above 250K leakage current associated with other thermally activated processes become more pronounced and cause deviations from a straight line fit.

The theoretical Arrhenius plots were generated by modelling and calculating the current density through the TBRTS under sufficient bias to critically align the $n = 1$ subband states and was done in two parts. Firstly a linear electric field was applied across the undoped spacers and active region of the structure, which is a good first approximation as at low bias the voltage is dropped predominately between the n+ contact layer and the δ-doped layer. For each potential profile Schrödinger's equation was solved within only the active region of the device and infinite potential barriers were assumed outside of this region. The quantum well confined state energy and wavefunction for each state was found and the bias increased until the $n = 1$ subband states were energetically aligned.

Secondly, at the bias required for energetic alignment the current density was calculated from the transmission coefficient (based on the method by Ando and Itoh [2]) via equation (5.4) formulated by Tsu and Esaki [6]:

$$J = \frac{em^* K_b T}{2\pi^2 \hbar^3} \int_0^\infty D(E,V) \ln \left(\frac{1 + \exp\left[\frac{(E_F - E)}{K_b T}\right]}{1 + \exp\left[\frac{(E_F - E - eV)}{K_b T}\right]} \right) dE \tag{5.4}$$

Where in the above expression e, m^*, K_b, T, $D(E,V)$, V, E_F and E are the electron charge, effective mass, Boltzmann constant, temperature, transmission coefficient, applied voltage, Fermi energy and Energy respectively.

The modelled tunnelling current Arrhenius plots produce good straight line fits for the lower asymmetry structures, however for the structures with higher asymmetry, and therefore where the energetic alignment of the $n = 1$ subband states occurs closer to the Fermi energy, the Arrhenius plots begin to curve. This is believed to be caused as at energies close to the Fermi energy the electron distribution is no longer Boltzmann like (which the Arrhenius plots assume) and therefore are no longer linear. In this situation it is the low temperature regions which are still most Boltzmann like and hence the linear fit gradients at these low temperatures are used for extraction of the activation energy for VMBE 762, VMBE 788 and VMBE 787.

From both the experimental and theoretical Arrhenius plot gradients it is clear to see

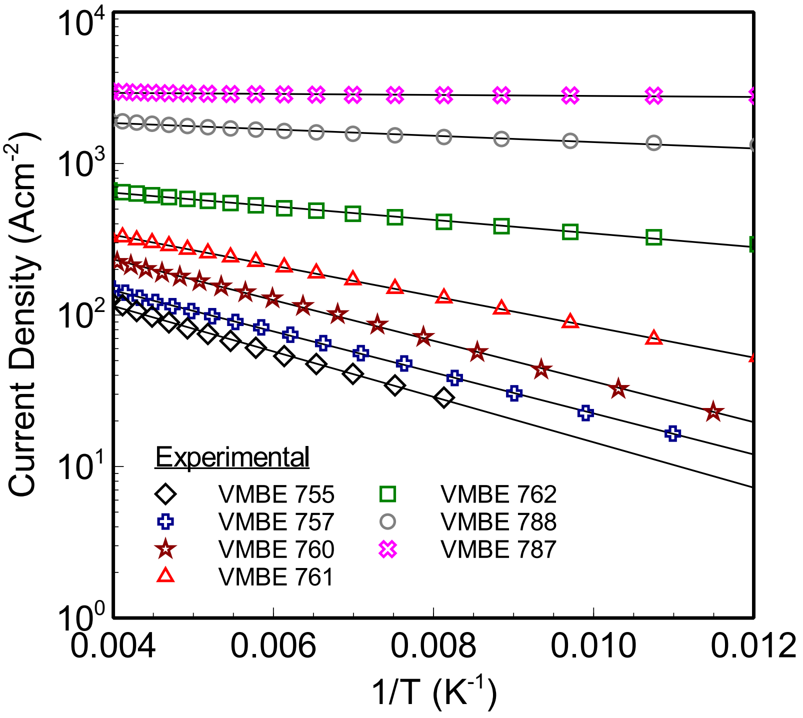

(a)

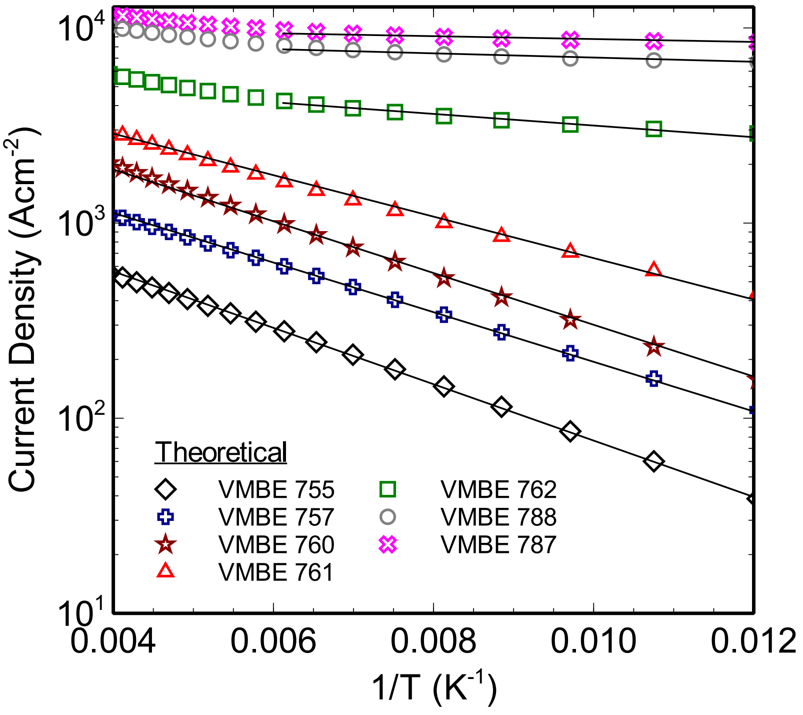

(b)

Figure 5.13: (a) The experimentally extracted Arrhenius plots for the series of seven VMBE TBRTS devices between 83K and 250K. Straight line fits to extract the gradient are made to each with the determined activation energies shown in figure 5.14. (b) The theoretically calculated Arrhenius plots for the series of seven VMBE TBRTS devices between 83K and 250K. Straight line fits to extract the gradient are made to each with the determined activation energies shown in figure 5.14.

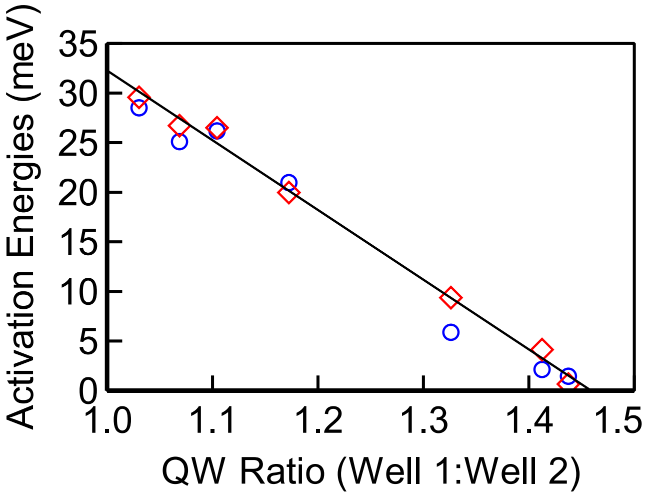

FIGURE 5.14: The experimentally determined (red diamonds) and theroretically calculated (blue circles) activation energies against quantum well width ratio (emitter:collector) for the $n = 1$ subband critical alignment current resonance. There is good agreement between the experimental and theoretical data with a straight line fit made to the experimental results.

that generally, as the collector quantum well width is reduced (and so there is increasing structure asymmetry) the activation energy decreases. The magnitude of the theoretically calculated current density is larger than that measured experimentally, however this is believed to be due to equation (5.4), which assumes the tunnelling current is only dependent on the longitudinal energy of the carriers. This therefore does not take into account the restrictions on tunnelling due to the matching of available k-states and so over estimates the total current through the modelled structure.

Plots of the extracted experimental and theoretical activation energies for each sample are plotted against quantum well width ratio in figure 5.14, with the theoretically determined values showing good agreement to the experimental results. There is a clear trend of decreasing activation energy with increasing quantum well asymmetry, with an activation energy of zero representing coincidental energetic alignment of the $n = 1$ subband and the Fermi Energy, which is nearly achieved in the most asymmetric structure.

5.3 Summary

In this chapter the temperature dependent current-voltage I(V) characteristics of a series of triple barrier resonant tunnelling structures between 3K and 293K (room temperature) have been investigated. With increasing temperature a resonance not observed at low temperatures emerges in the I(V) characteristic of the nominally symmetric structure. This feature is also observed in the series of asymmetric quantum well structures and increases in magnitude with increasing sample temperature.

This behaviour is rare in systems in which quantum mechanics dominates and is attributed to the energetic alignment of the quasi-bound $n = 1$ subband states. In the symmetric structure this alignment is broken with application of voltage across the structure and so is only observed at low voltages. However, with decreasing collector quantum well width and hence increasing confinement energy of the states in this well, this critical $n = 1$ alignment occurs at higher voltage and in closer proximity to the conduction band edge. A very large current resonance is observed once the $n = 1$ subband energetic alignment occurs coincidental with the conduction band edge and is the origin of the single resonance observed in the most asymmetric structure.

The activation energy of this critical $n = 1$ subband alignment has been extracted for each of the triple barrier resonant tunnelling structures studied and decreases with increasing sample quantum well asymmetry, where an activation energy of zero indicates coincidental energetic alignment of the $n = 1$ subband states and the Fermi energy. Theoretical activation energies have also been calculated from the calculated tunnelling current using the simple linear voltage drop model developed in chapter 4 and are in excellent agreement with the experimentally determined values.

Bibliography

[1] C P Allford, R E Legg, R A O'Donnell, P Dawson, M Missous and P D Buckle. 'Thermally activated resonant tunnelling in GaAs/AlGaAs triple barrier heterostructures'. In: *Semiconductor Science and Technology* 30.10 (2015), p. 105035.

[2] Yuji Ando and Tomohiro Itoh. 'Calculation of transmission tunneling current across arbitrary potential barriers'. In: *Journal of Applied Physics* 61.4 (1987), pp. 1497–1502. DOI: `http://dx.doi.org/10.1063/1.338082`.

[3] T Nagatsuma, M Fujita, Ai Kaku, D Tsuji, S Nakai, K Tsuruda and T Mukai. 'Terahertz wireless communications using resonant tunneling diodes as transmitters and receivers'. In: *Proc. Intern. Conf. Telecommunications and Remote Sensing (ICTRS 2014), Luxembourg*. Vol. 41. 2014.

[4] Tadao Nagatsuma. 'Terahertz communications technologies based on photonic and electronic approaches'. In: *European Wireless, 2012. EW. 18th European Wireless Conference*. VDE. 2012, pp. 1–4.

[5] P. Blood. *Quantum Confined Laser Devices: Optical Gain and Recombination in Semiconductors*. Oxford Master Series in Atomic, Optical, and Laser Physics. Oxford University Press, 2015. ISBN: 9780199644513.

[6] R. Tsu and L. Esaki. 'Tunneling in a finite superlattice'. In: *Applied Physics Letters* 22.11 (1973), pp. 562–564. DOI: `http://dx.doi.org/10.1063/1.1654509`.

Chapter 6

Triple Barrier Heterostructures for Terahertz Emitters

Terahertz radiation, which is also known as submillimeter radiation typically describes electromagnetic radiation with frequencies between 300 GHz and 10 THz [1]. Several optical and electronic devices have been developed to operate in this frequency range, but all suffer in general from low output power. They also tend to be substantial in size, and operate at undesirable low temperatures which results in such devices being incompatible for integration into modern electronic circuitry. The lack of a practical, compact and coherent THz radiation source has lead to the term “terahertz gap” [2] being used to describe this frequency range.

Whilst optical terahertz radiation sources are challenged by the difficulty in finding suitable low-energy band-to-band transitions, and the need for cryogenic cooling [3] to operate at these frequencies it is the carrier transit time which limits the operational frequency of many solid-state electronic devices [4]. Resonant tunnelling devices (RTDs) which exploit quantum mechanical tunnelling, which is inherently a fast process are therefore seen as promising candidates for compact, coherent terahertz emitters which will operate at room temperature. RTDs are widely recognised as the fastest solid-state electronic device with recent reports of measured THz emission of 1.55 THz [5].

The applications of THz radiation sources are numerous, such as enhanced security imaging [6] which exploits the unique “terahertz fingerprint” of many non-conducting materials, ultra-fast wireless communications for short-range high-capacity line of sight communication [7] and medical imaging techniques as THz waves, unlike x-rays are non-ionising and therefore do not damage biological tissue [8]. Therefore for this technology to be utilised across the many consumer applications, a cost-effective and scalable manufacturable process is a necessity and as such an electronics based approach is necessary.

6.1 Requirements for Terahertz Emission

In comparison to conventional electronic devices, the operational speed of resonant tunnelling devices (RTDs) is mainly governed by the tunnelling time through the structure, which in turn is dependent on the tunnelling probability through the structure, rather than a conventional transit-time. Therefore, as the active regions of tunnelling structure devices are very short then this lends itself to devices with very high cut-off frequencies, as tunnelling is inherently a fast process.

RTDs are therefore well suited to be exploited as high frequency oscillators due to the negative differential conductance regions exhibited in the current-voltage (I(V)) characteristics of such structures. This negative differential conductance allows the RTD to be used in a resonant circuit. The maximum oscillation frequency of an RTD, f_{MAX} is given by equation (6.1) [9] and based on the small-signal equivalent circuit of an RTD given by Brown et al. [10].

$$f_{\mathrm{MAX}} = \frac{1}{2\pi}\sqrt{\frac{1}{2L_{QW}^2 C_D}}\sqrt{2L_{QW} - \frac{C_D}{G^2} + \sqrt{\left[\left(\frac{C_D}{G^2} - 2L_{QW}\right)^2 - \frac{4L_{QW}(1+R_S G)}{R_S G}\right]}} \tag{6.1}$$

Where C_D is the space charge capacitance resulting from the charging and discharging effect of charge carriers within the device depletion regions, G is the negative differential conductance, R_S is the device series resistance which includes contact resistance, spreading resistance and the resistance of the emitter and collector regions. L_{QW} is known as the quantum inductance and represents the delay between the RTD current and the applied voltage caused by the finite time required for charge carriers to tunnel through the structure. The quantum inductance is given by,

$$L_{QW} = \frac{\tau_{\mathrm{rtd}}}{G} \tag{6.2}$$

where τ_{rtd} is the tunnelling time through the RTD structure. In situations where L_{QW} can be assumed to be negligibly small equation (6.1) reduces to [11]:

$$f_{\mathrm{MAX}} = \frac{1}{2\pi C_D}\sqrt{\frac{G}{R_S} - G^2} \tag{6.3}$$

Therefore to maximise the device oscillation frequency minimising the series resistance and parasitic capacitances whilst maximising the negative differential conductance is necessary, where the average negative differential conductance, G of a resonant peak can be calculated from,

$$G = \frac{\Delta I}{\Delta V} \tag{6.4}$$

where ΔI is the peak to valley current difference and ΔV is the peak to valley voltage difference.

The maximum power of a resonant tunnelling device with a static I(V) characteristic (i.e. in the steady state) which is represented by a cubic polynomial is given by [12]:

$$P_{\mathrm{MAX}} = \frac{3}{16}\Delta I \Delta V \tag{6.5}$$

However, the maximum RTD output power reduces with increasing frequency due to the intrinsic delay of the charge carriers travelling through the resonant tunnelling structure, τ_T, where,

$$\tau_T = \tau_{\mathrm{rtd}} + \frac{\tau_{\mathrm{dep}}}{2} \tag{6.6}$$

and τ_{dep} is the carrier transit time in the depletion region. This finite transit time reduces the negative conductance, G with increasing frequency and as such the frequency dependent maximum power output is given by [13]:

$$P_{\mathrm{MAX}}(f) = \frac{3}{16}\cos(\omega\tau_T)\Delta I \Delta V \tag{6.7}$$

Thus for high power output at high frequency a large negative differential conductance region (ΔI and ΔV) as well as a short device transit time are required.

It is also important to consider the power efficiency of the RTDs and since the output power of the device is related to the difference between the peak and valley voltages, ΔV and not the magnitude of the applied voltage itself then to minimise the wasted power, it is desirable for the current resonance peak to occur at a low voltage, whilst maintaining a large current.

6.2 GaAs/Al$_{0.33}$Ga$_{0.67}$As Triple Barrier Resonant Tunnelling Heterostructure Emitters

In this section the GaAs/Al$_{0.33}$Ga$_{0.67}$As triple barrier resonant tunnelling structure (TBRTS) devices described in chapter 3 and studied in detail in chapters 4 and 5 are examined for the purpose of being utilised as THz radiation sources. The whole series of seven nominally symmetric and asymmetric VMBE samples are studied with values for the calculated maximum oscillation frequency and frequency dependent power calculated for each device.

6.2.1 Negative Differential Conductance

As has been discussed in section 6.1 the average negative differential conductance of a current resonance peak can be calculated using equation (6.4). Figures 6.1 and 6.2 show the extracted peak to valley current (ΔI) and peak to valley voltages (ΔV) of the current resonance peak associated with the $n = 1$ critical subband alignment studied in chapter 5. The series of seven VMBE samples (from nominally symmetric to most asymmetric) are shown in these plots, with the $n = 1$ resonance chosen for analysis as it is still discernible at room temperature.

As expected for the triple barrier resonant tunnelling structures with a lower degree of quantum well asymmetry ΔI increases with increasing sample temperature between 3K and $\approx$ 200K which is due to the thermal promotion of charge carriers to energies equal to the energetically aligned $n = 1$ state (see chapter 5). With further increase in sample temperature ΔI then decreases due to the the enhancement of thermally activated background leakage current mechanisms (e.g. over the potential barrier transport).

For the structures with a higher degree of quantum well asymmetry (VMBE 762 and VMBE 788) the behaviour is similar, but for the most asymmetric structure, VMBE 787, where the $n = 1$ subband alignment is coincident with the Fermi level ΔI is significantly larger. The difference between the peak and valley current is a maximum at low temperatures, where the background leakage current is a minimum, but with increasing sample temperature this increases, whilst the peak current remains relatively stationary, thus

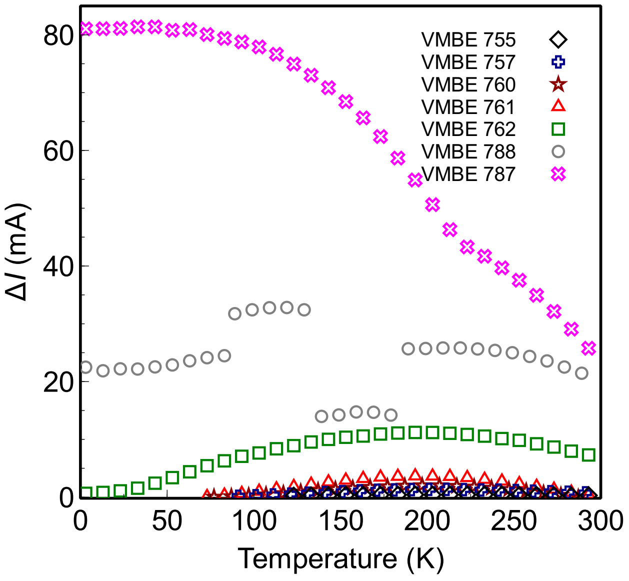

Figure 6.1: The extracted peak to valley current (ΔI) from the series resistance adjusted I(V) characteristics for the current resonance attributed to the $n = 1$ critical subband alignment for the series of VMBE TBRTS devices against sample temperature. Only every fifth data point is shown for clarity.

reducing ΔI with increasing temperature.

The discontinuities in the VMBE 788 data are attributed to sharp switches in valley voltage (and therefore current) which occur between 83K and 183K as previously mentioned in section 5.2.1. The origin of these transitions are discussed in section 6.2.3 along with the origin of what appears to be two regimes in the VMBE 787 data with a transition at ≈ 220K in figure 6.1.

Figure 6.2 shows the extracted peak to valley voltage, ΔV, from the series resistance adjusted I(V) characteristics for the series of seven VMBE TBRTS studied. At low temperatures the difference between the peak and valley voltage is large for the most asymmetric structure, and decreases with increasing temperature (as expected) due to an increase in the background leakage current. Again there are sharp transitions for VMBE 788 (between 83K and 137K) and VMBE 787 at ≈ 220K, and it also appears again there are two regimes for VMBE 787, with a switch occurring at ≈ 150K. These features are studied in more detail in section 6.2.3, but from figures 6.1 and 6.2 it is clear to see that VMBE 788 and VMBE 787 are the most promising candidates for a high average negative differential conductance.

The calculated average negative differential conductance from equation (6.4) for the series of VMBE TBRTS devices are shown in figure 6.3. Here it can be seen that for the two most asymmetric structures, VMBE 788 and VMBE 787, the mean negative conductance is far greater than the triple barrier resonant tunnelling structures with a lower degree of quantum well asymmetry. This therefore indicates that, as expected

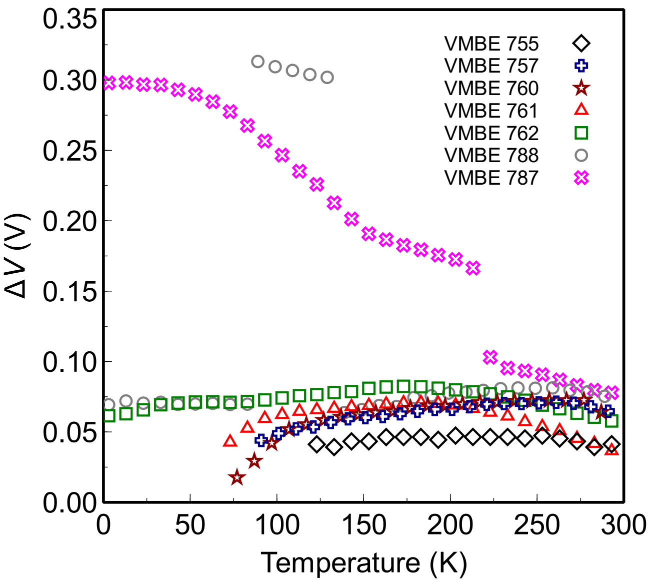

Figure 6.2: The extracted peak to valley voltage (ΔV) from the series resistance adjusted I(V) characteristics for the current resonance attributed to the $n = 1$ critical subband alignment for the series of VMBE TBRTS devices against sample temperature. Only every fifth data point is shown for clarity.

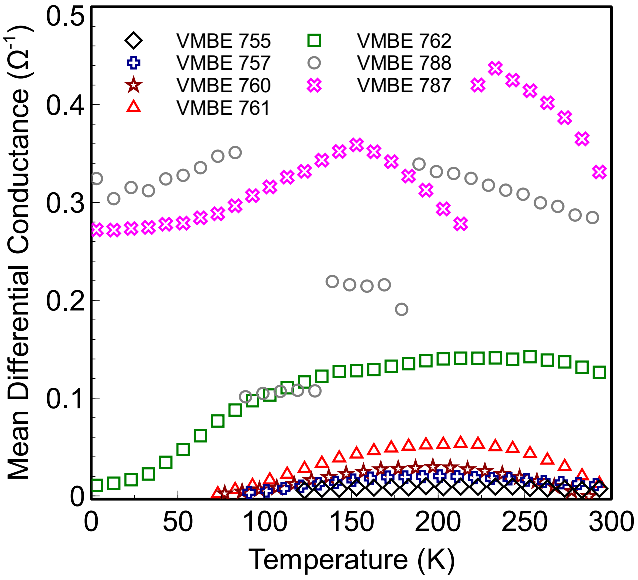

FIGURE 6.3: The calculated average negative differential conductance, G, using equation (6.4), plotted against sample temperature for the series of VMBE TBRTS devices. Only every fifth data point is shown for clarity.

the maximum frequency of oscillation (from equation (6.3)) is likely to be greater for the devices with the largest degree of quantum well asymmetry due to the large peak to valley currents exhibited. The maximum oscillation frequency of these two devices is calculated in section 6.2.3.

It is however, also interesting to note that despite exhibiting larger peak to valley current and voltage (ΔI and ΔV) values, at low temperatures the calculated mean negative differential conductance of the large single resonant peak observed in the I(V) characteristic of VMBE 787 is lower than that of VMBE 788.

6.2.2 Output Power

The calculated maximum output power for a resonant tunnelling device with a steady state I(V) characteristic is calculated from equation (6.5) and shown in figure 6.4 for the series of VMBE triple barrier resonant tunnelling structures against sample temperature. It is clear to see that in the steady state the maximum power of approximately 4.5 mW at low temperatures, emitted by the most asymmetric structure, VMBE 787 far exceeds those with a lower degree of asymmetry. The sharp discontinuity in the calculated maximum power for VMBE 788 is also quite significant, due to the large increase in both peak to valley current and peak to valley voltage observed in figures 6.1 and 6.2.

Although the calculated output power appears relatively large, the size of the mesa must be taken into account as large area devices suffer from excessive capacitance which decreases the maximum oscillation frequency (from equation (6.3)), which is discussed

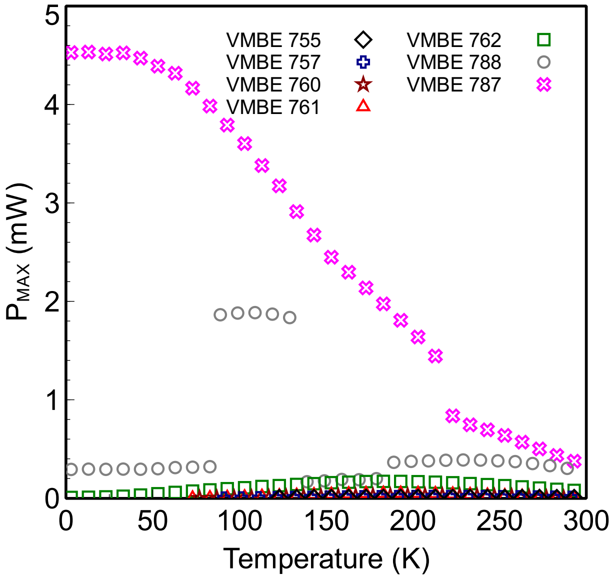

Figure 6.4: The calculated steady state maximum output power from equation (6.5) for the series of VMBE devices against sample temperature.

further in section 6.2.3. Figure 6.5 therefore shows the calculated maximum power density given the approximate mesa areas of the devices studied were ≈ 3480 μm^2. The extracted maximum output power density of ≈ 1.3 μWμm^{-2} falls well below that of the state of the art, optimised, InGaAs/AlAs double barrier resonant tunnelling structures which have a steady state power density of ≈ 0.62 mWμm^{-2} [14].

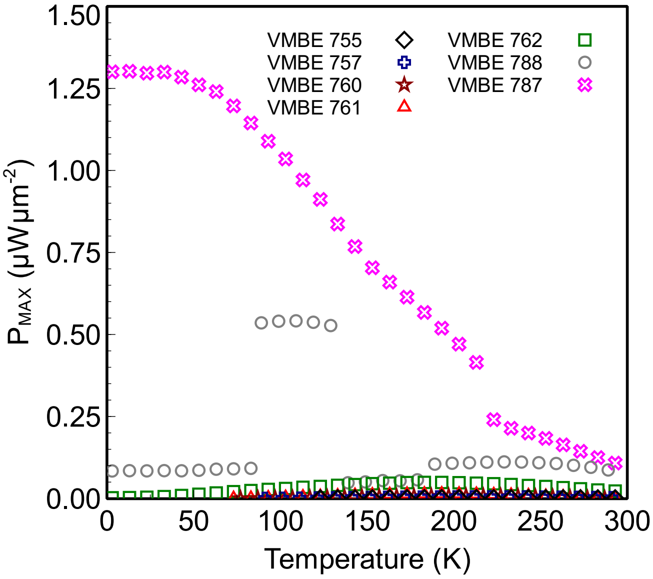

Figure 6.5: The maximum output power density against sample temperature calculated from equation (6.5) using values extracted from I(V) characteristics for series of VMBE devices with approximate mesa areas of 3480 μm^2.

6.2.3 Oscillation Frequency and Frequency Dependent Output Power

A theoretical maximum oscillation frequency for resonant tunnelling devices such as those studied in this thesis can be calculated from equation (6.3) provided that the quantum inductance, equation (6.2), is small. To calculate the maximum frequency f_{MAX}, the series resistance, R_S, device capacitance, C_D, and negative differential conductance, G, are also needed. Equation (6.4) has been used to calculate the average negative differential conductance (which has previously been shown in figure 6.3 and the temperature dependent series resistance for each device has been estimated from the series resistance adjustments made to the I(V) characteristics in section 4.6. The device capacitance, C_D for these structures has previously been estimated from the length of the depletion region. The capacitance was estimated to be 170 fF for a device with a mesa area of 100 μm^{-2} [15], thus the capacitance per unit area is found to be 1.7 fFμm^{-2}. However, as this is the device capacitance, then it is a worst case scenario value, and so practically with a reduction in device mesa area an improvement in oscillation frequency may be seen.

In section 6.2.2 the steady state maximum output power was calculated for the series of VMBE TBRTS devices. Although a useful value for comparison with the steady state power output of the state of the art InGaAs/AlAs double barrier structures, the actual output power of a device which is oscillating is given by equation (6.7) and is also dependent on that frequency of oscillation and the transit time of charge carriers through the structure, τ_T. Thus to calculate an estimated frequency dependent maximum output

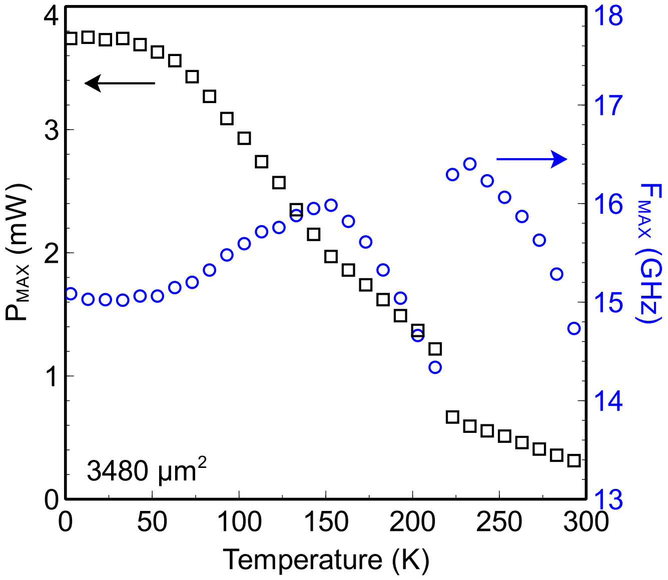

Figure 6.6: The calculated maximum oscillation frequency (blue circles) from equation (6.3) and frequency dependent maximum output power (black squares) from equation (6.7) for the most asymmetric TBRTS device, VMBE 787. The device has an active mesa area of ≈ 3480 μm^{-2}.

power an estimate of the tunnelling time, τ_{rtd} and the carrier transit time τ_{dep} in the depletion region (equation (6.6)) is required. The total carrier transit time for these structures was estimated to be $\approx$ 14 ps where τ_{rtd} was estimated from the full width at half maximum of the transmission coefficient through the TBRTS device and τ_{dep} calculated from the estimated length of the depletion region (from [15]) and the GaAs collector/emitter saturation velocity.

The calculated maximum oscillation frequency and maximum frequency dependent output power for the most asymmetric structure, VMBE 787, with a mesa area of $\approx$ 3480 μm^{-2} are shown in figure 6.6. The maximum calculated power at low temperatures remains relatively high in comparison to the steady state calculated power (figure 6.4) which, as expected decreases with increasing temperature due to the reduction in ΔI and ΔV as seen in figures 6.1 and 6.2.

The maximum oscillation frequency for these structures is calculated to vary between $\approx$ 14 GHz and $\approx$ 17 GHz depending on the sample temperature. Interestingly however there is an increase in the calculated maximum oscillation frequency with increasing sample temperature upto approximately 153K, at which point there is a definite change in the evolution of frequency with temperature. A sharp discontinuity is seen at approximately 220K where the calculated maximum oscillation frequency switches back to a higher value. These features are again attributed to those observed in figures 6.1 and 6.2 and as such the origin of these discontinuities are investigated here.

Figure 6.7 shows the peak to valley current difference, ΔI, for VMBE 787 with fits

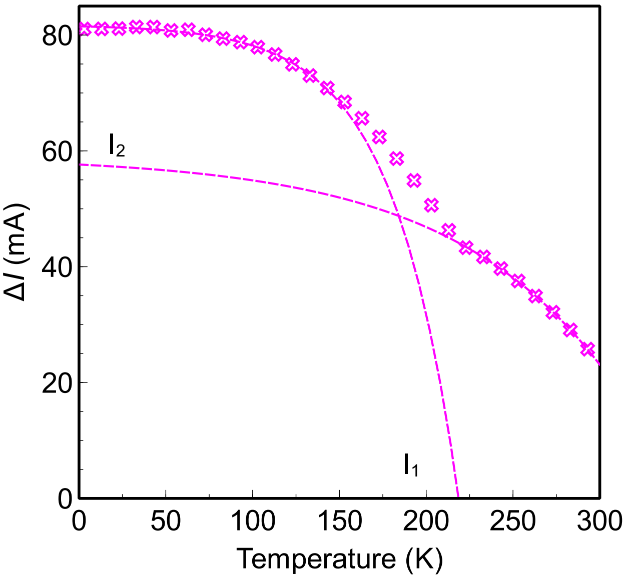

Figure 6.7: The extracted peak to valley current difference, ΔI, for the most asymmetric TBRTS, VMBE 787 for a device with mesa area $\approx$ 3480 μm^{-2}. Two clear regions with different dependency on temperature can be seen and exponential fits are made to both of these regions.

made to the two regions where the temperature dependence of ΔI differs. The low temperature fit, I_1 clearly shows a dependence in which ΔI reduces to zero by $\approx$ 220K, whilst the high temperature fit, I_2 albeit lower in magnitude than I_1 at low temperatures, remains present at room temperature. In the I(V) characteristics for VMBE 787 only one large current resonance is observed, which has an enhanced negative differential resistance region compared to that of VMBE 788 and less asymmetric structures, as previously shown in figure 4.30. Therefore given that the peak current magnitude and voltage remain relatively stationary with increasing sample temperature and it is the valley current that alters, figure 6.7 appears to indicate that the fits I_1 and I_2 trace the evolution of two separate valley currents, one which is hidden in the NDR region and only becomes visible with increasing sample temperature as the device transitions between the two.

Similar behaviour can be seen in figure 6.8 where there is a clear transition between the low temperature fit, V_1 which drops to zero at approximately 220K and the higher temperature fit V_2. The transition between the fits V_1 and V_2 occurs at $\approx$ 150K, which is the same temperature at which the fit measured data begins to deviate from the low temperature current fit, I_1. This indicates that between $\approx$ 150K and $\approx$ 220K the observed valley in the I(V) characteristic begins to transition, in current and voltage, between the initially observed valley and the “hidden valley”. The discontinuity in ΔV which occurs at $\approx$ 220K is coincident with the low temperature fits, I_1 and V_1 becoming zero and as such is due to the sharp switch in voltage to the “hidden valley” once the

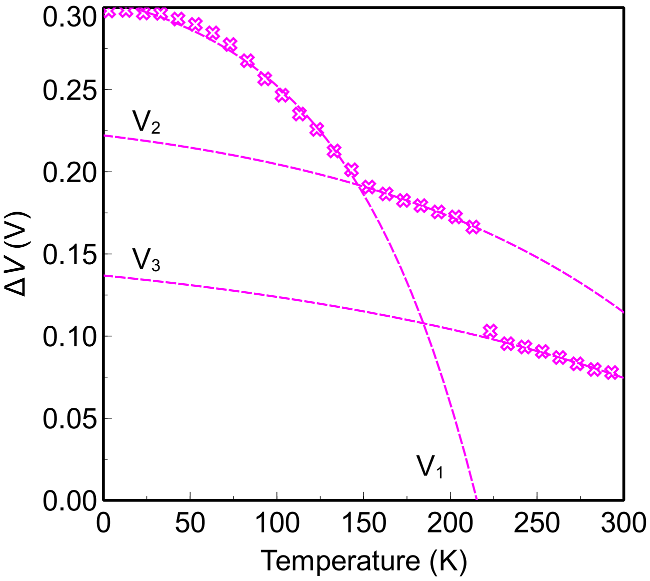

FIGURE 6.8: The extracted peak to valley voltage difference, ΔV, for the most asymmetric TBRTS, VMBE 787 for a device with mesa area $\approx$ 3480 $\mu\mathrm{m}^{-2}$. Two clear regions with different dependency on temperature can be seen and exponential fits are made to both of these regions. A fit to the high temperature region above the sharp discontinuity which can be seen is also made.

initially observed valley is overcome by the temperature dependent background leakage current.

Figure 6.9 shows the measured I(V) characteristics at 3K (solid blue) and 293K (solid red) for VMBE 787, with the position of the "hidden valley" indicated at 3K (red cross). In samples with a lower degree of quantum well asymmetry, such as VMBE 788, for which the I(V) characteristic is also shown in figure 6.9 (dashed blue) there are at least two resonance peaks observed, one attributed to the critical alignment of the $n = 1$ subband and the second, which appears at higher voltages attributed to the formation of a 2D emitter state and charge accumulation in the emitter quantum well. For VMBE 787 however, only one negative differential conductance region is observed which indicates that either a 2D emitter state does not form and so charge does not accumulate in the first quantum well in this structure, or that the magnitude of the $n = 1$ critical alignment resonant current is large enough and in close enough proximity to the charge accumulation resonance for the resonances to merge, thus resulting in a single NDR region, but with two distinctly different values of negative differential conductance (NDC).

Figure 6.9 shows the two regions of differing mean NDC, where a line has been drawn between the resonance peak current and the "hidden valley", G_1, and then from the "hidden valley" to the observed resonance valley, G_2. It can be seen that the gradients (and so mean NDC) of these two lines are distinctly different, thus suggesting that this

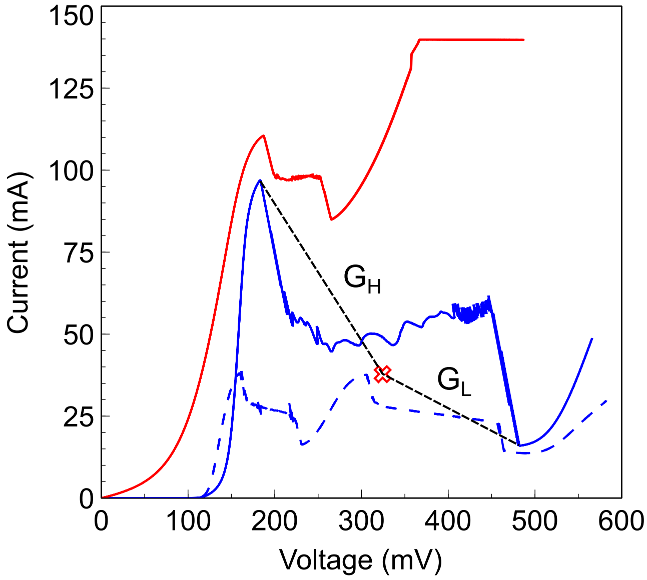

FIGURE 6.9: The experimentally measured I(V) characteristic for the most asymmetric sample VMBE 787 at 3K (solid blue) and 293K (solid red) with the position of the extracted "hidden valley" indicated by a red cross. The I(V) characteristic for the second most asymmetric structure VMBE 788 is also shown (dashed blue) along with line of average negative differential conductance from the resonance peak current to the hidden valley and from the hidden valley to the observed valley (dotted black).

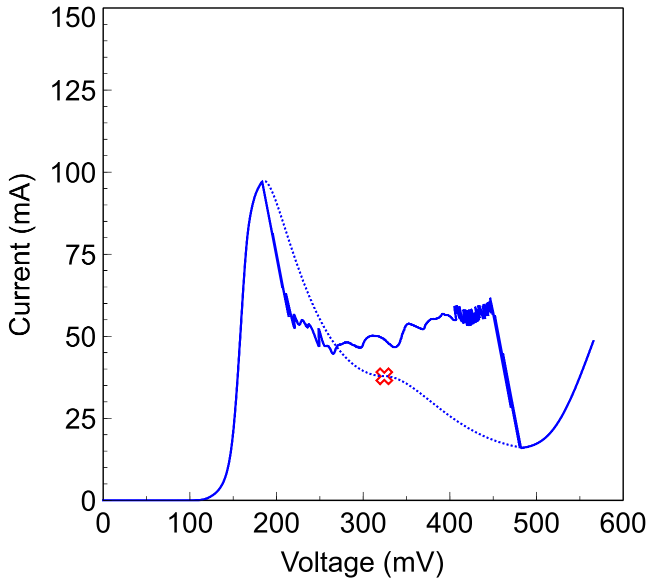

FIGURE 6.10: The experimentally measured I(V) characteristic for the most asymmetric sample VMBE 787 at 3K (solid blue) and an illustrated estimation of the steady state I(V) characteristic in the negative differential region (dotted blue). The combination of two separate resonances can form a "shoulder" in the NDR region, thus resulting in two regions with significantly different mean negative differential conductances.

resonance is a combination of two separate resonances which overlap such as to form one continuous NDR region. The "hidden valley" therefore can be more accurately described as a "shoulder" in the NDR region of the steady state I(V) characteristic, and is illustrated in figure 6.10. Interestingly, with this resonance feature potentially exhibiting two different mean NDC values, allows for the ability to significantly switch the frequency of oscillation of the device by a small change in the bias voltage.

Figure 6.11 shows the calculated maximum frequency and frequency dependent power against temperature for the negative differential conductance region, G_1 which is associated with the $n = 1$ critical alignment of figure 6.9 (i.e. the average NDC between the resonance peak and the hidden "shoulder") utilising ΔI from fit I_2 and ΔV from fit V_3. There is an increase in maximum oscillation frequency at low temperatures in comparison to figure 6.6, due to the increase in the mean negative differential conductance, G, but a decrease in the frequency dependent maximum power due at these temperatures due to decrease in $\Delta I \times \Delta V$. The calculated values agree with those in figure 6.11 as at high temperature (> 220K) the valley associated with the $n = 1$ resonance is no longer hidden but observed and measured in the experimental data.

$$\Delta I_{GL} = I_{\text{Peak}} - I_1 - I_{\text{Valley}} \tag{6.8}$$

$$\Delta V_{GL} = V_{\text{Valley}} - V_3 - V_{\text{Peak}} \tag{6.9}$$

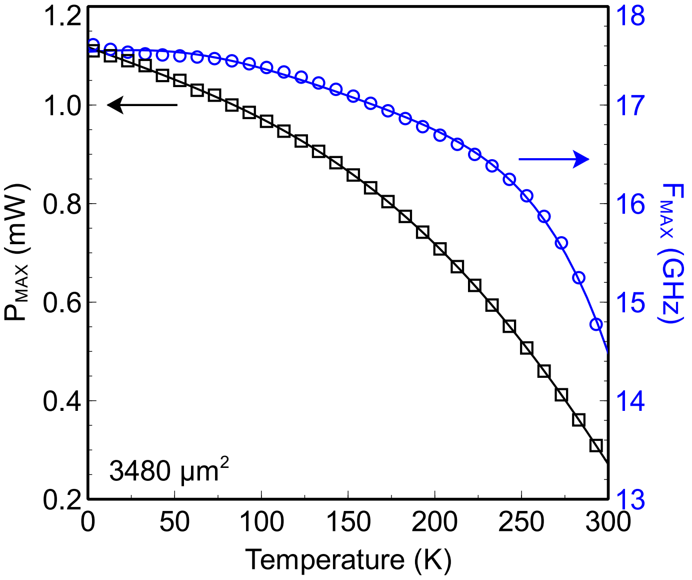

FIGURE 6.11: The calculated maximum oscillation frequency (blue circles) from equation (6.3) and frequency dependent maximum output power (black squares) from equation (6.7) for the region G_1 using the fits I_2 and V_3 for a device which has an active mesa area of $\approx 3480\ \mu m^{-2}$. Polynomial fits to both oscillation frequency and maximum output power are also shown.

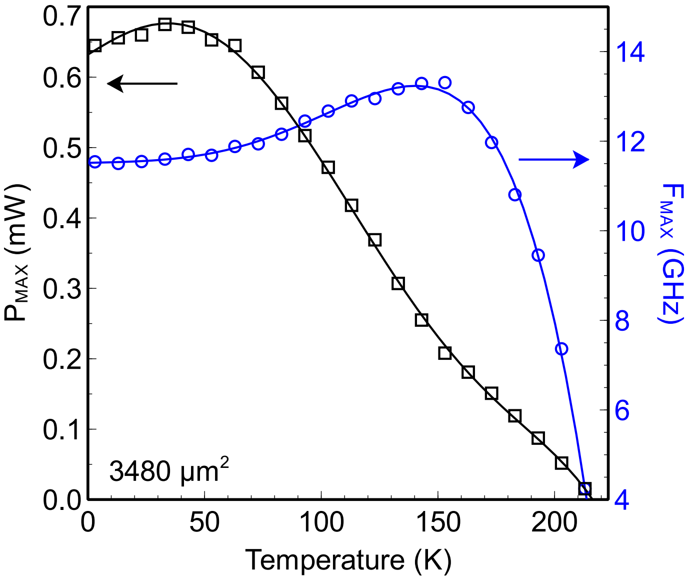

FIGURE 6.12: The calculated maximum oscillation frequency (blue circles) and frequency dependent maximum output power (black squares) in the region G_2 for a device which has an active mesa area of $\approx 3480\ \mu m^{-2}$. The values of ΔI and ΔV used in equations (6.3) and (6.7) were calculated from equations (6.8) and (6.9). Polynomial fits to both oscillation frequency and maximum output power are also shown.

Equations (6.8) and (6.9) have been used to calculate the values for ΔI and ΔV used in equations (6.3) and (6.7) for the region of lower negative differential conductance, G_2, which occurs between the hidden "shoulder" and the observed resonance valley at low temperatures. The calculated maximum oscillation frequency and maximum frequency dependent power are plotted against temperature for this NDC region in figure 6.12.

Due to the lower NDC in this region the maximum frequency of oscillation is lower than in G_1. f_{MAX} peaks at $\approx$ 13 GHz at $\approx$ 150K before rapidly decreasing to zero by $\approx$ 225K. The rapid decrease in frequency is due to the NDC region becoming enveloped in the background leakage current with increasing sample temperature, thus reducing ΔI and ΔV to zero. The calculated maximum output power is also lower in this region than for G_1 and again decreases to zero by $\approx$ 225K due to the reduction of ΔI and ΔV to zero at this temperature.

In these calculations the parasitic device capacitance C_D is assumed to be constant throughout the applied voltage range. However, as the feature associated with the region G_2 is attributed to the formation of a two-dimensional emitter state and charge accumulation in the first quantum well the device capacitance under these bias conditions is likely to increase, and thus the frequency of oscillation in this region decrease.

Figure 6.13 shows the calculated maximum oscillation frequency and frequency dependent power for both regions of negative differential conductance, G_1 (180 mV < V < 320 mV) and G_2 (320 mV < V < 480 mV) on the same figure. At low temperatures altering the voltage applied to the device such that it switches from the region G_1 to G_2 could result in a change in oscillation frequency of between $\approx$ 17.5 GHz to $\approx$ 11 GHz, albeit with a

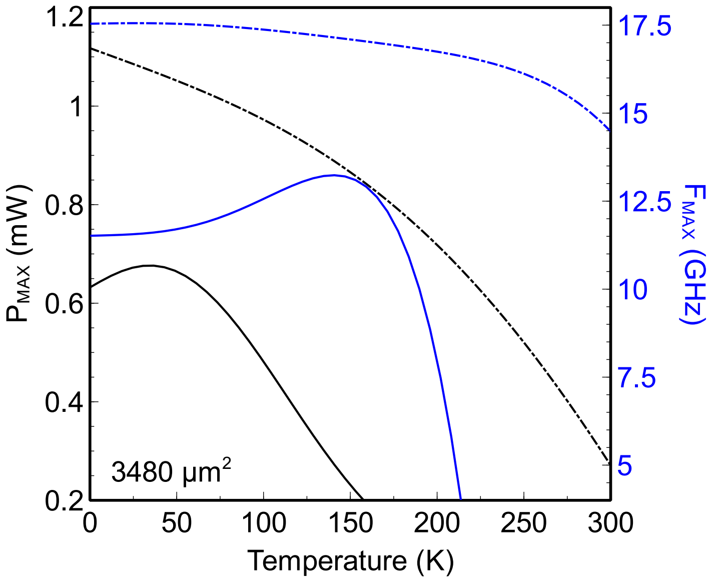

FIGURE 6.13: The polynomial fits to the maximum oscillation frequency (blue) and frequency dependent maximum output power (black) in both NDC regions, G_1 (solid lines) and G_2 (dash-dotted lines) for a device which has an active mesa area of $\approx 3480\,\mu m^{-2}$.

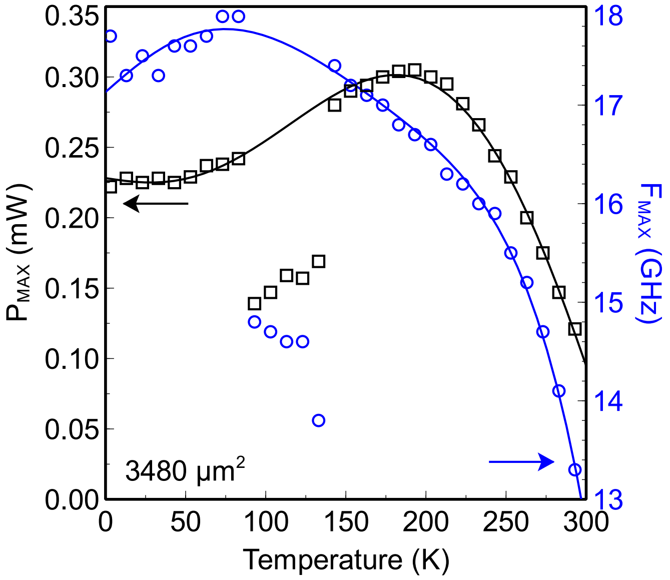

FIGURE 6.14: The calculated maximum oscillation frequency (blue circles) from equation (6.3) and frequency dependent maximum output power (black squares) from equation (6.7) for VMBE 788. Polynomial fits to both the maximum oscillation frequency and maximum output power are also shown.

decrease in output power of approximately 50%.

The maximum oscillation frequency and frequency dependent output power for the second most asymmetric device, VMBE 788 have also been calculated and are shown in figure 6.14. The calculated frequency of oscillation for this structure is similar to that of the extracted $n = 1$ resonance values from VMBE 787 (figure 6.11) despite lower values of negative differential conductance, G. This is a result of a difference in the series resistance, R_S, between the two devices, which at 3K for VMBE 787 is estimated to be 0.7 Ω whilst for VMBE 788 R_S is lower at 0.6 Ω. This illustrates an important point, as the series resistance of the device (or in fact also the capacitance) significantly affects the maximum oscillation frequency. Thus, whilst RTDs are a promising candidate to be utilised as high-frequency emitters for large scale manufacturing and quality control purposes the fabrication of devices with a specific series resistance and device capacitance must be repeatable, uniform across a wafer and tightly controlled.

The maximum frequency dependent output power for VMBE 788 is much lower than that of the $n = 1$ extracted values for VMBE 787 as one would expect, due to the smaller values of ΔI and ΔV. P_{MAX} however does increase with increasing sample temperature due to an increase in ΔI caused by the increasing magnitude of the $n = 1$ critically aligned subband peak resonance current, which in VMBE 788 is still partially thermally activated.

The discontinuity in calculated frequency and output power between 85K and 135K occurs due to the sudden switch in valley voltage (and therefore current), which forms one large single resonance peak similar to that of VMBE 787. This switch in voltage has previously been identified (figure 5.10(b)) and briefly discussed in section 5.2.1, however unlike the resonance observed in VMBE 787 the second resonance peak, associated with charge accumulation is clearly discernible at temperatures less than 87K and greater than 133K. This indicates that the cause of this switch is different in origin to that of VMBE 787 and at the time of writing the origin of this is still unclear.

6.2.4 GaAs/$Al_{0.33}Ga_{0.67}As$ Triple Barrier Heterostructure Summary

Several GaAs/$Al_{0.33}Ga_{0.67}As$ triple barrier resonant tunnelling structures have been studied in section 6.2 with a consideration of the structures being utilised as high-frequency oscillator sources. The main properties which govern the maximum oscillation frequency and the maximum output power have been calculated and are summarised in table 6.1 and compared to those of the current state of the art InGaAs/AlAs high-frequency oscillators presented in [16, 17].

Table 6.1: A summary of the comparisons between the important parameters for THz frequency emitters for the most asymmetric GaAs/$Al_{0.33}Ga_{0.67}As$ Triple Barrier Tunnelling Structures studied in this chapter against those of the state of the art InGaAs/AlAs double barrier structures extracted from [14, 17]

Parameter	**GaAs/$Al_{0.33}Ga_{0.67}$As TBRTS (3K)**	**InGaAs/AlAs DBRTS (RT)**
Mesa Area	3481 μm^2	0.2 μm^2
P_{MAX} Density	$\approx$ 1.3 μWμm^{-2}	$\approx$ 620 μWμm^{-2}
τ_T	14 ps	120 fs
C_D	170 fFμm^{-2}	6 fFμm^{-2}
G Density	0.43 μSμm^{-2}	38 mSμm^{-2}
f_{MAX}	18 GHz	1.42 THz
$P_{MAX}(f)$	0.22 mW (18 GHz)	1 μW (1.42 THz)

The GaAs/$Al_{0.33}Ga_{0.67}As$ triple barrier structures studied in this thesis in comparison to the optimised state of the art devices perform quite poorly across every parameter. However, with this being said many of the parameters shown in table 6.1 are dependent on material parameters such as the effective mass, m^*, conductivity, σ, and and optimised structure design to improve the peak current density. Thus a triple barrier resonant tunnelling structure, based on the already optimised design published in [14] should allow for an enhancement of the peak to valley current, ΔI due to a suppression of the off resonance background current thus enhancing the negative differential conductance of the device which enhances the frequency of oscillation and an improvement in the the frequency dependent output power.

6.3 Optimisation of Triple Barrier Heterostructures for High Power THz Emitters

Improvements in both frequency of oscillation and output power of resonant tunnelling diodes are believed to be possible by the modification of the design of the active region, from a double barrier structure to that of a triple barrier structure. The addition of a third potential barrier is essentially to reduce the background leakage current which dominates the off resonance valley current, whilst maintaining the high transmission coefficient through the device which contributes to a large on resonance current. This will in-turn improve the peak to valley current, ΔI, which is an important parameter for both the frequency of oscillation and maximum output power (section 6.1).

To achieve oscillation frequencies in the THz window with sufficient output powers to be utilised in applications such as security imaging or high capacity short range communications an optimised double barrier resonant tunnelling structure has been developed in the $In_{0.53}Ga_{0.47}As/AlAs$ (Indium Gallium Arsenide/Aluminium Arsenide) material system grown on lattice matched InP (Indium Phosphide) and reported by Kanaya et al. [14]. This and similar structures are currently being utilised in state of the art RTDs which have recently been reported operating with a frequency of 1.92 THz [18] at room temperature.

The current density-voltage characteristic for the optimised RTD structure with a collector spacer thickness of 12nm reported in [14] has been simulated in the WinGreen simulation package at 300K and is shown in figure 6.15(a), with the I(V) characteristic reported by Kanaya et al. shown in figure 6.15(b). The layer structure and modelling parameters

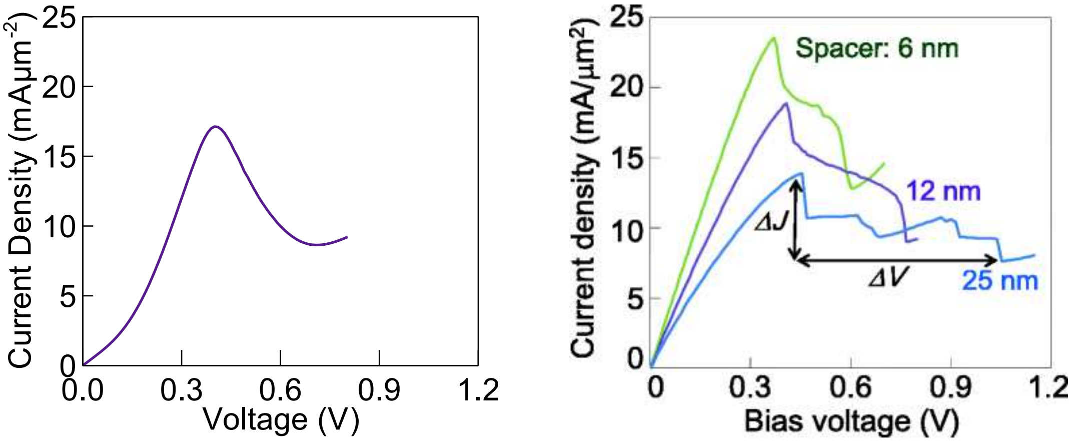

(a) (b)

FIGURE 6.15: (a) The simulated current density against applied voltage for the structure reported by Kanaya et al. [14]. There is very good agreement between the simulated and experimentally measured values for a 12nm collector, shown in figure 6.15(b). (b) The experimentally measured current density against voltage from [14].

used to produce the simulated data are presented in table 6.2 and from figures 6.15(a) and 6.15(b) it can be seen there is very good agreement between the experimental and simulated data. The material parameters are defined in a separate database with the values for the parameters such as electron effective mass, band gap energy, dielectric constant and valence band offsets required by the simulation extracted from [19–22].

Table 6.2: The WinGreen input parameters for the double barrier resonant tunnelling structure reported by Kanaya et al. [14]. These parameters are used throughout the simulations presented in this section, with only the layer thickness and material being altered.

Thickness (nm)[a]	**Material**	**Scattering Parameter**	**Doping (10^{16} cm^{-3})**	**Doping energy level (eV)**[b]
30	$In_{0.53}Ga_{0.47}As$	0.06	5000	0.005
5	$In_{0.53}Al_{0.10}Ga_{0.37}As$	0.06	5000	0.005
20	$In_{0.53}Al_{0.10}Ga_{0.37}As$	0.03	300	0.005
2	$In_{0.53}Al_{0.10}Ga_{0.37}As$	0.0034	0.01	0.005
M3	AlAs	0.0034	0.01	0.005
M11	$In_{0.90}Ga_{0.10}As$	0.0034	0.01	0.005
M3	AlAs	0.0034	0.01	0.005
12	$In_{0.53}Ga_{0.47}As$	0.0034	0.01	0.005
15	$In_{0.53}Ga_{0.47}As$	0.06	5000	0.005

---

[a] or monolayers, denoted by the prefix “M”.
[b] relative to the conduction band minimum.

The simulations performed in the following analysis of optimisation of triple barrier resonant tunnelling structures based on the Kanaya et al. design utilise the parameters presented in table 6.2 with only the active region (barriers and wells) layer thickness and material composition modified.

6.3.1 An Optimised AlAs/$In_{0.90}Ga_{0.10}As$ Triple Barrier Resonant Tunnelling Structure

To simplify the initial optimisation process the triple barrier resonant tunnelling structures were simulated without any charge accumulation effects in the active region. A series of structures were simulated based on that optimised by Kanaya et al. [14], with a third barrier added, initially for a structure with symmetric 11 monolayer $In_{0.90}Ga_{0.10}As$ quantum wells. The width of the collector well, W_C was then varied, with the emitter well, W_E kept constant at 11 monolayers (ml). The emitter quantum well width was then also varied with the collector quantum well held at 11 monolayers. The widths of the emitter, middle and collector barriers (B_E, B_{MB} and B_C respectively) of the structures remained constant throughout at 3 monolayers each. Details of each of these

Table 6.3: The widths of the active region layers simulated for a series of triple barrier resonant tunnelling structures, with Aluminium Arsenide (AlAs) barrier layers and $In_{0.90}Ga_{0.10}As$ quantum well layers.

Design	B_E (ml)	W_E (ml)	B_{MB} (ml)	W_C (ml)	B_C (ml)
ALL 1	3	11	3	11	3
ALL 2	3	11	3	10	3
ALL 3	3	11	3	9	3
ALL 4	3	11	3	8	3
ALL 5	3	11	3	7	3
ALL 6	3	11	3	6	3
ALL 7	3	10	3	11	3
ALL 8	3	9	3	11	3
ALL 9	3	8	3	11	3
ALL 10	3	7	3	11	3

structures simulated can be found in table 6.3. Figures 6.16(a) and 6.16(b) show the simulated I(V) characteristics for the structures described in table 6.3, along with the simulated I(V) characteristic for the double barrier RTD structure reported by Kanaya et al. For all of these structures there is an enhancement in the peak resonance current in comparison to the Kanaya et al. structure, due to the increase in voltage at which the resonance peak occurs. For a double barrier structure this would normally coincide with an increase in the valley current also, due to the increased background leakage current at higher voltages. However, for these triple barrier structures the addition of the extra barrier reduces the background leakage current, and hence for structures ALL 1, ALL 2

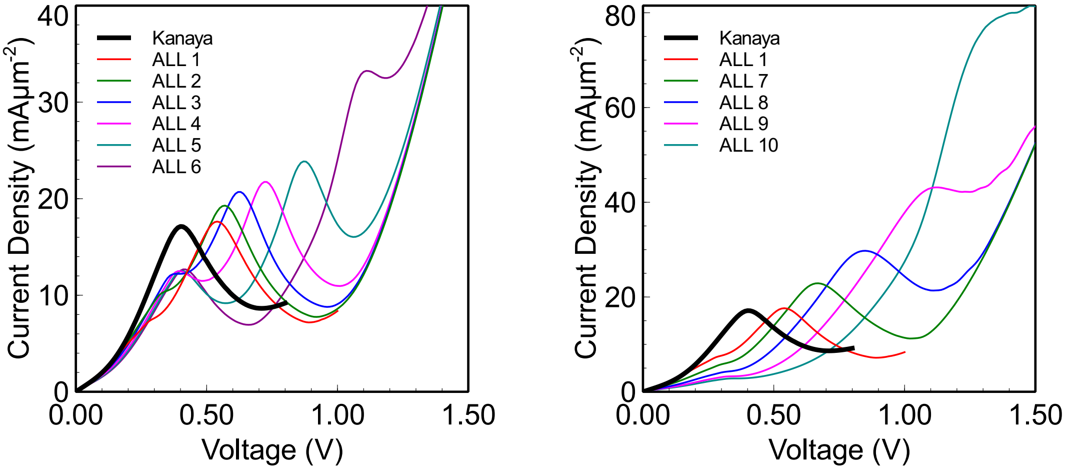

(a) (b)

Figure 6.16: The simulated current density against voltage characteristics for the structures detailed in table 6.3 with a quantum well width ratio, R (emitter:collector), of (a) R ≥ 1, (b) R ≤ 1. The simulated structure reported in [14] and shown in figure 6.15 are also given.

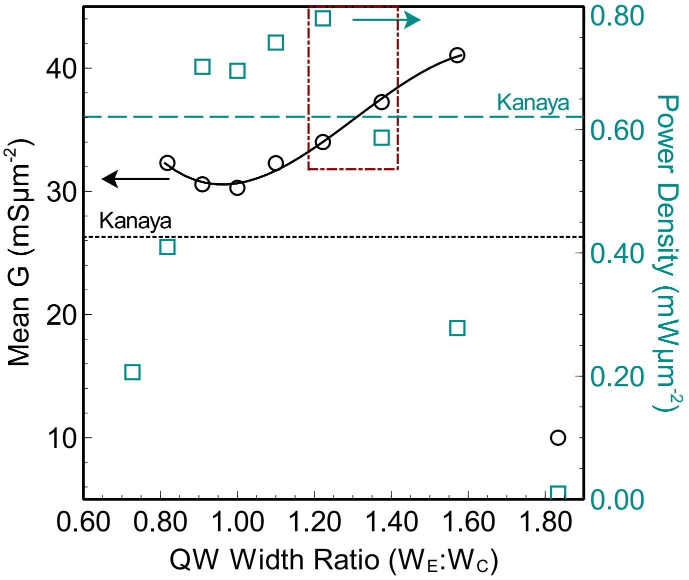

FIGURE 6.17: The calculated mean negative differential conductance, G (open circles) and steady state output power density (open squares) against the degree of quantum well width asymmetry (emitter:collector). The dotted and dashed line represent the calculated mean negative differential conductance and steady state output power density values respectively for the Kanaya et al. double barrier structure, whilst the dash-dotted box indicates those structures that offer the best negative differential resistance and output power density.

and ALL 3 the valley current is lower, but at a greater voltage than the Kanaya et al. simulated structure.

The structures with a quantum well width ratio, R (emitter:collector), of less than 1.0 (ALL 7 to ALL 10) also exhibit an increase in the peak resonance voltage compared to the simulated double barrier structure, due to the increased bias required to apply the same electric field across the active region. However there is less enhancement to the peak resonance current of these structures in comparison to those with a a quantum well ratio $R \geq 1$. The calculated mean negative differential conductance and steady state power density of the current resonances for each of the structures detailed in table 6.3 and the structure reported in [14] are shown in figure 6.17.

From figure 6.17 it is clear to see that the structures ALL 1, ALL 2, ALL 3 and ALL 7 out perform the double barrier structure by Kanaya et al. in both average negative differential conductance and steady state output power density. Practically however, there would be a high degree of risk of strain induced lattice relaxation and crystal defects forming during epitaxial growth as these structures have not been design to take into account strain introduced by the $In_{0.90}Ga_{0.10}As$ well and AlAs barriers as these are lattice mismatched to $In_{0.53}Ga_{0.47}As$. Modification of the structures to a strain compensated design is therefore required for any practical devices.

The double barrier structure by Kanaya et al. has been grown to be strain compensated across the active region. Due to the smaller lattice constant of the AlAs layers compared to those of the $In_{0.53}Ga_{0.47}As$ lattice matched to InP substrate, the AlAs layers are compressively strained. The $In_{0.90}Ga_{0.10}As$ layers however have a larger lattice constant than $In_{0.53}Ga_{0.47}As$ and as such are under tensile strain. With the correct ratio of AlAs layers to $In_{0.90}Ga_{0.10}As$ layers the compressive and tensile strain can be compensated. For the AlAs/$In_{0.90}Ga_{0.10}As$ on $In_{0.53}Ga_{0.47}As$ system this ratio is approximately 1.369 (AlAs:$In_{0.90}Ga_{0.10}As$) and as such the intended double barrier structure layers were likely to have been 8 ml AlAs (in total) and 11 ml $In_{0.90}Ga_{0.10}As$ respectively, which is a ratio of 1.375. However the simulated Kanaya et al. double barrier structure uses 6 ml of AlAs to replicate the I(V) characteristic, thus indicating the majority of the tunnelling current is due to a structure with 6 ml AlAs, rather than the intended 8 ml. As the tunnelling current has an exponential dependence on barrier width, the observation of an I(V) characteristic that can only be replicated using 3 ml barriers is not too suprising, as the current naturally takes the path of least resistance, i.e. the regions of the device where the barrier layers are only 3 ml thick, rather than the intended 4 ml.

As the structures in figure 6.17 with the best G and output power density are not strain compensated, and those structures which are do not offer any improvements on the double barrier structure then another solution must be sought. The two structures, ALL 4 and ALL 3 that are indicated in figure 6.17 by a dash-dotted box are structures, that with some adjustments to the thickness of the barrier layers can be modified to be strain compensated. This is simpler for ALL 4 than ALL 3 and as such the structure ALL 4 has been chosen to be optimised further, which has a large mean negative differential conductance, ΔI and ΔV, all of which occur at relatively low voltage in comparison to some of the other structures.

Table 6.4 shows the variations of the structure ALL 4, in which the width of the middle barrier which controls the coupling strength between the two quantum wells, has been

TABLE 6.4: The widths of the active region layers simulated for a series of triple barrier resonant tunnelling structures, with Aluminium Arsenide (AlAs) barrier layers and $In_{0.90}Ga_{0.10}As$ quantum well layers. The width of the middle barrier, B_{MB} has been varied by a monolayer between each structure.

Design	**B_E (ml)**	**W_E (ml)**	**B_{MB} (ml)**	**W_C (ml)**	**B_C (ml)**
ALL 4.1	3	11	1	8	3
ALL 4.2	3	11	2	8	3
ALL 4.3	3	11	3	8	3
ALL 4.4	3	11	4	8	3
ALL 4.5	3	11	5	8	3
ALL 4.6	3	11	6	8	3
ALL 4.7	3	11	7	8	3
ALL 4.8	3	11	8	8	3

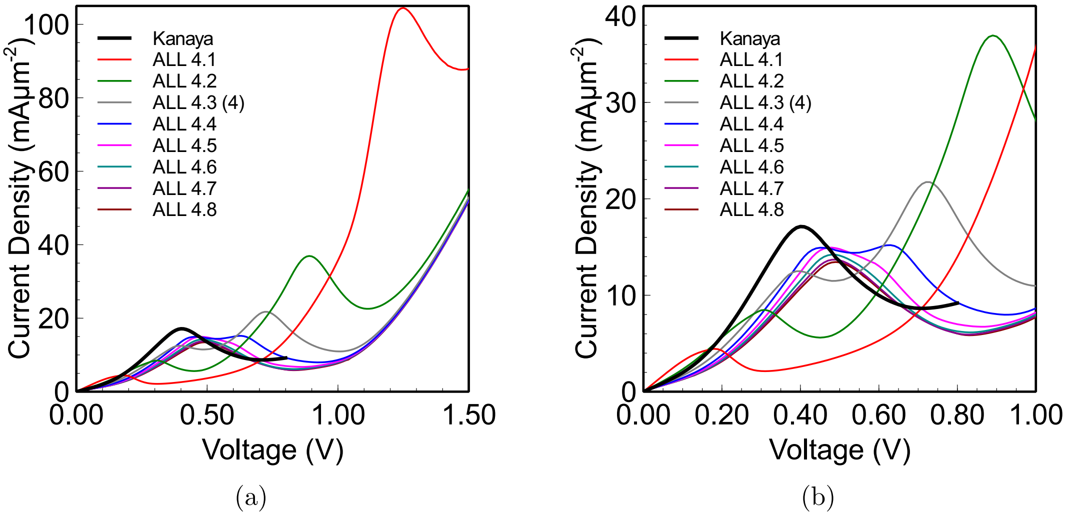

FIGURE 6.18: The simulated current density against voltage characteristics for the structures detailed in table 6.4 for varying middle barrier widths. The simulated structure reported in [14] and shown in figure 6.15 are also given.

varied for each structure. For completeness the width has been varied from 1 ml, to 8 ml, which for this structure is the required middle barrier width to engineer a strain compensated active region (given quantum wells of widths 11 ml and 8 ml).

The simulated current-density against voltage curves for each of the structures given in table 6.4 are shown in figures 6.18(a) and 6.18(b). The thinnest middle barrier results in the largest coupling and hence splitting in energy between the two quantum well

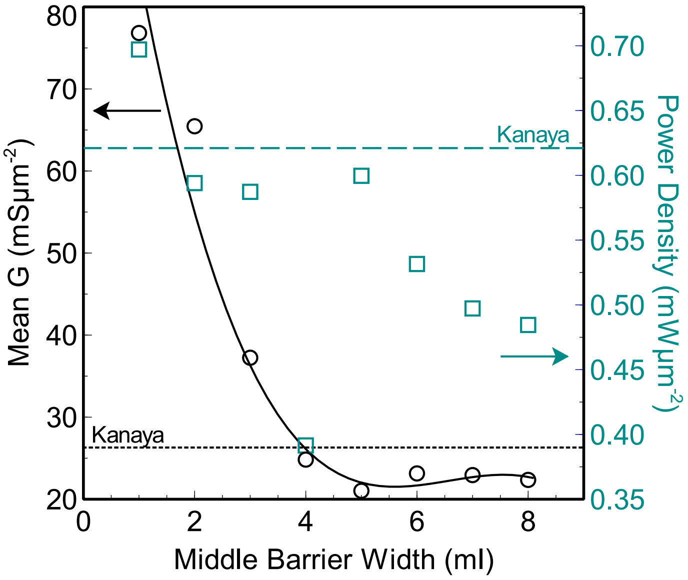

FIGURE 6.19: The calculated mean negative differential conductance, G (open circles) and steady state output power density (open squares) against the width of the middle barrier. The dotted and dashed line represent the calculated mean negative differential conductance and steady state output power density values respectively for the Kanaya et al. double barrier structure.

$n = 1$ subband states, as expected. This results in two resonances observed in the I(V) characteristics with a large difference in voltage between the two, the difference in voltage between the two resonances decreases with increasing middle barrier width, as the coupling, and so energy splitting of the $n = 1$ subband states decreases, with a single resonance observed once the thickness of the middle barrier reaches 5 ml. The mean negative differential resistance, G and steady state output power density for the largest resonance of each of the structures in table 6.4 are shown in figure 6.19.

The calculated values of negative differential conductance, G and steady state output power density for each of these structures show that with increasing middle barrier width, although the strength of the coupling decreases to allow the formation of a single resonance, this also decreases the mean negative differential conductance and the output power density below that of the structure developed by Kanaya et al. [14].

To analyse the efficiency of these structures a figure of merit suggested by Baba et al. [23], which is the ratio of the time-averaged electrical chip power ($\mathrm{P_{Chip}}$) to the steady state extractable power, $\mathrm{P_{MAX}}$ from equation (6.5) to approximate a device efficiency based on the input to output power is used. This efficiency and peak resonance voltage for each of the structures in table 6.4 are plotted against middle barrier width in figure 6.20.

As might be expected, the most efficient structures are those with a larger middle barrier, where the resonance peak occurs at lower voltage, but all of the triple barrier structures studied here have lower efficiency than that of the Kanaya et al. double barrier structure. However, structures ALL 4.5 and ALL 4.6 are only marginally less efficient than the

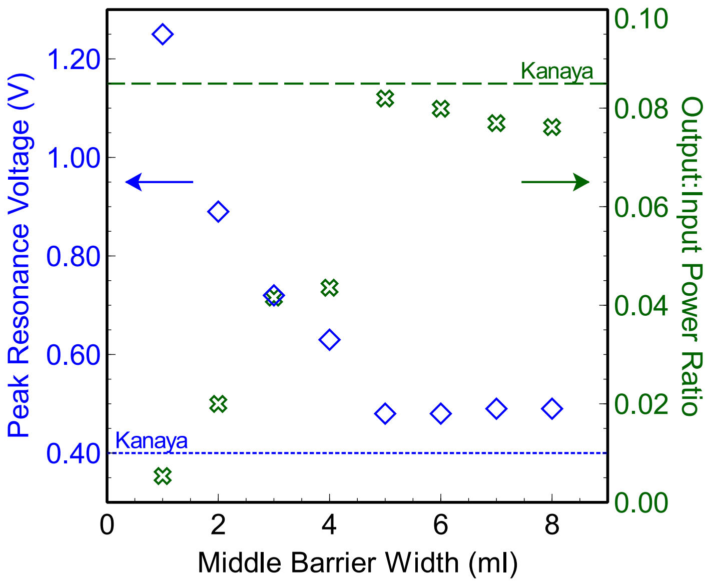

FIGURE 6.20: The calculated output to input ratio based on the figure of merit by Baba et al. [23] (open crosses) and the extracted peak resonance voltage (open diamonds) against the width of the middle barrier. The dotted and dashed line represent the peak resonance voltage and calculated input to output power ratio values respectively for the Kanaya et al. double barrier structure.

double barrier structure despite the increased peak resonance voltage because of the increased ΔI from the suppression of the off resonance background current.

The structure, ALL 4.8 which best fulfil the requirements for strain balance across the active region (19 ml $In_{0.90}Ga_{0.10}As$ and 14 ml AlAs) suffers from lower negative differential conductance and output power density than Kanaya et al. as well as lower power efficiency and as such this structure offers no benefits compared to the optimised double barrier structure.

Generally for a strain compensated structure it is the ratio of the total number of compressively and tensile strained monolayers which determines the overall strain value, provided the number of consecutive layers of a single type of strain do not exceed the critical thickness above which the lattice will relax, and thus creating defects in the crystal structure. Therefore, with a total of 19 ml of $In_{0.90}Ga_{0.10}As$ quantum well material, 14 ml of AlAs, which can be distributed within various thickness layers across the structure, are required to balance the strain.

Table 6.5: The widths of the active region layers simulated for a series of triple barrier resonant tunnelling structures, with Aluminium Arsenide (AlAs) barrier layers and $In_{0.90}Ga_{0.10}As$ quantum well layers. The width of the middle barrier, B_{MB} is kept constant at 6 ml whilst the emitter and collector barrier layers are varied between each structure. The total ratio of $In_{0.90}Ga_{0.10}As$ to AlAs material is also kept constant at 19 ml to 14 ml, which is a strain compensated system.

Design	**B_E (ml)**	**W_E (ml)**	**B_{MB} (ml)**	**W_C (ml)**	**B_C (ml)**
ALL 4.6a	4	11	6	8	4
ALL 4.6b	3	11	6	8	5
ALL 4.6c	2	11	6	8	6
ALL 4.6d	1	11	6	8	7
ALL 4.6e	5	11	6	8	3
ALL 4.6f	6	11	6	8	2
ALL 4.6g	7	11	6	8	1

Therefore given the relatively high efficiency and negative conductance and output power density of structure ALL 4.6, which has a middle barrier of 6 ml, this structure has been chosen to modify into a strain compensated active region, by the addition of two extra monolayers of AlAs distributed between the emitter and collector barriers. Table 6.5 shows the structure designs, where the width of the emitter and collector barriers are varied, whilst maintaining a strain compensated active region.

The simulated current density against voltage characteristics for each of the structures in table 6.5 are shown in figure 6.21 with the calculated mean negative differential conductance and steady state output power density against emitter barrier width for each structure given in figure 6.22. The calculated input to output power ratio and extracted resonance peak voltage for each of the designs are also plotted in figure 6.23

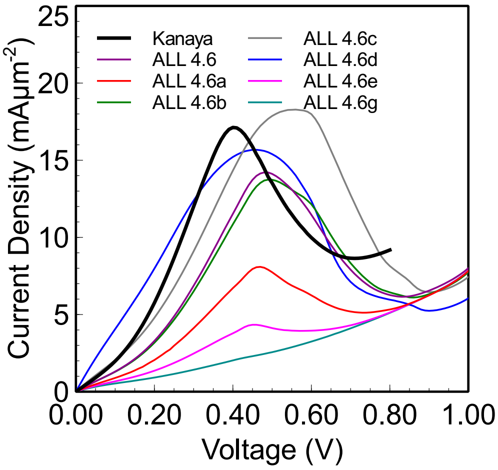

FIGURE 6.21: The simulated current density against voltage characteristics for the structures detailed in table 6.5 for varying middle barrier widths. The simulated structure reported in [14] and shown in figure 6.15 are also given.

against emitter barrier width.

The simulated I(V) characteristics for these set of structures show that with increasing emitter barrier thickness there is a decrease in tunnelling current through the structure, despite the total barrier thickness of the active region remaining constant. This indicates that it is the emitter barrier which dominates the current flow through the entire structure, rather than a combination of all of the barrier layers as it is the emitter barrier that

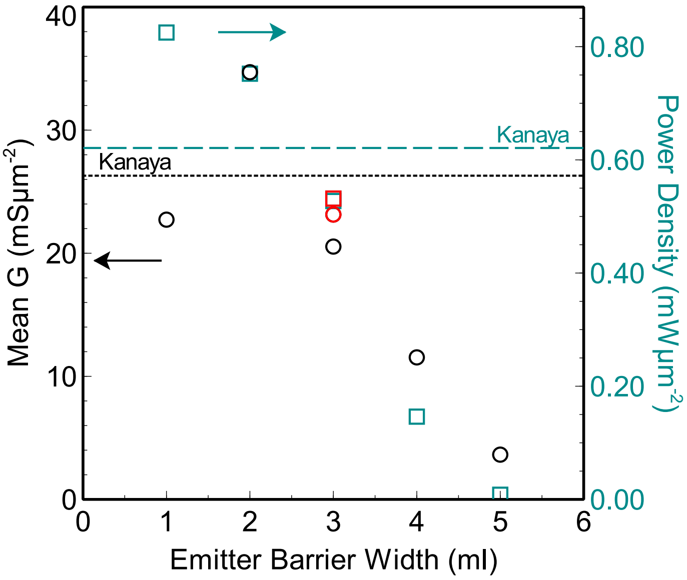

FIGURE 6.22: The calculated mean negative differential conductance, G (open circles) and steady state output power density (open squares) against the width of the emitter barrier. The dotted and dashed line represent the calculated mean negative differential conductance and steady state output power density values respectively for the Kanaya et al. double barrier structure. The red circle and square are included as a reference and represent the mean negative differential conductance and output power density respectively for the structure ALL 4.6, which is not strain compensated.

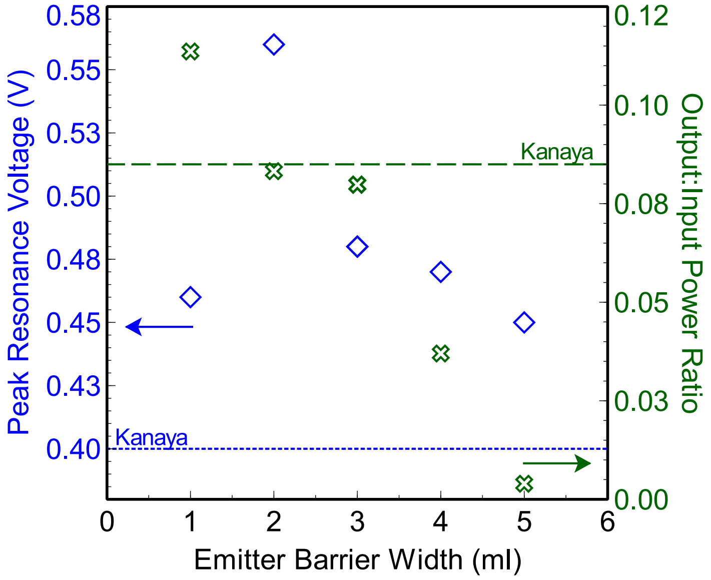

Figure 6.23: The calculated output to input ratio based on the figure of merit by Baba et al. [23] (open crosses) and the extracted peak resonance voltage (open diamonds) against the width of the emitter barrier. The dotted and dashed line represent the peak resonance voltage and calculated input to output power ratio values respectively for the Kanaya et al. double barrier structure.

controls the coupling between the quasi-confined quantum well states and the emitter electron states.

The shape of the simulated I(V) characteristic current resonance also varies with emitter barrier width due to the altering degree of confinement, where the energy of the quasi-confined state in the emitter quantum well decreases (and so is better confined) with increasing emitter barrier width, whilst the energy of the collector quantum well quasi-confined state increases with increasing emitter barrier width (as the collector barrier is reduced), hence the state is less well confined. A resonance was not observed in the simulated I(V) characteristic for design ALL 4.6g.

Figures 6.22 and 6.23 therefore show that the design ALL 4.6c, with an emitter barrier of 2 monolayers exhibits a current resonance which has a greater mean negative differential conductance, greater output power density and similar input to output power efficiency as the optimised structure developed by Kanaya et al. Thus, this design is a potential improvement on the current state of the art RTD structures currently being used.

The optimisation process has thus far ignored the effect of charge accumulation in the quasi bound quantum well states, however as has been shown in section 4.4.1 in triple barrier resonant tunnelling structures charge accumulation in the emitter quantum well can have a dramatic effect on the I(V) characteristics observed. In section 6.1 it has also been shown that the capacitance of RTD structures is an extremely important factor in determining the maximum frequency of oscillation of such devices, and so a structure in which a substantial amount of charge can accumulate is not desirable as this will increase

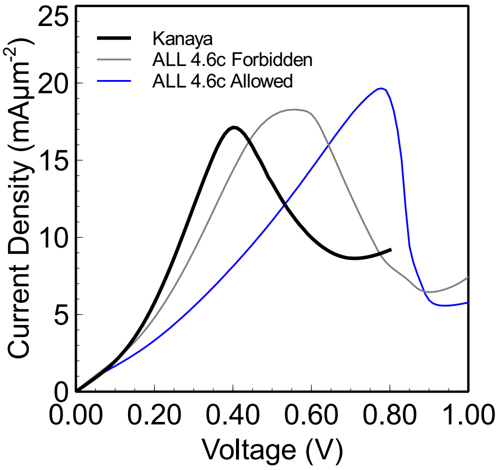

FIGURE 6.24: The simulated current density against voltage characteristics for the structure design ALL 4.6c given in table 6.5 where charge accumulation in the emitter quantum well is allowed and forbidden. The simulated structure reported in [14] and shown in figure 6.15 are also given.

the capacitance.

Figure 6.24 therefore shows the simulated I(V) characteristics for design ALL 4.6c with and without charge accumulation in the emitter quantum well permitted, from which it can be seen there is a dramatic difference in the simulated characteristics. A comparison between the two characteristics show that in the situation where charge accumulation in the emitter quantum well is allowed there is an increase in the resonance peak current, and a decrease in the off resonance valley current resulting in a larger peak to valley current, ΔI. This coincides with a decrease in the peak to valley voltage difference, ΔV and as such the average negative differential conductance of this resonance is much larger when charge is allowed to accumulated in the quantum well. Although at first this may seem advantageous, there is also a significant shift in the peak resonance voltage indicating a large amount of charge is accumulating in the emitter quantum well. Thus the structure design ALL 4.6c may have a large capacitance which would limit frequency of oscillation of the device and possibly negate any improvements in comparison to the optimised double barrier structure by Kanaya et al. which does not suffer from charge accumulation.

6.3.2 A Strain Compensated Triple Barrier Resonant Tunnelling Structure to Minimise Emitter Quantum Well Charge Accumulation

One disadvantage of a triple barrier resonant tunnelling structure (TBRTS) as a high frequency oscillator is that generally, due to the nature of the design of such a structure, significant charge accumulation in the emitter quantum well occurs. As has been shown in sections 6.1 and 6.3 this charge accumulation results in an increased capacitance across the device, which limits the maximum oscillation frequency. As a result a TBRTS which has improved performance as a high frequency oscillator over a symmetric double barrier resonant tunnelling structure (DBRTS) which does not suffer from charge accumulation in the quantum well is difficult to achieve without very careful consideration and structure design.

Triple barrier resonant tunnelling structures are often viewed as a DBRTS which have an energy filter, which limits the energy of the electrons incident on the double barrier structure to the energy of the emitter quantum well quantised states. The optimisation process described in section 6.3.1 was based on an approach in which the material composition of each of the quantum wells was identical and design varied to maximise the critical alignment of the $n = 1$ quantum well subband states allowing high transmission through the structure. The design was then modified to account for the difficulties in successfully growing such a structure and resulted in a design in which large charge accumulation occurred.

In this section a different approach has been taken, which considers the design requirements to minimise charge accumulation in the emitter quantum well and the ability to successfully and relatively simply grow such a structure. The requirement of a thin emitter barrier (≈ 2 or 3 monolayers) is also imposed from the evidence in figure 6.22 which showed the tunnelling current is dominated by the coupling between the three-dimensional emitter and the emitter quantum well state. These initial requirements constrain the number of parameters which can be varied and as such result in a limited number of structures that can be modified for optimisation. In reality however there are many more parameters than can be varied, such as the alloy compositions of the three dimensional emitter, individual potential barriers and individual quantum well regions. For simplicity this optimisation process only considers limited variations on the quantum well alloy compositions and the allowed quantum well/barrier widths for a strain compensated system.

Table 6.6: The widths of the active region layers of the starting structures for a series of triple barrier resonant tunnelling structures in which there is reduced charge accumulation in the emitter quantum well. All four structures are strain approximately strain compensated, utilising AlAs barriers and an $In_{0.53}Ga_{0.47}As$ collector quantum well. The alloy composition of the emitter quantum well for designs In53A.1, In53B.1 and In53C.1 is $In_{0.90}Ga_{0.10}As$, whilst a $In_{0.80}Ga_{0.20}As$ is used in the In53X.1 design.

Design	**B_E (ml)**	**W_E (ml)**	**B_{MB} (ml)**	**W_C (ml)**	**B_C (ml)**
In53A.1	4	11	2	11	2
In53B.1	3	10	2	11	2
In53C.1	3	9	2	11	2
In53X.1	3	13	2	11	2

Table 6.6 shows the starting possibilities for structures which comply with the requirements to minimise emitter quantum well charge accumulation whilst being strained compensated and exhibiting a high current density. Charge accumulation occurs in the emitter quantum well due to an imbalance between the number of carriers tunnelling into and the number of carriers tunnelling out of the quantum well. These rates are dependent on the transmission coefficient into the emitter quantum well and out of the emitter quantum well into the collector region of the device, and as such crudely the transmission probability through the emitter barrier must be less than or equal to the transmission probability through the middle barrier/collector well/collector barrier structure. This can be achieved by controlling the width of these barriers such that ($\mathrm{B_E} \geq \mathrm{B_{MB}} + \mathrm{B_C}$) as the transmission probability is crudely dependent on the barrier widths. In reality, for energies equal to carriers in the 3D emitter and with bias across the structure the transmission coefficient through the emitter barrier, $\mathrm{T_E}$ is lower than the middle barrier, $\mathrm{T_{MB}}$ which is lower than the collector barrier, $\mathrm{T_C}$ ($\mathrm{T_E} > \mathrm{T_{MB}} > \mathrm{T_C}$). Therefore the combination of a 3 ml emitter barrier, 2 ml middle barrier and 2ml collector barrier also fulfil the requirements to minimise charge accumulation.

The emitter well width has then been chosen to result in an active region which is as close to being strain compensated as possible, whilst the width of the collector well will be varied. The thin two monolayer middle barrier results in a large coupling and hence energy splitting between the quasi confined quantum well states and as such the transmission coefficient through the structure at these energies is very high. Tables 6.7 to 6.10 show the variations on the starting structures simulated with the calculated mean negative differential resistance, G, steady state output power density, resonance peak voltage and input to output power efficiency plotted against collector quantum well width for each variation in figures 6.25 to 6.28.

Table 6.7: The widths of the active region layers for a series of triple barrier resonant tunnelling structures in which there is reduced charge accumulation in the emitter quantum well. These designs are based on the staring structure In53A.1 in table 6.6 which has an $\mathrm{In_{0.90}Ga_{0.10}As}$ emitter quantum well. Only the width of the $\mathrm{In_{0.53}Ga_{0.47}As}$ collector quantum well is varied across each different design.

Design	**$\mathrm{B_E}$ (ml)**	**$\mathrm{W_E}$ (ml)**	**$\mathrm{B_{MB}}$ (ml)**	**$\mathrm{W_C}$ (ml)**	**$\mathrm{B_C}$ (ml)**
In53A.1	4	11	2	11	2
In53A.2	4	11	2	10	2
In53A.3	4	11	2	9	2
In53A.4	4	11	2	8	2
In53A.5	4	11	2	12	2
In53A.6	4	11	2	13	2
In53A.7	4	11	2	14	2

Table 6.8: The widths of the active region layers for a series of triple barrier resonant tunnelling structures in which there is reduced charge accumulation in the emitter quantum well. These designs are based on the staring structure In53B.1 in table 6.6 which has an $In_{0.90}Ga_{0.10}As$ emitter quantum well. Only the width of the $In_{0.53}Ga_{0.47}As$ collector quantum well is varied across each different design.

Design	**B_E (ml)**	**W_E (ml)**	**B_{MB} (ml)**	**W_C (ml)**	**B_C (ml)**
In53B.1	3	10	2	11	2
In53B.2	3	10	2	10	2
In53B.3	3	10	2	9	2
In53B.4	3	10	2	8	2
In53B.5	3	10	2	7	2
In53B.6	3	10	2	12	2
In53B.7	3	10	2	13	2

Table 6.9: The widths of the active region layers for a series of triple barrier resonant tunnelling structures in which there is reduced charge accumulation in the emitter quantum well. These designs are based on the staring structure In53C.1 in table 6.6 which has an $In_{0.90}Ga_{0.10}As$ emitter quantum well. Only the width of the $In_{0.53}Ga_{0.47}As$ collector quantum well is varied across each different design.

Design	**B_E (ml)**	**W_E (ml)**	**B_{MB} (ml)**	**W_C (ml)**	**B_C (ml)**
In53C.1	3	9	2	11	2
In53C.2	3	9	2	10	2
In53C.3	3	9	2	9	2
In53C.4	3	9	2	8	2
In53C.5	3	9	2	7	2
In53C.6	3	9	2	6	2
In53C.7	3	9	2	12	2
In53C.8	3	9	2	13	2
In53C.9	3	9	2	14	2

Table 6.10: The widths of the active region layers for a series of triple barrier resonant tunnelling structures in which there is reduced charge accumulation in the emitter quantum well. These designs are based on the staring structure In53X.1 in table 6.6 which has an $In_{0.80}Ga_{0.20}As$ emitter quantum well. Only the width of the $In_{0.53}Ga_{0.47}As$ collector quantum well is varied across each different design.

Design	**B_E (ml)**	**W_E (ml)**	**B_{MB} (ml)**	**W_C (ml)**	**B_C (ml)**
In53X.1	3	13	2	13	2
In53X.2	3	13	2	14	2
In53X.3	3	13	2	15	2
In53X.4	3	13	2	16	2
In53X.5	3	13	2	12	2
In53X.6	3	13	2	11	2
In53X.7	3	13	2	10	2

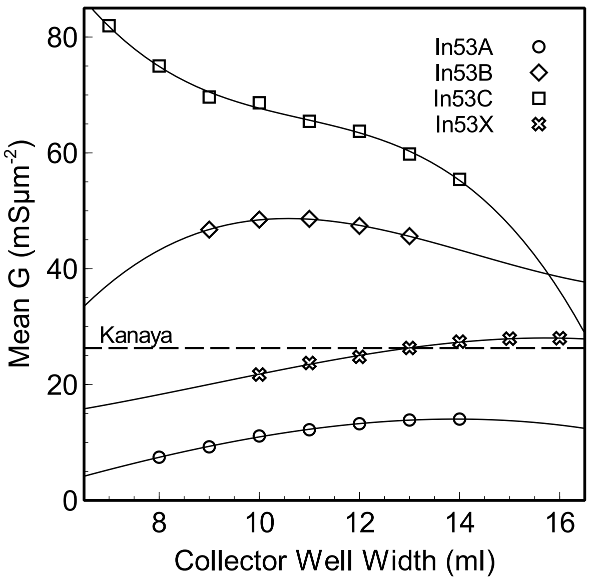

Figure 6.25: The calculated mean negative differential conductance, G, plotted against the varied width of the collector quantum well for the In53A (open circles), In53B (open diamonds), In53C (open squares) and In53X (open crosses) design variations detailed in tables 6.7 to 6.10. Third order polynomial fits to each data set are also shown whilst the dashed line represents the calculated mean negative differential conductance for the Kanaya et al. double barrier structure.

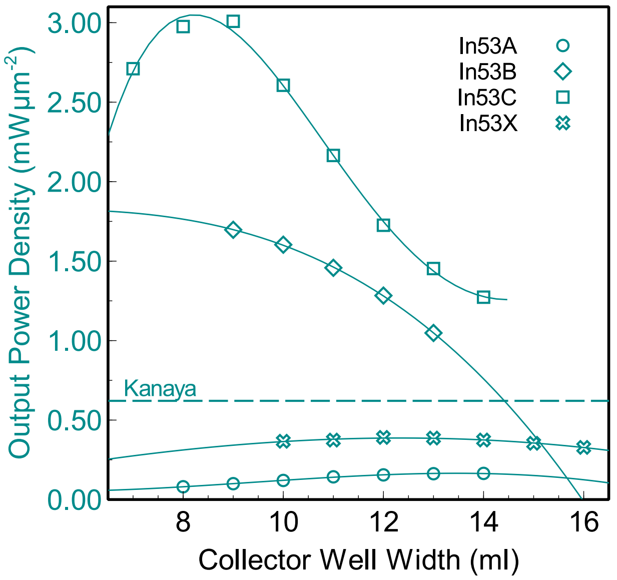

Figure 6.26: The calculated steady state output power density plotted against the varied width of the collector quantum well for the In53A (open circles), In53B (open diamonds), In53C (open squares) and In53X (open crosses) design variations detailed in tables 6.7 to 6.10. Third order polynomial fits to each data set are also shown whilst the dashed line represents the calculated steady state output power density for the Kanaya et al. double barrier structure.

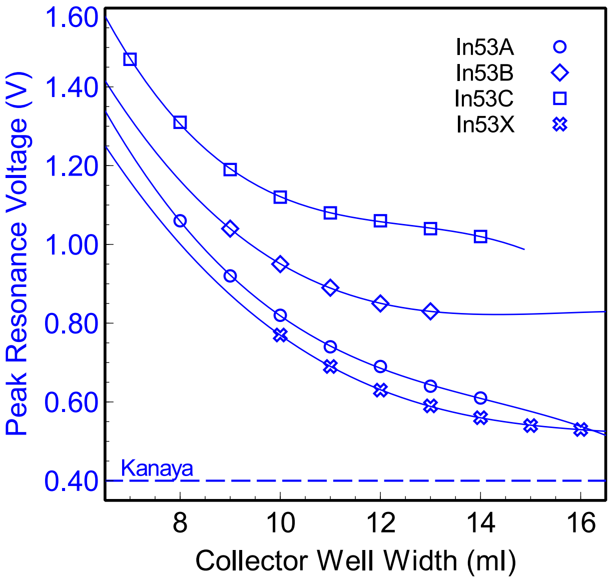

FIGURE 6.27: The extracted resonance peak voltage plotted against the varied width of the collector quantum well for the In53A (open circles), In53B (open diamonds), In53C (open squares) and In53X (open crosses) design variations detailed in tables 6.7 to 6.10. Third order polynomial fits to each data set are also shown whilst the dashed line represents the extracted resonance peak voltage for the Kanaya et al. double barrier structure.

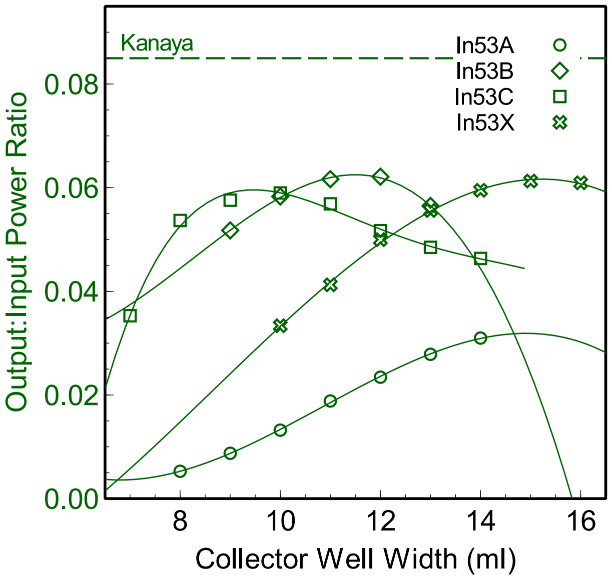

FIGURE 6.28: The calculated input to output power efficiency plotted against the varied width of the collector quantum well for the In53A (open circles), In53B (open diamonds), In53C (open squares) and In53X (open crosses) design variations detailed in tables 6.7 to 6.10. Third order polynomial fits to each data set are also shown whilst the dashed line represents the calculated input to output power efficiency for the Kanaya et al. double barrier structure.

From the simulated data it can be seen that with low efficiency, smaller negative differential conductance than the double barrier resonant tunnelling structure optimised by Kanaya et al. and low output power density the In53A designs perform poorly and do not offer any advantages over the other structures despite having a lower resonance peak voltage. This is attributed to the thicker, 4 monolayer emitter barrier, which has previously been shown in section 6.3.1 to dramatically decrease the tunnelling current through these structures.

The In53B set of designs however are much more promising, with nearly double the negative differential conductance and output power density than that of the optimised double barrier structure. The resonances in these structures however do occur at higher voltages and as such despite In53B.1 and In53B.6 being the most efficient of all of the designs they still have lower efficiency than the double barrier structure, with In53B.1 and In53B.6 approximately 6.16% and 6.21% efficient respectively. Although with the highest efficiency, good negative conductance and output power density the designs In53B.1 and In53B.6 appear to be the best all round improvement on the double barrier structure, being superior in two out of the three important parameters considered.

The series of In53C designs are very interesting structures, with resonances that occur at high voltages, but with extremely large ΔI and ΔV thus resulting in large output power density, negative differential conductance. These designs also appear to be relatively efficient with efficiencies between $\approx 4\%$ and 6%, due to the large peak resonance current in comparison to the off resonant current. These structures however do pose a higher degree of uncertainty in the calculated values due to the high voltages at which the resonances occur. At such high voltages there are many more leakage mechanisms which can contribute to the off resonant current, which these WinGreen simulations do not consider. The Gunn effect [4] for example is much more pronounced at higher voltages in these structures due to the indirect nature of the AlAs barrier bandgap and thus the series of In53C designs must be treated with some caution.

The final set of designs, In53X which utilise a $\mathrm{In_{0.80}Ga_{0.20}As}$ emitter quantum well rather than $\mathrm{In_{0.90}Ga_{0.10}As}$, offer the lowest resonance peak voltages of all of the triple barrier structure designs. However, despite good efficiency with the wider collector quantum wells (15 ml and 16 ml) and negative differential conductances similar to the double barrier structure the output power density for these structures is low and as such these structure overall also perform quite poorly.

Throughout this optimisation and improvement process it has become apparent that simply modifying a double barrier structure into a triple barrier structure with improved properties is not trivial and the results show that instead of a single optimised device, each design has some improvements, but sacrifices other aspects in order to achieve the benefits. Thus the design of the structures should be tailored to the application, rather than using a simple superior design. For example the series of In53C designs are likely to

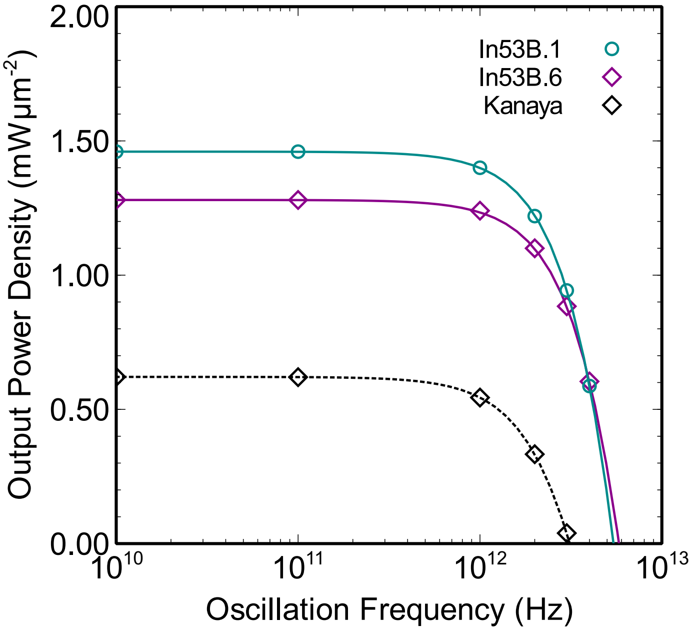

FIGURE 6.29: The calculated frequency dependent output power density for the optimised double barrier structure by Kanaya et al. [14], and improved triple barrier resonant tunnelling structure designs In53B.1 and In53B.6.

have superior output power density, and negative conductance but become less efficient as a result.

To compare the frequency dependent power of these simulated structures against the optimised double barrier structure the tunnelling time through the RTD, τ_{rtd} has been calculated from the full width half-maximum of the transmission coefficient for the best overall structures, In53B.1 and In53B.2 and found to be 16 fs and 13 fs respectively. The transit time through the collector depletion region, τ_{dep} is assumed to be equal to that calculated by Kanaya et al. [14] which is given to be 60 fs. The total delays of the charge carriers travelling through the structure, τ_T are therefore found to be 46 fs and 43 fs for designs In53B.1 and In53B.6 respectively from equation (6.6).

Figure 6.29 shows the calculated frequency dependent power density for the triple barrier RTD designs In53B.1 and In53B.6 along with the optimised double barrier structure by Kanaya et al. There is a clear improvement in the output power density in the THz region with the maximum frequency of oscillation also increased due to the reduction in the total transit time through the structure.

The results given in this section therefore demonstrate that improvements to the current state of the art THz RTD structure can be made by switching to a triple barrier structure rather than the conventionally used double barrier structure. It is likely that the triple barrier structures can be further optimised to increase device efficiency by altering the three-dimensional emitter region alloy composition such that the resonances occur at lower voltages. Further optimisation can also be carried out by altering the barrier and well compositions further as well as a re-optimisation of the collector spacer considering the trade off between the device capacitance and collector depletion region transit time, similar to that carried out by Kanaya et al. [14].

In reality however the large scale, low cost, high volume manufacturing of these structures is extremely challenging due to the complex engineering of the associated circuit required for such RTD devices and the epitaxial growth of such precise and thin structure layers. The variability of the tunnelling current for proposed electronic devices has been previously explored [24] and is still applicable today. Although research devices with a low yield are likely possible, a single monolayer variation in the emitter barrier can result in a dramatic change in the I(V) characteristic (as has been shown in section 6.3.1) and so result in a dramatically different device response. Therefore any attempt to scale such devices to low cost manufacturable yields will require significant work on the epitaxy and fabrication processes.

6.4 Summary

In this chapter the triple barrier resonant tunnelling structures studied in chapters 4 and 5 have been examined for the purpose of being utilised as potential THz radiation sources as a function of temperature. It has been found the highest maximum oscillation frequency of the 60 μm x 60 μm GaAs/Al$_{0.33}$Ga$_{0.67}$As TBRTS devices is 18 GHz at 3K, with a maximum output power of 0.22 mW at this frequency. The GaAs/Al$_{0.33}$Ga$_{0.67}$As devices perform poorly in comparison to the state of the art In$_{0.90}$Ga$_{0.10}$As/AlAs strained double barrier structures grown on In$_{0.53}$Ga$_{0.47}$As lattice matched to InP, which have a measured output power of 1μW at 1.42 THz at room temperature.

Simulations using the WinGreen package have been performed and the resulting I(V) characteristics analysed to develop an improved triple barrier resonant tunnelling structure in the In$_{0.90}$Ga$_{0.10}$As/AlAs material system which out performs the current state of the art double barrier structure. The final improved design increases the negative differential conductance and so has potentially faster maximum frequency of oscillation and increases the maximum output power density albeit with a decrease in device power efficiency. Further optimisation of this structure is likely possible with a re-optimisation of the collector depletion spacer length and emitter alloy composition however these simulations are beyond the scope of this thesis.

Many challenges still remain in the epitaxial growth and fabrication of these devices due to the tight constraints on barrier and well widths and variability across the wafer before devices of this nature can be manufactured on a large scale and at low cost. Therefore whether resonant tunnelling diodes will one day be utilised as compact solid state THz frequency electronic sources is still up for debate, however, structures of this nature still remain a very promising candidate to fulfil this need.

Bibliography

[1] *http://ieeexplore.ieee.org/xpl/RecentIssue.jsp?punumber=5503871*. URL. Terahertz Science and Technology, IEEE Transactions on, 2016.

[2] T. Nagatsuma. 'Generating millimeter and terahertz waves'. In: *IEEE, Microwave Magazine* 10.4 (2009), pp. 64–74. ISSN: 1527-3342. DOI: `10.1109/MMM.2009.932283`.

[3] Martin Brandstetter, Christoph Deutsch, Michael Krall, Hermann Detz, Donald C. MacFarland, Tobias Zederbauer, Aaron M. Andrews, Werner Schrenk, Gottfried Strasser and Karl Unterrainer. 'High power terahertz quantum cascade lasers with symmetric wafer bonded active regions'. In: *Applied Physics Letters* 103.17, 171113 (2013). DOI: `http://dx.doi.org/10.1063/1.4826943`.

[4] S. M. Sze and K. K. Ng. *Physics of Semicondcutor Devices. Third Edition.* John Wiley & Sons, 2007.

[5] T. Maekawa, H. Kanaya, S. Suzuki and M. Asada. 'Frequency increase in terahertz oscillation of resonant tunnelling diode up to 1.55 THz by reduced slot-antenna length'. In: *Electronics Letters* 50.17 (Aug. 2014), pp. 1214–1216. ISSN: 0013-5194. DOI: `10.1049/el.2014.2362`.

[6] *http://terasense.com/applications/homeland-security/*. URL. Terasense Group, Inc, USA, 2016.

[7] Ho-Jin Song and T. Nagatsuma. 'Present and Future of Terahertz Communications'. In: *Terahertz Science and Technology, IEEE Transactions on* 1.1 (Sept. 2011), pp. 256–263. ISSN: 2156-342X. DOI: `10.1109/TTHZ.2011.2159552`.

[8] *http://www.teraview.com/applications/index.html*. URL. TeraView Ltd, United Kingdom, 2016.

[9] T. C. L. Gerhard Sollner, Elliott R. Brown, C. D. Parker and W. D. Goodhue. 'Electronic Properties of Multilayers and Low-Dimensional Semiconductor Structures'. In: ed. by J. M. Chamberlain, Laurence Eaves and Jean-Claude Portal. Boston, MA: Springer US, 1990. Chap. High-Frequency Applications of Resonant-Tunneling Devices, pp. 283–296. ISBN: 978-1-4684-7412-1. DOI: `10.1007/978-1-4684-7412-1_16`.

[10] E. R. Brown, T. C. L. G. Sollner, C. D. Parker, W. D. Goodhue and C. L. Chen. 'Oscillations up to 420 GHz in GaAs/AlAs resonant tunneling diodes'. In: *Applied Physics Letters* 55.17 (1989), pp. 1777–1779. DOI: `http://dx.doi.org/10.1063/1.102190`.

[11] E. R. Brown, W. D. Goodhue and T. C. L. G. Sollner. 'Fundamental oscillations up to 200 GHz in resonant tunneling diodes and new estimates of their maximum oscillation frequency from stationary-state tunneling theory'. In: *Journal of Applied Physics* 64.3 (1988), pp. 1519–1529. DOI: `http://dx.doi.org/10.1063/1.341827`.

[12] C.S. Kim and A. Brandli. 'High-Frequency High-Power Operation of Tunnel Diodes'. In: *Circuit Theory, IRE Transactions on* 8.4 (Dec. 1961), pp. 416–425. ISSN: 0096-2007. DOI: `10.1109/TCT.1961.1086849`.

[13] S. Suzuki, M. Shiraishi, H. Shibayama and M. Asada. 'High-Power Operation of Terahertz Oscillators With Resonant Tunneling Diodes Using Impedance-Matched Antennas and Array Configuration'. In: *Selected Topics in Quantum Electronics, IEEE Journal of* 19.1 (Jan. 2013), pp. 8500108–8500108. ISSN: 1077-260X.

[14] Hidetoshi Kanaya, Riku Sogabe, Takeru Maekawa, Safumi Suzuki and Masahiro Asada. 'Fundamental Oscillation up to 1.42 THz in Resonant Tunneling Diodes by Optimized Collector Spacer Thickness'. In: *Journal of Infrared, Millimeter, and Terahertz Waves* 35.5 (2014), pp. 425–431. ISSN: 1866-6906. DOI: `10.1007/s10762-014-0058-z`.

[15] P.D. Buckle, P. Dawson, M.A Lynch, Chun-Yi Kuo, Mohammed Missous and W.S. Truscott. 'An inter-subband device with terahertz applications'. In: *Microwave Theory and Techniques, IEEE Transactions on* 48.4 (Apr. 2000), pp. 632–638.

[16] H. Kanaya, H. Shibayama, S. Suzuki and M. Asada. 'Fundamental oscillation up to 1.31 THz in thin-well resonant tunneling diodes'. In: *Indium Phosphide and Related Materials (IPRM), 2012 International Conference on*. Aug. 2012, pp. 106–109.

[17] Masahiro Asada, Safumi Suzuki and Naomichi Kishimoto. 'Resonant Tunneling Diodes for Sub-Terahertz and Terahertz Oscillators'. In: *Japanese Journal of Applied Physics* 47.6R (2008), p. 4375.

[18] Takeru Maekawa, Hidetoshi Kanaya, Safumi Suzuki and Masahiro Asada. 'Oscillation up to 1.92 THz in resonant tunneling diode by reduced conduction loss'. In: *Applied Physics Express* 9.2 (2016), p. 024101.

[19] Sadao Adachi. 'Energy-Band Structure: Energy-Band Gaps'. In: *Properties of Semiconductor Alloys*. John Wiley & Sons, Ltd, 2009, pp. 133–228. ISBN: 9780470744383. DOI: `10.1002/9780470744383.ch6`.

[20] Sadao Adachi. 'Energy-Band Structure: Effective Masses'. In: *Properties of Semiconductor Alloys*. John Wiley & Sons, Ltd, 2009, pp. 229–258. ISBN: 9780470744383. DOI: `10.1002/9780470744383.ch7`.

[21] Sadao Adachi. 'Deformation Potentials'. In: *Properties of Semiconductor Alloys*. John Wiley & Sons, Ltd, 2009, pp. 259–273. ISBN: 9780470744383. DOI: `10.1002/9780470744383.ch8`.

[22] Sadao Adachi. 'Heterojunction Band Offsets and Schottky Barrier Height'. In: *Properties of Semiconductor Alloys*. John Wiley & Sons, Ltd, 2009, pp. 275–305. ISBN: 9780470744383. DOI: `10.1002/9780470744383.ch9`.

[23] *Optimization of the epitaxial design of high current density resonant tunneling diodes for terahertz emitters*. Vol. 9755. 2016, 97552W–10. DOI: `10.1117/12.2212346`.

[24] Michael J Kelly. 'The unacceptable variability in tunnel currents for proposed electronic device applications'. In: *Semiconductor Science and Technology* 21.12 (2006), p. L49.

Chapter 7

Conclusion and Future Investigation

In this thesis a series of nominally symmetric and asymmetric triple barrier resonant tunnelling structures (TBRTS) have been studied between 3K and 293K with the aim of improving the resonant tunnelling structures utilised in the current state of the art resonant tunnelling diode high frequency oscillators. Three main areas have been investigated:

i) The resonant tunnelling behaviour of a nominally symmetric and asymmetric TBRTS have been studied at low temperatures to provide a thorough understanding of the origin of the current resonances observed in measured current-voltage (I(V)) characteristics. The asymmetric structures, which have varying degrees of quantum well width asymmetry have been investigated to provide insight into how to optimise TBRTS designs for maximum transmission when on resonance and thus exhibit high peak current densities.

ii) The behaviour of the nominally symmetric and asymmetric triple barrier resonant tunnelling structures have been examined as a function of increasing sample temperature to aid the understanding of such devices at room temperature.

iii) Modifications to the triple barrier resonant tunnelling structure layer design have been investigated via simulations to realise an improved structure which theoretically out performs the barrier tunnelling structures being used in the current state of the art THz resonant tunnelling diode oscillators.

The investigations carried out in relation to (i), (ii) and (iii) have been detailed in chapters 4 to 6 respectively. In this chapter the main results of these studies are summarised and some relative future investigations briefly discussed.

7.1 Conclusions

The study of triple barrier resonant tunnelling structures at low temperatures has highlighted the many differences between the conventionally studied double barrier structures and those of the triple barrier structures studied in this thesis. Despite seeming quite similar, the addition of a third potential barrier increases the complexity of the resonant tunnelling processes available considerably. Whereas in double barrier structures the simple energetic alignment of the quasi-bound quantum well states with the emitter electron distribution results in a single current resonance, there are several different energetic alignment conditions possible in a triple barrier structure. Individual energetic alignment of the emitter and collector quantum well states with the three dimensional emitter can occur as well as the coincidental energetic alignment of the quasi-bound quantum well states with each other to form a subband in which the transmission coefficient through the structure can approach one.

In chapter 4 current resonances observed in the current-voltage (I(V)) characteristics of a nominally symmetric triple barrier resonant tunnelling structure have been attributed to the energetic alignment of the individual localised quantum well quasi-bound states with the conduction band edge (emitter electron distribution) at low temperatures. A simple linear voltage drop model combined with the calculation of the quasi-bound quantum well state energies allowed for the prediction of the voltage at which the resonance peak would occur and both experimental and theoretical values were in good agreement.

The more complex WinGreen [1] modelling package has been used to simulate theoretical I(V) characteristics for the nominally symmetric structure and examine the effect of charge accumulation in the emitter quantum well. It has been shown that significant charge accumulation occurs in the emitter quantum well, and that as a result the emitter quasi-bound quantum well state pins on resonance and remains resonant over a much larger voltage range than is observable without charge accumulation. These results confirm the observation previously made using photoluminescence and photoluminescence excitation spectroscopy measurements [2] and are an example of the added complication in designing a triple barrier resonant tunnelling structure for high frequency oscillation.

Analysis of the I(V) characteristics of a series of asymmetric triple barrier resonant tunnelling structures in which the width of the collector quantum well was reduced showed the merging of two resonant tunnelling conditions where the emitter and collector quasi-bound quantum well states energetically aligned with each other and the three dimensional emitter electron distribution. In the most asymmetric structure the merging of these two resonances resulted in a dramatic increase in tunnelling current thus enhancing the resonant peak current considerably at low temperatures. Resonances associated with the pinning of the emitter quantum well state due to charge accumulation were also observed for the asymmetric structures, however these were suppressed in the structures where the collector quantum well width was too narrow for an $n = 2$ quantum well quasi-bound state to be formed. The energetic alignment of the $n = 1$ emitter quantum well state with the $n = 2$ collector quantum well state was therefore attributed to be the mechanism by which the charge in the emitter quantum well was released.

Perimeter versus area analysis of the series of triple barrier resonant tunnelling structures showed that whilst the off resonance background current was dominated by a process which scaled with area, the on resonance peak current scaled with device perimeter, which was unexpected. A simple model has been developed to show that this occurs due to the relative difference between the device series resistance and the resistance of the triple barrier active structure. It has been shown that when off resonance, where the structure has a high resistance the current distribution across the entire device is quite uniform. However, when on resonance, where the structure has a low resistance, the series resistance (e.g. GaAs contact layer) is much larger and hence the current takes the path of least resistance around the perimeter of the mesa. With a reduction in mesa area the effect diminishes and so the current distribution across the device becomes more uniform and thus an increase in the resonance peak current density is observed. This highlights the need for a highly conductive material to minimise the series resistance and this effect as well as the requirements for smaller area devices.

The effect of device self heating was also investigated in chapter 4 in which a small difference between continuous wave and pulsed measurements were observed. This difference however was negligible in comparison to the resonance peak current and so there were no significant effects from device self heating. No significant differences were seen in the I(V) characteristics in regions of charge accumulation and state pinning by using pulsed voltage measurements and thus it has been concluded that the charge accumulation process occurs on a much faster time scale than the applied voltage pulses on the order of a few hundred microseconds.

The work presented in chapter 5 focused on the study of the triple barrier resonant tunnelling structure I(V) characteristics over a wide temperature range from 3K to 293K and builds on previous published work [3]. The nominally symmetric structure has been examined with increasing sample temperature in which a novel current resonance which is not observed at low temperature emerges and increases in magnitude with increasing temperature. This behaviour is rare in systems which are controlled by quantum mechanical effects and is also observed in the triple barrier resonant tunnelling structures with asymmetric quantum wells, with the temperature at which the new feature emerges decreasing with increasing quantum well width asymmetry.

The emerging current resonance has been attributed to the energetic alignment of the $n = 1$ emitter and collector quantum well quasi-bound states to forming a doublet subband. In the nominally symmetric structure it has been found that this alignment occurs at energies well above the well defined emitter electron distribution and is only activated once the sample temperature has been raised sufficiently to promote charge carriers to energies equal to those of the aligned subband states. Transmission through these aligned states is extremely high and with increasing quantum well width asymmetry this alignment occurs at energies closer to the Fermi level due to the increased bias required to align the quasi-bound states. Thus charge carriers at lower energies tunnel through the structure and hence this resonance emerges at lower temperatures for structures with a higher degree of asymmetry.

The amount of energy required to activate this resonance condition (activation energy) has been extracted by analysis of Arrhenius plots of experimental data and theoretically calculated by simulating the current density through the structure when on resonance. Excellent agreement has been found between the experimentally extracted and theoretically calculated values in which an activation energy of zero equates to the subband alignment occurring at energies equal to the Fermi energy. The lowest activation energy was found to be in the most asymmetric structure where only a large single current resonance is observed.

The triple barrier resonant tunnelling structures studied in chapters 4 and 5 have been examined as to their potential to be utilised as high frequency oscillators as a function of temperature in chapter 6. It has been shown that the devices which can potentially operate at the highest frequencies are those with the largest peak to valley current ratios, as one would expect. The calculated maximum frequency of oscillation for the fabricated devices studied in this thesis was found to be $\approx 18\,\mathrm{GHz}$ at 3K with a calculated maximum output power at this frequency of $\approx 230\,\mu\mathrm{W}$, which is poor in comparison to state of the art resonant tunnelling oscillators which operate at room temperature [4].

The analysis of the frequency of oscillation and output power of these devices also indicated that the large single resonance observed at 3K for the most asymmetric structure is not a single resonance, but in fact two separate resonances which overlap but only form a single negative differential resistance region.

Simulations of the current-voltage characteristics for various triple barrier resonant tunnelling structures have been performed and are detailed in this chapter in an optimisation process design to improve on the current state of the art double barrier resonant tunnelling oscillators in use by switching to a triple barrier structure. An improved triple barrier structure which does not suffer from charge accumulation in the emitter quantum well and out performs the double barrier structures in both frequency of oscillation and output power density is presented. This structure takes into account the possibilities for epitaxial growth and utilises a strain balancing technique in the $\mathrm{In_{0.53}Ga_{0.47}As}$ lattice matched to InP with $\mathrm{In_{0.90}Ga_{0.10}As}$ quantum wells and AlAs potential barriers. However growth and fabrication of such a structure is still likely to be challenging and will require significant research before becoming manufacturable on a large scale at low costs.

7.2 Future Investigations

Further investigations of the work presented in this thesis are likely to focus on two main areas based on the work presented in chapter 6:

a) The development of a resonant tunnelling oscillator device utilising a triple barrier resonant tunnelling structure similar to the improved structure presented in section 6.3.2. With much of the fabrication and circuit design research already reported in the literature for double barrier resonant tunnelling structures the main challenge is likely to be the growth of high quality resonant tunnelling structures. The tolerances in each active region epitaxy layer are extremely small and as such the epitaxy of a these layers with monolayer precision is extremely difficult to achieve across large wafers. Therefore whether scaling such processes up to a manufacturable level at low cost is attainable is still up for debate, however it expected that it will be possible to fabricated research devices.

b) The continued optimisation of the triple barrier high speed oscillator structure to further improve the maximum frequency of oscillation and output power density. There are still many parameters of these structures which can be varied to improve the structure design such as:

    i) Vary the emitter alloy composition to reduce the voltage at which the current resonances occur.

    ii) Modify the quantum well alloy composition to fine tune quantum well state alignments.

    iii) Grade the potential barrier alloy compositions to result in a symmetric structure on resonance, and thus increase the transmission coefficient through the aligned states to one.

    Other material systems such as InSb/AlSb also offer advantageous properties for resonant tunnelling structures such as a reduced electron effective mass and high room temperature mobility over the popular InGaAs/AlAs material system. However, high quality epitaxy of these material systems is extremely difficult due to the lack of available lattice matched substrates.

Bibliography

[1] *https://www.hs-rm.de/en/faculty-of-engineering/about-us/people/personen-im-fb-ing/michael-indlekofer/research-and-development/nanoelectronics/index.html.* URL. Hochschule RheinMain, University of Applied Sciences, Faculty of Engineering, 2015.

[2] P.D. Buckle, P. Dawson, C.Y. Kuo, A.H. Roberts, W.S. Truscott, M. Lynch and M. Missous. ‘Charge accumulation in GaAs/AIGaAs triple barrier resonant tunneling structures’. In: *Journal of Applied Physics* 83.2 (1998), pp. 882–887.

[3] C P Allford, R E Legg, R A O’Donnell, P Dawson, M Missous and P D Buckle. ‘Thermally activated resonant tunnelling in GaAs/AlGaAs triple barrier heterostructures’. In: *Semiconductor Science and Technology* 30.10 (2015), p. 105035.

[4] Takeru Maekawa, Hidetoshi Kanaya, Safumi Suzuki and Masahiro Asada. ‘Oscillation up to 1.92 THz in resonant tunneling diode by reduced conduction loss’. In: *Applied Physics Express* 9.2 (2016), p. 024101.

Appendix A

Schrödinger-Poisson Modelling

One-dimensional self consistent Schrödinger-Poisson models can be used to simulate the electronic states in the conduction band of a semiconductor heterostructure. The Schrödinger equation is solved numerically to find the wavefuction of the allowed states and therefore the resultant space-charge distribution. Poisson's equation is then solved, calculating a modified band structure from the space-charge distribution of the solutions to Schrödinger's equation and the new, modified band structure is used to calculate new solutions to Schrödinger's equation. These equations are solved iteratively until the solutions have converged to within a predetermined tolerance.

In this appendix the basic theory used in the Schroödinger-Possion model will be developed and discussed whilst the model also considers modifications to the band structure due to dopant atoms, charge accumulation in the emitter and charge depletion in the collector regions of the structure the model used in this thesis assumes a linear voltage drop across the undoped spacers and device active regions. Charge accumulation in the quantum wells of the tunnelling structure is also considered in the model due to its affect on the operation and I(V) characteristics of these devices, however due to the computing resources required it has not been utilised in this thesis (a much quicker Green's function solution has been used in the WinGreen simulation package).

A.1 Computational Methods

There are a wide range of methods for solving ordinary and partial differential equations numerically, each with its own advantages and limitations. The methods used in this model, their advantages and limitations will be discussed.

A.1.1 Finite Difference Method

The finite difference method is a numerical method for approximating the solutions of ordinary or partial differential equations first developed in 1928 by Courant, Friedrichs and Lewy [1]. To solve a differential equation numerically the domain in which the solution is to be considered must be divided into a uniform grid of discrete points. In the case of the time-independent Schrödinger equation, the grid is imposed on the spatial element of the differential equation and finite difference equations are used to approximate derivatives.

It can be shown from a Taylor Series expansion that the centred finite difference method first order differentials with second order accuracy of a function $f(z)$ with grid step size δz is approximated to:

$$\frac{\partial f}{\partial z} \approx \frac{f(z+\delta z) - f(z-\delta z)}{2\delta z} \tag{A.1}$$

Similarly the second order differentials are approximated to:

$$\frac{\partial f}{\partial z} \approx \frac{f(z+\delta z) + 2f(z) - f(z-\delta z)}{\delta z^2} \tag{A.2}$$

The accuracy of these approximations depend on two factors, the discretisation error and the rounding error. The discretisation error (or truncation error) of the finite difference equations A.1 and A.2 can be shown to be proportional to δz^2 and as such can be reduced by using a finer grid with smaller grid step sizes, however this comes at the cost of increased computational time [2, 3]. The rounding error is the difference between the calculated approximation of a number, represented by a finite digit number and its exact mathematical real value. This error can be reduced by use of higher precision floating point numbers during computational calculations.

A.1.2 Variable Effective-Mass Shooting Equation

In real semiconductor heterostuctures the effective mass of charge carriers varies between dissimilar material layers. As a result, to correctly model the behaviour of the heterostructure the variable effective mass form of Schrödinger's equation in one dimension must be considered:

$$-\frac{\hbar^2}{2}\frac{\partial}{\partial z}\frac{1}{m^*(z)}\frac{\partial}{\partial z}\psi(z) + V(z)\psi(z) = E\psi(z) \tag{A.3}$$

Solving equation A.3 requires the use of a numerical method to calculate solutions for the energy eigenvalues, E and eigenfunctions, $\psi(z)$ for any $V(z)$. To do this a numerical method known as the "Shooting Method" [4] is used, and is a way of obtaining solutions to a boundary value problem by instead calculating solutions of an initial value problem.

Simple rearrangement of equation A.3 into a form suitable for the centred finite difference shooting method results in:

$$\frac{\partial}{\partial z}\frac{1}{m^*(z)}\frac{\partial}{\partial z}\psi(z) = \frac{2}{\hbar^2}[V(z)-E]\psi(z) \tag{A.4}$$

Expansion of the left hand side (L.H.S.) of equation A.4 leads to:

$$-\frac{1}{[m^*(z)]^2}\frac{\partial}{\partial z}m^*(z)\frac{\partial}{\partial z}\psi(z) + \frac{1}{m^*(z)}\frac{\partial^2}{\partial z^2}\psi(z) = \frac{2}{\hbar^2}[V(z)-E]\psi(z) \tag{A.5}$$

However, finite difference shooting equations derived from equation A.5 produce solutions with significant computational inaccuracies for systems with large discontinuities in the effective mass, $m^*(z)$. These inaccuracies are thought to arise from the delta-function like nature of $\frac{\partial m^*(z)}{\partial z}$ at the discontinuities and are problematic for simulation of systems with abrupt changes in effective mass, such as semiconductor heterostructures. A more accurate expression may be derived by expanding the L.H.S. derivatives of equation A.4 in terms of finite differences (equations A.1 and A.2):

$$\frac{\frac{1}{m^*(z+\delta z)}\left.\frac{\partial\psi(z)}{\partial z}\right|_{z+\delta z} - \frac{1}{m^*(z-\delta z)}\left.\frac{\partial\psi(z)}{\partial z}\right|_{z-\delta z}}{2\delta z} = \frac{2}{\hbar^2}[V(z)-E]\psi(z) \tag{A.6}$$

Further expansion of equation A.6 in terms of finite differences and making the transformation $2\delta z \rightarrow \delta z$ leads to the variable effective-mass shooting equation:

$$\frac{\psi(z+\delta z)}{m^*(z+\frac{\delta z}{2})} = \left[\frac{2(\delta z)^2}{\hbar^2}[V(z)-E] + \frac{1}{m^*(z+\frac{\delta z}{2})} + \frac{1}{m^*(z-\frac{\delta z}{2})}\right]\psi(z) - \frac{\psi(z-\delta z)}{m^*(z-\frac{\delta z}{2})} \tag{A.7}$$

Where the effective mass, $m^*(z \pm \frac{\delta z}{2})$ can be found by calculating the mean of the effective mass at two adjacent grid points, z and $z \pm \delta z$. Equation A.7 shows that for a known value of E if $\psi(z)$ and $\psi(z-\delta z)$ are known then the wavefunction at $\psi(z+\delta z)$ can be calculated. Following this, a simple transformation $z + \delta z \rightarrow z$ allows a fourth value of the wavefunction to be calculated, and so on, thus a complete wavefunction can be found.

A.2 Boundary Conditions and Practical Implementation

As with all solutions to ordinary or partial differential equations it is important to select proper initial and boundary conditions. It has been shown in section A.1.2 that from equation A.7 the full wavefunction, $\psi(z)$ at a given energy, E can be calculated given the first two values $\psi(z-\delta z)$ and $\psi(z)$. If a situation where the two known points, $\psi(z-\delta z)$ and $\psi(z)$ lie within a quantum well where $V(z)=0$, but the next point to be calculated lies across a heterojunction in a barrier then:

$$\frac{\psi(z+\delta z)}{m^*(z+\frac{\delta z}{2})} = \left[\frac{2(\delta z)^2}{\hbar^2}[-E] + \frac{1}{m^*(z+\frac{\delta z}{2})} + \frac{1}{m^*(z-\frac{\delta z}{2})}\right]\psi(z) - \frac{\psi(z-\delta z)}{m^*(z-\frac{\delta z}{2})} \tag{A.8}$$

Considering the limit where $\delta z \to 0$ such that the terms of δz^2 are eliminated and rearranging gives:

$$\frac{1}{m^*(z+\frac{\delta z}{2})}\left[\psi(z+\delta z)-\psi(z)\right] = \frac{1}{m^*(z-\frac{\delta z}{2})}\left[\psi(z)-\psi(z-\delta z)\right] \tag{A.9}$$

From which it is possible to see that this obeys the boundary conditions of continuity across a semiconductor interface known as the Bastard conditions [5]:

$$\frac{1}{m^*_{LHS}}\frac{\partial\psi}{\partial z}\Big|_{LHS} = \frac{1}{m^*_{RHS}}\frac{\partial\psi}{\partial z}\Big|_{RHS} \tag{A.10}$$

General initial conditions used for the shooting method solution of Schrödinger's equation take the form:

$$\psi(z-\delta z) = 0 \tag{A.11}$$

$$\psi(z) = 1 \tag{A.12}$$

These starting conditions are used due to their generality as they are applicable to any confining potential profile, whether or not it is symmetric. These also apply whether the eigenstate of interest is symmetric, antisymmetric or without definite parity. The actual magnitude of the eigenfunction is not relevant since the energy eigenvalues of the linear Schrödinger equation remain unchanged when the wavefunction is scaled by any constant. However it is worth noting that the wavefunctions obtained from this numerical calculation are not normalised, although this can be easily achieved by making the following transformation:

$$\psi(z) \to \frac{\psi(z)}{\sqrt{\int_{-\infty}^{\infty}\psi^*(z)\psi(z)\delta z}} \tag{A.13}$$

Until this point it has been assumed that the eigenvalue energy, E has been known, however, generally this is not the case and E is an unknown. Therefore ψ is actually a function of both position and energy, $\psi(z,E)$, and although a wavefunction can be generated for any E, stationary state solutions in a confining potential require that as $z \to \infty$ the wavefunctions must satisfy the boundary conditions:

$$\psi(z,E) \to 0 \tag{A.14}$$

$$\frac{\partial \psi(z,E)}{\partial z} \rightarrow 0 \tag{A.15}$$

For energies where there is no stationary state solution the wavefunction will diverge to $-\infty$ or $+\infty$. In the practical implementation of the variable effective-mass shooting equation the energy is systematically varied until the wavefunction switches from diverging to $+\infty$ to $-\infty$. Figure A.1 illustrates that between these two values of E an energy exists for which the wavefunction will tend to zero.

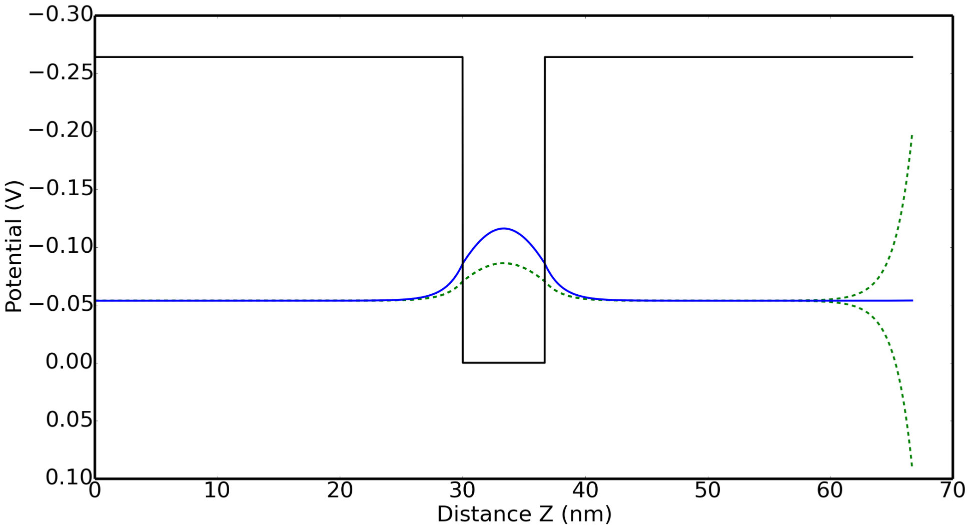

FIGURE A.1: Numerically obtained wavefunctions for an electron in a conduction band potential profile (solid black line) for a 67Å wide GaAs quantum well with $Al_{0.33}Ga_{0.67}As$ barriers of height 0.264 eV. The true n = 1 steady state solution is shown (solid blue line) at $E = -53.6414160$meV. Wavefunctions (dashed green lines) ±0.1neV the energy of the true solution are also shown diverging to $+\infty$ to $-\infty$.

If a switch of divergence is found then an iteration scheme is used to find the true solution. The Newton-Raphson method is a scheme for successively finding better approximations to the roots (or zeroes) of a real-valued function. Using an initial trial value, E_n, that is reasonably close to the true root, the function is approximated using a tangent line and the intercept of this line calculated. Typically the tangent intercept is a better approximation to the original trial value and the method is iterated until $\psi(\infty, E_n) \rightarrow 0$ within a predetermined tolerance. The Newton-Raphson equation for the *nth* iteration takes the form:

$$E_{n+1} = E_n - \frac{f(E_n)}{f'(E_n)} \tag{A.16}$$

Once the value of E for the true solution is found the energy can again be systematically varied until all the true solutions within the defined energy range have been found.

A.3 Poisson's Equation for Electrostatics

The methods described in section A.2 can be used to accurately describe systems with a single charge carrier, however, in many semiconductor devices there are often a large number of charge carriers. The spacial distribution of these charge carriers can give rise to a significant additional potential on top of the usual band edge potential and therefore it is necessary to solve the electrostatics of the system to accurately model the behaviour of semiconductor heterostructure devices.

The additional potential from the spacial distribution of charge carriers, V_ρ can be expressed using Poisson's Equation for Electrostatics:

$$\nabla^2 V_\rho = -\frac{\rho}{\epsilon} \tag{A.17}$$

Where ϵ is the permittivity of the material and ρ is the charge density of free charge carriers. The solution to equation A.17 can be obtained by using the relationship that:

$$\xi = -\nabla V \tag{A.18}$$

Where ξ is the electric field strength. The potential can then be calculated in the usual way:

$$V_\rho(z) = -\int_{-\infty}^{z} \xi \delta z \tag{A.19}$$

For a one-dimensional potential profile, $V_{CB}(z)$, a one-dimensional charge distribution will be produced and since the system is thought as infinite in the x-y planes then the charge density, $\rho(z)$ can be considered as an infinite plane ('sheet') with areal charge density $\sigma(z)$ and thickness δz.

As the areal charge density is infinite in the plane, then the strength of the electric field is constant for all distances from the plane. The total strength of the electric field perpendicular to the plane is therefore simply the sum of the individual contributions of the areal charge density with thickness δz:

$$\xi(z) = \sum_{z'=-\infty}^{\infty} \frac{\sigma(z')}{2\epsilon} \theta(z - z') \tag{A.20}$$

Where the function $\theta(z - z')$ has been included to account for the vector like nature of the electric field and is defined as:

$$\theta(z - z') = +1, \quad \text{where } z \geq z' \tag{A.21}$$

$$\theta(z - z') = -1, \quad \text{where } z < z' \tag{A.22}$$

In a doped semiconductor there are two contributions to the areal charge density. The first contribution comes from the ionised impurity atoms and the second from the free charge carriers. Generally the average spatial distribution of ionised impurities is known from the growth specifications[*], however the spacial distribution of free charge carriers needs to be calculated from the probability distributions of the carriers in the semiconductor heterostructure. Therefore net areal charge density is given by :

$$\sigma(z) = q\left[N\psi^*(z)\psi(z) - D(z)\right]\delta z \tag{A.23}$$

Where q is the charge of the majority carriers, N is the total number of free charge carriers per unit cross-sectional area, $D(z)$ is the volume density of dopants and $\psi^*(z)\psi(z)$ is the probability distribution of the subband ψ. If the charge carriers are distributed over more than one subband then the areal charge density is summed across the relevant subbands.

A.4 The Self-Consistent Schrödinger-Poisson Model

The potential $V_\rho(z)$ due to the charge density can have a significant effect on the overall potential profile $V(z)$. It is therefore necessary to ensure that this is taken into account when modelling the behaviour of semiconductor devices. To do this the potential $V(z)$ in equation A.1.2 is modified by making the following transformation:

$$V(z) \rightarrow V_{CB}(z) + V_\rho(z) \tag{A.24}$$

where $V_{CB}(z)$ represents the band edge potential with zero doping. However, the charge distribution required to calculate V_ρ depends on the the wavefunctions $\psi(z)$ and so it is necessary to iteratively solve Schrödinger's and Poisson's equations. To do this a closed loop is formed in which Schrödinger's equation is solved, the potential V_ρ from the resulting charge distribution is then calculated and added to the original band edge potential. Schrödinger's equation is solved once again and the process is repeated until the energy eigenvalues converge to a within a predetermined tolerance, at which point the wavefunctions are considered to be solutions of Schrödinger's and Poisson's equations simultaneously. The solutions are therefore described as self-consistent.

The first loop of the self-consistent cycle produces the majority of the change in the potential due the charge distribution and can have a significant effect on the potential profile. Figure A.2 shows the effect of the additional potential due to accumulation of electrons in a doped quantum well

---

[*] However this is not always the case, due to the diffusion of dopant or the dopant being carried forward on the growth plane. Generally cross referencing with cross sectional secondary ion mass spectrometry (SIMS) analysis is used to determine the actual level of doping.

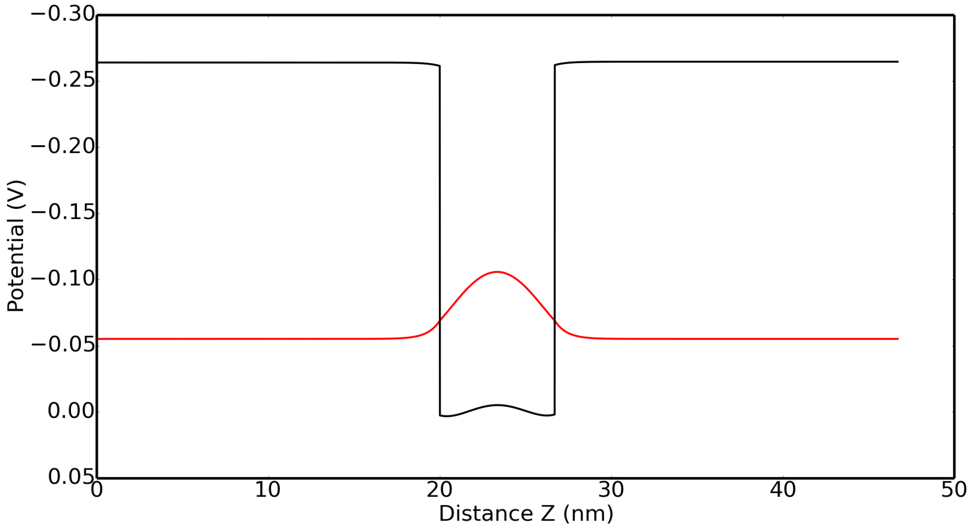

FIGURE A.2: Numerically obtained conduction band potential profile (black) for a 67Å wide n-type doped GaAs quantum well with doping density $1 \times 10^{19} cm^{-3}$ between two $Al_{0.33}Ga_{0.67}As$ undoped barrier regions with barrier height 0.264V. The probability distribution of the n=1 confined solution is also shown (red).

Although the change in potential is small compared to the barrier potential it has a measurable effect on the energy of the n = 1 steady state in the quantum well, raising the energy by approximately $1.5meV$ compared to an undoped system. It is therefore easy to see why a self-consistent model must be used to accurately model the behaviour of semiconductor devices.

Bibliography

[1] Vidar Thomée. ‘From finite differences to finite elements: A short history of numerical analysis of partial differential equations’. In: *Journal of Computational and Applied Mathematics* 128.1–2 (2001), pp. 1–54.

[2] J. M. Ortega and W. G. Poole Jr. *An Introduction to Numerical Methods for Differential Equations*. Pitman Publishing Inc, 1981.

[3] W. F. Ames. *Numerical Methods for Partial Differential Equations*. Second. Academic Press Inc, 1977.

[4] P. Harrison. *Quantum Wells, Wires and Dots*. Second. John Wiley & Sons, Ltd, 2005.

[5] G Bastard. *Wave Mechanics Applied to Semiconductor Heterostructures*. Halsted Press, New York, 1988.

Appendix B

The WinGreen Simulation Package

The WinGreen simulation package is a freely avaiable software package developed by K. M. Indlekofer and J. Malindretos [1], with version 2.1 being used in the simulations described in this thesis. WinGreen is based on a non-equilibrium Green's function approach to quantum transport in lateral layered heterostructures. Detailed information on the physical background and operation of the WinGreen package can be found in the WinGreen help documentation, however a brief overview of some of the principles and input parameters used in this thesis are explained here.

WinGreen simulations are one-band calculations which consist of many layers of simulated material (one for each monolayer) that can be described by six parameters for each layer:

i) The effective mass.

ii) The scattering parameter (which is an optical potential)

iii) The valence band energy offset

iv) The layer doping concentration (however WinGreen only support n-type doping)

v) Doping donor energy level (relative the conduction band edge)

vi) Relative dielectric constant

The material specific parameters such as effective mass, valence band offset and relative dielectric constant are described for each material in a separate material database file, along with the dimensions of a monolayer. For the structures studied in this thesis the materials database has been constructed from values extracted from [2–5].

The simulation package jobfile creation wizard then allows the user to define the simulated device structure in several different layers across three regions, the emitter, device and collector. The user defines which layers make up the device region because only there thermodynamic non-equilibrium is assumed in the calculation i.e. the emitter and collector are reservoirs with a given chemical potential (Fermi level) and temperature, where a non-equilibrium distribution is calculated via Green's functions which take into account particle injection and absorption. The appropriate choice of boundary conditions is therefore very important, however for devices such as tunnelling structures the barrier positions are usually an appropriate choice (as the reservoirs are considered low resistance regions, whilst the device region is considered to be resistive).

The parameters required for each layer in any of the regions are:

i) The layer thickness (nm or monolayers-if a prefix "M" is used).

ii) The layer material (which is defined in the materials database)

iii) The scattering potential

iv) The layer doping concentration

v) Doping donor activation energy

General simulation parameters such as the emitter and collector starting potentials (which is useful to reduce computation time), the start and end voltages, with the number of voltage steps and sample temperature are also set in the jobfile creation wizard. The simulations performed in this thesis using the WinGreen package calculated the charge distribution quantum mechanically throughout the entire structure however the WinGreen package also offers the ability to calculate the charge distribution quantum mechanically for the device region only for or bulk charge throughout the structure.

Several optional output files are available to be calculated in the WinGreen package, such as the conduction and valence band potentials, calculated current density, transmission coefficient and local density of states (LDoS). For the majority of structures simulated in this thesis the local density of states has not been calculated except for those structures for which it is shown in chapter 4.

Details of the input parameters for the layers simulated in sections 4.3.1 and 4.3.2 are shown in tables B.1 and B.2 respectively. The WinGreen simulation package does not consider degenerately doped materials and therefore to simulate this affect at low temperature a large doping activation energy (1.42 eV below the conduction band edge) is used as shown in tables B.1 and B.2 for the heavily doped contact layers, ensuring that at low temperature (3K) the carriers remain ionised. For room temperature simulations such as those reported in chapter 6 the correct ionisation energy has been used as this temperature all of the carriers are ionised and contribute to the conduction band.

Table B.1: The WinGreen input parameters for the double barrier resonant tunnelling structure simulations shown in section 4.3.1.

Thickness (nm)[a]	**Material**	**Scattering Parameter**	**Doping (10^{16} cm^{-3})**[b]	**Doping energy level (eV)**[c]
20	GaAs	5e-7	700	1.4200
10	GaAs	5e-7	30	1.4200
10	GaAs	5e-7	0.01	0.0054
4.5	$Al_{0.33}Ga_{0.67}As$	1e-10	0.01	0.0054
M23.8	GaAs	1e-10	0.01	0.0054
4.5	$Al_{0.33}Ga_{0.67}As$	1e-10	0.01	0.0054
20	GaAs	5e-7	0.01	0.0054
M1	GaAs	5e-3	S300	1.4200
20	GaAs	5e-7	700	1.4200

---

[a] or monolayers, denoted by the prefix “M”.
[b] or sheet density, denoted by the prefix “S”.
[c] relative to the conduction band minimum.

Table B.2: The WinGreen input parameters for the double barrier resonant tunnelling structure simulations shown in section 4.3.1.

Thickness (nm)[a]	**Material**	**Scattering Parameter**	**Doping (10^{16} cm^{-3})**[b]	**Doping energy level (eV)**[c]
20	GaAs	5e-7	700	1.4200
10	GaAs	5e-7	30	1.4200
10	GaAs	5e-7	0.01	0.0054
4.5	$Al_{0.33}Ga_{0.67}As$	1e-10	0.01	0.0054
M23.8	GaAs	1e-10	0.01	0.0054
4.5	$Al_{0.33}Ga_{0.67}As$	1e-10	0.01	0.0054
M23.8	GaAs	1e-10	0.01	0.0054
4.5	$Al_{0.33}Ga_{0.67}As$	1e-10	0.01	0.0054
20	GaAs	5e-7	0.01	0.0054
M1	GaAs	5e-3	S300	1.4200
20	GaAs	5e-7	700	1.4200

---

[a] or monolayers, denoted by the prefix “”.
[b] or sheet density, denoted by the prefix “S”.
[c] relative to the conduction band minimum.

Bibliography

[1] *https://www.hs-rm.de/en/faculty-of-engineering/about-us/people/personen-im-fb-ing/michael-indlekofer/research-and-development/nanoelectronics/index.html.* URL. Hochschule RheinMain, University of Applied Sciences, Faculty of Engineering, 2015.

[2] Sadao Adachi. ‘Energy-Band Structure: Energy-Band Gaps’. In: *Properties of Semiconductor Alloys.* John Wiley & Sons, Ltd, 2009, pp. 133–228. ISBN: 9780470744383. DOI: `10.1002/9780470744383.ch6`.

[3] Sadao Adachi. ‘Energy-Band Structure: Effective Masses’. In: *Properties of Semiconductor Alloys.* John Wiley & Sons, Ltd, 2009, pp. 229–258. ISBN: 9780470744383. DOI: `10.1002/9780470744383.ch7`.

[4] Sadao Adachi. ‘Deformation Potentials’. In: *Properties of Semiconductor Alloys.* John Wiley & Sons, Ltd, 2009, pp. 259–273. ISBN: 9780470744383. DOI: `10.1002/9780470744383.ch8`.

[5] Sadao Adachi. ‘Heterojunction Band Offsets and Schottky Barrier Height’. In: *Properties of Semiconductor Alloys.* John Wiley & Sons, Ltd, 2009, pp. 275–305. ISBN: 9780470744383. DOI: `10.1002/9780470744383.ch9`.

Appendix C

Photoluminescence Excitation Measurements (PLE)

In 1997 a novel method for optical characterisation of resonant tunnelling structures using photoluminescence excitation (PLE) spectroscopy was reported [1]. This method allowed for non-destructive characterisation of as-grown semiconductor wafers without the need for expensive and time consuming device fabrication and electrical measurements.

Photoluminescence (PL) spectroscopy had previously been shown to be a powerful technique for studying several different characteristics of resonant tunnelling structures [2, 3], however characterisation of resonant tunnelling structures with zero applied bias remained difficult. These problems were caused in essence due to the rapid escape of the photo-injected charge carriers from the quantum wells before any recombination could occur and so resulted in very little, or no photoluminescence observed from the quantum well regions.

The novel technique is a variant on Photoluminescence Excitation (PLE) spectroscopy in which the luminescence intensity from the resonant tunnelling structure contact layers was monitored. Using this technique transitions involving the $n = 1$ electron to $n = 1$ heavy hole and $n = 1$ electron to $n = 1$ light hole were observed where the photocreated electron/hole pairs and excitons in the quantum well rapidly escape into the heavily doped contact layers. This results in an increase in the luminescence observed from the heavily doped contact layers and therefore from the energy of the luminescence observed the width of the quantum associated quantum well can be estimated.

The technique described here was used to estimate the widths of the quantum wells in the GaAs/$\mathrm{Al_{0.33}Ga_{0.67}As}$ triple barrier resonant tunnelling structures described in table 3.1. Similar techniques to these have since been used in the optical characterisation of resonant tunnelling structures [4, 5].

Bibliography

[1] P.D. Buckle, P. Dawson, M. Missous and W.S. Truscott. 'Full wafer optical characterisation of resonant tunnelling structures using photoluminescence excitation spectroscopy'. In: *Journal of Crystal Growth* 175-176.PART 2 (1997), pp. 1299–1302.

[2] M S Skolnick, D G Hayes, C R H White, P E Simmonds, L Eaves, A W Higgs, M Henini, O H Hughes, G W Smith and C R Whitehouse. 'Optical Spectroscopy of Double Barrier Resonant Tunneling Structures'. In: *Physica Scripta* 1991.T39 (1991), p. 271.

[3] M S Skolnick, P E Simmonds, D G Hayes, C R H White, L Eaves, A W Higgs, M Henini, O H Hughes, G W Smith and C R Whitehouse. 'Electron transport in double-barrier resonant tunnelling structures studied by optical spectroscopy'. In: *Semiconductor Science and Technology* 7.3B (1992), B401.

[4] P.D. Buckle, P. Dawson, C.Y. Kuo, A.H. Roberts, W.S. Truscott, M. Lynch and M. Missous. 'Charge accumulation in GaAs/AIGaAs triple barrier resonant tunneling structures'. In: *Journal of Applied Physics* 83.2 (1998), pp. 882–887.

[5] C.-Y. Kuo, M.A. Lynch, A.H. Roberts, P.D. Buckle, P. Dawson, M. Missous and W.S. Truscott. 'An electrical and optical study of electrons in triple barrier structures'. In: *Physica E: Low-dimensional Systems and Nanostructures* 2.1–4 (1998), pp. 815–819. ISSN: 1386-9477. DOI: http://dx.doi.org/10.1016/S1386-9477(98)00166-0.